Multi-segmented magnetic nanowires as multifunctional theranostic tools in nanomedicine

A Dissertation
SUBMITTED TO THE FACULTY OF
UNIVERSITY OF MINNESOTA
BY

Anirudh Sharma

IN PARTIAL FULFILLMENT OF THE REQUIREMENTS
FOR THE DEGREE OF
DOCTOR OF PHILOSOPHY

Adviser: Bethanie J.H. Stadler, Co-advisor: Allison Hubel

JULY 2015

Acknowledgements

I would like to express my sincere gratitude to Professor Stadler for giving me this opportunity to pursue this exciting area of research by providing me with the resources, expertise and guidance through the length of my PhD program.

I would like to thank Professor Hubel for providing me with the expertise in biology, guidance and essential laboratory training in biological applications of nanomaterials.

I would like to thank my funding programs. This work was primarily supported by the Grant in Aid, University of Minnesota and supported partially by the MRSEC Program of the National Science Foundation under Award Numbers DMR-0819885.

Parts of this work were carried out in the University of Minnesota Nanofabrication Center, Characterization Facility, and the University Imaging Center, which receive partial support from NSF through the NNIN program. I would like to thank the helpful staff in all these facilities.

Finally, I would like to thank all my laboratory members for providing a stimulating lab environment.

Dedication

This thesis is dedicated to my loving parents and sister.

Abstract

Nanomedicine is the development and use of nanostructured materials that have unique diagnostic and therapeutic effects owing to their size and structure. Current research efforts in this field have focused on eliminating cancer using novel nanoparticle-based therapeutics, e.g. heat induced tumor destruction via light or AC magnetic field excitation. This Ph.D. research presents a novel multifunctional nanoparticle, the multilayered magnetic nanowire, as a unique, robust and effective diagnostic and therapeutic (theranostic) platform for applications in translational nanomedicine.

Here, multilayered magnetic nanowires are synthesized *de novo* using high-throughput electrochemical deposition in nanoporous templates. The presented applications in nanomedicine exploit the fiber-like shape of the nanowire, which is used advantageously for magnetic multiplexing, drug-delivery and synthesis of artificial biomaterials through self-assembly. This research has addressed important engineering questions pertaining to the design and synthesis of the nanowire, including shape, size, composition, magnetic properties, surface functionalization, nanoparticle aggregation and integration of this technology with various biomedical applications. Further, the ensuing cellular and immunological responses were examined in-depth using a variety of techniques including cell-based assays and microscopy in order to address biocompatibility, immunogenicity, inflammatory properties, cytotoxicity and proliferative effects. The proven success of the multilayered nanowire in these applications makes it an indispensable diagnostic and therapeutic tool in nanomedicine and regenerative technology.

TABLE OF CONTENTS

List of Tables

List of Figures

Chapter 1

Chapter 2

Chapter 3

Chapter 4

Chapter 5

Chapter 1: Introduction

1.1 Nanotechnology

Nanotechnology is defined as the synthesis and study of functional materials, devices and systems through control of matter at the scale of 1 to 100 nm in at least one dimension and exploitation of novel properties and phenomena at the same scale[1].

1.2 Necessity of nanotechnology in cancer research

The past quarter century has seen an upsurge in fundamental discoveries in molecular and cancer biology. However, this has not been matched by a commensurate advance in clinical applications and eradication of diseases. This is, in part, due to, limitations of current technological tools in their capability to diagnose the disease and administer a targeted therapeutic with negligible side effects. The National Nanotechnology Initiative has therefore proposed the development of nanoscale tools for the detection and targeted eradication of diseases such as cancer[1] and, together with the National Cancer Institute's initiative, has led the emergence of nanomedicine.

1.3 Nanomedicine

Nanomedicine is the development and use of nano-structured materials that have unique diagnostic and therapeutic effects owing to their size and structure[2]. Strictly speaking, these material properties and associated effects are not always characterized by a step change in response on entering the nano-scale [3]. However, a gradual change in some effects is observed as the size of the entity is increased beyond the nanoscale to the micro scale. The National Cancer Institute (NCI) and the US National Institute of Health

(NIH) have set a goal of eliminating death and suffering due to cancer within this decade[4].

In order to achieve this goal, the NCI has put forward a cancer nanotechnology plan as one of the solutions with a special emphasis on multifunctional therapeutics [4–6].

1.4 Applications in Nanomedicine

Applications of nanoparticles in nanomedicine include:

1) Drug delivery: drugs/proteins are conjugated with particles to improve pharmacokinetics and bioavailability. The particle substrate can be polymeric, organic (liposomal) or inorganic (metallic) [5,7,8].

2) Therapeutic nanoparticle drugs: These nanoparticles have distinct therapeutic effects based on the structure and composition of particles. Examples of nanoparticle-based therapies are drug-delivery using dendrimers [7] and hyperthermia from iron oxide nanoparticles [9]. They differ from small molecule drugs in that they have superior pharmacokinetics [10].

3) Imaging contrast agents: Here nanoparticles can be used as imaging contrast agents in biological assays or animal models when combined with imaging techniques such as magnetic resonance imaging (MRI), localized surface plasmon resonance (LSPR), Raman spectroscopy or fluorescence microscopy. Unique magnetic and optical properties of the nanoparticles are exploited here. Example: plasmonic gold particles, iron oxide nanoparticles and quantum dots [11,12].

4) *In vitro* diagnostics/detection: Various sensing techniques including atomic force microscopy (AFM), magnetic sensing, and cantilever integrated with microfluidics for biomolecular sensing [13,14].

5) Biomaterials: Includes self-assembled nanobiomaterials [15] and artificial matrices [16,17] synthesized using nanoparticles for tissue engineering and *in vitro* modeling of diseases.

Drug delivery applications dominate the current nanomedicine landscape in terms of research activity and publications [2].

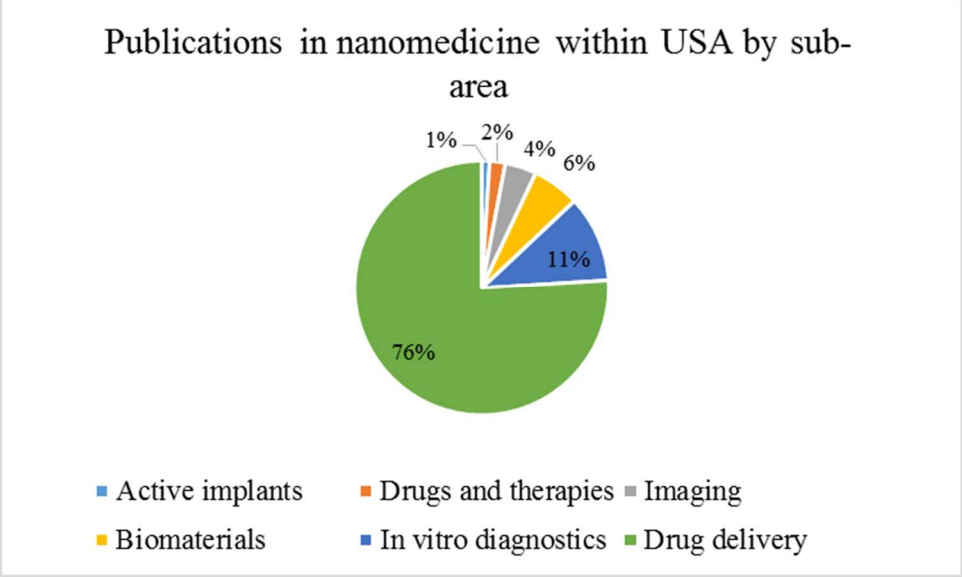

Figure 1.1: Breakdown of nanomedicine publications by sub-areas. Source: Science Citation Index (1984-2004) [2].

1.5 Testing nanomaterials with cells

The development of a therapeutic platform involves various stages. However, targeting, studying and manipulating cells with *in vitro* (cell culture) assays generally precedes any kind of animal testing. This is because the cell is the most fundamental unit of life which is responsible for a host of processes in every living organism – signal transduction, oxygen transport, muscle contraction, immune response, homeostasis and a range of metabolic activities [18]. Technologically, it is important to understand regulation of these activities because they are sources of regenerative medicine for translational clinical therapy (eg. stem cell research). Moreover, study of cellular responses help understand progression of diseases as they are fundamental biomarkers for various diseases including cancer.

The nanoscale size of nanoparticles allows binding and internalization by cells. This allows characterization of the trafficking mechanisms and pathways. The internalization mechanism and kinetics depend on the physical dimensions of the nanoparticles, the surface coating, the nanomaterial, the cell phenotype and environmental conditions like pH and temperature.

For example, when the surface of the nanoparticles are functionalized with specific ligands, various intracellular or membrane components of the cell can be targeted. Additionally, attachment of specific ligands to nanoparticle surfaces enables elicitation of specific cellular response to biomolecular cues presented by the ligand which may vary with ligand density, ligand chemistry, functional groups and environmental conditions.

1.6 Multifunctional nanoparticles

Multifunctional nanoparticles integrate various functions such as diagnostic and therapeutic capabilities into one platform. For example, the nanoparticle can have a conjugated drug but at the same have the capability of being used as an imaging contrast agent using MRI [19,20]. Thus, the nanoparticle can be tracked from the site of administration to the tumor site. On reaching the intended destination, the nanoparticle can be actuated/designed to release the drug at the tumor site. This requires addressing important engineering questions pertaining to the design and synthesis of nanoparticles, including shape, size, composition, magnetic properties, surface functionalization, nanoparticle aggregation and integration of this technology with various characterization/imaging techniques and platforms. The ensuing cellular responses require biological and immunological examination using techniques that include cell-based assays and microscopy to address biocompatibility, immunogenicity, inflammatory properties, cytotoxicity and proliferative effects. As a first step, these factors are evaluated *in vitro*.

1.7 Magnetic nanowires as multifunctional theranostic platforms:

Nanowires are cylindrical shaped nanoparticles with one dimension ≤ 100nm. The length of the nanowire can vary from 100 nm to generally up to 10s of μm.

The **hypothesis** of my thesis is that multilayered magnetic nanowires can be engineered to exhibit controlled magnetic, optical and surface properties to serve as integrated multifunctional platforms for applications in nanomedicine. Specifically, the topics that will be discussed include nanowire synthesis and properties, magnetic

multiplexing in biological assays, addressing particle aggregation and biocompatibility, targeting of cancer cells in drug-delivery applications and finally, using nanowires as a constituent element to engineer 3D self-assembled structures.

The following results will be shown:

1) Multilayered Au/Ni/Au nanowires can be synthesized in a high-throughput manner using electrochemical deposition in porous templates.

2) The magnetic properties of nanowires can be exploited to demultiplex a mixture of two magnetically different nanowires in diagnostic assays. As high as 97.5% accuracy can be obtained using first order reversal curves (FORC).

3) Ni segments of Au/Ni/Au nanowires can be chemically coated with a novel surface chemistry composed of heterobifunctional PEG in order to mitigate aggregation, improve experimental reproducibility and reduce cellular toxicity.

4) RGD-PEG-functionalized nanowires show increased cancer cell-targeting efficiency compared to PEG-coated nanowires. Additionally, RGD-functionalized nanowires elicit specific cellular responses such as proliferation and internalization which further lead to mitigation of aggregation through dispersal of nanowires in cell-culture. These results have important implications in drug-delivery

5) Magnetically aligned collagen-nanowire matrices can be synthesized to function as controlled microenvironments providing tunable mechanical and biomolecular cues to cells.

Nanowire dimensions can be controlled based on the choice of synthesis methods. Chapter 2 will focus on synthesis and characterization of nanowires using high-throughput electrochemical deposition in templates.

Chapter 3 focuses on the magnetic properties of the nanowires and how they can be exploited in a multiplexing application such as “barcoding”. Here, a mixture of two magnetically different nanowires will be demultiplexed using first order reversal curves (FORC).

Chapter 4 will introduce the interactions of nanowires with cells. Here, data from experiments conducted with the intended purpose of “tagging” (attaching) cells with nanowires will be presented. However, the central point of this chapter is the need for quality control in order to reduce heterogeneity in designed experiments with nanowires and cells and therefore, ensure repeatability.

The central point of chapter 4 paves the way for chapter 5 which focuses on surface functionalization of nanowires to address two main issues surrounding the use of inorganic nanoparticles for nanomedicine applications – aggregation and biocompatibility.

Chapter 6 builds on the surface coating introduced in chapter 5 by attaching a functional component, the RGD ligand, to it in order to specifically target osteosarcoma cells. Here, the use of the RGD-labelled nanowire as a potentially powerful therapeutic modality will be discussed. Some interesting cellular effects observed with RGD functionalized nanowires will also be discussed.

In chapter 7, the nanowire will be used in conjunction with collagen to engineer synthetic extracellular matrices through self-assembly.

Before closing this introduction, advantages of using nanowires over popularly used nanospheres are highlighted. While in literature, mostly spherical nanoparticles have been fabricated and employed in the nanomedicine applications [5], the nanowire has distinct advantages over the nano-sphere owing to its shape anisotropy. *:*

(i) The cylindrical geometry also allows segmentation along the length of the nanowire. Based on the thicknesses of the magnetic segments, suprafactorial magnetic signatures can be fabricated for nanowires in a barcoding application. This capability is unique to the nanowire and cannot be attained using nanospheres. This is discussed in greater detail in chapter 3.

(ii) Additionally, having segments of different materials (like Au and Ni) along the length of the nanowire allows developing different surface chemistries for the different layers which can serve different functions in a biological environment (Au segments can be used as fluorescent/radiolabel beacons while Ni segments can be used for specific targeting. Alternately, Au segments can be conjugated to a drug while Ni segments can be conjugated with a cell targeting peptide). This is discussed in greater detail in chapters 5 and 6.

(iii) A single nanowire has higher surface area than a single nanospherical particle of equal mass [21,22]. This implies a higher probability of targeting cells which is important for applications such as magnetic separation[22,23]. Moreover, a higher density of ligands on a larger surface results in stronger multivalent interactions[5] with the cells to

stimulate a specific responses. It also means a larger quantity of drug can be adhered to the surface per gram of nanomaterial for drug-delivery applications. The discussions pertaining to drug-delivery applications are explained at greater length in chapter 5.

(iv)The fibrillar geometry of the nanowire can be used to mimic certain extracellular matrix elements such as fibronectin when the nanowire is appropriately functionalized to present specific molecular cues to the cells in a multivalent fashion. While nanospheres have shown limited multivalent interactions by varying the ligand density, the nanowire allows greater control of ligand density and material-sequence along the nanowires length. Additionally, the fibrous shape of the nanowire allows induction of anisotropy at a larger length scale in artificial extracellular matrices through self-assembly.

Chapter 2: Synthesis and characterization of nanowires.

2.1 AAO

2.1.1 Templates for nanowire growth: Anodized alumina (AAO):

For the applications covered in this thesis, nanowires are fabricated through the electrochemical deposition inside porous templates. Candidate porous materials that are used as templates for electrodeposition are anodized aluminum oxide (AAO), block copolymer and track etched polymeric membranes [24–26].

Anodized aluminum oxide can be fabricated by oxidation of aluminum films/foils in an acidic electrochemical bath. Structurally, AAO is composed of hexagonally closed packed cells, with a pore at the center of each cell (figure 2.1). The pores can be controllably synthesized to be a few nanometers or 100s of nanometers in diameter. The length of the pores can be increased up to 100 μm. Thus, this method is preferred for fabrication of high-aspect ratio and high density pores.

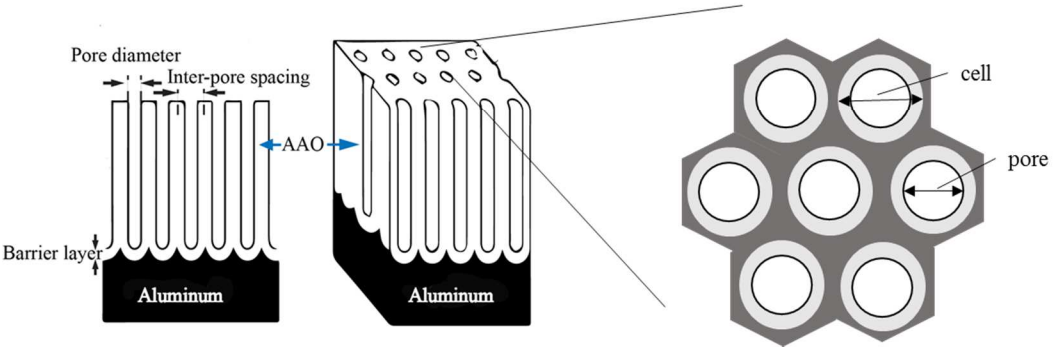

Figure 2.1: Schematic showing the porous structure of AAO.

2.1.2 AAO Fabrication process:

The basic schematic for anodization is shown in figure 2.2:

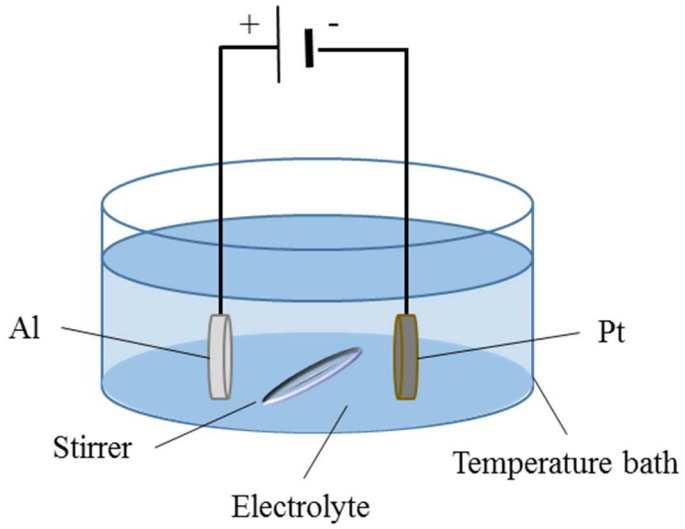

Figure 2.2: Electrochemical setup for anodization of aluminum for synthesizing nanoporous AAO.

This involves setting the aluminum sample to be anodized as anode (+) and a counter electrode (Pt) as cathode (-). Next the electrodes are immersed in an acidic bath which is maintained at a fixed temperature. Weak acids lead to the formation of barrier layer oxide and stronger acids lead to porous oxide formation. However, the type of oxide film also depends on the anodization time; a barrier type oxide can be converted to a porous oxide by increasing anodization time [27–29].

2.1.3 Mechanism:

Oxide formations starts at the metal-oxide interface at the bottom of the pores which leads to the conversion of aluminum film/foil to barrier-type oxide (figure 2.1). Next, the barrier oxide at the metal-oxide interface undergoes dissolution and conversion to porous oxide. This dissolution is attributed to increased localized fields at the barrier layer at the pore bottoms. A new barrier layer is formed at the metal-oxide interface and the process repeats. Steady state is reached when the rate of dissolution equals the rate of barrier layer formation. This leads to the formation of cylindrical pores. At the end of the anodization process, a barrier oxide layer exists at the bottom of the pores. This dielectric barrier oxide layer prevents electrodeposition in the pores, and thus, needs to be dissolved before template synthesis of nanowires. This can be achieved either via pulsed anodization [30], longer second anodization time in the case of a metallic sputtered back contact[31] or chemically etching the barrier layer oxide by floating the sample over phosphoric/chromic acid etchant (see methods section).

2.1.4 Kinetics*:*

The time lapse behavior of galvanostatic or potentiostatic anodization of aluminum is shown in the figure 2.3.There are 4 zones that can be defined in the process of pore formation and growth [32]. For galvanostatic conditions, the initial linear increase in voltage is associated with the growth of the non-conductive barrier oxide layer (stage a). As anodization progresses with time, tiny channels (pore precursors) propagate through the thickness of the oxide layer (stage b) which eventually leads to electric breakdown of the barrier layer (peak, stage c) with accompanied pore growth. This

process culminates with a steady-state growth of pores and constant voltage (stage d). Under constant potential anodization conditions, the current density initially decreases and quickly reaches a valley owing to the non-conductive barrier layer (stage a). Then a linear increase in current is seen as conductive channels are formed through the thickness of the oxide until a maxima is reached (stage b). Following this peak, a small reduction in current density (stage c) is followed by steady state current associated with pore growth (stage d).

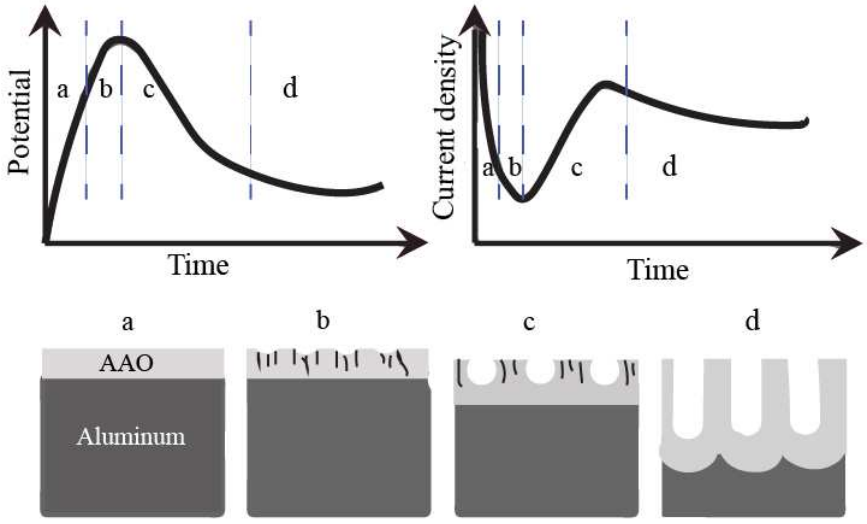

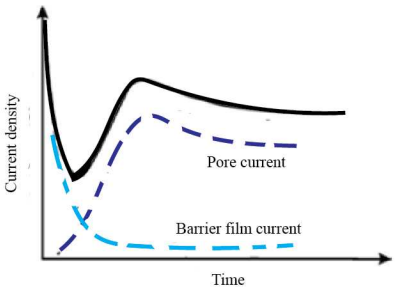

Figure 2.3: Kinetics of AAO formation from aluminum[32].

This behavior of current density can be explained as an overlay of two processes as shown in figure 2.3. Initial current density is mostly dominated by barrier formation until the pore formation current is larger and dominates the process. The barrier formation proceeds under constant field strength leading to the formation of uniformly thin film and uniform current distribution at the interface of the oxide and aluminum. Local variations on the aluminum surface and at the interface such as defects, cracks, dimples from nano-imprinting or grain boundaries can lead to inhomogeneities in field strength at these sites and result in non-uniform current distribution. This non-uniform distribution in current can cause increased oxide dissolution at the sites leading to the initiation of the pore growth process. This process can be exploited to create periodic artificial dimples or recesses on the aluminum surface which can act as nucleation sites for enhanced dissolution of the barrier oxide and formation of ordered pores.

2.1.5 Process parameters (qualitative relationships):

The pore diameter and the inter-pore spacing show a linear dependence on the applied voltage [33]. However, other parameters such as temperature, pH of the acid bath and stirring indirectly affect the pore diameter [34]. Under potentiostatic conditions, higher temperature leads to greater dissolution of the oxide, especially under strongly acidic conditions [34]. Increased stirring leads to increased uniformity in local temperature at the metal oxide interface. A reduction in pH (more acidic conditions) leads to the reduction in threshold potential for field-assisted dissolution at the pore bottom

leading to a quicker anodization rate [34]. The porosity, defined as the ratio of surface area occupied by the pores to the total surface area, generally varies between 8% and 30%, depending on the anodizing potential, electrolyte used and pH. Most commercial pores have a nominal porosity of ~ 10% (e.g., Synkera Inc.).

2.1.6 Reactions:

The anodization of aluminum proceeds through reaction at the surface of aluminum with the anionic species O^{2-} and/or OH^- [34] as follows:

$2H_2O + 2e^- \rightarrow 2OH^- + H_2$

$O_2 + 2H_2O + 4e^- \rightarrow 4OH^-$

$2Al^{3+} + 3H_2O \rightarrow Al_2O_3 + 6H^+ + 6e^-$

$2Al + 6OH^- \rightarrow Al_2O_3 + 3H_2O + 3e^-$

$2Al + 3O^{2-} \rightarrow Al_2O_3 + 6e^-$

Main contribution of the anodic current comes from oxidation of aluminum

$Al \rightarrow Al^{3+} + 3e$ (associated with porous oxide growth)

2.1.7 The advantages of template fabrication compared to colloidally prepared particles are:

(i) Highly ordered pores can be fabricated through self-assembly. The order and dimensions can be controlled at the nanometer scale by controlling process parameters such as temperature, choice of acidic bath and voltage.

(ii) This method overcomes the limitations of conventional lithography including time and cost.

(iii) While lithography is capable of long-range ordered pores compared to self-assembled pores, nano-imprinting of aluminum prior to anodization achieves the same result (section 2.2.1). The large area stamp itself can be fabricated using lithography. Additionally, this stamp can be used multiple times for synthesis of 100s of ordered pore samples before they degrade. The nano-dents on the surface of aluminum direct the nucleation and growth of pores.

2.1.8 Two-step anodization vs pre-patterned growth for synthesis methods

Porous aluminum oxide through the two-step anodization method involves two anodization steps and multiple complementary steps. Pre-treatment steps of aluminum involve degreasing (in acetone and ethanol) and electro-polishing. The next step involves anodization of the aluminum surface under acidic conditions (180V in 0.1M phosphoric acid at 1^0C for 30 minutes) and constant potential. The formed oxide layer is then chemically etched to reveal the new aluminum surface which has dimples/recesses which act as masks for the second anodization step. The second anodization is then conducted under identical conditions as the first anodization. This leads to the formation of regular closed packed hexagonal pores. The aluminum base can be removed via chemical etching with wet etchants (refer to section 2.3.1 for experimental details).

In contrast, pre-patterned growth starts with artificially creating nano-patterned dimples on the surface of aluminum using a stamp containing ordered arrays of pillars or needles (section 2.2.1). The concave recesses in the aluminum surface are negatives of the convex pillars on the stamp. The stamp or mold itself is synthesized using e-beam lithography or interference lithography and pattern transfer techniques. Imprinting can be

done by simply using a hydraulic press. Once the imprinted pattern is formed on the aluminum surface, only a one-step anodization process is required (180V in 0.1M phosphoric acid at 1^0C for 30 minutes) for formation of highly periodic and monodisperse pores ($d_{interpore}$ = 385.6 nm). The pre-patterned dimples serve as nucleation points for vertical pore growth. Figure 2(a,b,c)) show hexagonally closed packed pore-arrangement. (refer to sections 2.3.2 and 2.3.3 for experimental details).

2.2 AAO Results

2.2.1 Structure of AAO

After the first anodization of aluminum, an array of pores is formed which suffers from polydispersity in pore diameters and inter-pore spacing. These templates also lack long range order despite exhibiting a close-packed-like pore arrangement (Figure 2.4).

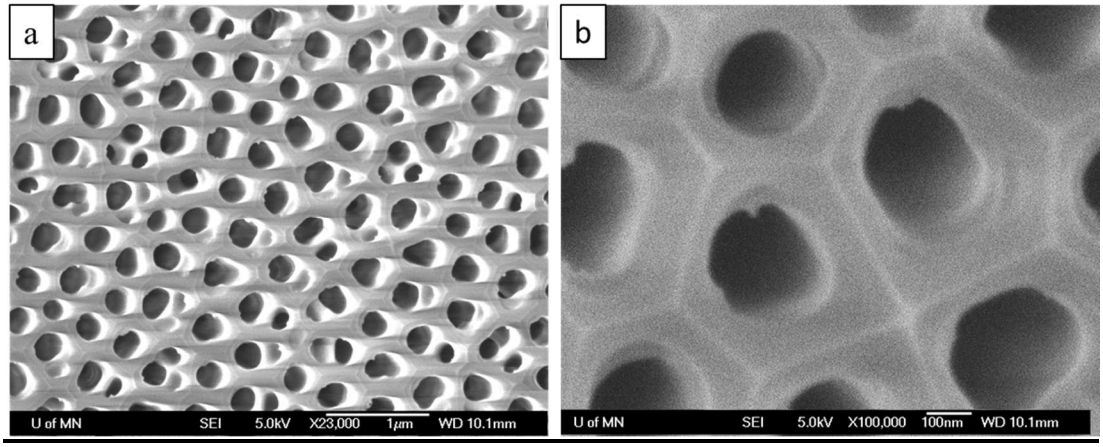

Figure 2.4 Top surface SEM images of first anodized AAO. The observed closed packed structure is not very periodic. The average pore diameter here is 67.7 nm with σ=9.5%. The average inter-pore spacing is 92.7 nm with σ = 13.3%.

To improve the lattice arrangement and obtain long range order, two-step anodization is conducted. Here, the first anodized AAO is etched using 1M NaOH (section 2.3.1). The exposed aluminum surface now has concave recesses that serve as nucleation points for the next anodization step (figure 2.5). The exposed aluminum surface is then re-anodized under identical conditions to form porous AAO. These pore still suffer from polydispersity in pore diameters and inter-pore spacing (figure 2.5). A pore-widening step using 5% wt. phosphoric acid can help reduce the polydispersity in pore diameters.

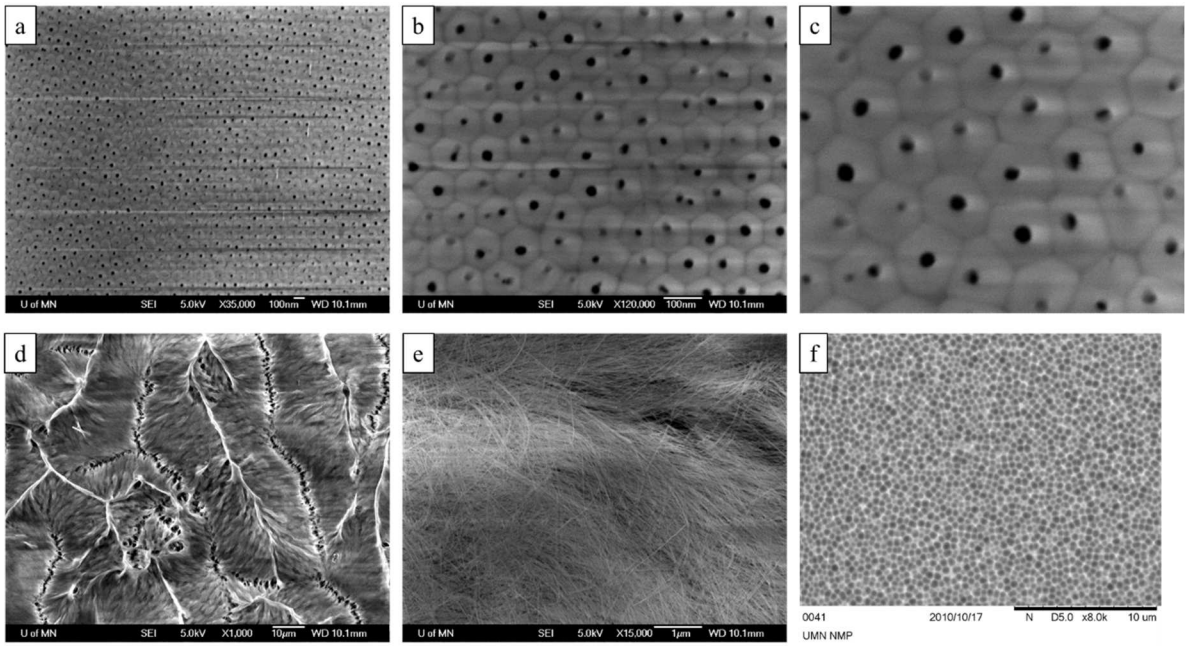

Figure 2.5 Second anodization of AAO. (a-c) Top-view SEM images of second-anodized AAO surface taken at various magnifications. Average pore diameter = 25.3 nm with σ =

19%. Average inter-pore spacing = 100.2 nm with σ = 13.53%. (d and e) show AAO in the process of being etched in 1M NaOH; it acquires fibrous structure before complete dissolution. Figure 2.5(f) shows the recesses on the Al surface after the AAO is completely etched. These dimples act as nucleation sites for subsequent pore growth through second anodization.

Pre-patterned AAO, in contrast, exhibits long-range order and mono-disperse pore diameters, commensurate with the imprint area of the stamp (figure 2.6 and 2.7). Following imprinting using a hydraulic press (1000 lb/sq.in), anodization was done by applying a constant voltage under acidic conditions (sections 2.3.2 and 2.3.3 for experimental details).

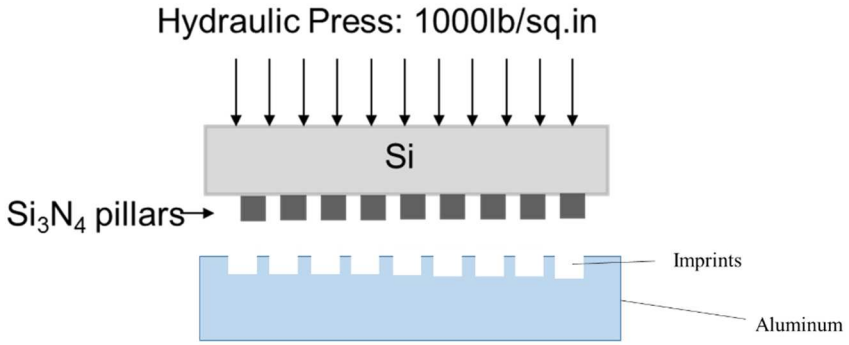

Figure 2.6: Schematic showing imprinting of Al surface with a home-made silicon nitride stamp using a hydraulic press.

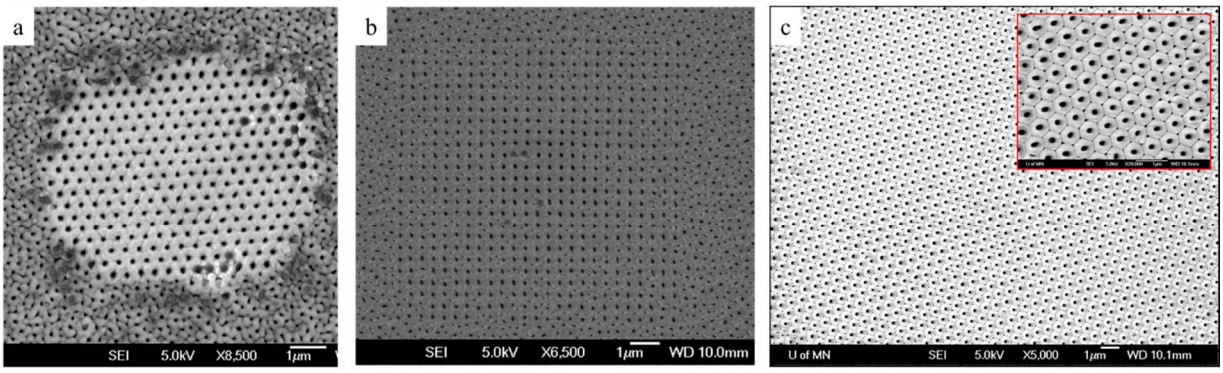

Figure 2.7: AAO formed on nano-imprinted Al. (a) shows a section of anodized aluminum after imprinting with 9.6 μm x 9.6 μm stamp. The average pore diameter in this region is 102.7 nm with $\sigma = 9.233\%$. The average inter-pore spacing is 385.6 nm with $\sigma = 2.82\%$. The surrounding space is standard first-anodized AAO (no imprint). (b) shows a square nanopore array. Anodization under same conditions as (a) does not yield a perfect square array. Defects, such as pores between imprinted pores, are observed which suggests, self-assembly of pores still prefers a hexagonally closed packed arrangement. (c) shows ordered hexagonally close-packed pores which have intentionally been synthesized such that smaller pores are seen between the larger pores using a process called pore multiplication [35].

The standard deviations in pore diameters and interpore spacing in AAO from all three methods are tabulated below:

AAO synthesis method	***σ in pore diameter***	***σ in interpore spacing***
1-step anodization	9.5%	13.3%

2-step anodization	19%	13.53%
Pre-patterned AAO	9.233%	2.82%

Table 1: Comparison of standard deviations in pore diameters and interpore spacing from the three methods used to synthesize AAO.

Thus, pre-patterned AAO is a highly desirable method of AAO synthesis because of small polydispersity in pore-diameters and inter-pore spacing.

2.2.2 Silicon nitride stamps

For imprinting aluminum surfaces to fabricate patterned AAO, silicon nitride imprint stamps were synthesized by low pressure chemical vapor deposition (LPCVD) of silicon nitride on silicon (100) wafers. This was followed by e-beam lithography of 100 nm diameter circles, patterned hexagonally or as a square-lattice, on a layer of negative photoresist (NEB-31) spun-coat on the wafer. After developing the resist, the pattern is transferred to the underlying silicon nitride layer using reactive ion etching (refer to section 2.3.2 for experimental details). Thus, an array of silicon nitride pillars is created with ~100 nm diameter and variable inter-pillar spacing (400nm, 200nm, etc) (figure 2.8). As observed by the dark-field scattering image in figure 2.9, the highly periodic stamp pillars scatter light with a bright yellow-green hue; the scattered wavelength is dependent on the angle of incidence and the inter-pillar spacing, similar to a diffraction grating.

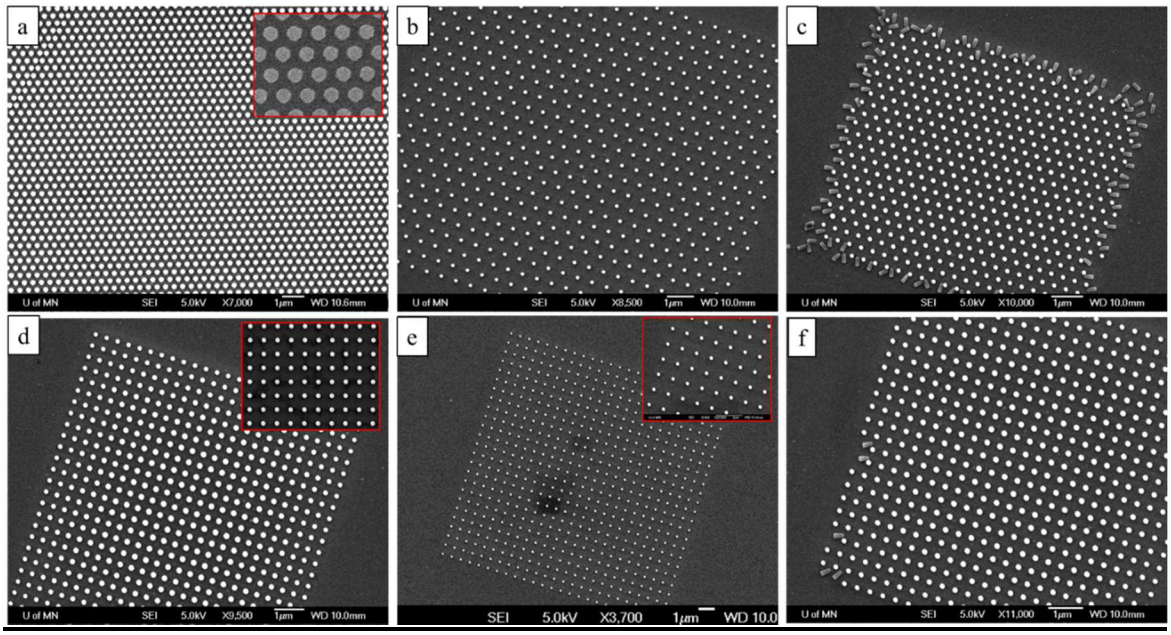

Figure 2.8. Silicon nitride stamps. Hexagonal-lattice arranged nanopillars (length = 297.3 nm with σ = 3.18%) with (a) average diameters 245 nm and σ = 3.19%, inter-pillar spacing (center to center) 391.8nm and σ = 2.08%, (b) average diameter 127.4 nm and σ = 5.94%, inter-pillar spacing 566.4 nm with σ = 2.23%, (c) average diameter 134.6 nm and σ = 4.14%, inter-pillar spacing 391.8 nm and σ = 2.09%. (d, e, f) square-lattice nano-pillars have similar diameters and tolerances.

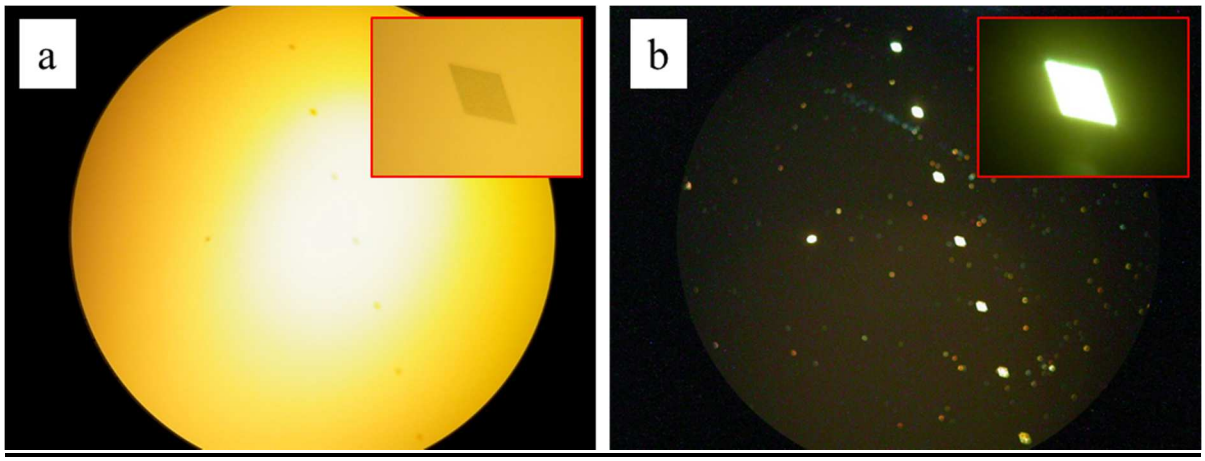

Figure 2.9: Bright-field (a) and corresponding dark-field microscopy (b) images of home-made silicon nitride stamps.

2.3 Methods:

2.3.1 Double anodization of aluminum

A rectangular piece of aluminum, 50µm x 5 cm x 5 cm, was cutoff from Al 4N foil roll. The piece was rinsed in acetone to remove any organics from the surface. The sample was then electropolished at 18V (sample connected to positive electrode) and 7^0C in electropolishing solution composed of 1:5 (v/v) perchloric acid and ethyl alcohol. The surface is rinsed with acetone, methanol, iso-propyl alcohol and DI water. Next, the first anodization of the sample is carried out for 16 hours at 180 V in 1% wt. H_3PO_4 using a Keithley power source (Sourcemeter 2400) and electrochemical setup shown in figure 2.2. The AAO, thus formed, is etched using AAO etchant (6% wt. phosphoric acid and 1.8% wt. chromic acid) for 5 hours. The exposed aluminum surface is then rinsed once more with acetone, methanol, iso-propyl alcohol and DI water. A second anodization is then carried out at 180 V and 1^0C for 4 hours in 1% wt. H_3PO_4 using the same setup as

before. In order to strip the underlying aluminim layer, immerse sample in $HCl/CuCl_2$ aluminum etchant (5% v/v concentrated HCl and 5g/l $CuCl_2$) for 3.5 minutes. Air agitation is used. To break the barrier layer, the sample is immersed in H_3PO_4/CrO_3 solution (12.5 % v/v H_3PO_4 and 120g/l CrO_3) at 65^0C for 90 seconds or immerse in 6% v/v H_3PO_4 at room temp for 45 minutes. The sample is rinsed again with acetone, methanol, iso-propyl alcohol and DI water and then, dried and coated with 1 nm gold or carbon for SEM imaging.

2.3.2 Synthesis of silicon nitride stamps

A 100 nm silicon nitride layer was deposited on Si (100) wafer using low pressure chemical vapor deposition (LPCVD). The nitride surface was rinsed with acetone, methanol, isopropyl alcohol and DI water. A pre-bake step is applied to the nitride coated wafer (125^0C for 1 minute). The wafer is then spin-coated with negative e-beam resist NEB-31 (4000 rpm for 30 seconds). A pre-exposure bake step at 100^0C was carried out for 2 minutes. The sample was then loaded into the Raith 150 electron beam lithography system. A 50 x 50 (for e.g.) matrix of hexagonally-packed arranged dots was designed using the Raith 150 software. The dot to dot spacing was arranged to be 400 nm. In order to obtain 100 nm diameter spot sizes, an exposure time of 24 ms/dot was used. The process was run at a voltage of 20 KV with a dose factor of 0.06 and an exposure dose ~ 0.1pC. The sample was the unloaded, and exposed to a post-exposure bake step oat 95^0C for 45 seconds. The sample was then developed using NEB-31 developer, MF-CD-26, for 40 seconds. After rinsing and drying the wafer, the pattern was transferred to the nitride layer using plasma etching with STS-etcher (nit3 recipe with 14 nm /min).

2.3.3 Nano-imprinting and AAO synthesis

Using a hydraulic press, the silicon nitride stamp pattern is imprinted on to the surface of the 50µm x 5 cm x 5 cm aluminum sample (cutoff from Al 4N foil roll) by applying a force of 1500 lb/sq.in. The sample is then rinsed with acetone, methanol, iso-propyl alcohol and DI water and anodized under second anodization conditions explained before.

2.4 Nanowire synthesis theory

2.4.1 Nanowire synthesis:

Metallic nanowires can be grown in AAO pores using electrochemical deposition. As shown in figure 2.10, a three electrode system is used for electrodeposition of metal into the pores. AAO sample with its metallic contact on one side serves as the cathode, a platinum mesh electrode as counter electrode (anode) and the voltage is measured between the AAO sample and Ag/AgCl reference electrode. Refer to section 2.5.1 for experimental details.

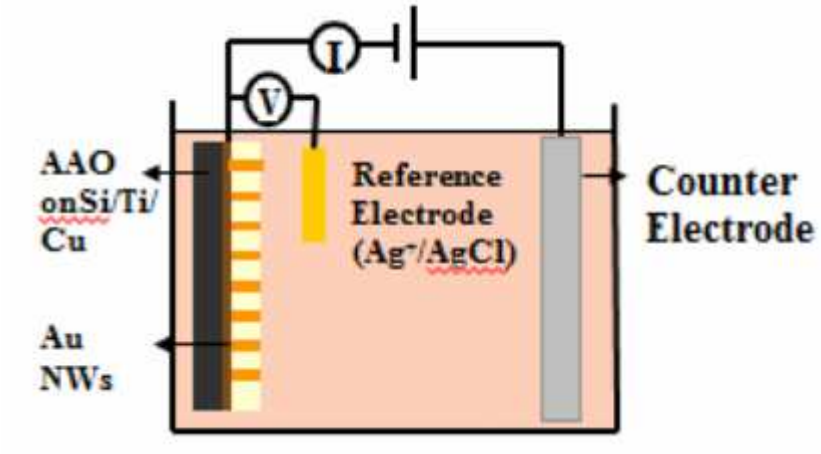

Figure 2.10: Schematic showing the three electrode deposition system to electrochemically deposit materials into porous AAO templates.

2.4.2 Advantages of template fabrication of nanowires:

1) Low polydispersity in nanowire lengths: The nanowires are grown simultaneously in a batch under the same conditions, so there is less variability in properties. This is a very repeatable method because the nanowire growth is proportional to charge transferred which can be controlled externally. As the amount of material electrodeposited is proportional to the charge transferred, this method of growth gives great controllability in lengths down to 1nm.

2) High Throughput: This method makes possible simultaneous fabrication of billions of nanowires in a single batch.

3) Low cost of fabrication: Potentiostatic power supply, three electrodes and an electroplating bath are the main components needed for this method. Further, since the electrodeposition processes are time-controlled, the nanowire growth is relatively quick.

4) Further, this process also allows segmentation of nanowires with different materials i.e., different materials can be grown along the length of a single nanowire by appropriate choice of electroplating solutions.

Thus, this method is very advantageous for high-throughput synthesis of large batches of nanoparticles with low polydispersity.

2.4.3 Mechanism and kinetics of nanowire deposition:

Nanowire deposition process into AAO pores can be divided broadly into three zones[36], shown in figure 2.11:

Zone 1: The filling of AAO pores with metal during electrodeposition.

Zone 2: This zone corresponds to formation of hemispherical caps at the surface. As the surface area seen by the metal ions at the cathode increases, the current increases. The non-uniform filling of pores is attributed to the non-uniform current distribution across the pores.

Zone 3: corresponds to all hemispherical caps merging on the surface and the onset of film formation. Thus, a higher current is observed due to overall higher surface area.

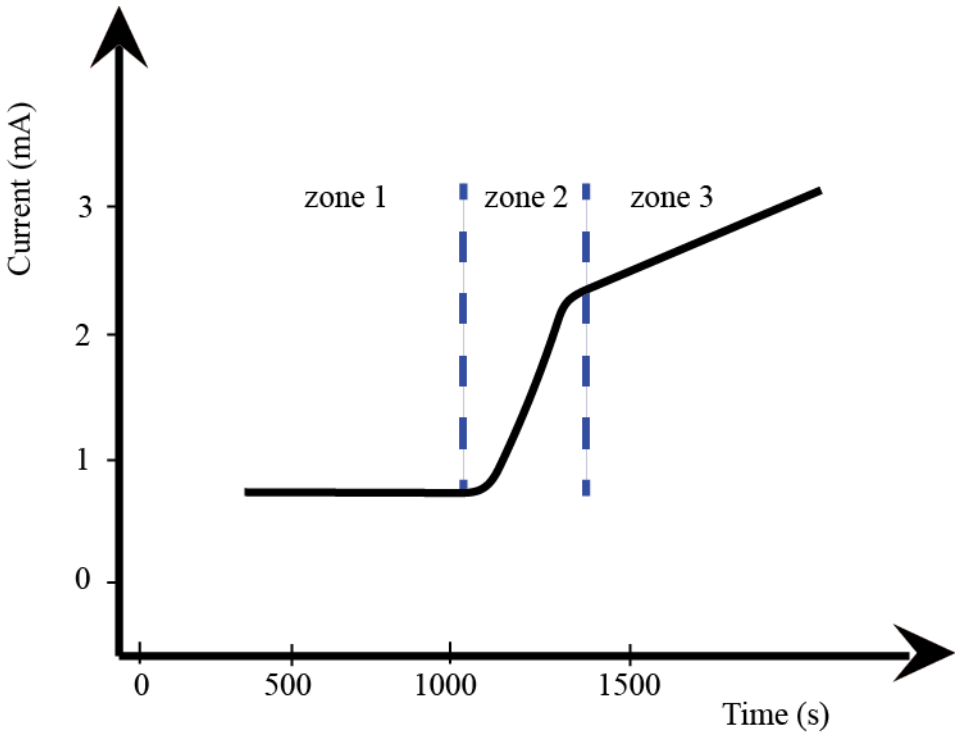

Figure 2.11: Nanowire deposition current vs time can be divided into 3 zones (for long deposition times or thin pore with nanowire outgrowth).

Kinetics of nanowire deposition

Electrodeposition in the nanoporous AAO, in most cases, can be given by diffusion-controlled limiting current defined by Cottrell condition and a correction term (steady state non-linear diffusion term) [37]. Convection and migration are neglected according to this model.

$$i(t) = I_d nFDAc_b\sqrt{\frac{D}{\pi t}} + nFDAc_b/r \qquad \text{Equation 2.1}$$

n=number of electrons in the reaction, F is the Faraday constant, r is the pore radius, D is the diffusion coefficient, c_b is the bulk concentration of the electroactive species.
The contact at the pore bottom is approximated as a disk electrode. The nano-electrode array is, therefore approximated as an array of recessed nano-electrodes which obey the Cottrell equation only for a short time.
The expression for the time independent diffusion-controlled current at the recessed nano-electrodes is

$$i(t) = i_{dpores} = 4\pi nFDc_b r^2/(4L + \pi r) \qquad \text{Equation 2.2}$$

where L is the membrane thickness.

During the initial nucleation process (as depicted in figure 2.12), two diffusion layers are formed, one inside the pores and another outside the pores as indicated by D_2 and D_1, respectively. 'c_m' is the concentration of the species at the pore mouth and 'c_b' is the bulk concentration of the electrolyte. The diffusion inside the pores is linear, while outside the pores, it's linear only for about a millisecond following which it is steady-

state spherical diffusion. The diffusion zone inside the pores becomes thinner with time as the deposition thickness increases. The rate of deposition is also dependent on the effective electrode surface area which can be evaluated from Fick's second law in one dimension under appropriate boundary conditions.

We have at $t = 0$, for all x, $c(x, 0) = c_b$.

As $x \rightarrow \infty$, for all t, $lim\ c(x, t) \rightarrow c_b$

$c(0, t) = c_m$

It can be assumed that c_m remains constant for a short period of time (milliseconds) and under this assumption the diffusion current calculated is:

$$I_{eq}(t) = nF\pi r_d^2(c_b - c_m)/(\pi^{\frac{1}{2}}t^{\frac{1}{2}}) \qquad \text{Equation 2.3}$$

from modified Cottrell equation [34]

From Faraday's law, the amount of material deposited is directly proportional to the amount of current.

$I_{eq} = I_{pore}$

$\pi r_d^2 j_{eq} = \pi r^2 j_{pore}$

If r_d is the radius of the equivalent surface, then the area,

$S_{eq} = \pi r_d^2$ can be written as

$$S_{eq} = \frac{\frac{4r^2\pi(Dt\pi)c_b}{2}}{(4L + \pi r)(c_b - c_m)}$$

For pore density of N (pores/cm^2), the total equivalent area is $N.S_{eq}$.

From Avrami theorem [38],

$$S = 1 - e^{(-N.S_{eq})} \qquad \text{Equation 2.4}$$

so that, Growth current calculated from fractional surface area and current density is

$$I = nF\left(\frac{D}{\pi r}\right)^{\frac{1}{2}}(c_b - c_m)\left(1 - e^{\left[\frac{4n\pi.\pi^2(Dt\pi)^{\frac{1}{2}}c_b}{(4L+\pi r)(c_b - c_m)}\right]}\right) \qquad \text{Equation 2.5}$$

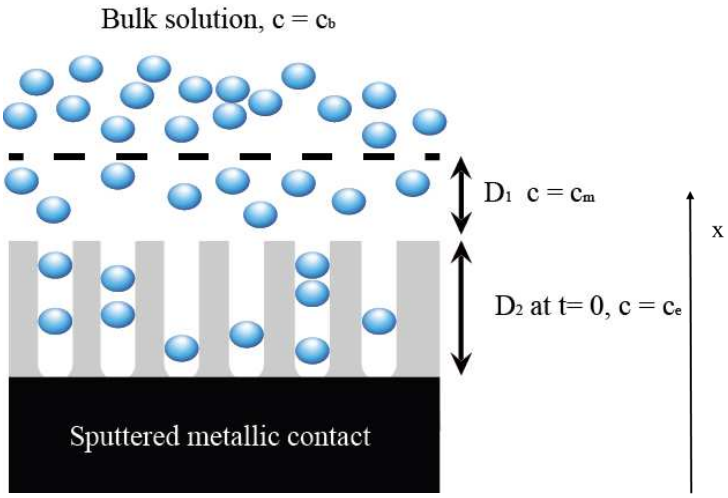

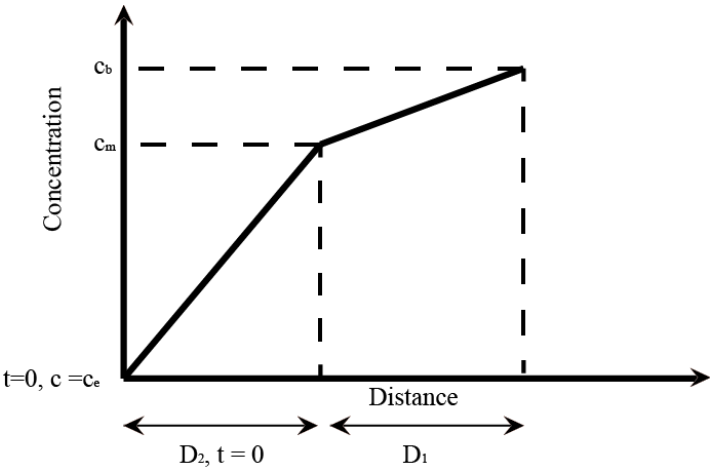

Figure 2.12: Kinetics of electrochemical deposition into porous templates [39].

2.4.4: Optical/spectral characterization of nanowires

2.4.4.1 Reflectance microscopy:

Reflectance microscopy can be used to image multilayers of metals with different bulk reflectances, in metallic films and nanoparticles. Metals such as Au, Ni, Ag, Pt and Cu have wavelength-dependent reflectances [40]. By choosing the appropriate incident wavelength, multilayered metals and heterostructures can be imaged using this technique. Also, as shown in [40], the bulk reflectance values correlate closely with particle reflectance values.

2.4.4.2 Differential interference contrast (DIC) imaging:

Also known as Nomarski imaging, this technique is similar to phase contrast microscopy and is based on changes in the phase (as opposed to absorption or reflectance) of light as it passes through a sample that contains materials with different refractive indices. Different refractive indices change the phase by different values. These changes in phase are converted by a detector into proportional amplitude changes which is used to create the contrast image. While this technique is not very useful for imaging contrast between heterogeneous metallic layers in a nanowire or thin films, due to poor resolution at the nanoscale, it is a useful technique for resolving bio-distribution of nanostructures in transparent samples such as cells.

2.4.4.3 Electron microscopy:

Electron microscopy is often used to characterize the structure, morphology, physical dimensions and material constitution of nanomaterials. This technique exploits the wave-nature duality of electrons to use an accelerated high-energy electron beam to image the sample. The wavelength of the electron beam is given by

$\lambda = h/\sqrt{(2meV)}$

where, h = Planck's constant

e = electron charge

m = electron mass

Substituting the values of electron charge, mass and Planck's constant, we get

$\lambda = 1.23/\sqrt{V}$ nm.

Thus, for 10 KV, the wavelength is ~ 0.0123 nm. In theory, this wavelength can achieve a resolution of 0.005 nm. However, most electron microscopes have a resolution ~ 0.1 nm because of lens aberrations which are harder to correct in electron microscope compared to light microscopes (due to smaller NA at the center of the lens).

The design of the SEM is shown in figure 2.13. A field emission gun with a cathode made of tungsten is used as the electron gun which generates the electrons at a high voltage (1-30 KV). This beam is then focused using a pair of condenser lenses. An aperture is used to block the high-angle incident electrons. A set of magnetic coils is then used to raster scan the beam across the sample surface. An objective lens is then used to focus this beam on to the sample. An interaction volume is defined within the sample about the point of intersection of the electron beam with the sample surface. The signal responses produced within this interaction volume contain elastically scattered electrons (back scattered electrons), inelastically scattered electrons (secondary electrons) and characteristic X-rays. SEM images are formed using scattered secondary electrons collected from closer to the surface (deeper secondary electrons are lost). These secondary electrons are then accelerated towards a scintillation detector, amplified using

a photomultiplier and displayed. The brightness of the image corresponds to the number of electrons.

Back-scattered electrons (BSE) are collected from closer to the sample surface than secondary electrons and are higher energy electrons. These electrons can also be collected and imaged. BSE mode is often used to show contrast between materials having different atomic numbers. Higher atomic number metals back scatter electrons more strongly and thus appear brighter. This technique when combined with X-ray analysis using energy dispersive x-ray spectroscopy makes available a wealth of information regarding the material composition of the nanomaterials.

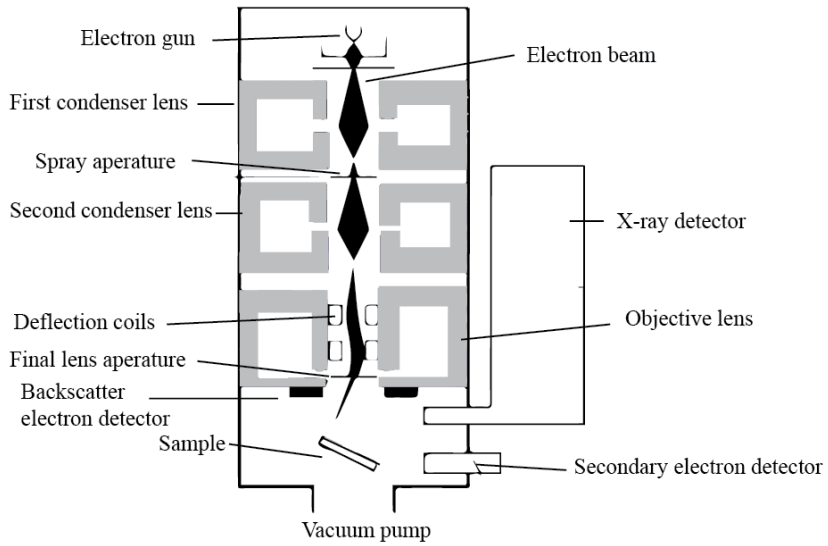

Figure 2.13: Schematic showing design of scanning electron microscope (SEM).

2.4.4.4 UV-vis spectroscopy and dark-field microscopy (far-field plasmonic spectra)

Plasma waves are longitudinal electromagnetic charge-density waves (coupled electron and electromagnetic waves) which result in the shift of the electron-gas with respect to the ion lattice. The quanta of such plasma waves are referred to as plasmons. This shift in electron gas is accompanied with a restoring force due to formation of transient electric dipoles which lead to an oscillator-like behavior. This behavior is governed by the electron density, charge and mass, and particle geometry. Like any oscillator, resonance can be excited at a specific excitation frequency/wavelength (plasmon resonance) which depends on the dielectric function of the metal and the surrounding material. Metals such as Au, Ag, Ni and Cu exhibit plasmon resonance which can be exploited for imaging applications [41,42].

The quasi-static theory and dipole approximation help describe dipole resonance modes on arbitrary shape nanoparticles by approximating the electromagnetic field as that from a point dipole located at the center of the particle (true for distances much larger than the dimensions of the nanoparticle-far-field domain). In this regard, for distances much larger the wavelength of the electromagnetic wave, far field spectra obtained from spherical waves is proportional to r^{-1} where, r is the distance from the nanoparticle [43]. This far-field spectra can be obtained/imaged experimentally using UV-vis spectrometry and dark-field microscopy (section 2.5.4).

For nanoparticles with dimensions smaller than the excitation wavelength, the electromagnetic field can be assumed to be continuous over the particle's volume.

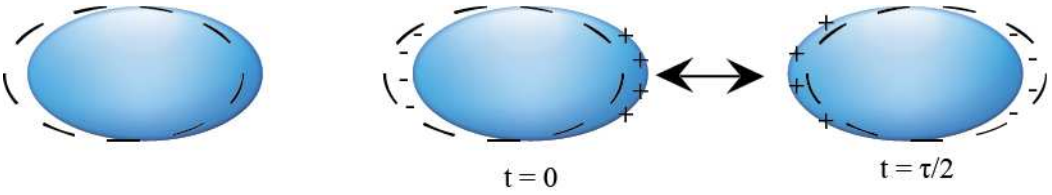

Figure 2.14: Plasmonic resonance in an ellipsoidal particle according to dipole approximation.

Considering the general case of an ellipsoidal metallic nanoparticle, the polarizability α_i, along ellipsoidal axis i, is given by

$\alpha_i = (4\pi/3)(abc)\ (\varepsilon_m - \varepsilon_e)/[\varepsilon_e + A_i(\varepsilon_m - \varepsilon_e)]$ (SI Units) [44]

Where,

ε_m = dielectric function of metal

ε_e = dielectic function of environment

A_i = shape constant ($0 < A_i < 1$), determined by the ratio of ellipsoidal axes.

a, b and c are ellipsoidal half axes. For spherical particles, a=b=c, $A_i = 1/3$

Thus, the polarizability of a nanoparticle depends on the nanoparticle shape and dielectric function of the metal and the environment and helps determine the scattering and absorption cross-sections of the nanoparticle.

$C_{abs} = k.Im(\alpha)$ [44]

$C_{scat} = k^4 \left| \alpha \right|^2 / 6\pi$ [44]

Since, α is proportional to particle volume, absorption is dominant for smaller nanoparticle dimensions and scattering is dominant for large nanoparticle dimensions.

Far-field spectra from arrays of Au/Ni/Au multilayered nanowires is obtained using UV-vis spectroscopy. For nanowires, as there is an associated shape anisotropy, plasmon resonance can be excited either along the diameter of the nanowire or the nanowire length. Thus, the excitation of plasmon resonance is also dependent on the polarization of incident light with respect to the nanowire axis. For light polarized along the short axis of the nanowire, localized plasmon resonance is excited with a resonance-wavelength peak which is independent of the nanowire length (Figure 2.15).

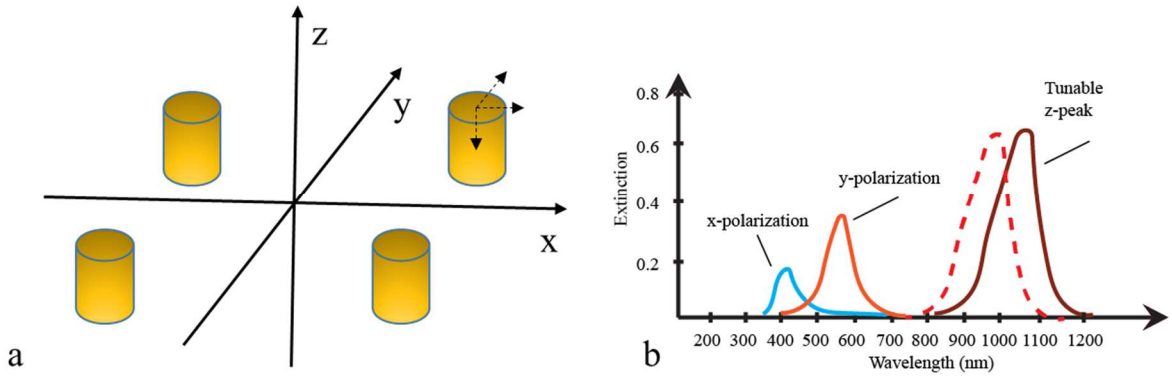

Figure 2.15: Far-field spectra from plasmonic nanowires. This spectra can be obtained by scanning visible-NIR wavelength range using a table-top spectrometer in reflectance mode. If the top surface of the nanowire (xy plane) is elliptical (not perfectly circular), then two plasmonic peaks corresponding to x-polarization and y-polarization will be observed (quadrupole resonance). For a circular cross-section, only one peak corresponding to diameter will be seen. The blue-shifted peak corresponds to the shorter diameter and the red-shifted peak corresponds to the longer diameter. A plasmonic peak corresponding to the nanowire length along z-axis will also be observed depending on the

angle of incidence of illuminating light. This plasmonic peak corresponding to the length (z-peak) is red-shifted with reference to both x and y-polarization peaks and depends strongly on the aspect ratio [45,46].

For normal incidence, a nanoparticle array appears as a diffraction grating and thus, the scattered light intensity and spectral width is dependent on the grating order which is given by the incident light wavelength and the grating constant 'd' (Figure 2.16). In this regard, three relevant regions exist which describe the nature of the scattered light spectra.

For $d < \lambda$, only one mode of transmission exists, i.e., the zeroth order along the transmission direction and thus minimal scattering occurs. For $d = \lambda$, first order diffraction is seen, and scattering is observed along two main directions, parallel and perpendicular to the transmission direction. For $d > \lambda$, multiple diffraction orders exist, with defined scattering angles [44].

With increase in scattering modes, the spectral width also increases (figure 2.16). Typically, in a UV-vis spectrometry experiment, where wavelength is scanned over a given range, one peak, corresponding to an overlay of all three regions, is observed as the three peaks have overlapping ranges. Further, the scattering from the arrays causes increase in spectral width of plasmonic peaks from individual nanowires. Experimentally, a cumulative effect of individual resonances and array scattering is observed.

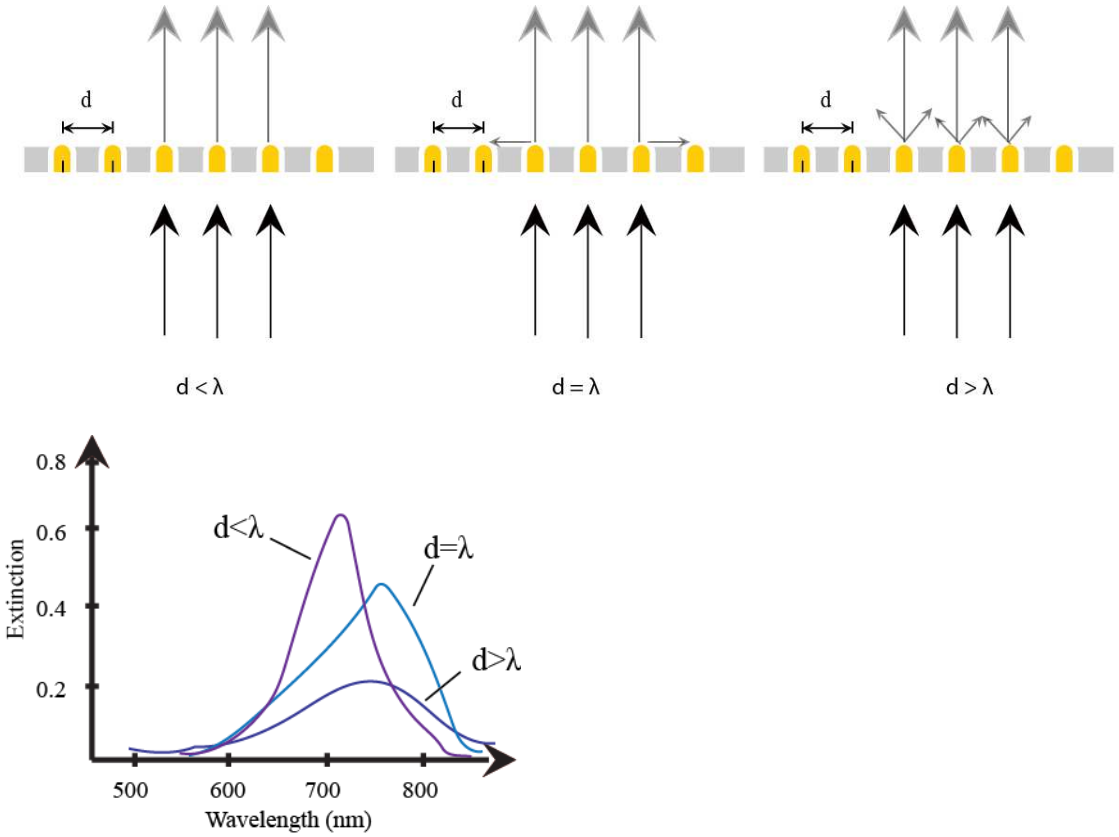

Figure 2.16: Far-field spectra from arrays of nanowires. Depending on the inter-particle distance 'd' compared to λ, multiple diffraction orders can be observed. The number of orders decide the spectral width and the peak intensity[44].

Plasmonic properties of the nanowires can be exploited for either imaging applications or bio-sensing applications. Individual nanowires exhibit localized surface plasmon resonance (LSPR), and thus, can be used as contrast agents in various imaging applications. As gold nanoparticles are biocompatible, they can be used for *in vivo* imaging.

2.5 Nanowire results

2.5.1 Electrodeposition of nanowires

The barcode nanowire fabrication scheme is depicted in figure 2.17. After deposition of the nanowires, the anodic alumina was acid-etched and the sample was sonicated in DI water for 1 minute to release the barcodes. The nanowires were subsequently washed 3x with DI water and 3x with ethyl alcohol by collecting them on the beaker side wall using a magnet. Finally, they were added to fresh phosphate buffered saline (PBS) in a glass vial. For detailed experimental steps, refer to section 2.6.1.

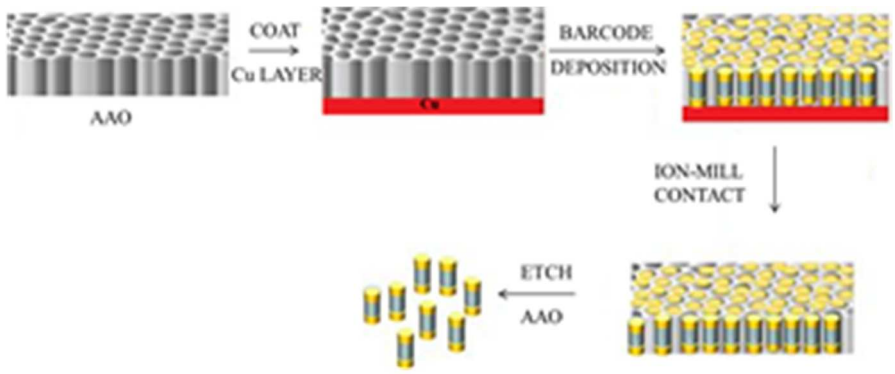

Figure 2.17: Fabrication scheme of multilayered nanowires.

2.5.2 Electrodeposition: Simulation and experimental current densities

Primary Current Distribution:

The cathode is approximated as a recessed disk electrode. This is depicted in figure 2.18. For primary current distribution, the interfacial resistance $R_a = 0$ since kinetics and transport are neglected. Laplace's equation is solved with the following boundary conditions:

Potential, $\Phi = 0$ as $z^2 + r^2 \rightarrow \infty$

$\Phi = V$ at z = 0 and $r < r_0$

$d\Phi/dz = 0$ at $z = L$ and $r > r_0$

$d\Phi/dr = 0$ at $r = r_0$ and $0 < z < L$

This model does not take into account concentration gradients which makes it a very approximate model.

For modeling,

$2r_0$ = 100 nm = diameter of the pore.
L= 1 μm = length of pore
Distance between anode and Cathode: 1 μm
Insulator: Anodic Alumina
Bottom electrode potential (Cathode) = -0.7V
Anode: 0V
Sides: Insulator
Electrolyte: Au plating solution: KAu(CN)2
Conductivity k: 33e6 S/m
Temperature: 333 K

Table 2.1 Paramaters for simulation of nanowire electrodeposition

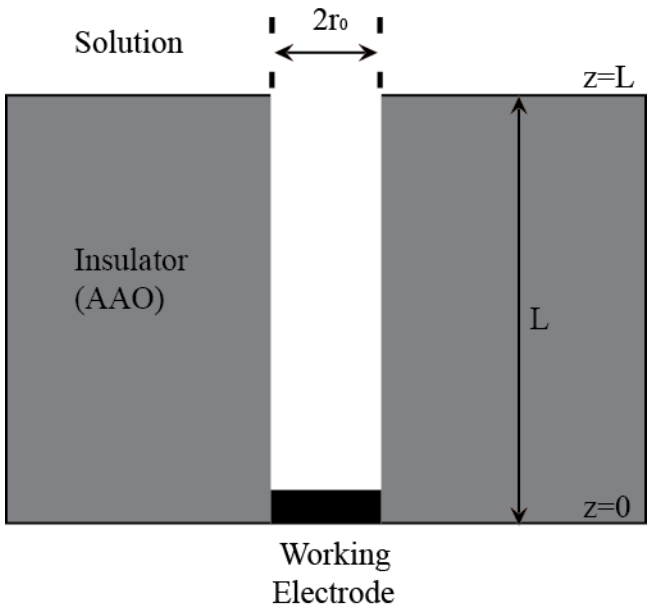

Fig 2.18. Model for derivation of current and potential distribution for electrodeposition of nanowires in AAO.

The model and results from COMSOL are shown in figure 2.19. The figure on the right shows the potential distribution across the two electrodes. We observe that the potential drops at a greater rate inside the pore and levels off outside the pore.

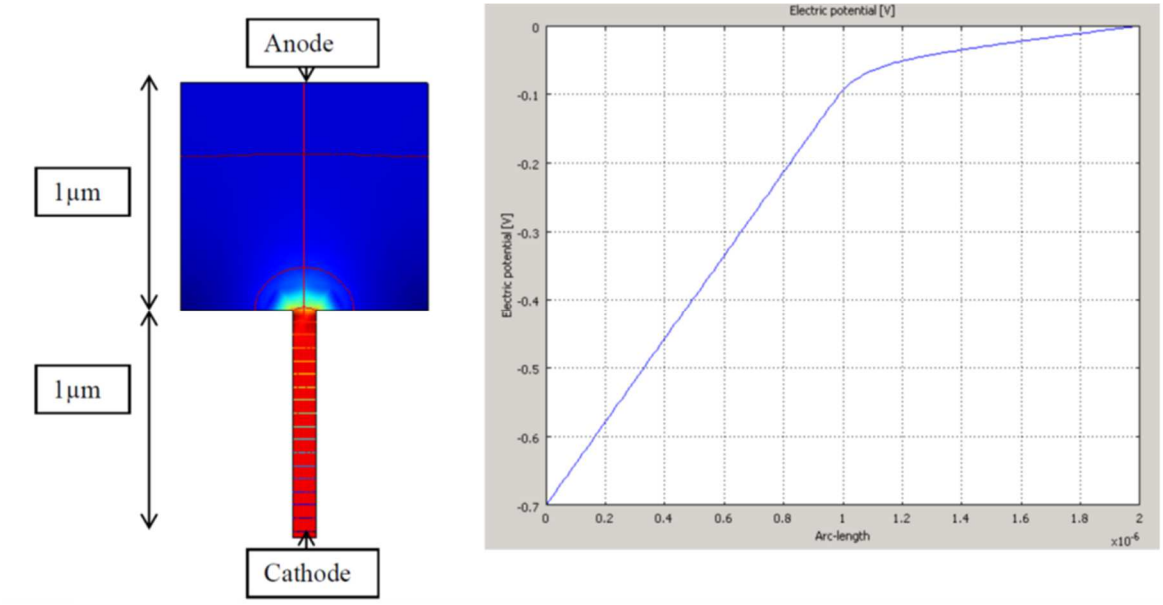

Figure 2.19: COMSOL simulation of potential distribution across the pore length and outside the pore.

The current distribution is fairly uniform for long pores since the disk electrode is bounded by insulator at right angles. The equipotential lines are parallel to the x-axis between the anode and cathode. For small pores of the order of 100 nm diameter, the primary current distribution is fairly constant at the pore bottom near the cathode as shown in the figure below. The plot remains unchanged for different length of pores. 0.5 µm, 1 µm and 2 µm pores were tested (which are typical pore lengths) and the curves overlap as indicated in figure 2.20. The diameter of the pore was not changed since 100 nm is a typical value used in my experiments and thus, I would like to simulate similar conditions.

From COMSOL, boundary integration values at cathode for:

0.5µm long pores = 3.529e6 A/m

1µm long pores = 2.001333e6 A/m

2μm long pores = 1.072383e6 A/m

To obtain the average currents, I_{avg}, the above values are multiplied by pore diameter (100 nm).

Resistance Calculations are in close agreement:

1) For 0.5μm long pore,

V/I = 0.7/.3529 = 1.983Ω

B/k = 0.5E-6/(π*.25E-14*33E6) = 1.93Ω

(B= pore length/pore area, therefore B/k is geometrically calculated resistance)

2) For 1μm long pore,

V/I= .7/.20013 = 3.5 Ω

B/k = 1E-6/(π*.25E-14*33E6) = 3.86 Ω

3) For 2 μm pores,

V/I = 0.7/.10723= 6.5 Ω

B/k = 2E-6/(π*.25E-14*33E6) = 7.72 Ω

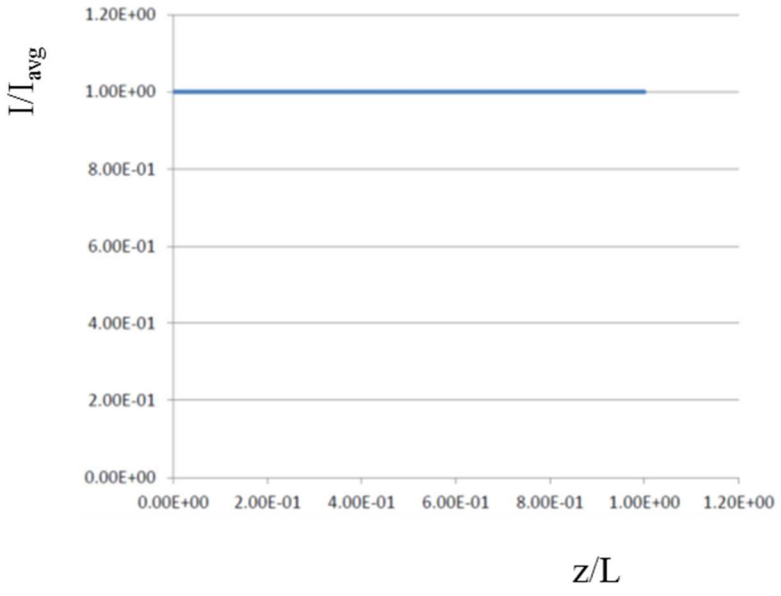

Figure 2.20: COMSOL simulation of I/I_{avg} vs normalized position along the pore length (z). The pore length (L) for each case is constant (0.5 μm, 1 μm and 2 μm)

As pore length decreases, the diffusion limited current increases due to decrease in thickness of porous membrane and increase in ion flux towards the electrode surface. Thus, resistance decreases with decrease in pore length.

Now varying voltage and keeping geometry same,

V=0.7V, I=.20013A

R=3.5 Ω

V=0.9V, I=.257A

R= 3.50Ω

V=1.1V, I=0.314A

R= 3.50 Ω

It is observed resistance depends only on geometry of the cell.

Thus, the following conclusions are drawn:

(1) If ΔV is fixed, geometry is varied and I is computed, R_{cell} is computed. B changes for different geometries and hence resistance changes.

(1) For fixed geometry, ΔV is varied, I is computed and $R_{cell} = \Delta V/I$, remains constant.

Figure 2.21 shows the primary current distribution. The surface plot indicates the current density variation, the contours indicate equipotential surfaces. At the pore mouth, the equipotential surface is a hemisphere and indicates the need for adopting a spherical diffusion model. The arrows indicate current distribution. The zoomed in portion indicates the current distribution at the pore mouth. The current distribution at the corners seems to be higher than at the center as is expected from a primary distribution model. The current density plot indicates sharp rise at the corners. Note that at the pore bottom where the deposition occurs, the current is very uniform.

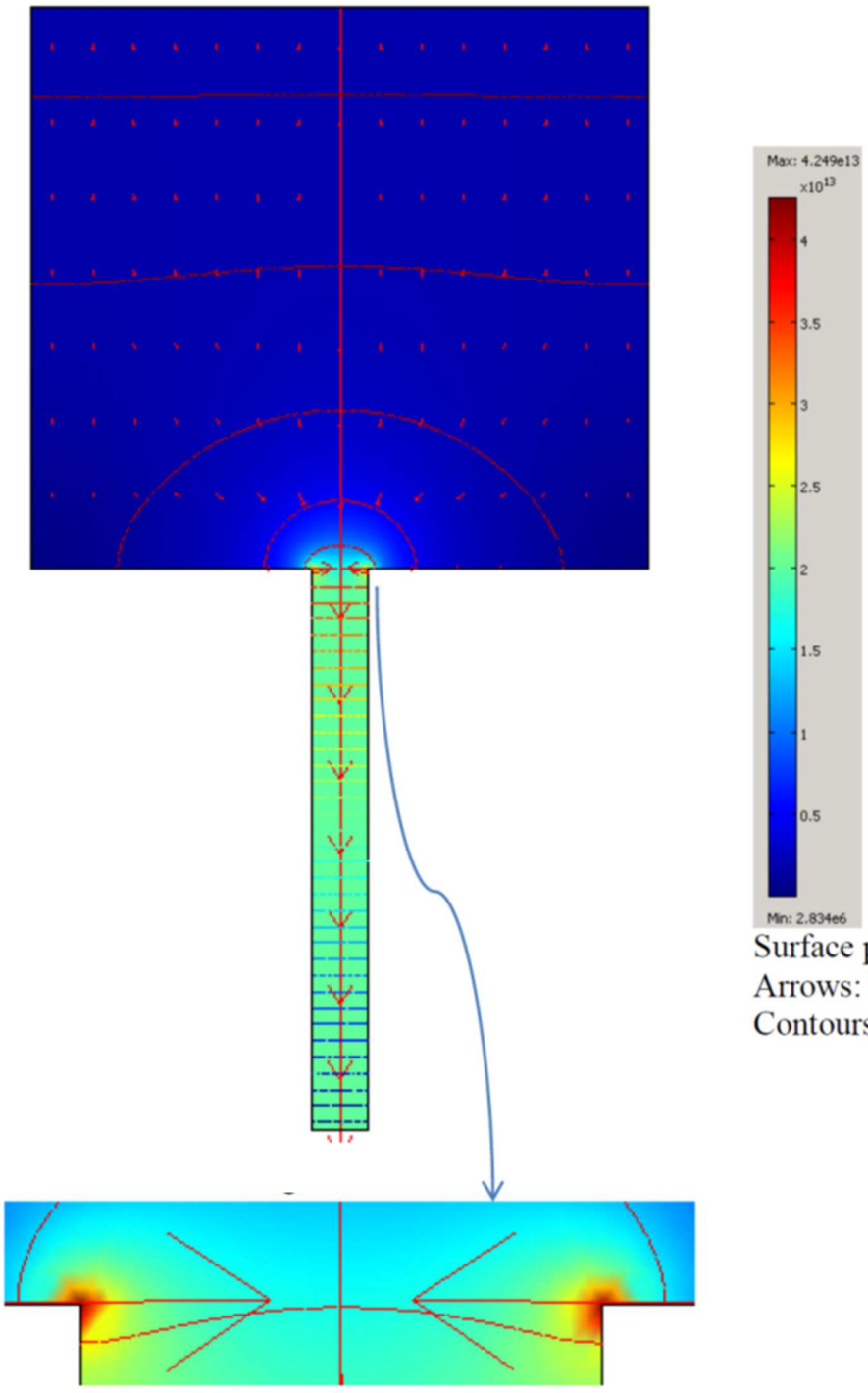

Surface plot: Current density
Arrows: Current density
Contours: Potential

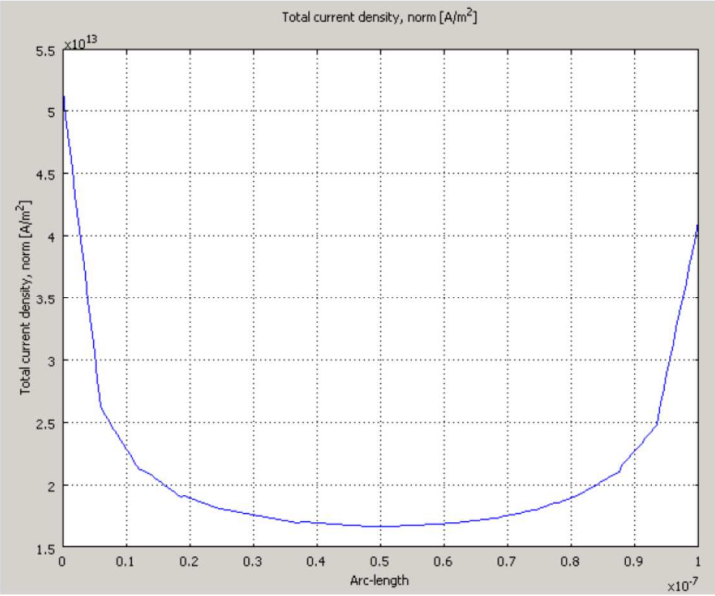

Figure 2.21: COMSOL simulation showing contour plot of primary current density in AAO pore. The line plot shows the current density at the pore mouth.

Secondary Current distribution:

In this analysis, activation over-potential will be taken into account using the Butler-Volmer equation defined below.

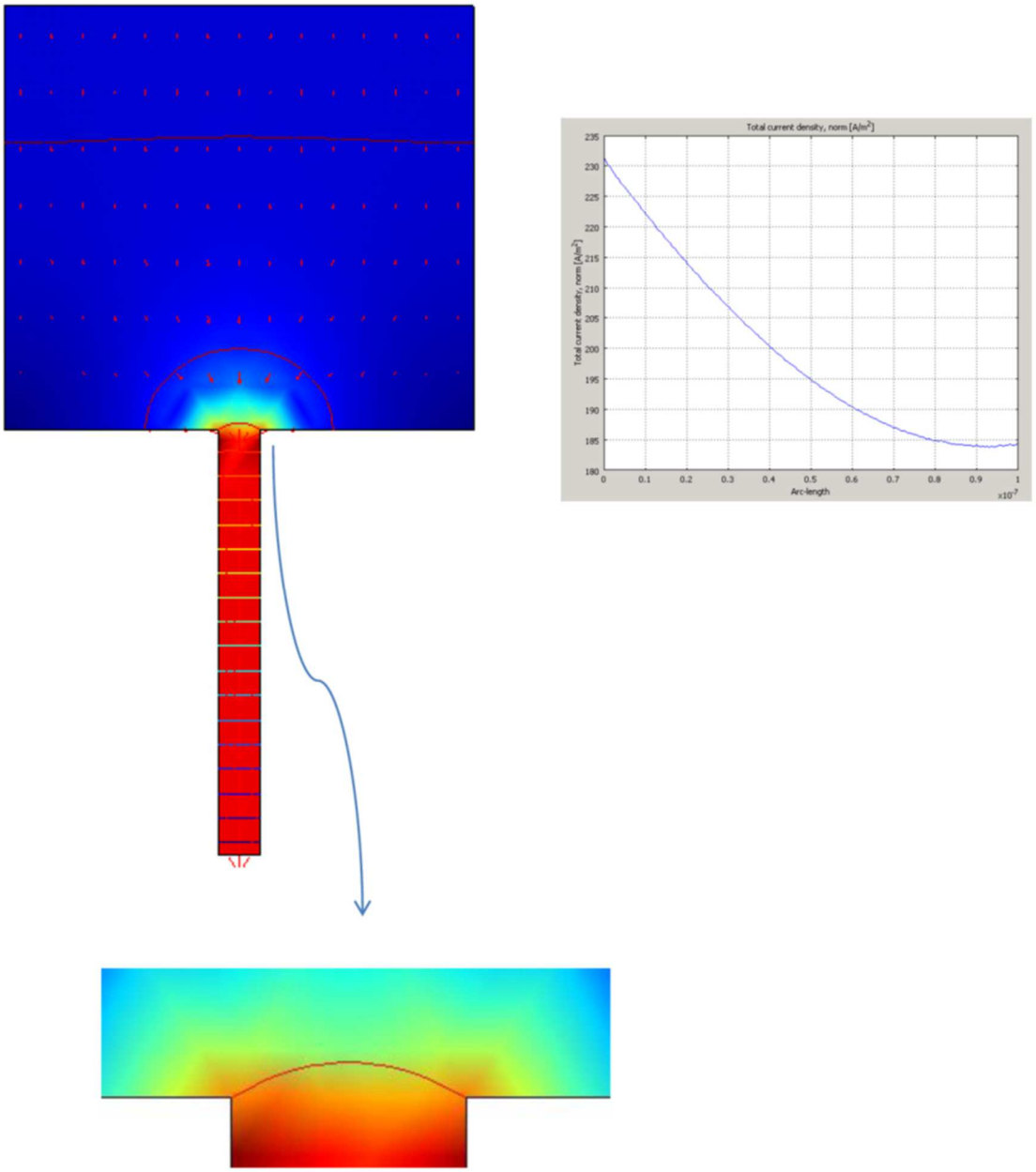

Figure 2.22: COMSOL simulation showing surface and contour plot of secondary current density in AAO pore. The line plot shows the current density distribution at the pore mouth.

The potential difference of 0.7V is taken into account by applying the voltage at the anode and defining the current equation given by Butler-Volmer at the cathode.

The equation is given by i = = i_0*exp((α_a*F*V)/(R*T))-i_0*exp((-α_c*F*V)/(R*T))

$$i = i_0 e^{(\frac{\alpha_a FV}{RT})} - i_0 e^{(\frac{-\alpha_c FV}{RT})}$$ equation 2.6

=1e-3*exp((.5*96487*V)/(8.314*333))-1e-3*exp((-.5*96487*V)/(8.31*333))

i_0 = 1E-3 A/m^2,T=60^{0}C=333K

R=8.314 J/mol.K = universal gas constant

Faraday constant= 96487C/mol,

$\alpha_a = \alpha_c$ =0.5.

The secondary current distribution also yields a uniform current at the pore bottom as it did for primary distribution, owing to the small dimensions of the pore (identical to figure 2.20). The boundary integration value is 1.993316e-5 [A/m] and therefore I_{avg} is 199.33A/m^2.

The total current inside an AAO membrane can be evaluated by calculating the current inside one pore and multiplying it by the number of pores in the plated area. Thus, from the above boundary integration value, the current at the pore bottom for 1 pore is ~ 2x10^{-5} x 100 x 10^{-9} ~ 2x10^{-12} A. The total current inside a sample of area 0.5cm^2 (typical plating area) and pore density 2 x 10^9 pores/cm^2 (Synkera AAO pores), the expected current is ~ 2mA. This will be compared with experimentally obtained values in figure 2.24.

In contrast to primary distribution at pore mouth, the secondary distribution at the pore mouth is more uniform as can be seen in the zoomed in portion of the pore mouth and the accompanying plot in figure 2.22.

For Tafel approximation,

i = -1e-3*exp((-V*0.5*96487)/(8.31*333)) was used for the current expression at the cathode and the boundary integration value over the cathode is 2.005063e-5 A/m

and for linear approximation,

i = -1e-3*((V*1*96487)/(8.31*333)) was used.

Similar results were obtained, where uniformity in current distribution was observed at the pore bottom. The current distribution between the anode and cathode are shown in figure 2.23. In the pore, the current density is fairly constant and changes drastically at the pore opening and finally levels off outside the pore.

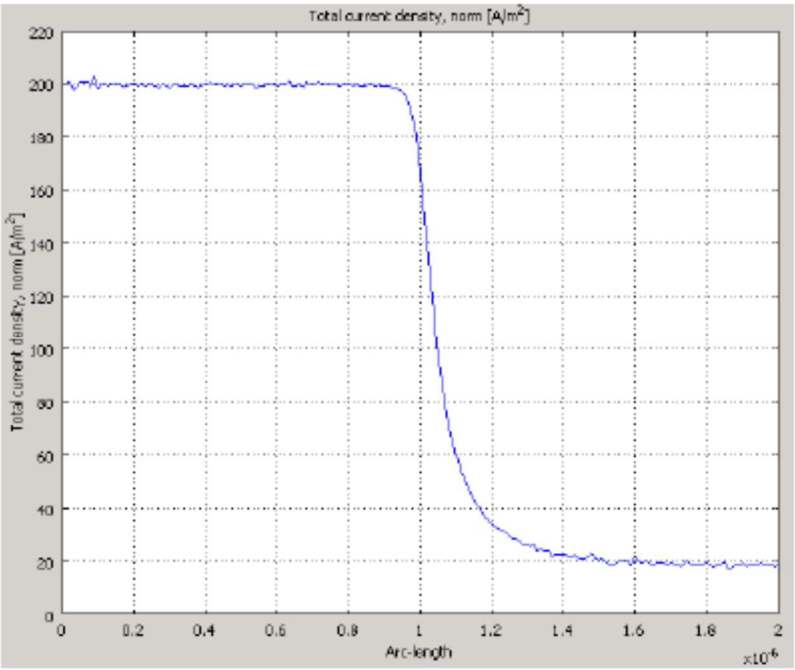

Figure 2.23: COMSOL simulation showing current density variation between cathode (arc length 0) and anode (2E-6).

Figure 2.24 shows experimentally obtained current densities for Au nanowires electrodeposited in AAO templates under potentiostatic conditions (V=0.7V). Figure 2.24(a) shows nanowires grown in thin templates (~1µm thick and 100 nm pore diameters). The growth under these conditions can be divided into three zones similar to

figure 2.11. Comparing the deposition current inside the pores (1 mA) to simulation results from secondary current distribution (2 mA), we can say that the simulation using secondary current distribution is reasonably good approximation. The smaller current observed experimentally can be due to a number of factors including bulk solution resistance (bulk resistance was neglected in simulations), non-ideal AAO structure and microstructural defects in pore channels.

However, divergence of the simulation model from experimental values is observed distinctly for thicker membranes. For thick AAO templates (~ 50 µm thick and 100 nm pore diameters), a much smaller current (~ 10 µA) is observed during potentiostatic deposition of Au. The deposition current, in this case, is limited by the much slower diffusion of ions down the long pore channels caused by increased resistance due to pore inhomogeneities along the length. The current remains constant at 10 µA for the time-scale shown in figure 2.24b. Small fluctuations in current can be attributed to stirring/agitation of the electroplating bath during electrodeposition.

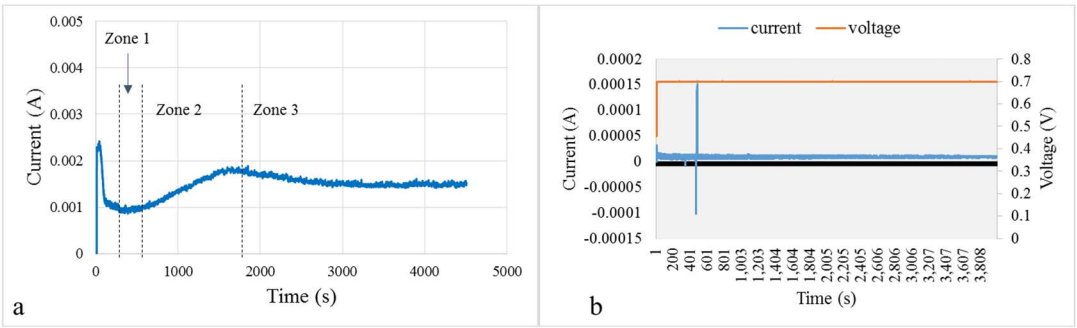

Figure 2.24: Experimental deposition current vs time for Au nanowires in (a) 1µm thick AAO templates (100 nm diameter pores) and (b) 50 µm thick AAO template (100 nm diameter pores).

2.5.3 Length, material and structural characterization.

SEM is a high-resolution technique that is especially used to resolve the dimensions of the nanowires and the incorporating multilayers. While light microscopy (bright-field/dark-field, reflectance and DIC) can be used for qualitative analysis (presence of different layers) and limited quantitative analysis (nanowire density or population in a sample), it lacks the ability to resolve the dimensions of the nanowires because of the diffraction limit (resolution = $\lambda/(2N.A.)$ =400-600/(2 x1.25) = 160-240 nm).

When imaged in back-scattered electron (BSE) mode (as opposed to imaging secondary electrons), the metallic multilayers of the nanowires can be resolved. This is especially useful when two metals with very different atomic numbers are used and one of them has a high atomic number. For example, Au/Ni can be imaged in BSE mode because Au has a high atomic number (79) and is a stronger electron scatterer than Ni. Alternately, EDX can be used to perform an elemental composition analysis of the multilayers. But, since characteristic x-rays are obtained from a depth of 2-5μm from the sample, single nanowires are difficult to map using this technique. Therefore, a bundle of nanowires that aligned and parallel to each other can be used to resolve and map the layers.

Figure 2.25 (a, b and c) shows SEM images of Au/Ni multilayered barcode nanowires of different Ni segment lengths (800 nm, 3 μm and 6 μm) and 50nm Au segment in secondary electron mode. The diameter of the nanowires is 100 nm. Typical

nanowire lengths used for 96 well experiments are 800 nm, 1 μm, 3 μm and 6 μm with standard deviations of ~10% (collected from at least 30 wires each).

The Au/Ni segments are clearly visible in the BSE mode of SEM as shown in figure 2.25 (d and e) and through EDX analysis of bundles of nanowires (figures 2.25 f and g). The Au segments were grown longer in figures 2.25 (d,e and f) to show the contrast between the different segments.

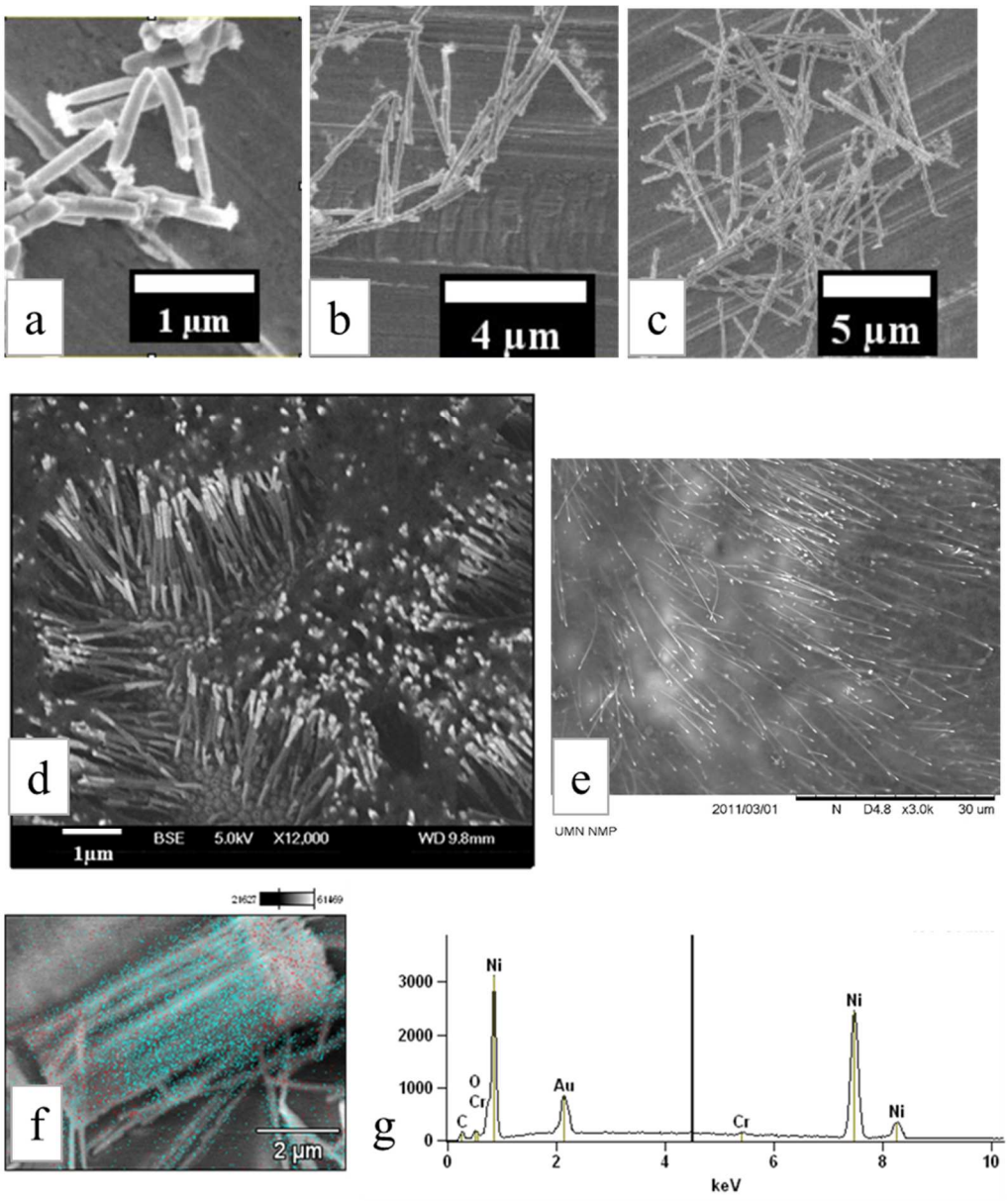

Figure 2.25: Length and material characterization of nanowires using SEM. (a,b and c) SEM micrographs (secondary electrons SEI mode) of 800nm, 3µm and 6µm long nanowires, respectively. In all the three cases, nanowire diameter is 100nm(*). (d and e) BSE/SEM images of Au/Ni multilayered nanowires display the contrasting layers. (f and g) Elemental analysis of Au/Ni/Au nanowire bundles obtained from JEOL6500 energy

dispersive spectroscopy (EDS). An X-ray map is overlaid on the grayscale image. In figure 2.25 f, the blue layer corresponds to the Ni segment and the red layer corresponds to gold segment.

Reflectance microscopy images can be used to qualitatively indicate the presence of different materials along the nanowire length. Reflectance microscopy images of Au/Ni nanowires reveal the Au tips owing to difference in reflectance between the Au and Ni segments (figure 2.26). An excitation wavelength of 600-700 nm can be used to image the different layers in a heterostructure because, in this wavelength range, the two metals have very different reflectance values (0.38 (Au) and 0.58 (Ni) relative reflectances [40]). Though, the diameter (100 nm) may be too small to resolve using light microscopy, the nanowire segment lengths can be resolved as long as they are above the diffraction limit (the edges of the wire would appear blurred). In fact, even at an incident wavelength of 430nm, Ni has a reflectance value which is 1.5 times larger than gold [40].

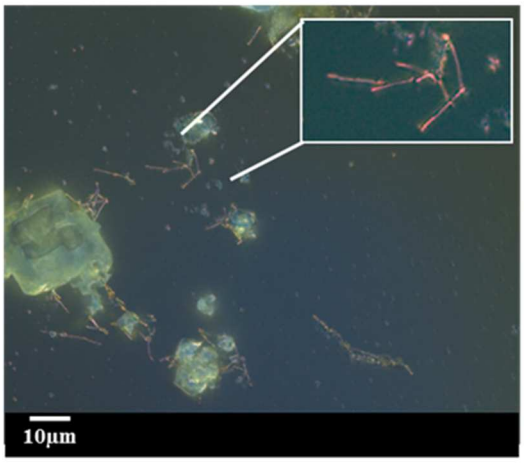

Figure 2.26: Reflectance microscopy image of Au/Ni multilayered nanowires. The nanowires were immersed in phosphate buffered solution during sample preparation. Thus, salt crystals are also seen in the image.

The nanowires synthesized using electrodeposition are polycrystalline. XRD Peaks representative of face-centered cubic (FCC) Au and FCC Ni are observed (figure 2.27).

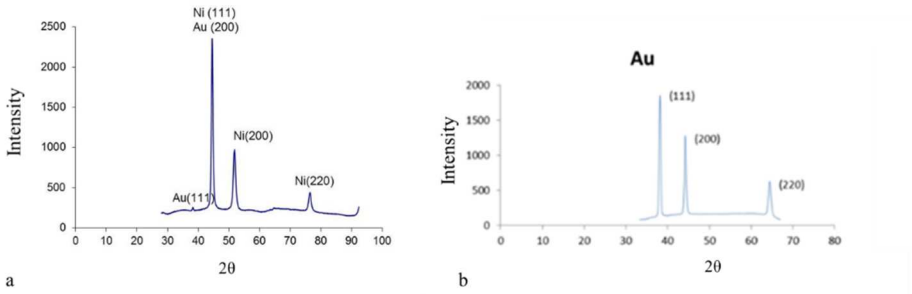

Figure 2.27: XRD characterization of (a) Au/Ni/Au nanowires and (b) Au nanowires.

2.5.4 Plasmonic properties of Au-segments in nanowires

As explained in section 2.4.4.4, for Au/Ni/Au nanowires (100 nm diameters) in AAO template with light incident on the top surface, the spectra is dependent on the dimensions of the Au segments, periodicity of the nanowires, excitation wavelength, polarization of light and angle of incidence. The spectral width of the peaks is also dependent on the inter-particle spacing, as explained in figure 2.15. Energetic relaxation

and absorption losses through electron-electron, electron-phonon and surface scattering at the Au/Ni interface would also contribute to increase in spectral width of observed plasmonic peaks.

UV-vis-NIR spectra were obtained from arrays of gold nanowires in AAO. At angular incidence of $\theta=45^0$, the far-field spectra (reflectance) is as shown in figure 2.28. The two peaks correspond to the plasmonic peaks due to the x and y polarized resonances from one end of the nanowire (compare to figure 2.15). The two resonances results from anisotropy of the diameter of the nanowire (figure 2.28c). The diameters are not perfectly circular.

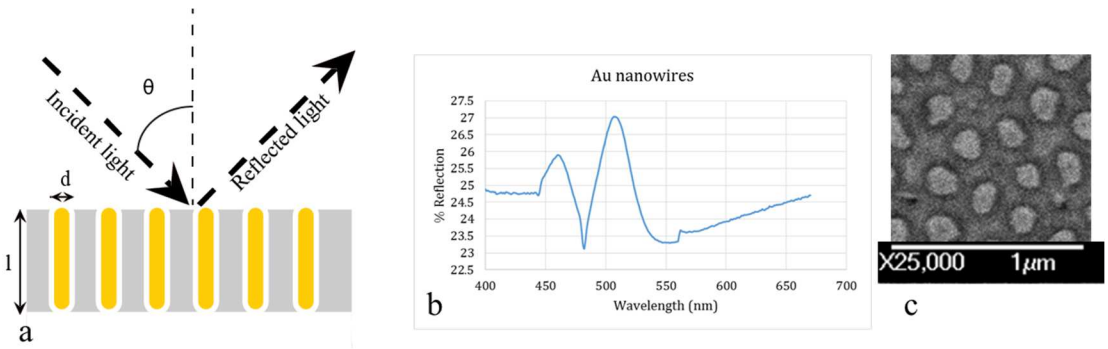

Figure 2.28: Experimentally observed far-field spectra from Au nanowires. (a) Schematic showing the interaction of light from spectrophotometer with arrays of Au nanowires in AAO. (b) Plasmonic peaks (x and y-polarized peaks) from Au nanowires resulting from the ~ 100 nm nanowire tip. (c) The nanowire tips are not perfectly circular as shown in SEM image (c).

At normal incidence ($\theta = 0^0$) to top surface of arrays of Au/Ni/Au (incident direction parallel to the length of the nanowires), two dips are seen in the transmittance (figure 2.29) corresponding to the reflectance/scattering peaks from figure 2.28.

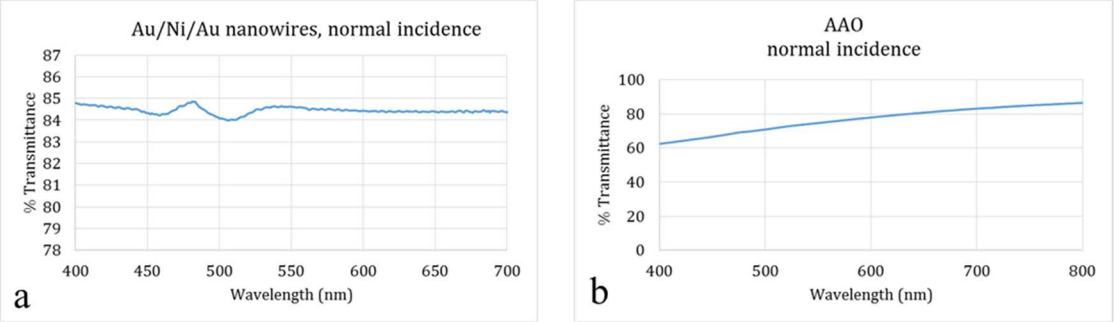

Figure 2.29: (a) Transmittance spectra obtained through arrays of Au/Ni/Au nanowires in AAO with incident light parallel to the lengths of the nanowires ($\theta=0^0$).

For a suspension of Au/Ni/Au nanowires (with 390 nm thick Au segments and 100 nm diameter) in DI water, the twin peaks associated with the diameter are observed in the 450-550 nm range. However, another peak is observed at a higher wavelength (~ 980 nm) (figure 2.30). As discussed in figure 2.15, this corresponds to the plasmon resonance peak associated with Au segment length. This experimentally observed peak at 980 nm is compared with Mie scattering results in the following section.

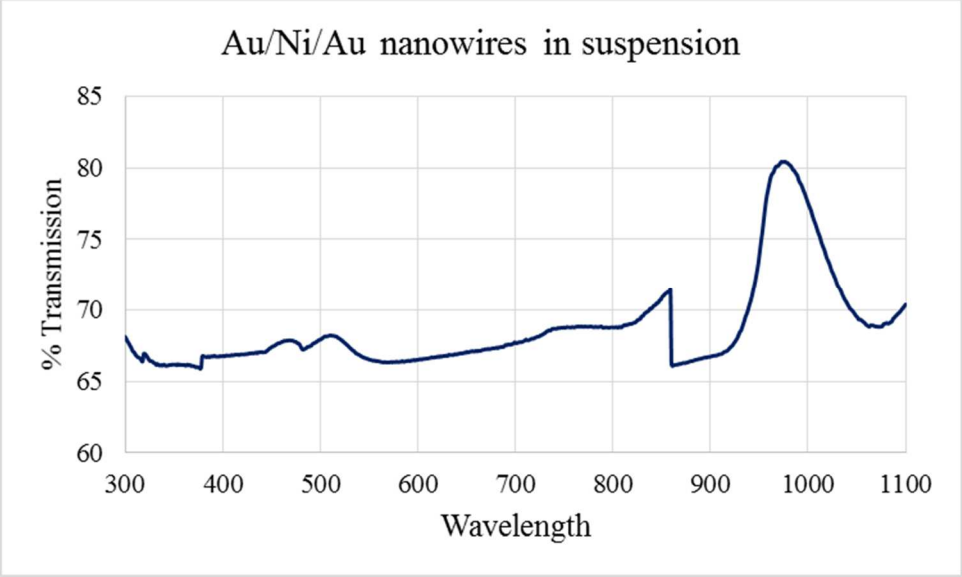

Figure 2.30: Transmission spectra obtained from a suspension of Au/Ni/Au in DI water. Here, the Au segments are approximately 390 nm in length and 100 nm in diameter. The aspect ratio, AR, of the gold segments is therefore, 3.9. Ni segments are ~ 3 μm long. The abrupt change in transmission at 860 nm is because of change in detectors in the spectrophotometer at the infra-red wavelength.

Comparison with Mie scattering theory of nanowires in [suspensions

The optical extinction spectrum for a collection of gold nanowires can be obtained theoretically using an extension of Mie scattering [47]. For a collection of N particles of volume V, the extinction coefficient is given by the dipole approximation

$$\kappa = \left[\frac{2\pi NV\varepsilon_m^{\frac{3}{2}}}{3\lambda}\right]\sum_j\left[\frac{\frac{\varepsilon_2}{P_j^2}}{\left\{\left(\varepsilon_1+\frac{(1-P_j)\varepsilon_m}{P_j}\right)^2+\varepsilon_2^2\right\}}\right] \qquad \text{equation 2.7}$$

where,

P_j are the depolarization factors measured along the three nanowire axes A, B and C with A> B~C (B and C are measured along the nanowire diameter and A is measured along the nanowire length)

$$P_A = \left[\frac{1-e^2}{e^2}\right]\left[\left(\frac{1}{2e}\right)\ln\left\{\frac{1+e}{1-e}\right\} - 1\right]$$

$$P_B = P_C = (1 - P_A)/2$$

$$e = \sqrt{\left[1 - \left(\frac{B}{A}\right)^2\right]} = \sqrt{\left[1 - \left(\frac{1}{R}\right)^2\right]}$$

R = aspect ratio (AR) = A/B

Assuming dielectric function of gold from [48], plotting the longitudinal resonance κ vs λ ($P_j = P_A$) for various AR , we get figure 2.31

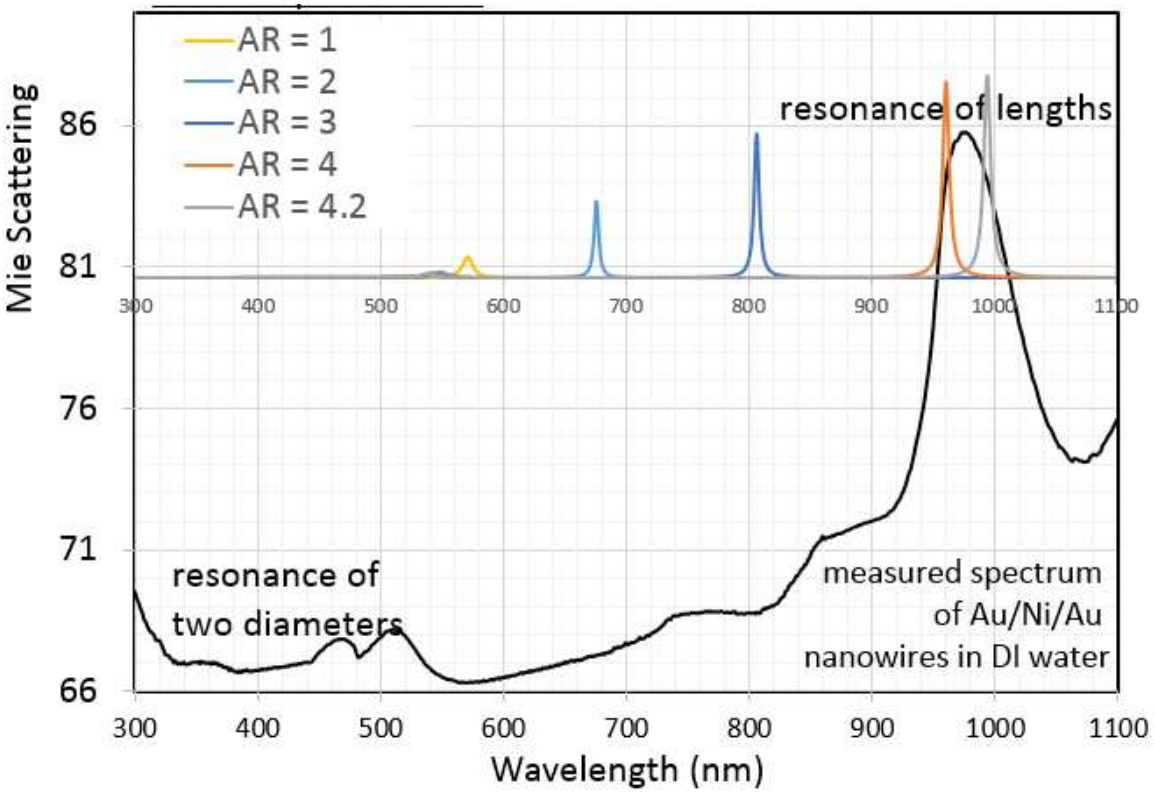

Figure 2.31: Comparison of experimentally obtained far-field spectra (black line) with calculated Mie scattering results (colored plots) for nanowires in suspension.

This is in close agreement with the measured lengths of Au segments (~0.39 μm and AR ~ 3.9) calculated from SEM images and electrodeposition rates. The broadening of the spectra, as explained in section 2.4.4.4, can be attributed to absorption and scattering losses as well as interactions between nanowires in suspension.

2.6 Nanowire Methods:

2.6.1 Electrodeposition of nanowires

Nanowires were electrodeposited inside porous anodic aluminum oxide using a three-electrode electrochemical cell for electrochemical deposition (figure 2.17). A 100nm thick Ti adhesion layer film followed by a 400nm thick Cu layer was sputtered on one side of the template to serve as the working electrode. A platinum mesh, purchased from Technic Inc., was used as the counter electrode. A Ag/AgCl glass electrode, purchased from BASi, was used as the reference electrode. The Au plating solution was used to deposit a Au seed layer at constant current of 100μA. This was followed by a nickel deposition at constant voltage of 0.9V from a $NiSO_4$ bath set at 75^{o}C and using a potentiostat from Arbin instruments. This was followed by another constant current Au deposition for 10 minutes. The Au caps protect the Ni layer from being over-etched during the AAO etching step. The growth electrode was removed using ion-milling or wet-etching.The AAO membrane was etched in 1M NaOH for 2 hours. An ultrasonicator bath set at 33KHz and 1 Hz sweep was used to ultrasonicate the AAO, once every 20

minutes for 5 minutes in order to free wires into solution without breaking the multilayers in a single nanowire [49]. Using a magnetic stand, the nanowires were collected at the walls of the glass vials in which they were previously suspended and were subsequently washed 3x with DI water and 2X with ethanol and suspended in ethanol for future use [50].

2.6.2 Imaging nanowires: (SEM/EDX and optical microscopy)

For optical microscopy, 100 µl of the ultrasonicated ethanolic nanowire solution was pipetted onto a glass coverslip and was sandwiched using another glass coverslip on top. Zeiss Axioplan 2 upright microscope with oil-immersion lens was used to obtain DIC images.

For SEM/EDX imaging of nanowires, 100 µl of the ultrasonicated ethanolic nanowire-solution was pipetted onto a strip of Cu tape on an SEM stub (Ted Pella, Inc). The ethanol solution was allowed to dry and JEOL 6500 was used to image the nanowires. EDX was carried out at 20KV and current setting level 15 to attain a deadtime ~ 40%.

2.6.3 Measurement of UV-VIS-NIR spectra from nanowires

For nanowires in suspension, 0.5 ml of nanowire suspension in DI water was ultrasonicated to disperse the nanowires uniformly. The sonicated sample was transferred to a square-base quartz cuvette (path length = 10 mm) which was placed in the lambda 950 UV/vis/NIR spectrophotometer for measurement. A wavelength scan range of 300-1200 nm was defined and a step size of 1 nm was selected. The spectra was obtained in transmission mode.

For arrays of nanowires in AAO (metallic contact etched), the AAO sample edges were taped to the sample holder using 3M double sided transparent tape. The long axes of the

nanowires were parallel to the direction of incident light. Spectra was collected in transmission mode as previously described. For reflectance measurement, the universal reflectance accessory (URA) in lambda 950 was attached. Similar to transmission measurements, a wavelength scan range of 300-1200 nm was defined and a step size of 1 nm was selected.

2.7 Conclusions

In this chapter, synthesis of multilayered magnetic nanowires through high-throughput electrochemical deposition in porous templates was shown. Specifically,

(i) Pre-patterned AAO is a highly desirable method of AAO synthesis as it has lowest polydispersity in pore-diameters and especially, inter-pore spacing from all the compared methods.

(ii) Nanowire dimensions can be precisely controlled in the electrochemical deposition method. As a uniform current density is achieved during deposition, the amount of metal deposited can be precisely controlled by controlling the amount of charge that is passed to reduce the metal ions.

(iii) Nanowire dimensions were further characterized using SEM. The multi-layers were resolved by imaging back-scattered electrons from the nanowire samples. This was used in conjunction with EDX on bundles of nanowires for elemental-composition analysis.

(iv) Far-field spectra from Au segments of Au/Ni/Au multilayered nanowires was measured using spectrophotometry. The obtained plasmon resonance wavelength was comparable to calculated Mie scattering results for nanowires. The plasmonic gold ends can be potentially used as beacons (or imaging contrast agents) in biological studies.

Chapter 3: Magnetic characterization of "barcoded" nanowires and magnetic multiplexing

Magnetic nanoparticle based technologies are increasingly being adopted for *in vitro* applications like sensing[51], separation [52] and purification of proteins/biomolecules. They are employed in state-of-the-art *in vivo* therapeutic applications including drug-delivery [53] and hyperthermia [54]. The choice of the nanomaterial and associated magnetic properties of the nanoparticles govern the output efficiency such as sensitivity, separation/purification yield and tumor ablation.

This chapter will focus on the use of the magnetic nanowire as a multiplexing tool by exploiting the unique magnetic properties associated with its shape. Specifically, the following points will be covered:

(i) For a magnetic nanowire, magnetic properties such as saturation moments and fields, coercivities and remnant magnetizations can be controllably manipulated by choice of physical dimensions (diameters and aspect ratios). Thus, a nanowire with specific physical dimensions will have unique magnetic properties which can be used as signatures (barcodes) for that specific nanowire-sample.

(ii) First order reversal curves (FORC) and FORC diagrams will be presented as a method to demultiplex a mixture of two magnetically different nanowires accurately.

3.1 Theory of magnetic characterization of nanowires

3.1.1 Magnetic characterization of nanowires: hysteresis curves and energy considerations

Magnetic properties of nanomagnetic particles can be characterized by measuring hysteresis behavior using a vibrating sample magnetometer (VSM) (figure 3.1). The VSM measurements are based on the concept of flux change in a coil associated with vibration of a magnetic material or magnetized material near it. The sample to be measured is attached to one end of a non-magnetic rod which is suspended between the two poles of the magnet. The other end of the rod is driven by a loudspeaker cone which vibrates the rod at a set frequency. The oscillatory motion of the magnetic material induces an alternating emf in the detection coil which is amplified by a lock-in amplifier set at the same frequency as the vibration frequency. The magnitude of this emf is proportional to the magnetic moment of the sample. By sweeping the applied field across a range of values, the corresponding moment values at those fields can be recorded. This moment output vs field for ferromagnetic materials is a hysteresis loop and can be described by

$M = \chi_v.H$, or

$\sigma = \chi_m.H$

where,

M = magnetic moment per unit volume (SI units: A/m, cgs units: emu/cm^3)

σ = magnetic moment per unit mass (SI units: $A.m^2/Kg$, cgs units: emu/g)

H = applied field (SI units: A/m, cgs units: Oe)

χ_v = volume susceptibility (SI units: dimensionless, cgs units: emu/Oe.cm^3)

χ_m = mass susceptibility (SI units: m^3/Kg, cgs units: emu/g)

Generally, the VSM records moment ‘m’ vs field ‘H’. If ‘w’ is the mass of the magnetic material being measured

$$m = w\sigma = w\chi_m H \qquad \text{(equation 3.1)}$$

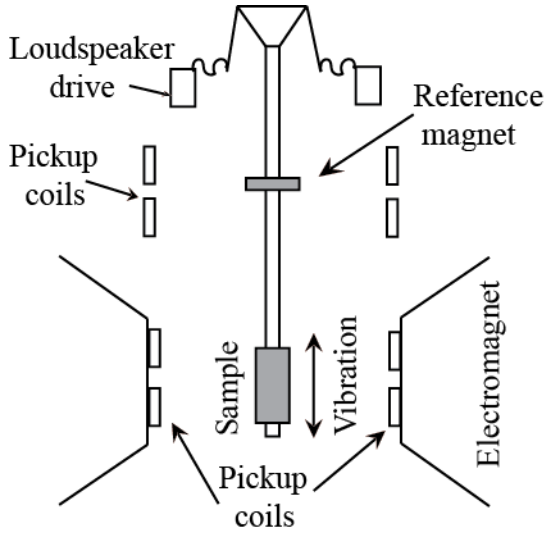

Figure 3.1: Schematic showing moment measurement using VSM. For detailed working, refer to [55].

Various features of the hysteresis loop, including shape and intersection with the abscissa and ordinate, can used to deduce the properties of these materials. The shape of the hysteresis loop itself is a function of various parameters including effective anisotropy (shape, microstructure), material, particle volume/size, frequency and amplitude of the magnetic field, orientation of the magnetic field direction with respect to particle axis (figure 3.2), magnetization history of the sample and magnetic interactions between nanoparticles. The saturating field (H_{sat}), remnant magnetization (M_r) and coercivity (H_c) are strongly dependent on the nanowire geometry and size whereas the

saturation magnetization (M_s) is a material property independent of shape or size. For Ni, the bulk M_s is 485 emu/cc at room temperature. The presence of an oxide layer on the surface and impurities, however, reduces this value to ~415-420 emu/cc (chapter 5). The switching field, H_{sw}, is the field at which the slope of the hysteresis loop is maximum ($d^2M/dH^2 = 0$).

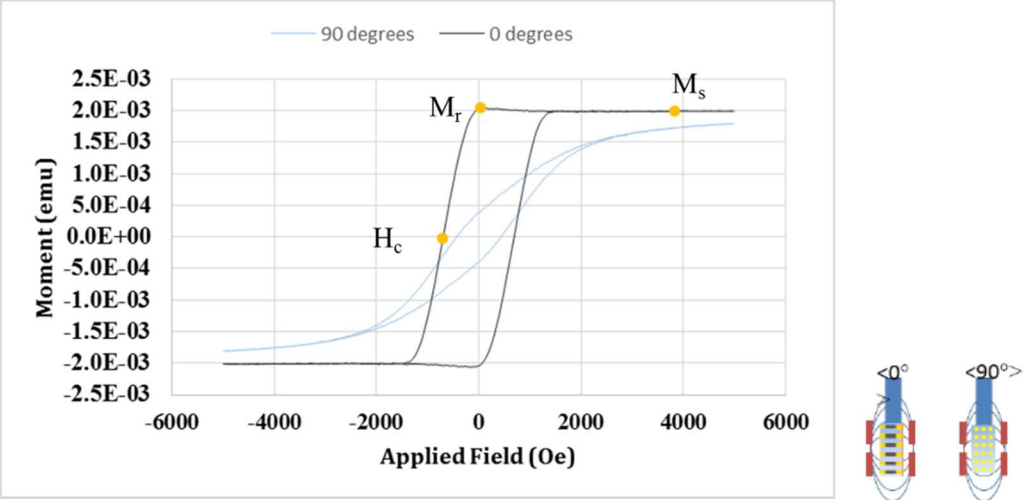

Figure 3.2: VSM hysteresis loops obtained from arrays of ferromagnetic nanowires as a function of orientation of the easy axis (long axis) with respect to the applied field direction. H_c, the coercive field (or coercivity), is the applied field at which the magnetization becomes zero. M_r, the remnant magnetization, is the magnetization at zero applied field. Saturation magnetization, M_s, is the magnetization when all the magnetic moments in the material are aligned to the applied field direction. The corresponding field value is the saturating field, H_{sat}. The hysteresis loops is measured from an array of Au/Ni/Au nanowires with fixed aspect ratio (AR) (35 nm diameter, AR≥100) Au~50 nm.

For a magnetic material, magnetic hysteresis loops can be calculated using energy considerations. The total energy, E, of the system of nanoparticles, in the presence of the applied field, is minimized to determine the magnetization state and hysteresis loop.

$E = E_{ex} + E_H + E_{EA} + E_{ca} + E_D$ (equation 3.2)

E_{ex} is the exchange energy, E_H is the Zeeman energy, E_{EA} is the magnetoelastic energy, E_{ca} is the crystalline anisotropy and E_D is demagnetization energy.

The exchange energy is the energy between two atomic spins/domains and results in magnetic ordering. It can be described by exchange stiffness constant, A, which is a function of material and size (number of domains). It has a value between 10^{-6} and 2 x 10^{-6} erg/cc [56]. However, for nanowires with radius below a critical value (r_{sd}), the nanowires are single domain and thus, the exchange energy due to multiple domains is negligible [57]. For high aspect-ratio nanowires (>10), the lower limit on the critical radius (300 nm for aspect ratio 10 [57] is well above the diameters of synthesized nanowires. Thus, most synthesized nanowires (diameters ≤100nm) can be assumed to be single domain along the diameter. Depending on length, the nanowires can be single or multi-domain. The exchange energy, then, arises from interactions between neighboring spins.

The Zeeman energy is the potential energy of the magnetization in an externally applied field which is minimum when the field and magnetization are aligned. $E_H = -$ **M.H,** where **H** is the external field vector and **M** is the magnetization vector**.**

The magnetoelastic energy is the energy due to stress /strain on a magnetic material, and is negligible for particles in suspension. This energy is dependent on

material properties. For nickel nanowires, the magnetoelastic energy is negligible compared to shape anisotropy dependent demagnetization energy [56].

The magnetocrystalline anisotropy energy is due to spin-orbital coupling of electrons in a material and it is influenced by the crystalline electric field (the arrangement of atoms) such that specific crystalline directions are energetically favorable for the magnetization to align with. The crystalline anisotropy is described by anisotropy constant K and the direction cosines of the magnetization. For FCC materials, such as nickel, $K < 0$ and easy axis is along [111] direction ($K = -4.54 \times 10^4$ erg/cc). For BCC materials, such as iron, $K > 0$ and easy axis is along [100] direction ($K = 4.8 \times 10^5$ erg/cc) [55]. This energy is considerably large for single crystal nanoparticles and highly textured surfaces but small for polycrystalline materials.

The demagnetization energy or magnetostatic energy is due to the demagnetizing field which arises from the shape of the material. It is easier to magnetize a cylindrical object along its long axis compared to the short axis. A sphere, on the other hand, shows no preference for magnetization direction and is just as easily magnetized in any direction.

The demagnetization energy $E_D = ½ N_d M_S^2$ (erg/cc), and demagnetization field $H_d = -N_d M_s$ where N_d is the demagnetization factor along the magnetization direction and M_s is the saturation magnetization of the material (emu/cc) [55]. The demagnetization factor N_d can be calculated for ellipsoidal shapes and can be extended to cylindrical models by taking the limits (extrapolation). Generally, for an ellipsoid with semi-axes a, b and c and corresponding demagnetization factors along a, b and c are N_a, N_b and N_c, respectively,

the factors can be related by $N_a + N_b + N_c = 4\pi$. For a prolate spheroid ($c > a = b$), and a large aspect ratio ($c/a > 10$), which a nanowire can be approximated to, $N_c = 0$ and $N_a = N_b = 2\pi$.

The shape anisotropy energy, $K_u = E_{Da} - E_{Dc} = -\pi M_s^2$. For a Ni nanowire, with $M_s = 415$ emu/cc, $K_u = 0.546 \times 10^6$ erg/cc. Note that this value is an order of magnitude higher than the crystalline anisotropy of Ni nanowire. Thus, for a nanowire, the effective anisotropy is generally well approximated by the shape anisotropy alone.

The saturating field is the field required to overcome the anisotropy energy, which is equal to the demagnetization field. The saturation field along the nanowire axis is 0 ($N_d = 0$) and perpendicular to the nanowire is $2\pi M_s$ ($N_d = 2\pi$). From calculation, $H_{sat} = 2\pi(415) = 3050$ Oe perpendicular to the nanowire axis. This is very comparable to the $H_{sat} \sim 3000$ Oe obtained from actual hysteresis loop (section 3.2.1).

Thus, magnetically, Ni is a great candidate material for nanoprobe applications in biology as it has a high value of saturation magnetization that can be exploited for mechanotransduction applications. As we will see in chapter 5, additional properties such as stability of nickel surface (compared to Fe) owing to a passive oxide layer as well as less cytotoxicity compared to Co make it a suitable ferromagnetic material for biological applications.

3.1.2 Magnetic characterization: Switching mechanisms

From the above energy analysis, it can be observed that the magnetoelastic energy and crystalline anisotropy can be neglected compared to shape anisotropy energy, exchange energy and Zeeman energy for single domain nanowires or high aspect ratio

ellipsoids. The magnetization state of a system can then be calculated by evaluating the minima in the energy expression in equation 3.2.

The two main mechanisms of magnetization reversal or switching in single domain nanowires are coherent rotation and curling [56] (figure 3.3). When no field is applied, the moments are aligned parallel to the easy axis (long axis) of the ellipsoid. The demagnetization energy and Zeeman energy are minimum in this case. In coherent rotation mechanism, the moments stay aligned to each other as they rotate away from the easy axis. Thus, in this case the exchange energy is zero. However, as the component of the moment along the hard axis (perpendicular to the long axis) increases, the demagnetization energy increases. In curling, the moments are not aligned to each other as they rotate away from the easy axis. In fact, they arrange so that the x-component (component perpendicular to long-axis) of moments cancel each other, thus minimizing the demagnetization energy. However, during such reversal, there exists finite exchange energy between unaligned spins. These mechanisms are shown in the schematic below, figure 3.3.

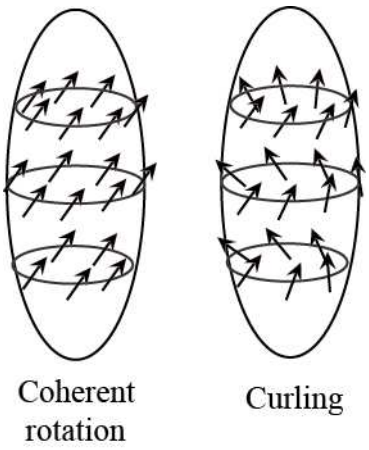

Figure 3.3: Coherent rotation and curling are two dominant moment reversal mechanisms in nanowires [56]. However, depending on nanowire dimensions transverse wall or vortex wall reversal mechanisms can be activated.

In reality, at a fixed orientation of the moments with respect to the easy axis, the switching mechanism is determined by the competition between demagnetization energy and exchange energy. The reversal mechanism with the lower energy between the two is preferred. The demagnetization energy perpendicular to the nanowire increases as the aspect ratio increase, thus curling may be a preferable rotation mechanism for very high aspect ratio structures. On the other hand, for smaller diameter nanowires, the exchange energy is high for unaligned moments as the angle between the moments increases with decreasing diameters. Thus, in this case, for small diameter nanowires, coherent rotation would be favorable. Therefore, there is a size dependence for the reversal mechanism such that coherent rotation is the dominant mechanism for small diameter nanowires and curling is the dominant mechanism for large aspect ratio nanowires.

There is a critical radius for transition from coherent rotation to curling and is given by

$$r_c = q\left(\frac{2}{N_a}\right)^{1/2}\sqrt{A}/M_s$$

[58], where q is the smallest solution of Bessel functions and is dependent on the aspect ratio of the prolate spheroid, A is the exchange constant, N_a is the demagnetization factor and M_s is the saturation magnetization.

For high aspect ratio nanowires, $N_a \sim 2\pi$. Thus, for nickel nanowires, the calculated critical radius is close to 25 nm. Note that this number is evaluated from taking the high (infinite) aspect ratio limit for a prolate spheroid model and thus, this critical radius value is only an approximation. Generally, for a nanowire sample that otherwise shows coherent rotation reversal, increasing the aspect-ratio increases the curling "component".

This point is clearer as we discuss the variation of coercivity with the orientation of the applied field with respect to the easy axis, θ_0 (figure 3.4). For this, the Stoner Wolfarth model will be used to evaluate the expected variation of coercivity. In coherent rotation, the total energy is given by the demagnetization energy (E_D) and the Zeeman energy (E_H).

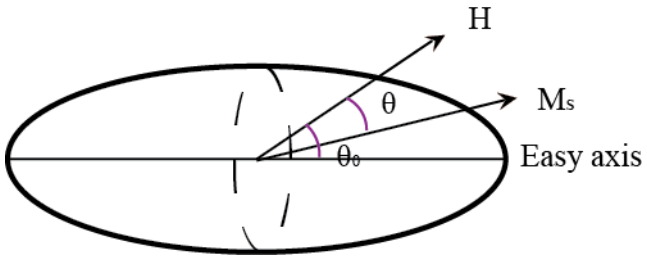

Figure 3.4: Stoner Wolfarth model for coherent reversal [55]. θ_0 is the angle between the applied field and the easy axis.

$$E = E_D + E_H = K_u sin^2(\theta - \theta_0) - H.M_s = K_u sin^2(\theta - \theta_0) - HM_s \cos\theta$$

This energy corresponds to the area of the hysteresis loop. Finding the minima in energy by taking $dE/d\theta = 0$, and calling $H/(2K_u/M_s) = h$, the reduced field and $M/M_s = m$, the reduced magnetization, we get

$$2m(1-m^2)^{1/2}\cos 2\theta_0 + (1-2m^2)\sin 2\theta_0 = \pm 2h(1-m^2)^{1/2} \quad \text{Equation 3.3}$$

The hysteresis loops can be calculated from this expression and m vs h can be plotted (figure 3.5). Figure 3.5 shows ideal hysteresis loops as a function of θ_0.

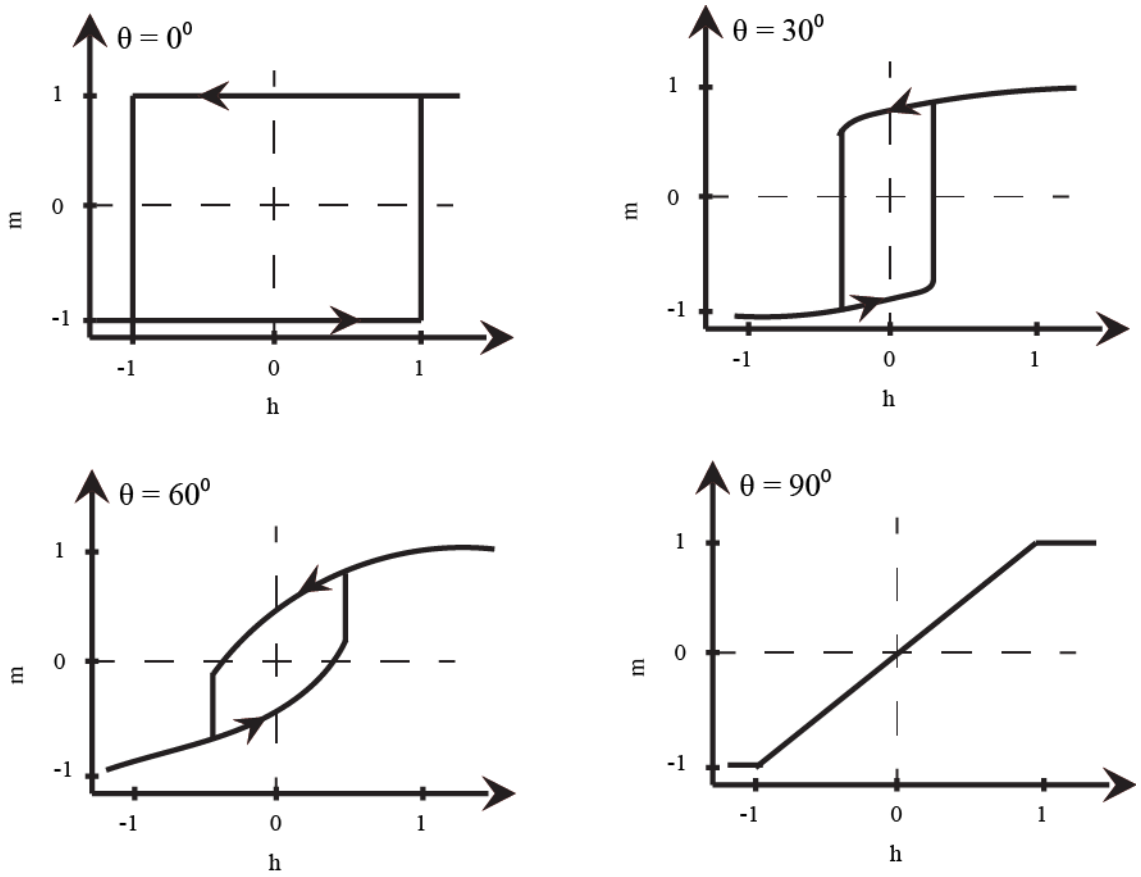

Figure 3.5: Calculated m-h hysteresis curves for coherent rotation model in ellipsoids for various applied field directions with respect to the easy axis [56].

If we call $H_c/(2K_u/M_s) = h_c$, the reduced coercivity, then the plot of h_c vs θ can be calculated by setting m= 0 in equation 3.3 (figure 3.6).

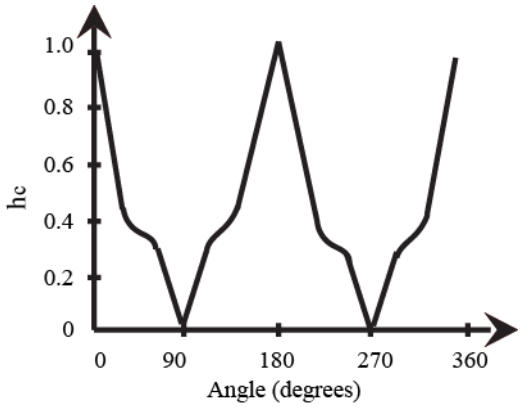

Figure 3.6: Plot of reduced coercivity, h_c vs θ_0 for coherent rotation model in a prolate ellipsoid. Refer to [56] for complete calculations and plots.

Similarly, the variation of coercivity with θ_0 for curling reversal mechanism can be calculated and plotted (figure 3.7).

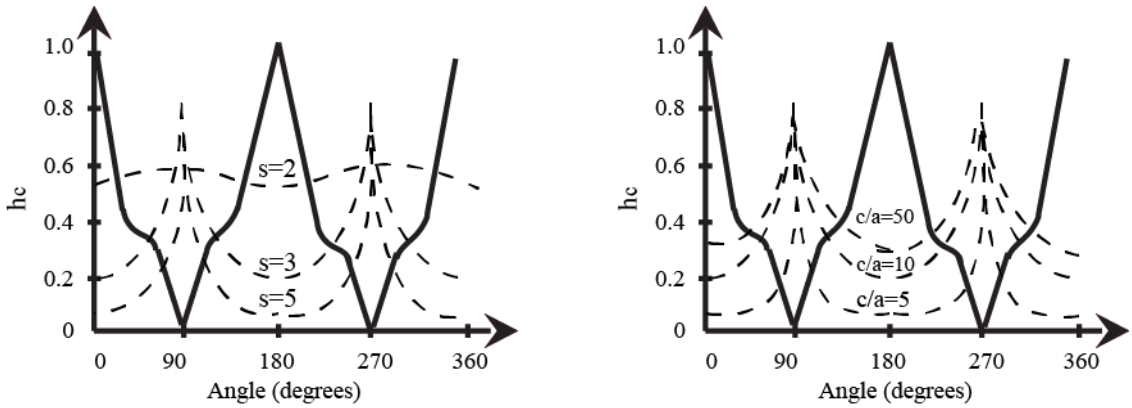

Figure 3.7: Plot of reduced coercivity, h_c vs θ_0 for curling model as (a) a function of nanowire diameter, given by $S = r/r_c$ and (b) function of aspect ratio (at S=3), given by c/a. Also, overlaid are h_c vs θ, from coherent rotation model (solid line). Refer to [56] for complete calculations.

As long as the reversal mechanism can be completely describe by coherent rotation, the coercivity is independent of aspect ratio or diameter of the nanowire/ellipsoid. In contrast, in curling mode, the coercivity changes with aspect ratio and diameter (figure 3.7). From a design perspective, the coercivity can be increased by increasing the aspect ratio and/or reducing the diameter (provided $r > r_c$). Note that the critical radius (r_c) is defined only for field parallel to the easy axis. Thus, for field perpendicular to the easy axis, generally coherent rotation is observed. Curling is observed mostly when field is parallel (or close to parallel) to the easy axis and $r > r_c$.

3.1.3 First order reversal curves and FORC diagrams

First order reversal curves (FORC) and FORC diagrams are very useful for detailed characterization of magnetic system such as magnetic rocks containing a mixture of magnetic minerals. It is routinely used by geologists for characterization of naturally occurring minerals, space rocks and collections of magnetic particles [59]. It is often employed to obtain information from a system containing a collection of particles which may have a distribution of magnetic properties such as coercivities and interactions.

The collection of the FORC diagram begins by saturating the magnetic system to a positive external magnetic field. Next, the applied field is lowered to a reversal field H_r. After reaching H_r, the field is increased back again to saturation, H_{sat} while measuring moment. The hysteresis arc resulting from the increase in field from H_r to H_{sat} is defined as a FORC (figure 3.8). For a reversal field H_r, and an applied field $H>H_r$, magnetization on the FORC is denoted by $M(H_r, H)$ and moment by $m(H_r, H)$. A FORC distribution is defined as

$$\rho(H_r, H) = -\frac{1}{2}\frac{\partial^2 M(H_r, H)}{\partial H_r \partial H}$$

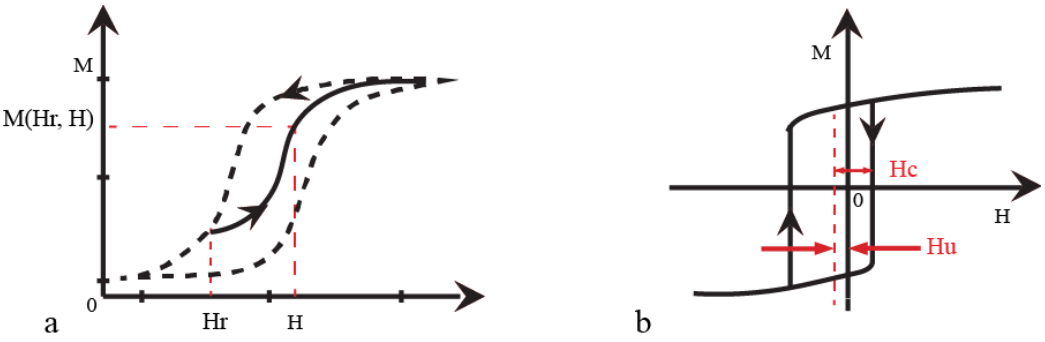

Figure 3.8: First order reversal curve (FORC). (a) shows definition of FORC (solid curve). (b) shows definition of coercive field (H_c) and interaction field (H_u) for a given FORC.

For a plot of moment 'm' vs H, FORC distribution is defined as

$$\rho(H_r, H) = -\frac{1}{2}\frac{\partial^2 m(H_r, H)}{\partial H_r \partial H} \qquad \text{Equation 3.3}$$

Invoking equation 3.1,

$$\rho(H_r, H) = -\frac{w}{2}\frac{\partial^2 (\chi_m H)(H_r, H)}{\partial H_r \partial H} \qquad \text{Equation 3.4}$$

Thus, ρ varies linearly with sample mass.

A plot of the FORC distribution in an intensity-contour plot is called a FORC diagram. The x-axis of a FORC diagram is defined as coercive field, $H_c = (H-H_r)/2$ and the y-axis is defined as interaction field, $H_u = (H+H_r)/2$ [59]. When a FORC curve is visualized as part of a minor hysteresis loop (called a hysteron, as shown in figure 3.8(b)), H_c corresponds to the coercivity of the hysteron and H_u corresponds to the bias or

the displacement of the center of the hysteron from zero. The bias is related to the interactions between the constituent elements of the system [59].

3.1.4 Multiplexed targeting and detection

A typical diagnostic assay employing nanoparticle technology involves selective targeting of a cell surface antigen (or a molecular marker) in a heterogeneous population of cells with an appropriately functionalized nanoparticle. This is followed by detection and separation of the targeted species.

Simultaneous high throughput analysis of a mixture of samples (cells or proteins) is important in cell sorting and disease diagnosis. Current methods largely employ fluorescent markers coupled with fluorescence microscopy or FACS. Here, the barcoding scheme is limited by number of fluorophores (spectrally resolvable colors) and intensities. This limits the number of samples that can be simultaneously analyzed. Here, Magnetic signatures from multi-layered ferromagnetic nanowires are proposed as alternative barcode tags.

Multiplexed detection can be achieved by using magnetically distinguishable nanoparticles coupled with a high sensitivity detection scheme such as FORC. The cylindrical geometry allows segmentation along the length of the nanowire and development of different magnetic signatures. The resulting magnetic signature is a function of the physical dimensions, the materials used for the multilayers and the sequence of the multilayers. Based on the thicknesses of the magnetic segments, suprafactorial magnetic signatures can be fabricated for nanowires in a barcoding

application. This capability is unique to the nanowire and cannot be attained using nano-spheres.

3.2 Results

3.2.1 Magnetic properties of nanowires: hysteresis and coercivity

Magnetization hysteresis loops were collected for arrays of 35 nm diameter (length ~ 6 μm, AR > 100) nanowires in porous AAO templates. When the applied field is parallel to the easy axis of the nanowires, the hysteresis loop is relatively square (figure 3.9). In this case, the remnance is almost equal to the saturation magnetization and the coercivity is maximum (~700 Oe) because the moments are aligned along energetically favorable easy axis ($\theta=0^0$) and would have to overcome the demagnetization energy barrier in order to switch to $\theta=180^0$. The saturating field is almost zero Oe since the moments are already preferentially aligned along the easy axis.

As the angle between the applied field and the easy axis increases, the hysteresis loop starts closing up. For example, when $\theta_0 = 60^0$, the area of the loop is 47.2% that of the square loop ($\theta_0 = 0^0$) and $M_r = 41.6\%$ of M_s and $H_c = 525$ Oe (compared to 700 Oe for $\theta_0 = 0$). Thus, the saturating field increases because it is more difficult to saturate the magnetization perpendicular to the wire (hard axis) because of the demagnetization energy.

For the same reason, the coercivity reduces as it is easier for the moment to rotate towards the energetically lower easy axis from the high-energy hard axis. For the case when $\theta_0 = 90^0$, the observed saturating field is ~3400 Oe compared to 3050 Oe obtained from calculation of demagnetization energy perpendicular to a high aspect ratio prolate

ellipsoid ($H_d = -2\pi M_s$). These results agree to a reasonable degree with the models proposed by Stoner Wolfarth (figure 3.5, section 3.1.2).

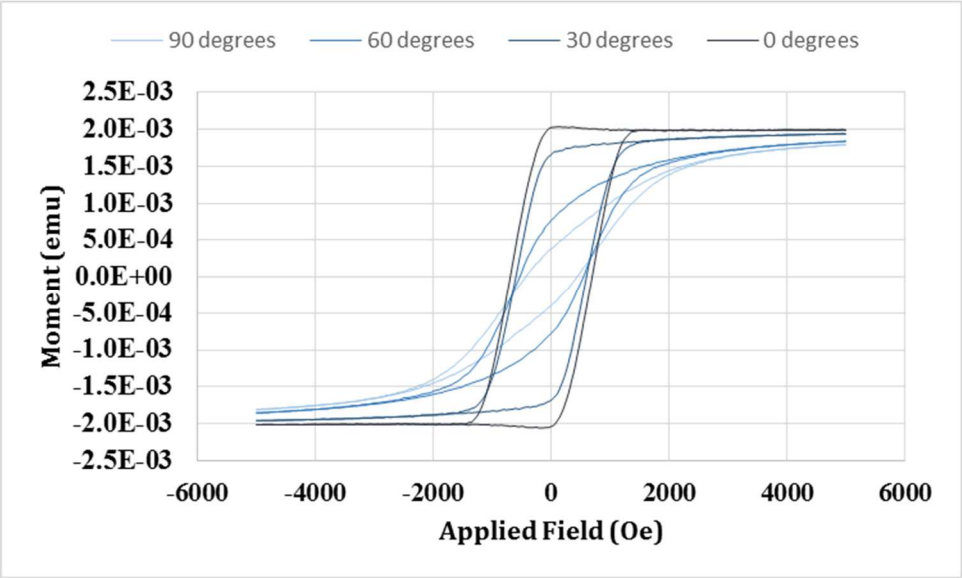

Figure 3.9: Hysteresis loops obtained from an array of Ni nanowires, 35 nm in diameter and aspect-ratio (AR) > 100. The hysteresis loops are recorded for various orientations of the applied field with respect to the easy axis.

When the coercivity from the hysteresis curves is plotted against angle between applied field and easy axis (θ_0), we get the curves shown in figure 3.10. The shape of coercivity vs angle plots are sensitive to changes in the diameters and aspect ratios of the nanowires and in principle, can be used as "magnetic signatures". Further, these plots can be used to infer the reversal mechanisms in the nanowires as discussed in section 3.1.2. From theory, we would expect small diameter nanowires to switch using coherent rotation mechanism and large aspect ratio particles to switch using curling or vortex wall (section 3.1.2). The critical radius for transition from coherent rotation to curling was

calculated to be 25 nm using Stoner-Wolfarth model. Thus, for diameters < 50nm, we would expect coherent rotation as the main reversal mechanism. This is mostly observed as shown in figure 3.10 when compared to figure 3.6. However, it is to be noted that even below the critical radius, the aspect ratio influences the shape of these curves. Aspect ratios > 1000 increase the demagnetization energy perpendicular to the wire significantly. Thus, a curling "component" is seen in the 18 nm diameter sample with aspect ratio greater than 1000, especially near the easy axes of the nanowire ($\theta_0 = 0^0, 180^0$). For nanowires with $r > r_c$, coherent rotation is still observed at higher angles ($\theta_0=90^0, 270^0$). However, at angles close to easy axis, curling is favored. The curling effect at these angles ($\theta_0 = 0^0, 180^0$) gets more pronounced for high aspect ratio structures (AR> 100).

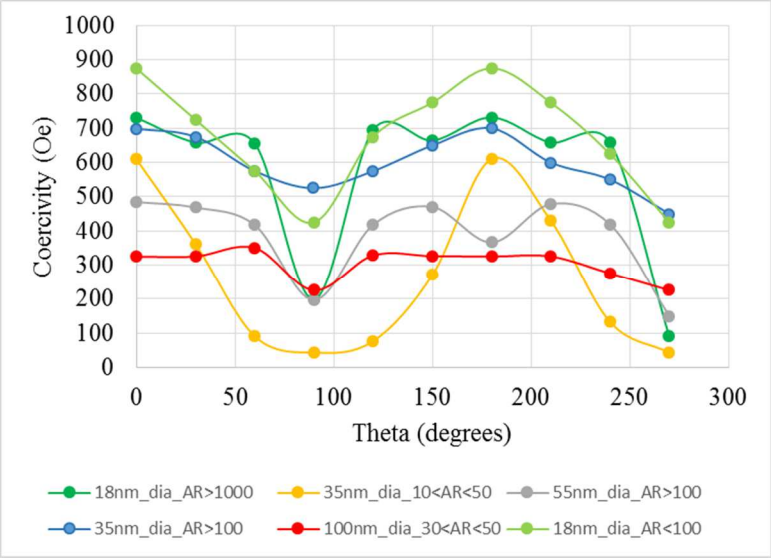

Figure 3.10: Coercivity vs angle (θ_0) for various nanowire samples with different aspect ratios and diameters in AAO, showing reversal mechanisms coherent rotation vs curling. Coherent rotation is generally observed for small diameter samples (r < 25 nm) and curling is seen in high aspect ratio structures mostly for r > 25 nm.

3.2.2 Can we use simple hysteresis loops for de-multiplexing a mixture of nanowire samples with unique signatures?

Consider two samples:

1) 18 nm diameter Ni nanowire sample (18-23, length 4.9 μm). Let's call this sample 'a' and call the population of nanowires n_a with mass w_a.

2) 100 nm diameter Ni nanowire sample (100-39, length 6 μm). Let's call this sample 'b' and call population of nanowires n_b with mass w_b.

3) Let 'c' be one mixture of 'a' and 'b' such that there are $n_c = n_a + n_b$ nanowires ($3*10^9 = 2.88*10^9 + 0.124*10^9$) and n_a: $n_b \sim 23:1$. The mass ratio, $w_a:w_b = 23*(18)^2(4900)/(100)^2(6000) = 0.74 \times 4900/6000 = 0.60$

4) Let 'd' be the second mixture of 'a' and 'b' such that there are $n_d = n_a + n_b$ nanowires ($14.284*10^9 = 14.16*10^9 + 0.124*10^9$) and n_a: $n_b \sim 115:1$. The mass ratio, $w_a:w_b = 115*(18)^2(4900)/(100)^2(6000) = 3.73 \times 4900/6000 = 3.04$.

Note that the magnetic signal from the 100 nm diameter sample 'b' is dominating even in mixture 'c' where n_a: $n_b \sim 23:1$. This is largely due to the higher volume (and therefore, mass) of 100 nm diameter nanowires compared to the 18 nm diameter nanowires and thus higher moment (m at saturation $=M_s.V$).

First, samples 'a' and 'b' are measured separately in a VSM and their hysteresis loops are obtained (figure 3.11). As discussed in section 3.1.2, the area of the hysteresis loop indicates energy dissipated by sample as heat through hysteresis losses. It is expected that the area of the hysteresis loop from a mixture of samples 'a' and 'b' would

be a simple addition of area of hysteresis from ‘a’ and area of hysteresis from ‘b’ (hysteresis ‘c’). However, an error of ~ 7 % is observed using MATLAB. This indicates either (i) error introduced due to limited sensitivity of VSM or, (ii) interactions between the nanowire samples or a combination of these factors.

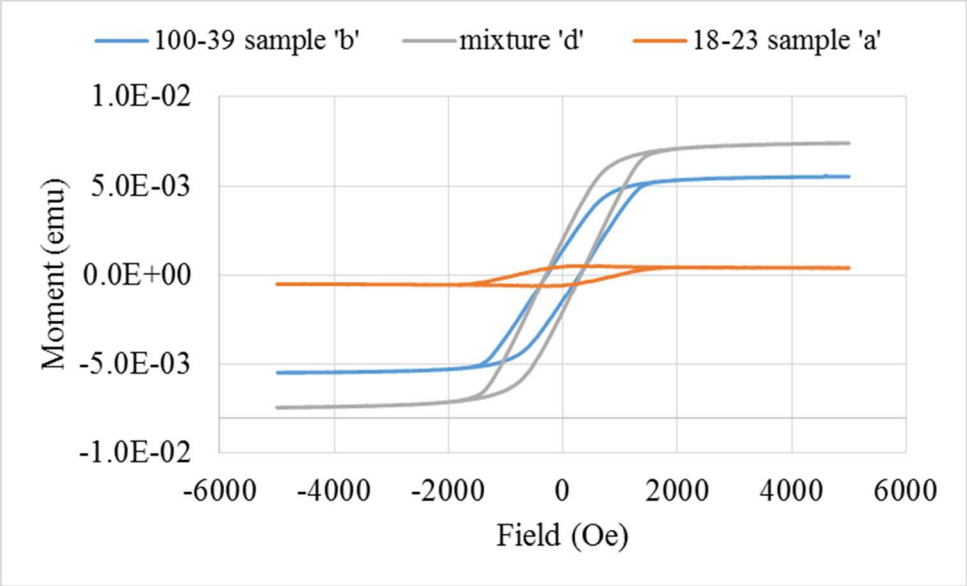

Fig 3.11: Simple hysteresis loops obtained for sample ‘a’ (18-23), sample ‘b’ (100-39) and mixture ‘d’. In all cases, the applied field direction was parallel to the lengths of the nanowires.

As seen in section 3.1.2, coercivity vs angle relations provide unique signatures for physically different nanowire samples. Plotting coercivity vs angle curves for samples ‘a’, ‘b’ and mixture ‘d’ (figure 3.12), we observe that ‘d’ can be expressed as a weighted sum of ‘a’ and ‘b’. However, we should exercise caution here as there are very few data points. Thus, a regression of ‘d’ on ‘a’ and ‘b’ obtained from the coercivity vs angle curves is not reliable.

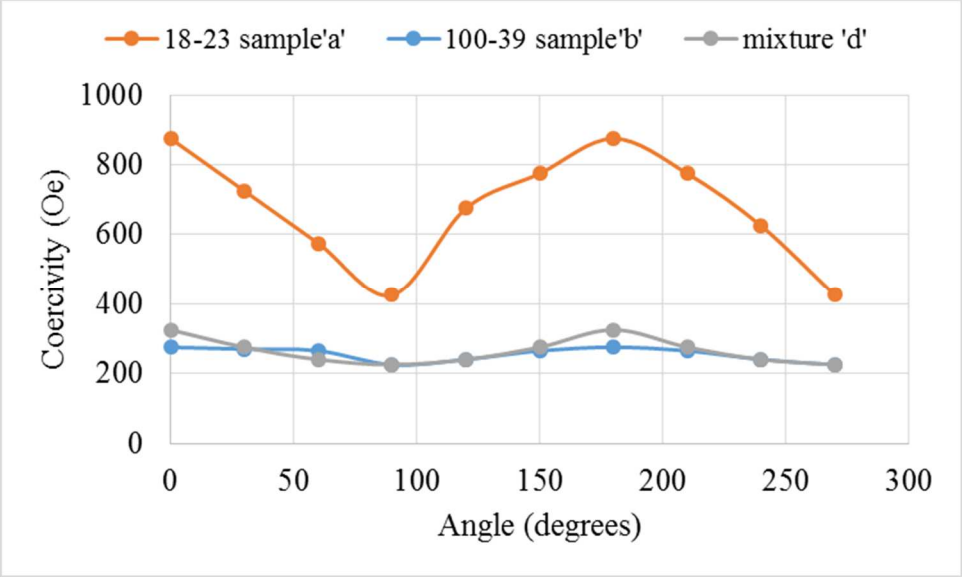

Fig 3.12: Coercivity vs angle (θ_0) for nanowire samples ‘a’ (18 nm diameter), ‘b’ (100 nm diameter) and mixture ‘d’ (measured in AAO).

3.2.3 FORC diagrams for demultiplexing a mixture

In the ensuing discussion, samples a-d mentioned in previous section will be used. Usually, for an array of nanowires, there is a distribution of coercivities/switching fields owing to small heterogeneities in the nanowire structures and inter-wire interactions. The observed hysteresis and switching field in a major hysteresis loop is generally, the peak of the distribution of these values. Thus, the information regarding the distributions of coercive field and interactions is lost in conventional VSM hysteresis loops. De-

multiplexing using only coercivity values can be misleading because the data values are averages rather than actual nanowire coercivities and the number of data points are limited.

First order reversal curves (FORC) offer a higher resolution method of measuring hysteresis of the whole sample as well as distribution in parameters of component nanowires. The detailed distributions of the magnetic samples allows deconvolution of a heterogeneous mixture of magnetic samples into its components.

FORC distributions of different weighted mixtures of ‘a’ and ‘b’, labelled ‘c’ and ‘d’ are obtained (discussed in section 3.2.2) and shown in figure 3.13 along with FORC diagrams (ρ vs H_c vs H_u) .

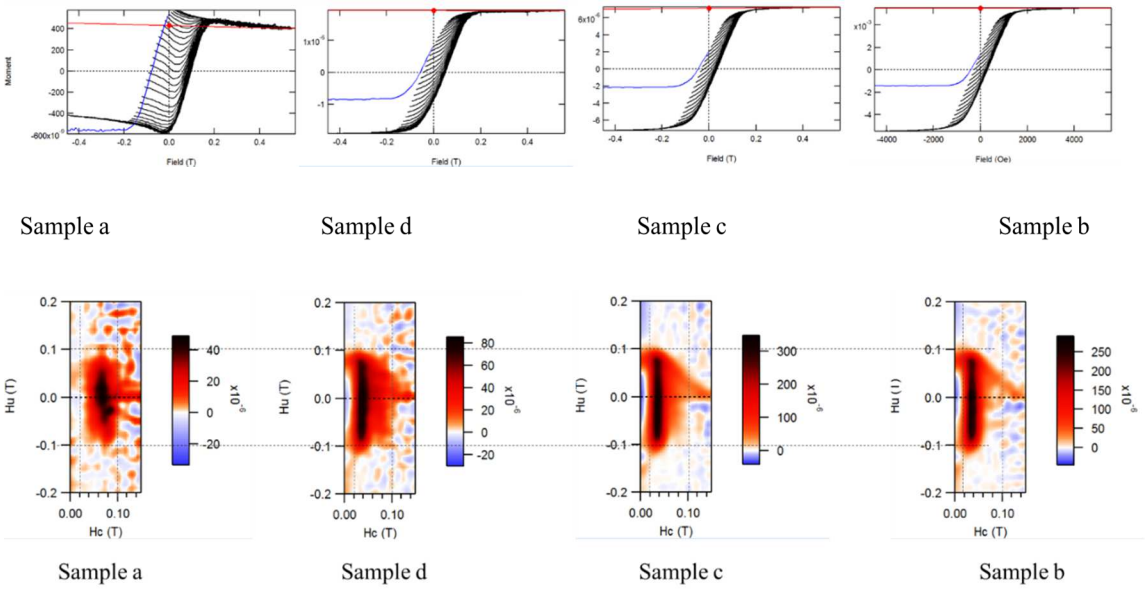

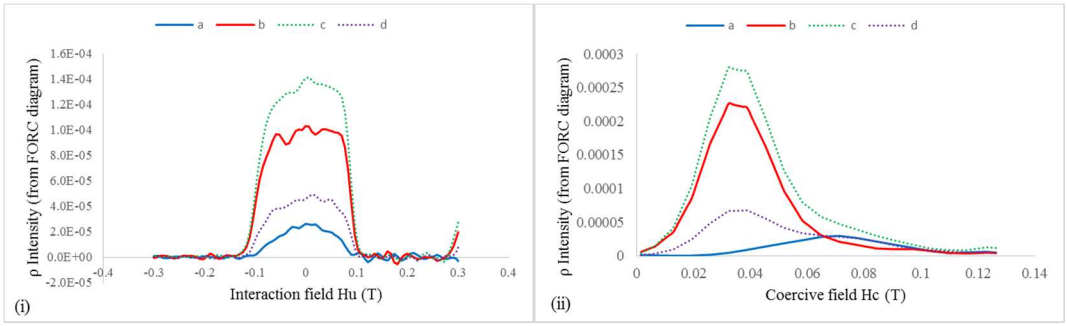

Fig 3.13: VSM FORC distributions (moment in emu in $A.m^2$ vs field in T) of samples 'a' and 'b' and mixtures 'c' and'd'. For mixture'd', units are expressed in cgs (moment in emu vs field in Oe. Conversion: 1T=10000Oe and 1emu = 0.001 $A.m^2$). Plotted below the FORC distributions are the respective FORC diagrams (ρ vs H_c vs H_u). These FORC diagrams are calculated after correcting for any paramagnetic/diamagnetic slope components in the hysteresis loops. The intensities obtained from FORC diagrams are plotted in (i) ρ vs interaction field and (ii) ρ vs coercive field. The Intensity vs coercive field plot (ii) is used to de-multiplex the mixtures 'c' and'd' into the component samples. The blue and red curves correspond to slope correction curves (not data from sample) routines in FORCinel.

From the FORC diagrams, we obtain FORC intensity vs Interaction field (figure 3.13(i)), where the intensity is averaged in the range of 0.02-0.1T H_c, and FORC intensity vs Coercive field (figure 3.13(ii)), where the intensity is averaged in the range of -0.1-0.1T H_u. These plots show the distribution of interaction field between the nanowires and distribution of coercivities of the nanowires, respectively.

The recorded variable in the VSM for each sample and their mixtures is the magnetic moment, which scales linearly with mass. We, therefore, expect that in a

mixture of two different samples, the moment of the mixture would be linearly dependent on the weighted moments of the individual samples.

For regression analysis, we choose the coercivity distribution (horizontal profile of ρ intensity vs coercive field) because this gives us a distribution of a physical property of the nanowire, i.e., the coercivity. (Interaction field involves more than two nanowires and the complex magnetic interactions between them, thus making it more difficult to resolve the property down to a single nanowire).

Further, from equation 3.4, the intensity of the coercive field distribution plot, ρ, scales linearly with sample mass 'w'.

From the horizontal profile (Intensity vs coercive field), a regression of FORC ρ intensity from FORC diagram of 'c', ρ_c, is evaluated on ρ_a and ρ_b using Minitab.

We obtain,

$\rho_c = -0.000001 + 0.7477\ \rho_a + 1.21574\ \rho_b$ equation 3.5

The residuals are plotted in figure 3.14. As indicated, the evaluated regression of ρ_c on ρ_a and ρ_b is linear and significant.

Comparing the coefficients of ρ_a and ρ_b with w_a and w_b,

From FORC, Coeff.(ρ_a)/Coeff.(ρ_b) = 0.615

We know that in mixture 'c', $w_a/w_b = 0.60$

Thus, the ratio of barcode 'a' to barcode 'b' in a mixture 'c' (n_a:n_b = 23:1) , as obtained from FORC, has an accuracy of 97.5%.

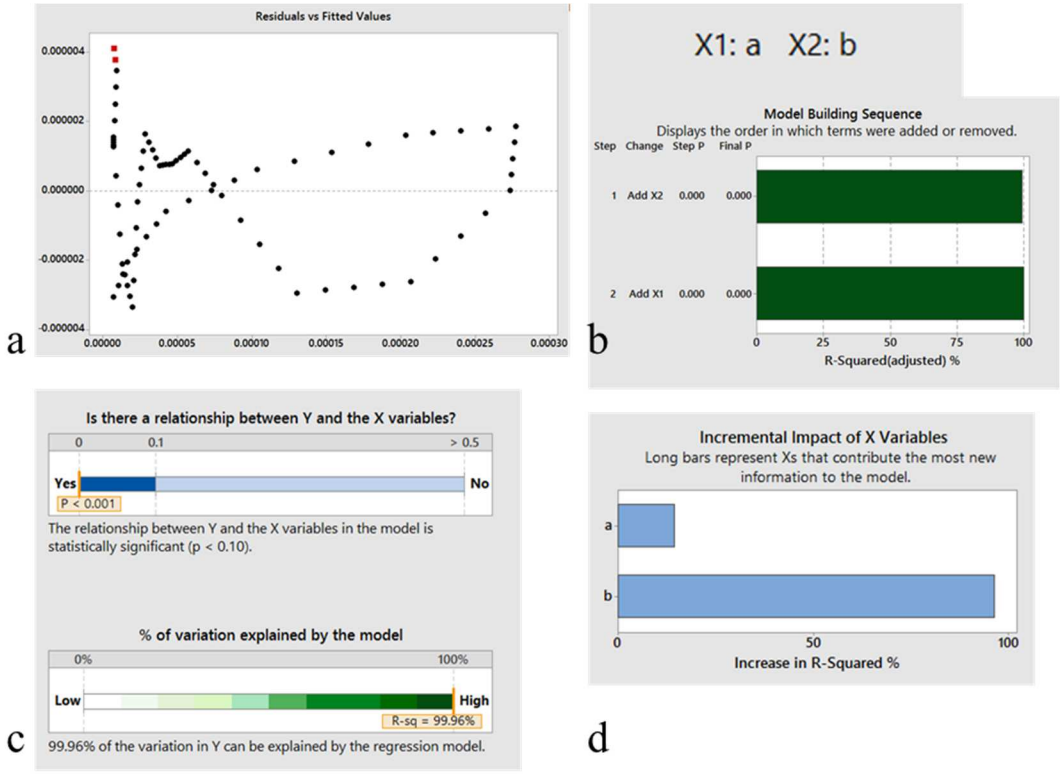

Figure 3.14: Regression analysis of ρ_c on ρ_a and ρ_b. (a) Plot of residuals vs fitted values shows a good fit with even distribution of points about 0. Red points (only two) indicate relatively large residues, but still small on an absolute scale. (b) Shows model building sequence and variation of R-squared with the addition of each variable to the model.(c) shows the computed significance value ($p<0.001$) and the degree to which variation in data points is explained by the model. (d) shows the incremental impact of each variable on the model. Clearly, increment in sample 'b' has a larger impact on the overall model compared to sample 'a'.

Similarly, a regression of ρ_d on ρ_a and ρ_b is computed from FORC intensity vs coercive field diagram.

We obtain,

$\rho_d = -0.000000 + 0.81\rho_a + 0.28\rho_b$ equation 3.6

The residuals are plotted in figure 3.15. As indicated, the evaluated regression of d on a and b is linear and significant.

Comparing the coefficients of ρ_a and ρ_b with w_a and w_b,

From FORC, Coeff.(ρ_a)/Coeff.(ρ_b) = 2.85

We know that in mixture 'd', $w_a/w_b = 3.04$

Thus, the ratio of barcode 'a' to barcode 'b' in mixture 'd' (n_a: n_b ~ 115:1), as obtained from FORC, has an accuracy of 93.75%.

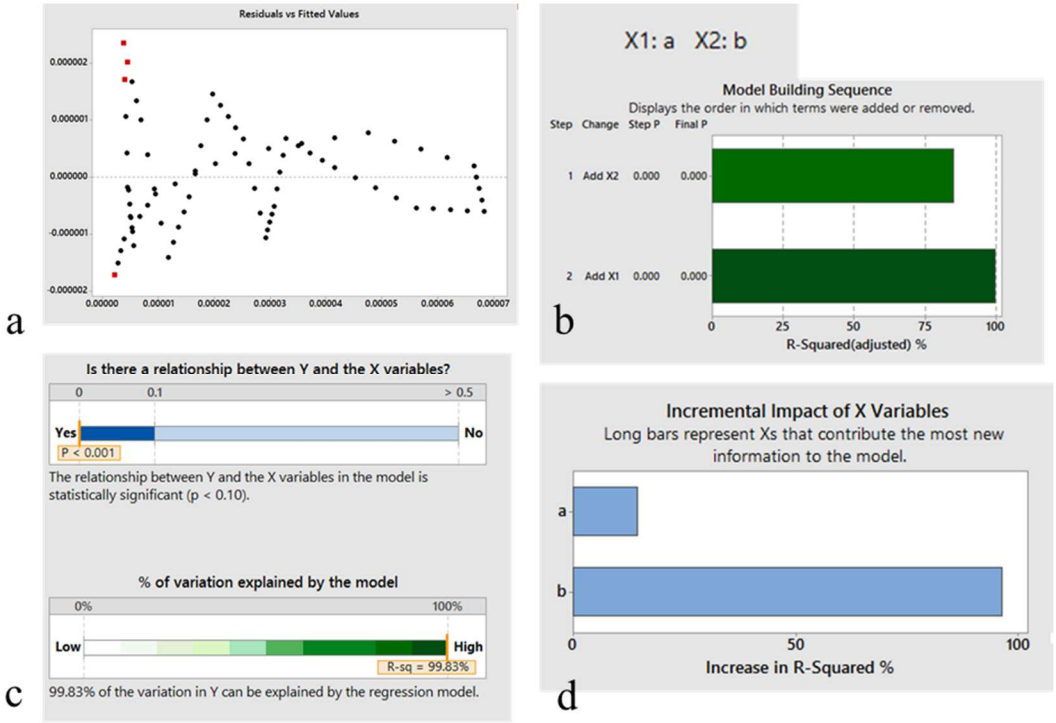

Figure 3.15 Regression analysis of ρ_d on ρ_a and ρ_b. (a) Plot of residuals vs fitted values shows a good fit with even distribution of points about 0. Red points (only four) indicate relatively large residues, but still small on an absolute scale. (b) Shows model building sequence and variation of R-squared with the addition of each variable to the model.(c) shows the computed significance value ($p<0.001$) and the degree to which variation in data points is explained by the model. (d) shows the incremental impact of each variable on the model. Clearly, increment in sample 'b' has a larger impact on the overall model compared to sample 'a'.

3.3 Methods

3.3.1 Measurement of simple hysteresis loops

All measurements are conducted on arrays of barcoded nanowires in AAO. Each sample, originally a 1cm x 1cm wafer, is broken into smaller pieces. The masses and dimensions of each wafer piece is measured using optical microscopy and Image J. First, the number of nanowires in the measured sample is calculated using sample area and pore (nanowire) density (obtained from SEM imaging and manufacturer specification sheet). Then, using paraffin grease, the sample is loaded on the sample holder (vibrating rod) of the Princeton micro-VSM. After affixing the rod to the socket of the VSM, the 'micromag' software is launched. Vibration amplitude of 1 and vibration frequency of 83 Hz are selected as operating parameters. The sample is centered between the pickup coils by adjusting 'x', 'y' and 'z' of the sample holder. Next, the applied field range is set as -0.5T

to 0.5T with a step size of 5mT. The VSM will acquire the hysteresis loop within this field range. Finally, select 'simple hysteresis' and press execute.

3.3.2 Measurement of coercivity vs angle curves

The experimental setup is same as above. However, instead of 'simple hysteresis', 'sequences vs orientations' tab is selected in the micromag software. Here, the rotation start angle (0^0), end angle (360^0) and rotation step size (30^0) are defined. This will enable an automated recipe that will acquire hysteresis loops sequentially at different orientations of the nanowires with respect to the applied field. Coercive field values are the x-intercepts of the simple hysteresis loops. Finally, these coercive field values are plotted against orientation.

3.3.3 Measurement of FORC curves and FORC diagrams

The experimental setup is similar to simple hysteresis loops. However, instead of 'simple hysteresis', choose 'First order reversal curves' option in the micromag software. The following parameters in the pop-up window are adjusted to shown values:

NForc = 83, H_{sat} = 0.56 T, H_{b1} = -0.2 T, H_{b2} = 0.2 T, H_{c1} = 0 T, H_{c2} = 0.15 T and averaging time = 0.5 seconds. Press 'execute'. FORC diagrams are evaluated using Igor Pro FORCinel. The paramagnetic/diamagnetic components are subtracted from the hysteresis loops before calculating FORC diagrams. FORC diagrams are evaluated using a smoothing factor of 3.

3.3.4 Statistical analysis

Statistical and regression analysis was carried out using Minitab for sets of data, each set containing at least 72 points.

3.4 Conclusions

In this chapter, it was shown that the magnetic properties of nanowires like hysteresis, coercivity, and coercivity vs orientation can be controllably designed by controlling the nanowire dimensions.

The FORC technique was used to decode a mixture of two magnetically different nanowire samples. This technique could detect one nanowire type from 23 nanowires of second type (1:23) in a mixture with an accuracy of 97.5%. In a mixture of nanowires with population ratios 1:115, the accuracy reduced to 93.75%. In conclusion, FORC is a strong technique to magnetically decode mixtures of magnetically different nanowires.

Chapter 4: Interactions between nanowires and cells

In this chapter, the interactions of nanowires with biological cells will be presented. Specifically, the following points will be covered:

(i) Attachment of magnetic nanowires to biological cells ("tagging" cells).

(ii) Influence of magnetic fields on magnetically "tagged cells" and magnetic separation of the same cells.

(iii) Presence of nanowires clusters in nanowire-cell samples contributing to errors and heterogeneity in nanowire-cell samples and thus, emphasizing the need for quality control in nanowire samples.

(iv) Imaging techniques for analysis of nanoparticles in cell-based experiments.

4.1 Theory:

4.1.1 Eucaryotic cells

The cells used in this study and most cell-culture studies are eucaryotic cells. These cells have DNA enclosed within a separate sub-membrane called the nucleus. The nucleus carries the information through DNA in the form of chromosomes which is passed to future generations of cells through cell division. Further, there are other sets of membrane-enclosed compartments (organelles) that specialize in the processes of digestion, sorting of proteins or biomolecules and secretion. In this regard, specific organelles like the mitochondria are charged with the role of generating energy (figure 4.1). A complex network of protein filaments within the cytoplasm form the cytoskeleton of the cell, which gives them structure, controls their shape and guides mobility. These cells are the essential components of all multicellular organisms.

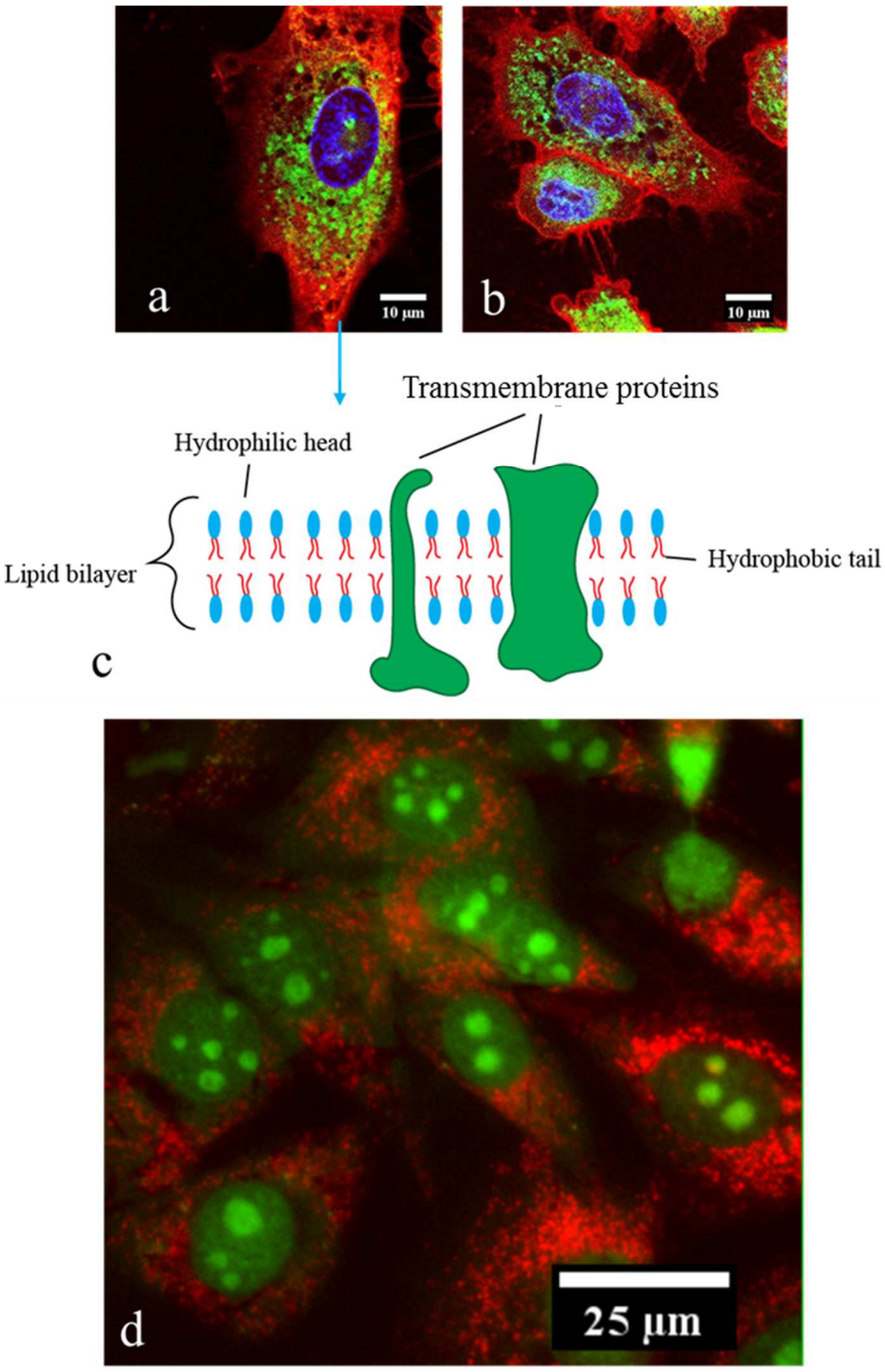

Figure 4.1 Eucaryotic cells. (a,b) Confocal fluorescence images of eucaryotic cells (osteosarcoma cells OSCA-8) stained with various fluorescent markers. The nucleus is

stained with a blue nucleic acid stain (Hoechst 33343), acidic lysosomes located in the cytosol are stained with green fluorophore (lysosensor green) and the plasma membrane is stained with a red fluorophore (Cellmask red plasma membrane stain). (c) Schematic showing structure of the plasma membrane. The plasma membrane is composed of a lipid bilayer and transmembrane proteins[18]. (d) Osteosarcoma cells stained with green nucleic acid stain (Syto green) to label the nucleus and orange stain to label the mitochondria (Mitotracker orange) residing intracellularly in the cytosol.

4.1.2 Eucaryotic cell lines are widely used for cell culture experiments

In the laboratory, eucaryotic cells are obtained from disrupting live animal tissue. However, the obtained cells cannot be cultured directly *in vitro*. This is because outside the animal, the cells stop dividing after some time due to absence of enzymes and growth factors that are generally available to them inside a live animal. Thus, the cells obtained in this manner are modified genetically for continued proliferation. This process is called cell transformation. Once the cells are transformed, they are cultured in an aqueous environment that provides them with the necessary proteins, sugars, nutrient, growth factors and enzymes (this mixture is called cellular medium). The cells are now called an immortalized cell line. Some examples of popular immortalized cell lines include 3T3 fibroblasts (mouse), HeLa epithelial (humans), C57/Bl6 macrophages (mice) and OSCA-8 osteosarcoma (canine).

4.1.3 Plasma membranes enclose all cells

Cells are enclosed in plasma membranes which act as selective barriers across which they can traffic nutrients from the environment and excrete waste materials to the environment (figure 4.1(c)). The plasma membrane is constituted by amphiphilic molecules called phospholipids which have a hydrophobic tail (composed of hydrocarbons) and a hydrophilic head[18]. Thus, the plasma membrane is composed of a bilayer of phospholipid molecules formed through self-assembly and non-covalent interactions such that hydrophilic portions are exposed to the aqueous environment whereas the hydrophobic tails are hidden within the bilayer. This layer is about 5 nm thick as determined using TEM [18]. Further, the plasma membrane has different classes of embedded proteins aiding in the transport of necessary molecules across the membrane, catalyzing membrane-associated biochemical reactions like ATP synthesis, serving as structural links between the cytoskeleton and the extracellular matrix or a neighboring cell and eliciting specific cellular responses when interacting with specific external molecules or ligands.

4.1.4 ELISA, fluorescence and confocal microscopy

4.1.4.1 Enzyme-linked immunosorbent assay (ELISA) and immunofluorescence

ELISA is a biochemistry assay which is used to detect presence of a protein (mostly antigens) in a liquid sample. It is based on the principle of highly specific interactions between antibodies and antigens with the additional use of an enzyme to amplify the fluorescent signal.

Antibodies are proteins that are secreted by the (adaptive) immune system in order to recognize and eliminate foreign molecules or microorganisms (antigens). They

have high specificity in targeting antigens (they can distinguish between two protein molecules that differ only in one amino acid). An attached fluorescent molecule to the (primary) antibody can be used to recognize and image antigens. However, this fluorescent signal intensity is dependent upon the number of antigen molecules in the sample and therefore, it can be weak. In order to amplify this signal, a group of secondary antibodies with conjugated fluorophores can be used instead, to target the primary antibody-antigen complex[18] (figure 4.2). In ELISA, an enzyme such as alkaline phosphatase is linked to the secondary antibody which on binding to the primary antibody-antigen complex catalytically produces an inorganic phosphate and in turn, thousands of molecules constituting a colored precipitate. Thus, this is a very sensitive detection method and allows 100s of experiments to be conducted in parallel in multi-well plates. On the other hand, this technique exhibits low spatial resolution due to diffusion of precipitate molecules in the assay. Thus, for high spatial resolution of proteins/biomolecules, fluorescence microscopy is used.

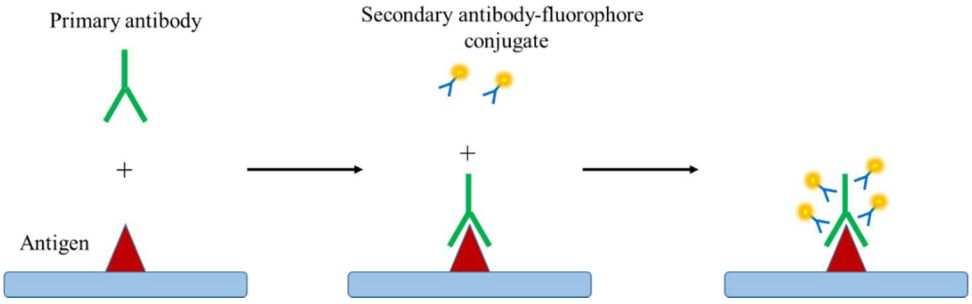

Figure 4.2: Principle of ELISA. This involves binding of antigen to primary antibody and labeling primary antibody with secondary antibody-fluorophore conjugate[18].

4.1.4.2 Fluorescence microscopy

When fluorescent molecules are excited at a specific wavelength, they emit light at a longer wavelength which can be selectively filtered and collected using a detector. Fluorescence microscopy can be used to visualize cells and image specific proteins, intracellular components and molecules in cells by staining them with fluorescent dyes (figure 4.1). The fluorescence microscope setup shown in figure 4.3 (a) includes two sets of filters, one to filter the light before it reaches the sample (excitation wavelength) and the other to filter the light obtained from the sample (emission wavelength), a dichroic mirror and a high energy excitation source. Specific staining of molecules and proteins can be achieved by conjugating fluorophores to antibodies (figure 4.2). These antibodies can target membrane and intracellular proteins with high specificity. However, epi-fluorescence has low resolution for samples thicker than 2 μm. For thicker samples, confocal microscopy is used.

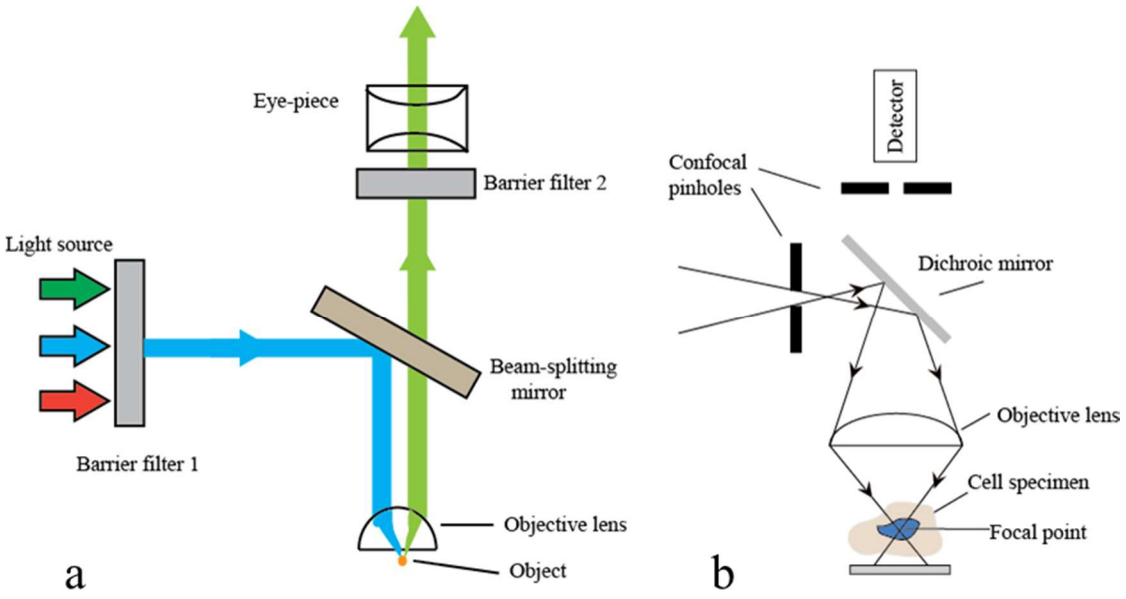

Figure 4.3 Schematics showing principles of (a) epifluorescence microscopy and (b) confocal microscopy. Refer to [18,60] for detailed descriptions.

4.1.4.3 Confocal microscopy

Confocal microscopy is a high resolution technique which is used to obtain optical sections (z-sections) from biological samples such as cells and tissues owing to its narrow depth of focus and ability to remove glare from out-of-focus sections. In epi-fluorescence microscopy, light from a Xenon or Mercury lamp bathes the entire sample, and the emitted fluorescent light is captured by a camera or detector. In contrast, in confocal microscope, a laser light source is used to illuminate a point on the sample and is scanned across the surface to obtain an optical section. Extraneous light from out-of focus z-planes are blocked by the pinhole apertures. Both pinhole apertures, placed in front of the source and placed before the detector, are spatially confocal (have the same foci) and thus, the microscope is called confocal (figure 4.3(b)).

4.1.5 Electron microscopy for resolving fine structure of the cells and spatial localization of nanowires:

While light microscopy techniques yield important spatio-temporal information about interactions between nanowires and cells, they are limited in resolution to above ~160-240 nm. Electron microscopy can usually resolve the sub-cellular organelles and filaments, which are often less than 100 nm. The advantage of using an electron beam for imaging is that the electron wavelength (and therefore, resolution) can be made very fine by increasing the velocity of the electrons by applying an accelerating voltage. For example, at an accelerating voltage of 100 KV, the electron wavelength is ~ 0.004nm and the corresponding microscope resolution, in theory, could be as low as 0.002 nm. Practically, most electron microscopes have a resolution ~ 0.1 nm because of lens aberrations which are harder to correct in electron microscope compared to light microscopes (due to smaller NA at the center of the lens).

However, imaging biological samples like cells with SEM/TEM requires following complex and time-consuming specimen preparation protocols. The specimen to be imaged is fixed with a fixative like gluteraldehyde which cross-links the membrane proteins covalently to each other. At this point the cell/tissue is no longer alive. Similar to light microscopy, the electron microscopy sample is then stained with an electron dense material like osmium tetroxide[61]. This binds to the cross-linked proteins as well as the membrane lipid-bilayers. The penetration depth of the electron beam is generally very small. Thus, in order to attain sub-cellular resolution, the cell samples are dehydrated and permeated with a monomeric resin which penetrates the cell and polymerizes it into a

plastic block [61]. Then, thin sections of this polymerized sample are sliced with a diamond knife and are imaged. While analyzing the images, obtained using electron micrsocopy, it should be kept in mind that the sample preparation techniques might alter the actual structure of the cell. Thus, electron microscopy is generally used in conjunction with other imaging techniques.

4.2 Results

4.2.1 Incubation of bare nanowires with osteosarcoma cells (OSCA)

After a 24 hour incubation period of osteosarcoma cells with nanowires in an incubator set at 37^0C and 5% CO_2, the detached cells were observed under an inverted Nikon TE 200 microscope. The motion of the cells was recorded as a magnet (1 KOe) was moved in a semi-circular contour along the periphery of the flask holding the cells. This qualitative test revealed a large fraction of the cells responding to the moving magnet indicating several cells were "tagged" with barcode magnetic nanowires (figure 4.4). The term "tagged" describes nanowires attached to the cell membrane as well as nanowires uptaken by the cell.

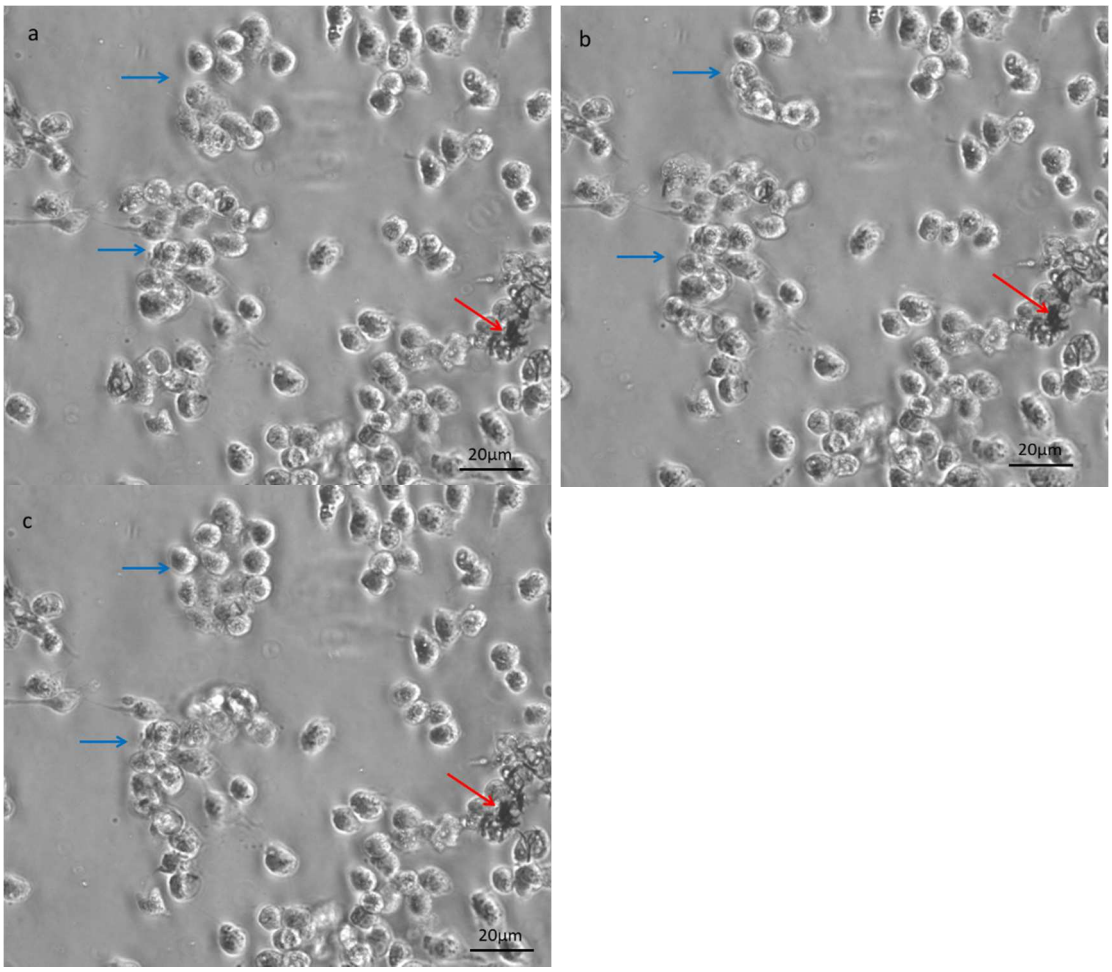

Figure 4.4: (a), (b), and (c) show motion of nanowire-tagged cells (blue-arrows) in response to a moving NdFeB magnet(*) as seen under an optical microscope in brightfield. The red arrows indicate nanowire clusters surrounded by OSCA cells. The video time lapse over which the response was recorded lasted about 2 minutes. The frames shown above were still-shots taken from the video.

A hemocytometer was used to get a quick estimate of the fraction of cells moving. This fraction increased from nearly 69% to 100% in samples taken from post-separation samples (the nanowire concentration was constant at 1pM.). This increase was

due to improvements in the design of the magnetic separation field. Instead of simply holding NdFeB magnets to the side of the petri dish holding the cells, a 6.8 kOe field with 5.15T/m gradient was applied across the entire sample. An interesting point was that cells without nanowires did not respond to applied magnetic fields, which is important for separation.

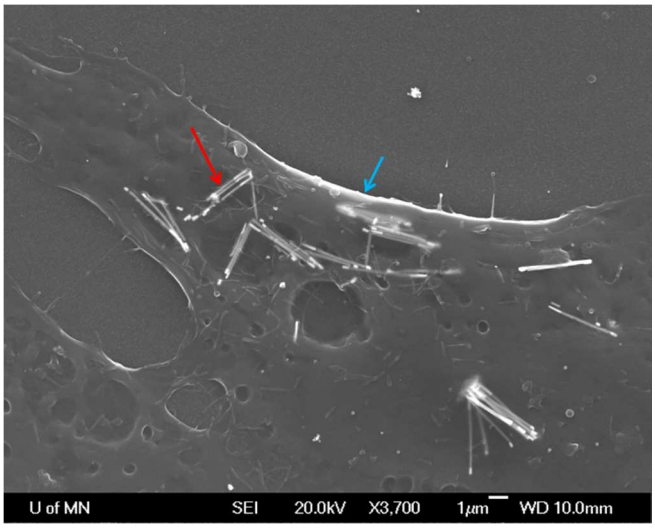

Figure 4.5: SEM micrograph showing Au/Ni/Au nanowires inside and on membrane of OSCA cell (air-dried)(*). Though the nanowires clump in small numbers, the cell has uptaken the bundles allowing separation. Blue arrow shows the cell membrane and the red arrow shows Au/Ni/Au barcode nanowires.

Figure 4.5 shows an SEM image of barcoded nanowires with (Au/Ni/Au) multi-layers inside and on the cell membrane. A more thorough SEM analysis of the tagged cell samples revealed large clusters of nanowires endocytosed by cells. Since these clusters

were large, they weren't entirely uptaken by cells. As seen in the following SEM images in figure 4.6, some of the clusters appear to be partially endocytosed while individual wires and smaller clusters appear to be inside membranes. The endocytosis mechanism is most likely non-specific fluid-phase (see chapter 6) for such large particles. TEM image in figure 4.6 (b) indicates the encapsulation of nanowires within intracellular membrane-enclosed compartments called vacuoles.

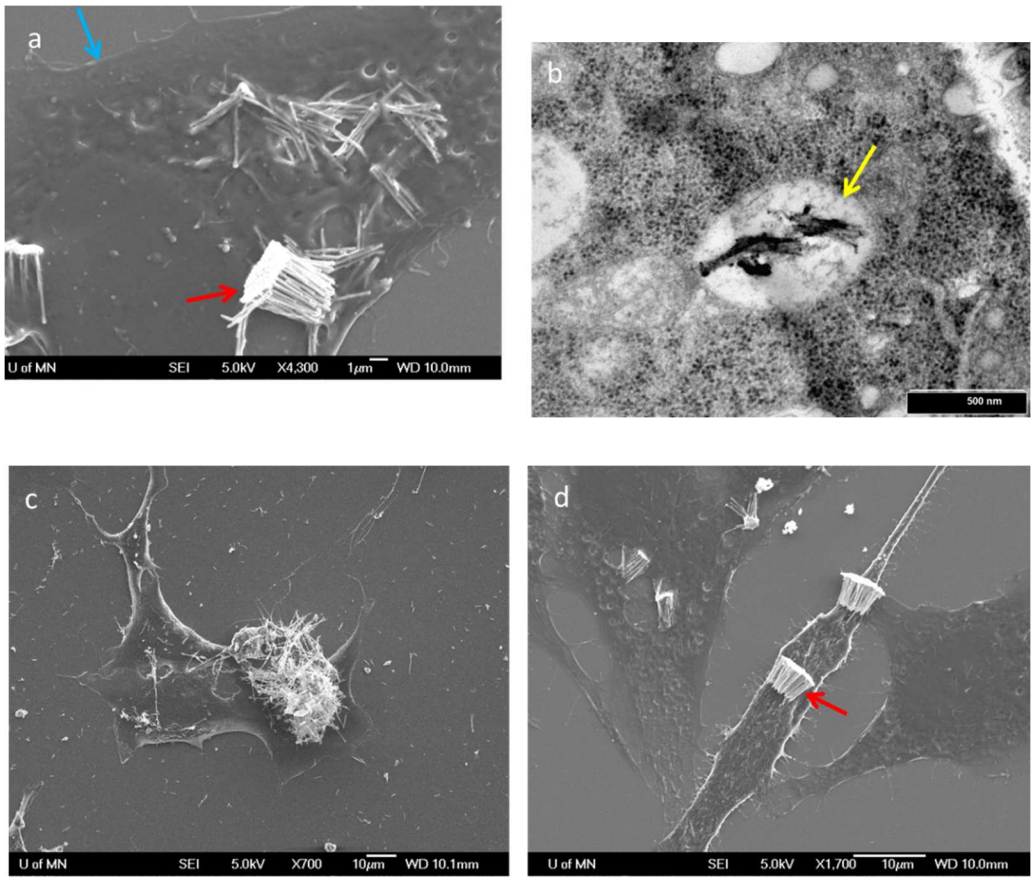

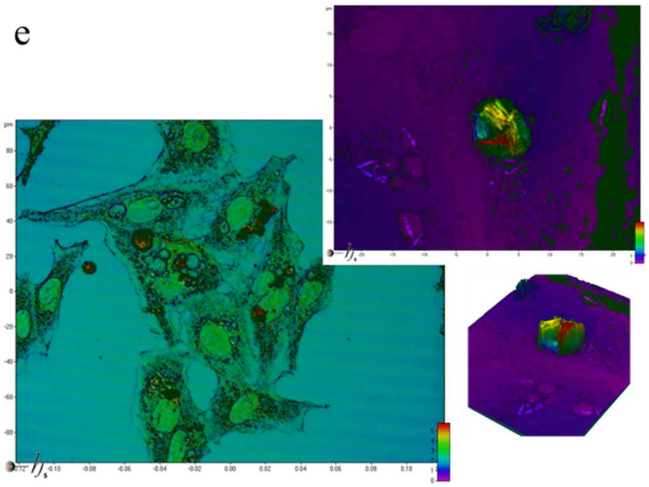

Figure 4.6: (a), (c), and (d) SEM images of a cell with individual nanowires and clumps of nanowires(*). Notice that all clumps/clusters were uptaken or partially endocytosed by cells (b) TEM image of nanowires inside a vesicle of the OSCA cell. Red arrows show nanowire clusters, the blue arrow shows cell membrane and the yellow arrow shows a membrane-enclosed vesicle inside the cell with barcode nanowires. (e) shows z-mapping of nanowire clusters with respect to the cell membrane using a laser-scanning confocal microscope. The purple color in the inset depicts the plasma membrane. The nanowire cluster can be observed to occupy a large volume outside the membrane, as indicated by the z-color profile.

4.2.2 Concentration dependence of magnetic separation:

Initial cell incubation experiments with nanowire clusters for non-specific uptake revealed that for nanowire concentrations in the range of 0.01pM to 0.18pM, a larger fraction of cells appeared to have uptaken nanowires when the clusters were reduced by ion-milling. This was determined by cell separation studies which showed that 39 – 47.9% of the original number of 1.28 million cells was separated out when clusters were

reduced by ion-milling. In comparison, [23] reported 49.3% of their original cells separated with nanowire concentration of 60000 particles/ml (or $1x10^{-4}$ pM). Once separated, our cells were optically verified to be tagged with nanowires by their response to a magnet that was moving along a circular contour surrounding the cells (100% of the separated cells were moving). In contrast, only 7.8% to 30.14% of the original number of cells was separated when nanowire samples were not ion-milled. This smaller fraction was most likely due to sedimentation of larger clusters, which decreased the number of free nanowires in solution available for uptake. However, aggregation was still observed even after milling the growth contact. This can be attributed to magnetic interactions between the nanowires (see chapter 5).

Thus, the major conclusion from these experiments is that aggregation of nanowires should be addressed in order to reduce sample heterogeneity and produce repeatable results.

4.2.3 A barcoding experiment: proof of concept:

To illustrate the applications of magnetic nanowires for barcoding a heterogeneous cell population, the following experiment was conducted as proof-of-concept. Two different cell lines were used as the species to be targeted in a mixture: A549 human lung carcinoma cells and human foreskin fibroblasts (HFFs). Corresponding to these cell lines, two nanowire samples were prepared that were dimensionally different:

(i) Segment lengths 3 μm 0.3 μm Au/ 3.1 μm Ni and diameter 100 nm –barcode 1

(ii) Segment lengths 0.12 μm Au/1.8 μm Ni/ 0.3 μm Au and diameter 100 nm-barcode 2

To optically verify barcoding, the A549 cells were stained with only a blue nuclear stain, whereas the HFF cell lines were stained with a blue nuclear stain and a green plasma membrane stain. For the nanowires, barcode 1 was labelled with an antibody-green fluorophore conjugate which would specifically target membrane proteins (EpCAM) on A549 cells and barcode 2 was labeled with a non-fluorescent antibody label specific to membrane proteins (Vimentin) on HFF cells (figure 4.7).

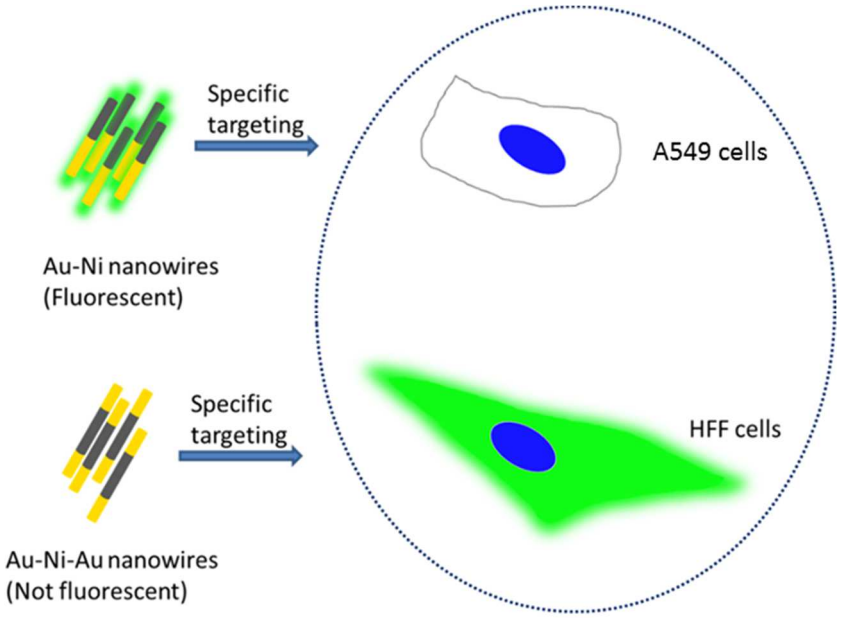

Figure 4.7: Schematic showing barcoding scheme: Fluorescent barcode 1 was labelled with antibodies targeting A549 cells and barcode 2 was labelled with antibodies targeting HFF cells.

An overlay of DIC, reflectance and fluorescence imaging was conducted to spatially resolve the nanowires with respect to the cells and the different cell lines from each other. Figure 4.8 shows both A549 and HFF cells co-cultured together 50:50. Consequently, the cell-medium consists of a 50:50 mixture of A549 and HFF media.

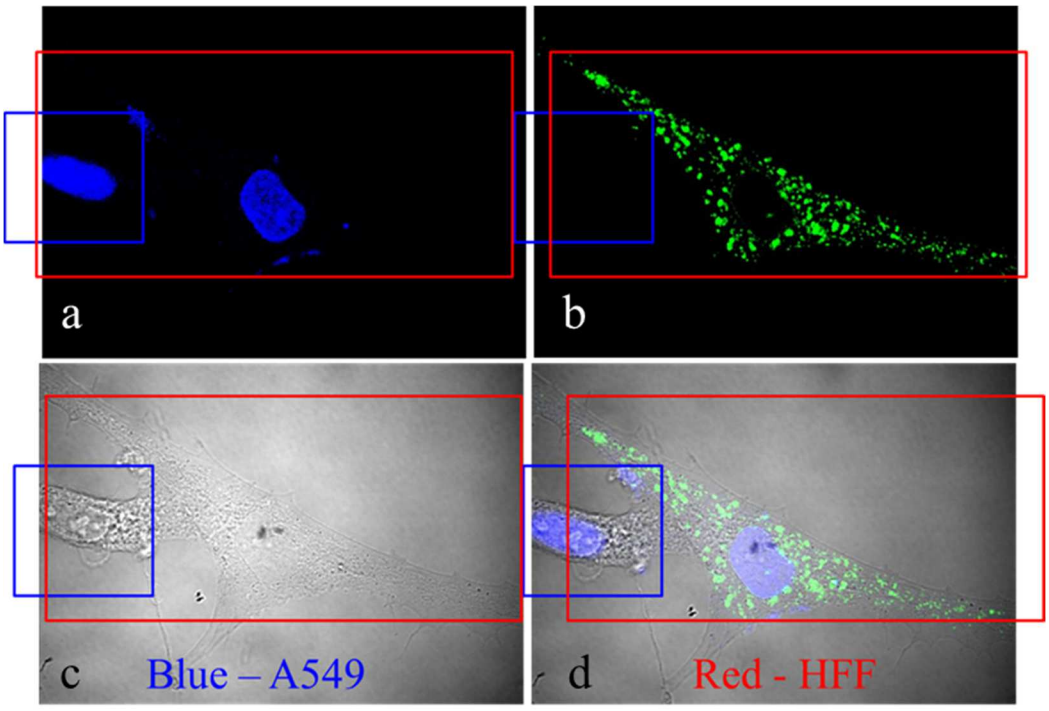

Figure 4.8: Confocal and DIC microscopy overlay showing co-cultured A549 cells and HFF cells. (a) Confocal microscopy image in blue channel showing blue fluorescence from stained nuclei of A549 cells and HFF cells. (b) Confocal microscopy image in green channel showing no fluorescence from A549 cells and green fluorescence from the membrane of stained HFF cells. (c) DIC image of the same cells (d) Overlay of all three channels showing distinctly the A549 cell and the HFF cell.

A mixture of barcodes 1 and barcode 2 was titrated into the medium at different ratios with respect to cell populations and allowed to incubate for 6 hours at 37^0C and 5% CO_2. Specifically, nanowires to cell ratios of 0:1, 1:1, 25:1, 50:1 and 100:1 were tested with barcode1: barcode 2 maintained at a ratio of 1:1 (see methods section 4.3.3). Following incubation, the cells were fixed and immersed in PBS for confocal imaging.

As designed initially, the green fluorescent nanowires (barcode 1) specifically attached to A549 cells (labelled with blue nuclear stain only) whereas the non-fluorescent nanowires (barcode 2) specifically attached to HFF cells (labelled with blue nuclear stain and green plasma membrane stain). This is depicted in figure 4.9 and figure 4.10.

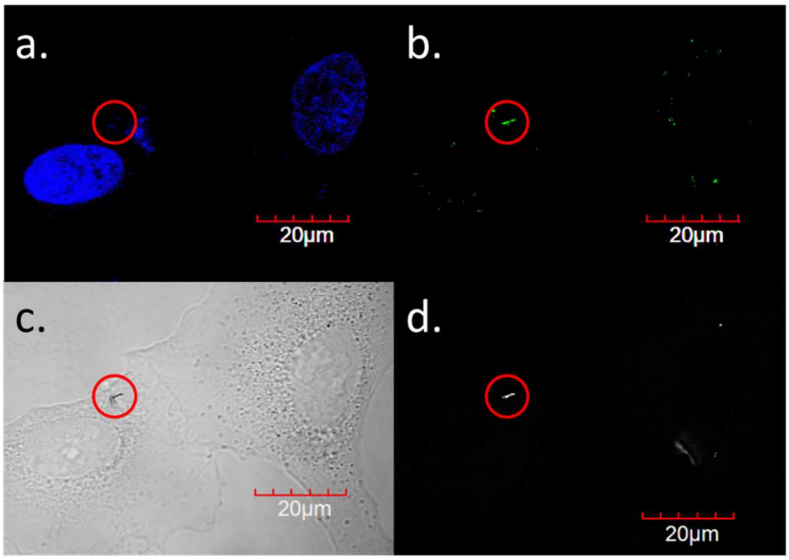

Figure 4.9: Microscopy techniques used to identify targeting of barcode 1 to A549 cells. (a) shows the blue-fluorescent nuclei of A549 cells as observed in the blue fluorescent channel of the confocal microscope. (b) The green fluorescent channel of the confocal microscope shows fluorescence from the nanowire (labelled with a green fluorophore) but no fluorescence from the cell membrane which is consistent with the fact that the A549 cells were not labelled with a green fluorophore. (c) DIC microscopy is used to resolve the location of the nanowire with respect to the cell membrane. (d) Reflectance microscopy confirms that the fluorescent particle observed in the green channel of the confocal microscope is indeed a metallic nanowire.

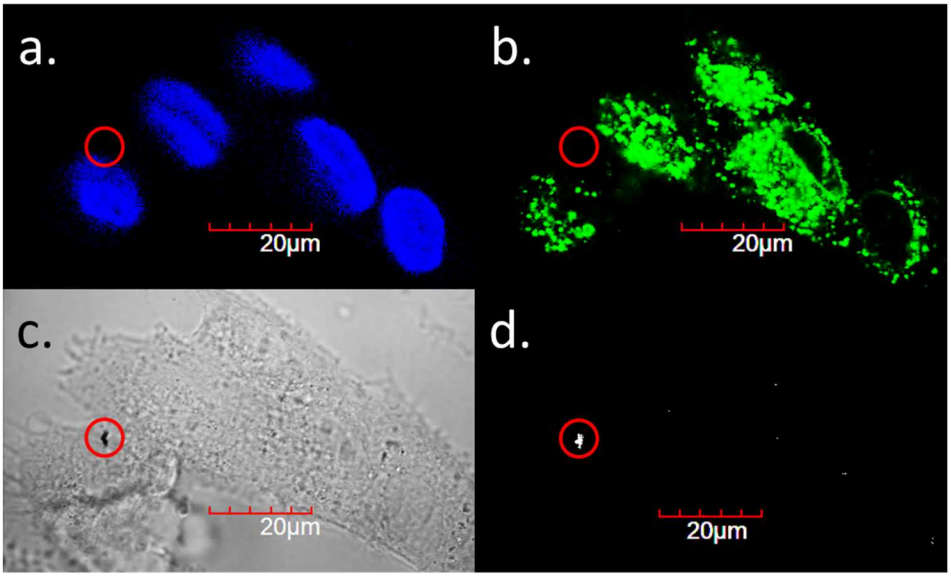

Figure 4.10 Microscopy techniques used to identify targeting of barcode 2 to HFFs. (a) shows the blue-fluorescent nuclei of HFF cells as observed in the blue fluorescent channel of the confocal microscope. (b) The green fluorescent channel of the confocal microscope shows fluorescence from the cell membrane which is consistent with the fact that the HFF cell membranes were labelled with a green fluorophore. Just with this information, we cannot confirm the presence of barcode 2 in the assay, since it was not labelled with a fluorescent marker. (c) DIC microscopy is used to detect any particulate matter and further, resolve the location of the particulates with respect to the cell membrane. (d) Reflectance microscopy detects any nanowires in the assay and differentiates between stray particulate matter and metallic nanoparticles. Thus, overall we observe barcode 2 has indeed targeted HFFs.

Figures 4.9 and 4.10 show specific targeting of A549 cells and HFF cells, respectively. Metallic nanoparticles are identified and separated from other potential

particulate matter in the medium using reflectance microscopy which reveals bright metallic nanowires. This was used in conjunction with two fluorescent channels (blue and green) in a confocal microscope and DIC microscopy to confirm nanowire identification, tagging and cell-line identification.

An important question that arises from these experiments is that whether barcode 1 non-specifically targets HFFs and barcode 2 non-specifically targets A549 cells in the mixture of cells. If so, can we quantify the specificity of interaction and the (undesirable) cross-targeting of cells? This cross-targeting of the barcodes in this experiment was not quantified and is one of the main experiments to be conducted in the future in order to address and improve specificity of targeting.

4.3 Methods

4.3.1 Cell culture

The canine osteosarcoma (OSCA-8) cell line is an immortalized cell line derived from a tumor sample taken from the left shoulder of a two year old male Rottweiler dog. The diagnosis of osteosarcoma was confirmed and the tumor was classified as an osteoblastic variant. OSCA cells were cultured in Dulbecco's Modified Eagle Medium (DMEM, GIBCO) cell culture media supplemented with 10% fetal bovine serum (FBS), Primocin (InvivoGen) and 4-(2-hydroxyethyl)-1-piperazineethanesulfonic acid (HEPES, GIBCO). Cells were cultured in T75 tissue culture flasks (Corning) and incubated at 37°C and 5% CO2 atmosphere until highly confluent. For seeding OSCA-8 cells in flat-bottom 6-well culture plates (CytoOne), cells in DMEM media were dispensed at 134μL/well (1.28million cells per well for confluence).

The cells in the 6-well plates were allowed to incubate with various concentrations of nanowires at 37°C for 24 hours. After 24 hours, the medium containing nanowires was removed and the cells washed with phosphate buffered saline to remove any unattached wires. The attached cells were then detached using trypsin and neutralized with FBS. The trypsin/FBS/ detached cell/nanowire solutions in the 6 wells were then centrifuged to form a cell pellet and the supernatant was extracted. The cell pellets were re-suspended in 1 ml fresh media and uniformly mixed. A 0.68T magnet (SUPERMACs from Miltenyi) with 5.15T/m gradient was used for separation of tagged cells. The separated cells were then re-suspended in 1ml fresh media. The efficiency of tagging and separation (measured by bright field microscopy / hemocytometry) was studied as a function of nanowire concentration (measured by VSM). Separation efficiency was defined as the percentage of the initial number of cells (average 1.28 million cells) that were removed from the sample using SuperMACS magnet.

A549 cells were isolated from a 58 year old Caucasian male, immortalized and cultured in A549 medium (450ml F-12K medium [ATCC # 30-2004] 1.26 g/L D-Glucose, 2mM L-glutamine, 220mg/L Sodium Pyruvate and no HEPES + 50ml fetal bovine serum (FBS)). For passaging the cells, follow the steps outlined below:

1. Aspirate media from flask
2. Wash 1x with DPBS
3. Add 3ml trypsin and incubate at 37C for ~ 3 min
4. Add 7ml A549 media to flask
5. Transfer to 15 ml centrifuge tube and centrifuge at 1000rpm for 10min

6. Remove supernatant

7. Resuspend in 15 ml and reseed in flasks at a lower density

a. Typical split ratio is 1:3 to 1:8 from an 80-90% confluent flask

b. Passage every 3-4 days

HFF cells are adherent fibroblast cells originally isolated from newborn human foreskin. These are cultured in HFF medium (420ml 1X DMEM [ATCC # 30-2002], 4.5 g/L D-Glucose, L-glutamine (4mM), 110mg/L Sodium Pyruvate + 5 ml Penicillin – Streptomycin solution + 75 ml FBS). For passaging the cells, follow the steps outlined below:

1. Aspirate media from flask

2. Wash 1x with DPBS

3. Add 3ml trypsin and incubate at 37C for ~ 3 min

4. Add 7ml HFF media to flask

5. Transfer to 15 ml centrifuge tube and centrifuge at 1000rpm for 10min

6. Remove supernatant

7. Resuspend in 15 ml and reseed in flasks at a lower density

a. Typical split ratio is 1:2 to 1:5 from an 80-90% confluent flask

b. Passage every 3-4 days

4.3.2 Electron microscopy (SEM) of cells

In preparing samples for electron microscopy (SEM/TEM), 0.6 million cells were plated on a glass coverslip with 0.1pM nanowire solution (media/PBS) and allowed to incubate for 24 hours at 37°C. 1pM of nanowires means there were 6.023x1023 x 10-12

nanowires in 1 liter of solution (PBS). The medium was then removed and the nanowires were washed with PBS to remove unattached nanowires. This was followed by a rinse step in cacodylate buffer (pH=7.4). The coverslip with the cells and the nanowires was immersed for two hours in 2.5% glutaraldehyde/0.1M cacodylate buffer solution at pH=7.4 followed by another rinse step (3x) with cacodylate buffer at pH=7.4. The samples were dehydrated in increasing concentrations of ethanol for 10 minutes each (starting with 25% ethanol, 50%, 70%, 85% 95% and 100%). Next, the samples were critical-point dried and carbon coated for electron microscopy.

4.3.3 Barcoding experiment: specific tagging of cells with nanowires

For this experiment, two cell lines were used: A549 human lung carcinoma and human foreskin fibroblasts (HFFs). Corresponding to these cell lines, two nanowire samples were prepared according to protocols listed in chapter 2 that were physically different-

(i) Segment lengths 3 μm 0.3 μm Au/ 3.1 μm Ni and diameter 100 nm –barcode 1 (bc1)

(ii) Segment lengths 0.12 μm Au/1.8 μm Ni/ 0.3 μm Au and diameter 100 nm-barcode 2 (bc2)

Barcodes 1 and 2 were functionalized with heterobifiunctional PEG (NH_2-PEG-COOH) using protocols discussed in chapter 5. Total number of nanowires for barcodes 1 and 2 were evaluated using VSM (refer chapter 5 for protocols).

N_{bc1} = 200.4 million nanowires in 1.5 ml DI water. This was divided into 6 aliquots, each aliquot containing 33.4 million nanowires (n_{bc1}) in 0.25 ml DI water. Dilute the 0.25ml aliquot to 0.6ml with DI water.

Therefore, $N_{bc1} = 6.n_{bc1}$ and n_{bc1} = 33.4 million in 0.6ml.

N_{bc2} = 267.3 million nanowires in 1.5 ml DI water. This was divided into 6 aliquots, each aliquot containing 49.5 million nanowires (n_{bc2}) in 0.25 ml DI water. Dilute the 0.25ml aliquot to 0.6ml.

Therefore, $N_{bc2} = 6.n_{bc2}$ and n_{bc2} = 49.5 million in 0.6ml with DI water.

The cells and nanowires are then loaded into a glass-bottom 96 well plate (ThermoFisher Scientific) in the format shown in table 2. Each well in a 96 well plate is an independent experiment. However, each well is triplicated to measure deviations under identical conditions.

	1	2	3	4	5	6	7	8	9	10	11	12
A	BC1 +A549 (0:1)	BC1 +A549 (1:1)	BC1 +A549 (25:1)	BC1 +A549 (50:1)	BC1 +A549 (100:1)							
B	BC1 +A549 (0:1)	BC1 +A549 (1:1)	BC1 +A549 (25:1)	BC1 +A549 (50:1)	BC1 +A549 (100:1)							
C	BC1 +A549 (0:1)	BC1 +A549 (1:1)	BC1 +A549 (25:1)	BC1 +A549 (50:1)	BC1 +A549 (100:1)	1/2	(A1)/2 + (E1)/2	(A2)/2 + (E2)/2	(A3)/2 + (E3)/2	(A4)/2 + (E4)/2	(A5)/2 + (E5)/2	
D							(B1)/2 + (F1)/2	(B2)/2 + (F2)/2	(B3)/2 + (F3)/2	(B4)/2 + (F4)/2	(B5)/2 + (F5)/2	
E	BC2 +HFF (0:1)	BC2 +HFF (1:1)	BC2 +HFF (25:1)	BC2 +HFF (50:1)	BC2 +HFF (100:1)	1/2	(C1)/2 + (G1)/2	(C2)/2 + (G2)/2	(C3)/2 + (G3)/2	(C4)/2 + (G4)/2	(C5)/2 + (G5)/2	
F	BC2 +HFF (0:1)	BC2 +HFF (1:1)	BC2 +HFF (25:1)	BC2 +HFF (50:1)	BC2 +HFF (100:1)							
G	BC2 +HFF (0:1)	BC2 +HFF (1:1)	BC2 +HFF (25:1)	BC2 +HFF (50:1)	BC2 +HFF (100:1)							
H												

Table 2: Experimental layout of 96 well plate used to conduct simultaneous experiments on barcoding. Each well corresponds to a single experiment. A1, B1 and C1 are essentially the same experiment repeated three times. Wells along a row are all distinct experiments differing from each other by value of a single variable. BC1 and BC2 refer

to barcode nanowire 1 and barcode nanowire 2 respectively. The numbers in the parenthesis () correspond to ratios of initially titrated nanowires to cells in culture. For e.g., (100:1) refers to 100 nanowires per cell.

(i) A549 cells are stained in T75 flasks with Hoechst 33342 nuclear stain and HFFs are stained with Hoechst blue nuclear stain as well as WGA- green plasma membrane (life technologies) following established protocols.

(ii) Each well is replicated three times (B1-B5 and C1-C5 are replicates of A1-A5, F1-F5 and G1-G5 are replicates of E1-E5 and so on). A1-A5 (B1-B5 and C1-C5) are loaded with A549 cells as follows:

(iii) 100 µl of A549 cells at loading density of 16000 cells/ml (1600 cells per well) + 270 µl A549 medium.

E1-E5 are loaded with HFFs as follows:

100 µl of HFFs at loading density of 16000 cells/ml (1600 cells per well) + 270 µl HFF medium.

C7-C11 are loaded with 50:50 , A549 : HFF cells as follows:

50µl of A549 cells at 16000 cells/ml + 50µl of HFFs at 16000 cells/ml + 135µl A549 medium + 135µl HFF medium.

(iv) After plating, the cells are allowed to incubate for 12 hours at 37^0C and 5% CO_2 to facilitate attachment of the cells to the well bottoms. After 12 hours, medium volume in each well is adjusted to 300 µl.

(v) n_{bc1} nanowires from barcode 1 are functionalized with anti-EPCAM-FITC conjugate (refer to chapter 5 for protocols) and re-immersed in 0.6ml A549 medium. n_{bc2} nanowires from barcode 2 are functionalized with anti-vimentin and re-immersed in 0.6 ml HFF medium.

(vi) Next, population of cells inside wells is evaluated using hemocytometer and using multiplication rates of A549 cells and HFFs. Nanowires are titrated such that nanowires: cell ratios of 0:1, 1:1, 25:1. 50:1 and 100:1 are tested while maintaining net medium volume per well constant at 300 µl. In wells C7-C11, half the contents of well A1-A5 are added to half the contents of E1-E5 respectively. The nanowires and cells are allowed to incubate for 6 hours at 37^0C and 5% CO_2.

(vii) Following incubation, the contents of each well are rinsed three times with PBS. The cells are then fixed with 10% Formalin for 10 minutes and rinsed again with PBS 3x. The cells are stored in PBS until imaged.

(viii) For imaging the wells, Olympus Fluoview FV1000 inverted confocal microscope was used. An oil-immersion 40x lens (IX2-DIC40, NA = 1.3) was used to acquire an images from 4 channels with corresponding excitation/emission filters: fluorescent blue channel (Ex/Em 350 nm/461m), fluorescent green channel (480nm/535nm), DIC and reflectance. The Fluoview software was used in conjunction with Image J to analyze images and overlay the four channels.

4.4 Conclusions

In this chapter, basic interactions of nanowires with biological cells were presented.

Following incubation of osteosarcoma cells for fixed periods of time and under controlled environmental conditions, magnetic nanowires were observed to attach to cell membranes and internalized within membrane-enclosed compartments inside the cell. These results were verified through light microscopy (while applying magnetic field gradients to the sample) and SEM/TEM imaging.

More importantly, large nanowire clusters were observed in the cell-nanowire samples which result in heterogeneity in environmental factors governing cell behavior. These clusters also produce errors in experimental measurements and interpretations. Clustering/aggregation can be attributed to magnetostatic interactions between nanowires and inadequate pre-processing of the nanowire samples required to eliminate physical clusters. Thus, there is a need for quality control of the nanowire samples in order to employ their full potential in biological applications.

Chapter 5: Coating nanowire surfaces with functional polymers for mitigating aggregation and cytotoxicity: Quality Control

5.1.1 Issues with inorganic nanoparticles

While nanoparticles have strong advantages for applications in drug delivery (chapter 6) and tissue-engineering (chapter 7), these have to be weighed against the issues surrounding magnetic and/or inorganic nanoparticles – biocompatibility and nanoparticle aggregation, which ultimately control biodistribution *in vitro* or *in vivo*. Thus, the use of a nanoparticulate material for biological interactions entails optimization of biocompatibility and addressing aggregation without loss of or much compromise on the ultimate function of the nanoparticle.

For example, superparamagnetic iron oxide particles are employed for magnetic separation, drug delivery and hyperthermia applications [54] largely because they can be made biocompatible and they aggregate less. However, superparamagnetic particles need very large magnetic fields (to saturation) in most of these applications. They have no remnant magnetization which is advantageous to reduce clustering but they are also limited by aggregation related issues. Hydrophobic and Van der Waals forces cause them to agglomerate, induce dipole-dipole attractions and exhibit ferromagnetic behavior through large cluster sizes and anisotropy via chaining [62]. These agglomerates ultimately dictate the interactions with cells and organisms. Although there has been some success with conventional superparamagnetic spherical nanoparticles [63,64] they

require high magnetic fields for most studies where an effective motion-based response is required.

In contrast, if ferromagnetic particles with remnant magnetizations can be stabilized in solution (by coating them with polymeric coatings) at working concentrations, they can be used in cell assays with very low applied fields and have the potential to transform these technologies due to their inherent anisotropic shapes. Compared to commercial microcarriers, such as AccuBeads (Bioneer) and DynaBeads (Life technologies), nanowires have higher saturation magnetizations (25-40 emu/cc [21,65] vs. 415 emu/cc [21]).

This chapter will cover the following main points:

(i) A detailed discussion of aggregation and cytotoxicity-related issues surrounding magnetic nanowires will be presented.

(ii) A polymeric surface coating (PEG) will be used to coat the Au/Ni/Au nanowires using novel surface-chemistry in order to mitigate aggregation and enhance biocompatibility.

(iii) The surface coating will be optically characterized using SEM and fluorescence microscopy and chemically characterized using FTIR and XPS.

(iv) The stability of the surface-coated nanowires will be assessed using VSM measurements and UV-vis-NIR spectrophotometry.

(v) The biocompatibility of the nanowires will be assessed using cell-based cytotoxicity assays.

5.1.2 Aggregation of magnetic nanoparticles:

Several forces act between nanoparticles in suspension including van der Waals forces, forces due to overlap of electric double layer, hydration, hydrophobic forces and magnetostatic interactions. The sum total of these forces determine the final state and biodistribution of the nanoparticles in solution.

1) Van der Waals forces:

These are short range electromagnetic forces that act between molecules or atoms that are neutral charged. These forces can exist between polar molecules, polar and non-polar molecules or only non-polar molecules (London forces). The potential between to atoms/molecules separated by a distance r, is described by

$V = a_{11}/r^{12} – b_{11}/r^{6}$

The first term on the right hand side represents a repulsive force due to the overlap of electron orbits of two atoms whereas the second term is an attractive force arising from electric dipole interactions between polar/non-polar molecules.

The interaction potential between two nanoparticles can be evaluated from the above equation by integration of this equation over all the interacting molecules existing in these particles.

2) Overlap of electric double layers:

In a suspension of metallic oxide nanoparticles in aqueous solutions, an electric double layer is developed on the surface of the nanoparticles, usually due to adsorption of OH^- groups on the particle surface. Further, depending on the pH of the aqueous

suspension, these hydroxides can develop positive or negative charges as shown below [66]:

$$M—OH + H^+ \rightarrow M—OH_2^+$$

$$M—OH + OH^- \rightarrow M—O^- + H_2O$$

The pH at which the charge on the particle surface is zero is called the point of zero charge (PZC). For pH < PZC, the nanoparticle surface is positively charged and for pH>PZC, the nanoparticle surface is negatively charged.

This surface charge further attracts ions of opposite charge as well as water molecules in the solution through electrostatic, van der Waals forces and hydrogen bonds. These charged ions and counter-ions create an electric-double layer. When two particles approach each other very closely, the electric double layer from these particles might momentarily overlap but causes repulsion and prevents aggregation.

3) Hydration forces: These forces originate from overlap of hydrogen-bonded water molecules on the nanoparticle surface.

4) Hydrophobic forces: These forces cause hydrophobic nanoparticle surfaces to cluster together in aqueous suspensions to minimize surface area exposed to water.

5) Magnetostatic interactions between nanowires (in suspension and in arrays):

Magnetic nanowires can be approximated as dipoles depending on the nanowire length. We will revisit this concept of length range for dipole approximation validity later. For now, if we assume that two nanowires approaching each other in a suspension are dipoles and are relatively positioned as shown in figure 5.1, then the dipole forces and energy is given by:

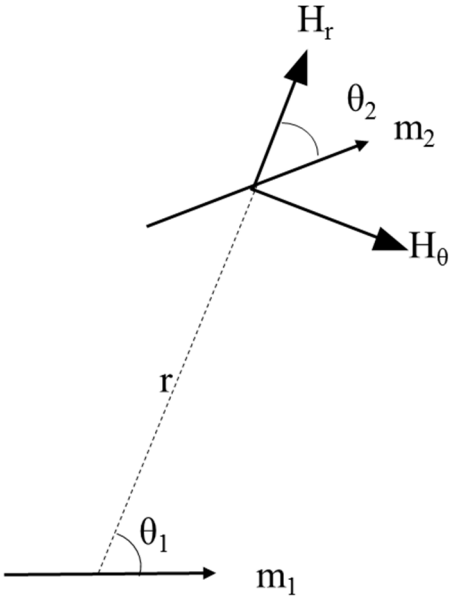

Figure 5.1 Dipole-dipole interactions between nanowires.

$H = [m/ (r^2 + l^2/4)^{3/2}] (3\cos^2\theta + 1)^{1/2}$,

Where,

H = the field due to one dipole at a point P, distance r away

θ = angle between the magnetic easy axis of one dipole and the line joining the center of the dipole to point P.

l = length of the dipole.

The potential energy, E, between two dipoles oriented as shown in the figure, is given by

$E = m_1m_2/(r^2 + l^2/4)^{3/2} [\cos(\theta_1 - \theta_2) - 3\cos\theta_1\cos\theta_2]$.

This energy is the mutual potential energy of the nanowires and is also called the interaction energy between nanowires. As seen, this energy is minimum

when $\theta_1 = \theta_2 = 0^0$, i.e. the nanowires are parallel to each other and to the line joining their centers. Thus, they form chains. As we will see, nanowire chaining is indeed observed in cell culture. When $\theta_1 = \theta_2 = 90^0$, the nanowires are parallel to each other but perpendicular to the line joining their centers. In this case, the energy between the nanowires is maximum. An antiparallel arrangement of the nanowires, where $\theta_1 = 90^0$ and $\theta_2 = 270^0$, also yields a negative energy indicating an energetically favorable configuration compared to most arrangements but still less stable than the chaining configuration. Thus, while nanowire stacking and chaining are observed in most assays involving uncoated nanowire suspensions, nanowire stacking is not as energetically favorable compared to chaining and is therefore, less frequently observed in cell culture.

In an array of nanowires, such as those in AAO, calculation of energy due to dipole-dipole interactions involves summing the above energy over all possible nearest neighbor pairs of nanowires. However, as the length of the nanowire increases and the density of packing increases, calculation of interaction energy using pure dipole approximation leads to inconsistencies. As discussed in [67], for longer nanowires with aspect ratio > 20, the interaction energy approaches the monopole approximation i.e, approximating the nanowires as monopoles leads to consistent calculations in energetics. As depicted in figure 5.2, the interaction energy increases with increase in aspect ratio. We will find consistent data in the "results" section.

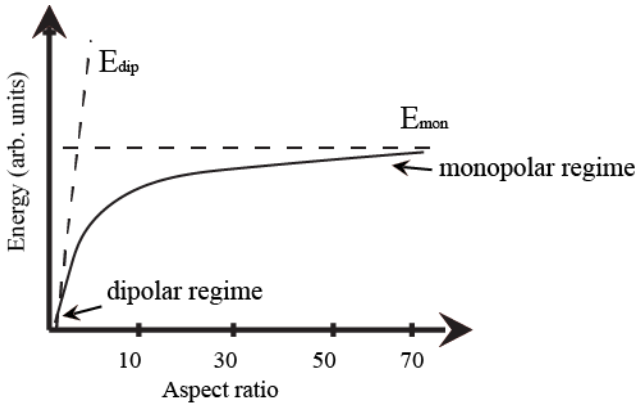

Figure 5.2. Plot defining behavior of a nanowires as a dipole or a pair of non-interacting monopoles as function of nanowire aspect ratio[67]. For a high aspect ratio nanowire, the monopole approximation is more consistent with observations.

5.1.3 Particle toxicity: Are there nano-specific effects?

With increasing adoption of nanoparticle-based platforms in translational medicine and regenerative technology, it has become essential for toxicologists to assess particle toxicity and correlate it with specific physicochemical attributes of the nanoparticle such as size, shape, surface area, surface charge, surface chemistry and purity. These factors influence the biologically effective dose for the intended result (for example, therapeutic outcome). According to [68], biologically effective dose is defined as the "entity within any mass dose of the particle that drives a critical form of toxicity in tissues such as inflammation, genotoxicity and cellular proliferation. If only a portion of the total mass dose is biologically effective dose, then the implication is that a quantity of the retained mass dose is not biologically effective."

Conventionally, particle toxicologists use mass per cell/tissue as a measure of administered nanoparticle dose (except for nanofibers or cylindrical particles where number of particles are used instead [68]) simply because it is a convenient, measureable physical attribute of the nanoparticles. It is not to be confused with the driving component of the toxicity, which may be any of the physicochemical attributes of the nanoparticle. Increasing the administered mass of the particles, generally also increases the driving component of the nanoparticles, however the correlation is strictly qualitative and varies with changes in particle attributes.

While, generally, there is gradual increase in toxicity as the particle size decreases, owing to increased surface area per unit mass and associated surface reactivity, there is no evidence of a step-increase in particle toxicity as it enters the nano-scale (where at least one dimension < 100 nm). It is generally observed that the mode of toxicity or the driving component is same in most cases of nanoscale vs particles above the nano-threshold. Therefore, to perceive nanomaterials with an associated nano-specific toxicity is fallacious. For example, in the case of quartz crystals, the driving component of toxicity is the active surface area and in the case of asbestos, the active component is the fiber length.

Thus, as it is the accepted and widely adopted standard in the scientific community, I will use nanowire numbers per cell to describe the dose and explore cytotoxicity as a function of various attributes such as length and surface chemistry. These results will be used to determine the driving or dominant component of toxicity.

5.1.4 Ni toxicity: material carcinogenesis

The International Agency for research on cancer (IARC) has declared nickel compounds (nickel sulfide, combination of nickel sulfides, sulfates and some oxides) as carcinogenic (Group 1). However, there being insufficient evidence, metallic nickel and alloys are declared as possibly carcinogenic (Group 2B) [69]. Nickel exposure has been implicated in cases of skin allergies, lung fibrosis and cancer of the respiratory tract, especially among workers in nickel polluted environments [69]. Thus, nickel toxicity has been the subject of various epidemiological and experimental studies and their use in biological applications needs to be addressed.

Some of the factors influencing nickel toxicity that need careful consideration: 1) *Nanomaterial dose (mass)*: As is true for most inorganic materials, there is a dose-dependent toxicity and most cytotoxic effects occur at high doses of nickel. For example, in humans, soluble nickel concentration above 1 mg/m^3 and insoluble nickel concentrations above 10 mg/m^3 are associated with cancer of the respiratory tract [69]. 2) *Solubility of the material*: While diffusion of Ni^{2+} across the cell membrane and transport of Ni^{2+} through calcium/iron transport channels contribute to cytotoxicity, the main source of toxicity is phagocytosis (internalization) of insoluble particles by cells followed by intracellular compartmentalization in membrane enclose compartments surrounding the nucleus and degradation through fusion of endosomes and lysosomes [70]. **The extent of toxicity is determined by the efficiency of phagocytosis and dissolution of Ni to Ni^{2+} (degradability). Both these requirements must be met**. Once internalized and degraded, the routes of toxicity can be genetic or epigenetic [71].

Genetic routes include generation of DNA-damaging reactive oxygen-species (ROS) and inhibition of DNA repair. Epigenetic routes include DNA hypermethylation, histone hypoacetylation, activation and silencing of genes and transcription factors involved in cellular hypoxia and interference of Ni^{2+} with metabolism of essential metals (Ca^{2+}, Fe^{2+}, Mn^{2+}).

3) *Chemical form of the material*: As discussed before, compounds of Ni such as sulfides and some oxides are more cytotoxic than their metallic/alloyed forms.

4) *Model of study* (*in vitro* vs *in vivo)*: Inorganic nanomaterials can exhibit very different toxicities in cell culture (*in vitro*) compared to animal or human models (*in vivo*). Their use in *in vitro* applications such as cell/protein purification, separation and imaging cellular and receptor dynamics can be met with low or negligible cytotoxicity because of low exposure time of the cells to these materials and flexibility in particle removal after processing. In contrast, persistence of these materials in animal bodies due to the inability or inefficiency of the mononuclear phagocytic system (MPS) and reticuloendothelial system (RES) to detect and/or clear them from the body causes acute toxicity [72].

5) *Route of administration (in vivo):* In animal models such as mice, soluble nickel compounds have generated tumors when administered through intrarenal (i.r.), intramuscular (i.m.), intraperitoneal(i.p.), inhalation, intraocular(i.o), subcutaneous(s.c) and intra-articular(i.a.) means [69].

6) *Co-administration with other mutagens*: Sometimes when nickel compounds are administered with other carcinogenic materials, the might have a synergistic effect possibly due to modulation of the immune system.

7) *Shape and persistence*: Most anisotropic particles/fibers have shown an associated length-dependent toxicity both *in vitro* and *in vivo* (For example, asbestos and carbon nanotubes (CNTs) for lengths greater than 15μm)[73]. This increase in toxicity with length can be attributed to persistence or the inability of the reticuloendothelial system (RES) and mononuclear phagocytic system (MPS) to clear these particles from the body.

In fact, owing to various pioneering work [73], a fiber pathogenicity paradigm (FPP) was put forward by scientists. According to this theory, a fiber has *in vivo* pathogenicity when it has the following physicochemical attributes:

1) Diameters less than 3 μm to allow aerodynamic penetration into the lung.

2) A length greater than 15 μm to frustrate macrophage mediated clearance.

3) A resistance to dissolution or breakage leading to biopersistance in the organism.

Intraperitoneal (i.p.) administration of nanofibers in mouse models showed that fibers (of different materials including Ag, CNTs and Ni) longer than 4 μm led to pleural inflammation and mesothelioma [73]. This is characterized by increase in cell numbers, granulocytes and eosinophils within 24 hours as determined by lavage [73] and increased thickening of the submesothelial cell layer with increased nanowire length as determined by histological sections after 7 days [73]. For nickel nanowires, in particular, strong dose-dependent inflammation was observed for nanowires longer than 20 μm and no inflammation or fibrosis was seen for nanowires shorter than 5 μm.

8) Intracellular redox activity of nickel derivatives is an important factor in cellular toxicity [69]. This is related to the solubility of nickel.

As we will see in the results section, a lot of these factors can be addressed by coating the nanowires with a layer that prevents degradation and dissolution of nickel inside the cell.

5.1.5 Molecular markers of inflammation and cytotoxicity

Cytokines are low molecular weight regulatory proteins or glycoproteins secreted by white blood cells and other immune cells in response to a number of stimuli. These proteins help in regulating the development of effector T-cells (cells from the adaptive immune system) and thus mediate a response to a foreign body[74]. Cytokines bind to receptors on target cells and trigger signal transduction pathways that alter gene expression in target cells. Figure 5.3 shows this flow of processes.

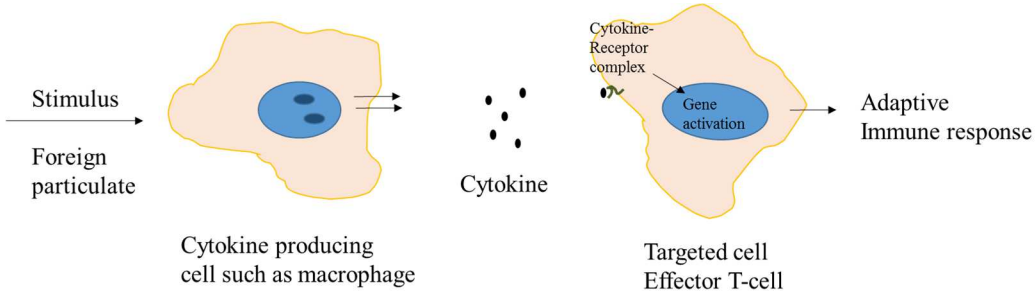

Fig 5.3: Cytokine release by macrophages and chain of processes leading to an adaptive immune response

The two cytokines tested in cytotoxicity studies with Au/Ni/Au nanowires are cytokines of the innate immune system including Interleukin-1 (IL-1β) and Tumor necrosis factor (TNF-α). These are both secreted by macrophages and induce an inflammatory response to a foreign object and consequently alert the adaptive arm of the immune system. These cytokines represent the first line of defense of the organism against a foreign body. In particular, IL-1 causes inflammation in the vasculature and

liver and induces a fever by affecting the hypothalamus [75]. In addition to the above effects, TNF-α causes cell death and neutrophil activation [75]. Measurement of these cytokines were done *ex vivo*, i.e., with cells collected from tissue extracted from mice under natural conditions with minimum alterations.

5.1.6 Surface functionalization using linker molecules

On account of their high surface area to volume ratio, nano-oxide particles (e.g., TiO_2, FeO_2) are often highly reactive at the surface leading to complex interactions with organic/biological matter. While high reactivity can be a toxicity concern, it can be advantageous if this property is controlled. For example, using the surface reactivity to conjugate linker molecules (eg, bifunctional PEGs) will impart colloidal stability to the nanoparticles, mask the surface of the metal oxide from the biological environment thereby subside toxicity via ion-leaching and enable conjugation of peptides, antibodies and/or other proteins for selective targeting applications. Colloidal/suspension stability is important both, for *in vitro* assays, where aggregation is mitigated, thus making experiments repeatable and *in vivo* where biodistribution is controlled by the stability of the nanoparticles [76].

The attachment of proteins to the linker molecules on the surface of the nanoparticle, called surface functionalization or derivatization, changes the behavior of the particle in the context of cell-nanoparticle interactions. Peptides, antibodies or small molecule therapeutics can be used for selective targeting of cells and promote active internalization, apoptosis and/or other receptor-mediated behavior. However, the kinetics

of interactions of functionalized nanoparticles can be quite different in cell culture vs inside an organism.

5.1.7 Nanoparticle environments influence the evolution and fate of the surface coating:

Most cell cultures have environments that are relatively static (temperature, composition, humidity and neutral pH) over the time of measurement in an experiment, thus the nanoparticle surface properties remain relatively constant over this time period.

The environment inside an organism, however, from the nanoparticle's "perspective" is constantly changing. Generally, nanoparticles can enter the body of the organism via ingestion, inhalation or skin penetration. The sequence of steps followed by the nanoparticle inside an organism is shown in figure 5.4:

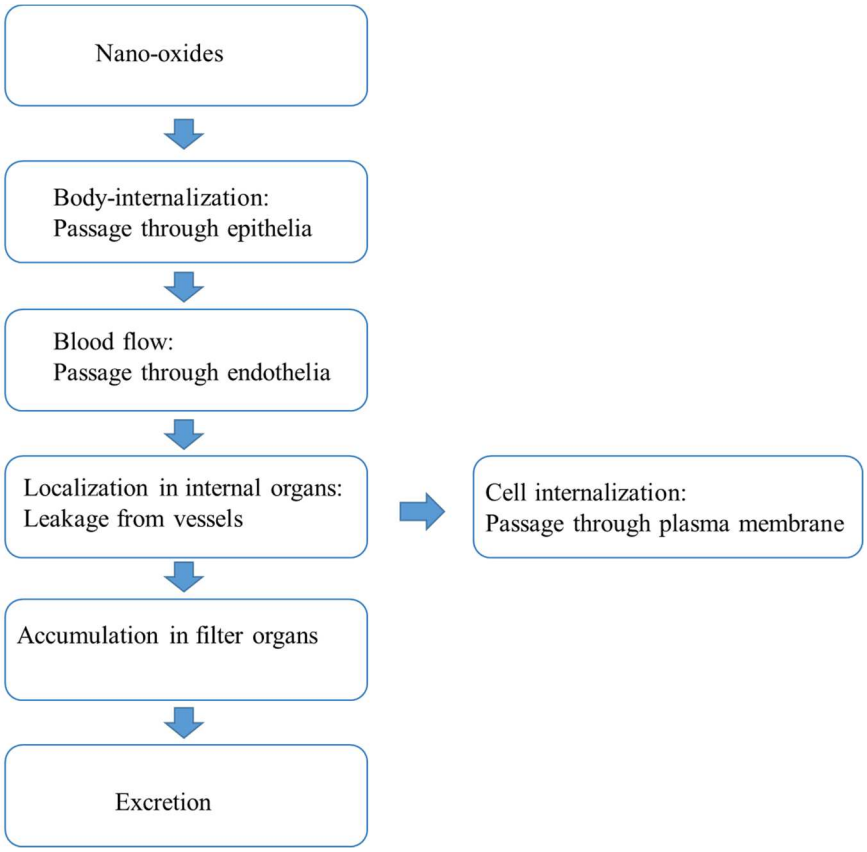

Figure 5.4 Flow chart depicting the course of the lifetime of a nanoparticle after being ingested by (or administered to) a live organism [77].

Thus, once the nanoparticles are past the epithelial barrier (skin, lungs, intestine) through discontinuities or otherwise (actively due to their nanoscale), they can cross the endothelial barrier via fenestrations to enter the blood flow. Alternately, they can transport through leaky vasculature (e.g., tumors), inflammatory sites and/or small discontinuities to localize within organs. Then, the nanoparticles can be internalized by cells through specific receptor interactions or non-specifically and follow intracellular trafficking routes. Alternately, blood flow can transport these particles to filtering and excretory organs where they are expelled out of the system. Through the course of its life-time in the organism's body, the nanoparticle encounters several different environments that differ in biological composition, pH and flow conditions. This may lead to adsorption of various proteins on the surface of the nanoparticle as it traffics through the body. This coating, often called "protein corona" [77], can modify the properties of the nanoparticle away from its intended design. Thus, an *in vivo* application calls for a more robust nanoparticle design that can handle the variations in environmental conditions inside the body and yet be cleared out of the body after it has served its function. In these cases, there is a need for separating the chemical identity of the nanoparticle from its "biological identity" [77], which is largely influenced by the surface coating and geometry, for analysis of their effects on cells/organisms which includes biocompatibility studies.

5.1.8 Designing surface coatings for multilayered nanowires

The surface coating of the nanowire is designed keeping the final application of the nanoparticles in mind, whether it is tumor ablation through hyperthermia or for drug-delivery applications. However, this has to be achieved while providing efficient solutions for particle stability and biocompatibility which are influenced by the environment. Thus, the final surface chemistry is determined at the intersection of the three factors.

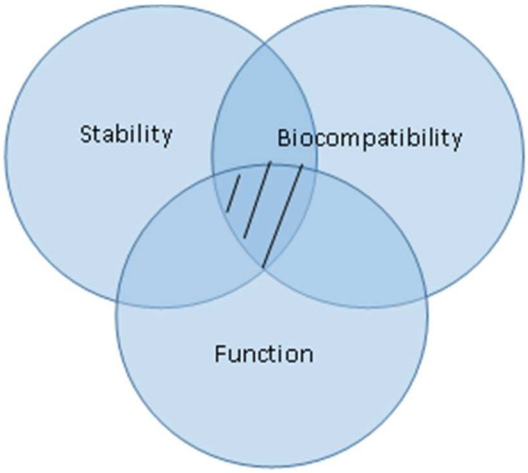

Figure 5.5 Essential factors defining the design of a nanoparticle for a biomedical application like drug-delivery.

The advantage of using multilayered nanowires, in the context of surface functionalization, is that the different material layers of the nanowires can be functionalized with different ligands that can serve complimentary purposes in a biological environment. For example, using the high affinity of thiol molecules to the gold surface, a radiolabel or a fluorescent molecule can be selectively attached to the gold layers only. Thus, the surface coating on the gold layers could serve as imaging beacons for both *in vitro* and *in vivo* applications. On the same nanowire, the nickel layers can be functionalized with a drug or a cell targeting peptide (eg. RGD) using amine/carboxylate binding (chapter 6). Thus, the surface coating on the nickel layers will serve to target the biomolecular species or biological cell of interest (figure 5.6). This flexibility in design allows integration of various functions, such as imaging and specific targeting, on the same nanoparticle, and thus such a nanoparticle is appropriately called a multifunctional nanoparticle.

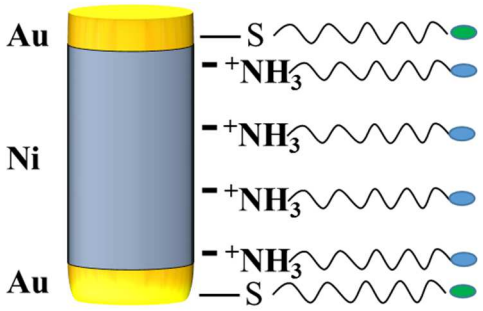

Figure 5.6: Schematic showing functionalization of Au and Ni segments of the multi-layered nanowire with different ligands by exploiting their unique surface chemistries.

5.1.9 Important chemical reactions

Carbodiimides are cross-linkers used to form an amide bond between carboxylate functional group from one molecule and an amine functional group from another molecule. They are called zero-length cross-linkers because they do not introduce an external chemical structure between the conjugating molecules [78]. Carboxylic acid functional groups from one molecule reacts with N-substituted carbodiimide to form o-acylisourea derivative, which is highly reactive and thus, only an intermediate complex. This reactive complex can react with a nucleophile, such as a primary amine functional group from another molecule to form highly stable amide bond (figure 5.7(a)).

N-hydroxysuccinimide (NHS) or sulfo-NHS ester containing reagents can be used to form an amide bond between two molecules as shown below. These react with a nucleophile, such as amine functional group, to form an acylated product accompanied by a release of NHS leaving group (figure 5.7(b)).

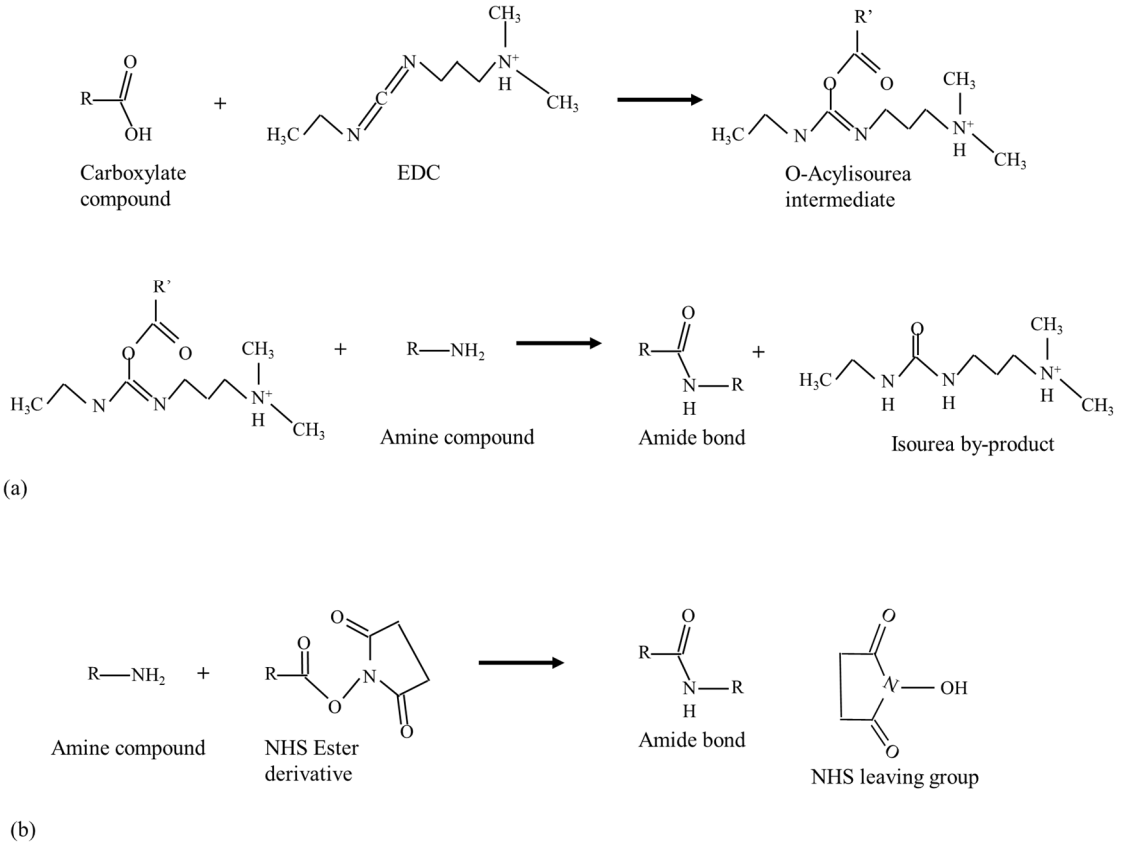

Figure 5.7: Chemical reactions facilitating formation of an amine bond between two compounds through (a) EDC reaction and (b) NHS Ester derivative.

Thiol containing molecules form coordinate (or dative) bonds with metal ions and metal surfaces through the unshared electron-pair on sulphur atoms.

5.1.10 Flow cytometry (FACS)

A flow analysis cell sorter (FACS) or flow cytometer is used to sort and separate specific cells marked with fluorescent markers in a mixture. In this technique, an antibody-fluorophore conjugate is used to label specific cells which are marked in order to separate them from a heterogeneous mixture of cells. These cells are allowed to flow in

a single file through a channel and are excited by a laser source one cell at a time (figure 5.8). Following measurement of fluorescence emission from each cell, a vibrating nozzle generates droplets, such that each drop encloses one cell. Based on the recovered fluorescence signal from each cell, this droplet is either poitively or negatively charged. These charged droplets are separated out into two streams by application of an electric field. Thus, all labelled cells are sorted out in one stream which flows into a cell collector container. In this way, upto 10000 cells can be sampled per second. Thus, FACS is a high throughput cell sorting and separation technique.

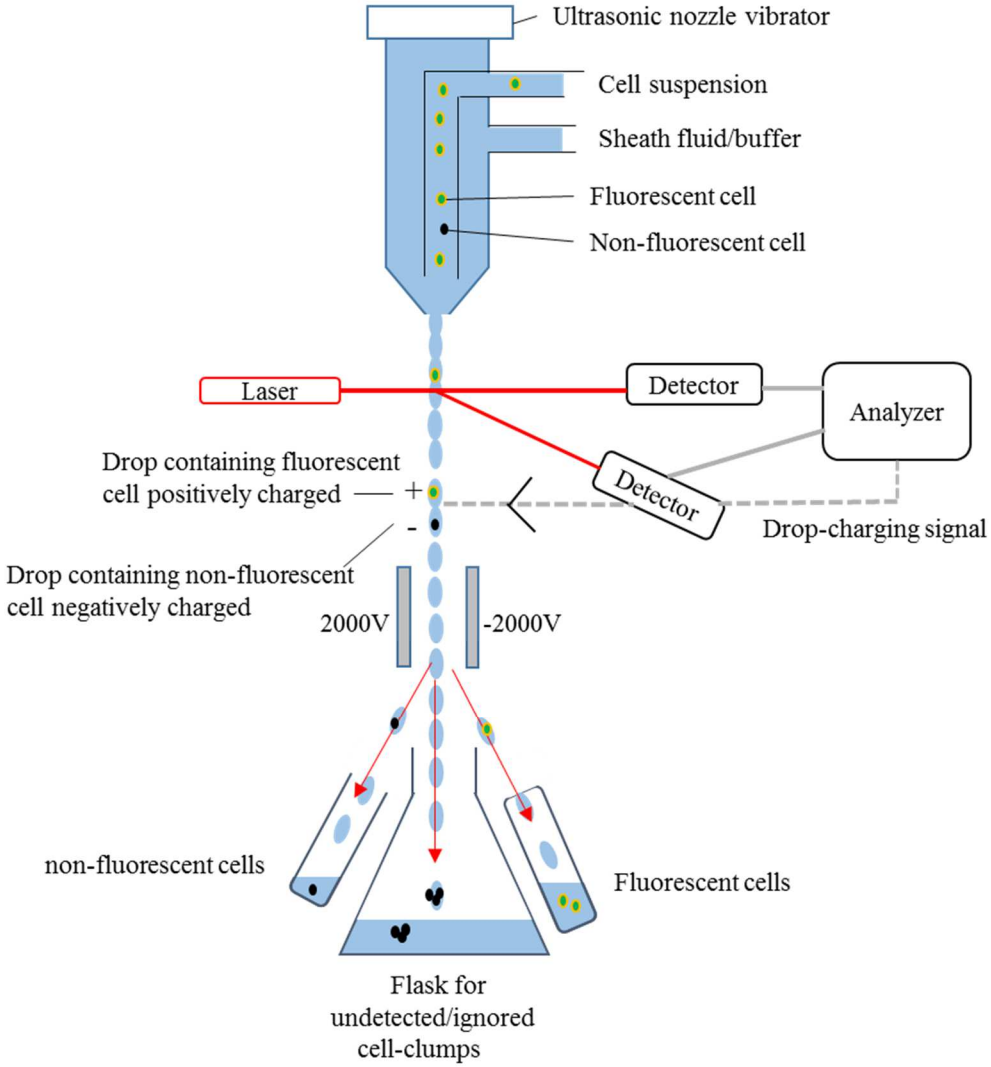

Figure 5.8: Schematic showing principle of flow analysis cell sorter (FACS).

5.2 Results

5.2.1 Nanowire clusters:

Energy-dispersive X-ray spectroscopy (EDS) and SEM imaging revealed that parts of the nanowire growth contact layer had remained attached to the nanowires despite sonication. Therefore, a new method was used to remove the growth contact prior

to AAO etch. It was found that ion-milling the growth contact following electrodeposition into AAO pores was effective in removing this contact layer. Multiple wafers can be loaded simultaneously for ion-milling yielding high-throughput. Alternately, wet etching of Cu back contacts can be used for shorter etch times using a highly selective copper etchant (Cupric tetrafluoroborate in ethylene glycol + 2-butene 1,4 diol + triethylorthoformate)[79] and 30% vol. peroxide for tungsten adhesion layers .The growth contact removal (before and after) is shown in Figure 5.9.

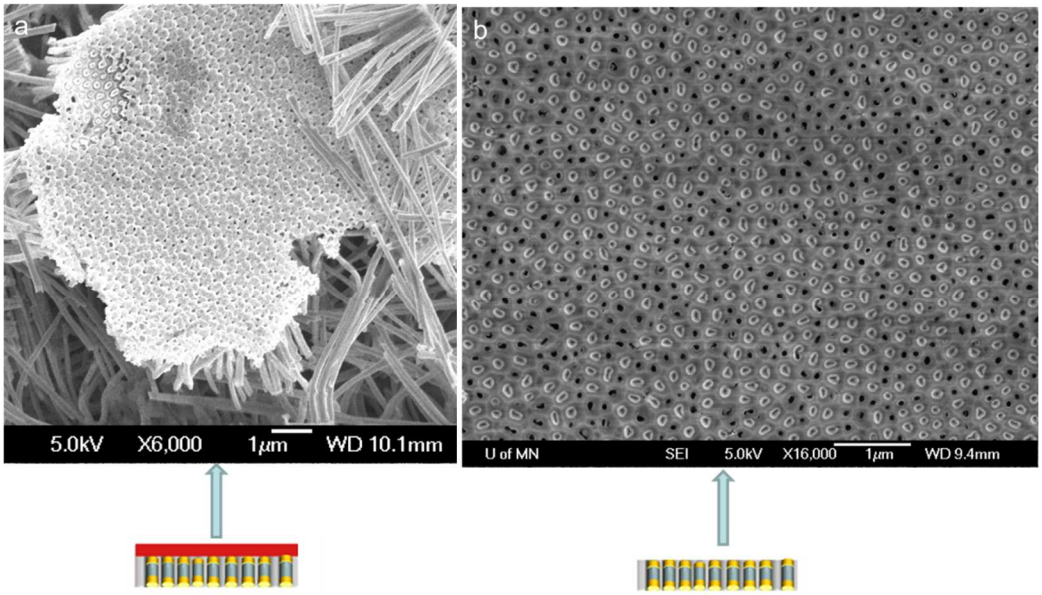

Figure 5.9 Nanowire clusters(*) (a) SEM image of a segment of growth contact that remained attached to nanowires after sonication- yielding a large cluster. (b) SEM image of the contact side of a nanowire array after the growth contact was removed by ion-milling. Note that the metal wires wear preferentially compared to the oxide template during ion-milling, so the gold ends appear somewhat hollow or missing.

5.2.2. Magnetic interactions between nanowires: FORC diagrams to quantify dipole interactions

In order to quantify dipole-dipole interactions between nanowires as a function of length, first order reversal curves (FORC) were obtained for nanowire arrays in AAO matrix. For a detailed explanation of this method, please refer to chapter 3.

Here, two nanowire lengths were tested: 3μm and 6μm, while keeping diameters constant at 100nm. As shown in figure 5.10, the interactions between longer nanowires are larger, as indicated by the range of biases of the hysterons (minor hysteresis arcs) from the center. This is better depicted in the associated FORC diagrams below the FORC curves. H_u represents the interaction field between the nanowires obtained from a statistical analysis of the distribution of biases in the hysterons (from zero). In the 6μm nanowire case, a wider spread is seen in interaction field as compared to the 3μm nanowire.

If interaction energy formula for dipoles (figure 5.1) were used to calculate the interaction energies between the nanowires in the parallel configuration, it would appear that the 3 μm long nanowires would have higher interaction energy compared to the 6 μm nanowires. This is especially expected for field values at saturation or close to saturation. However, as discussed in the theory section, the dipole approximation does not hold well for nanowires with high aspect ratios (>10), arranged in arrays. In this regime, the monopole approximation is consistent with results. As expected from this model, the interaction energy increases with increase in aspect ratio (figure 5.2), which is consistent with the observed results. Extending these results to nanowire suspensions, high aspect

ratio nanowires are less likely to stack along their lengths on the application of an external field and more likely to chain end to end compared to smaller aspect-ratio nanowires. Further evidence of aggregation of nanowires in aqueous solutions was discussed in section 4.2.2.

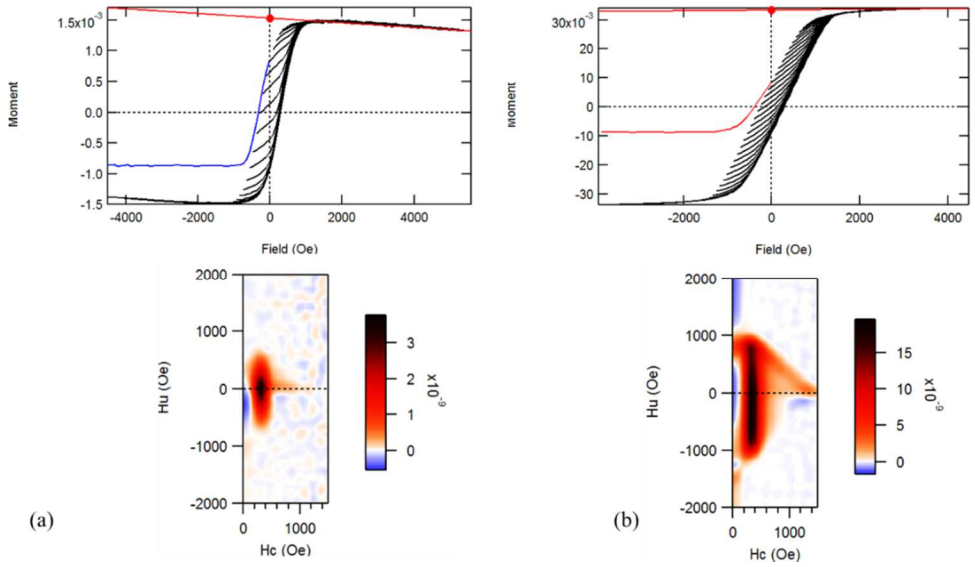

Figure 5.10: FORC distributions (moment in emu vs field in Oe) and diagrams for (a) 3 µm long (100 nm diameter) and (b) 6 µm long (100 nm diameter) nanowires in arrays. Paramagnetic/diamagnetic slope components were corrected prior to calculation of FORC diagrams.

5.2.3. Mitigating aggregation: PEG coating and Au ends

Polymeric coatings prevent aggregation through steric repulsion between the polymer molecules on the surfaces of different nanoparticles. In addition, hydrophilic forces keep the nanoparticles stabilized in suspension. Using functional polymers with terminal groups enables conjugation of proteins/antibodies for specific targeting of cells.

Polyethylene glycol (PEG) based electrostatically bound coatings, which have the general formula – $(\text{-O-CH}_2\text{-CH}_2)_n$ —, is employed for the following reasons:

1) The coating imparts hydrophilicity to the nanoparticles, as these are water soluble polymers [80], thus stabilizing them in suspension through hydrophilic interactions and steric repulsion. This mitigates aggregation due to stacking of nanowires.

2) PEG coatings reduce non-specific adsorption of proteins and prevents formation of corona [77]. This in turn increases blood circulation time for *in vivo* applications.

3) PEG coatings prevent ion leeching and hence, increases biocompatibility [77].

4) Terminal groups on the PEG linker molecules allow conjugation of peptides, antibodies, etc for selective/active targeting of cells, tissue or disease markers.

5) They are soluble in aqueous as well as organic solvents.

6) For *in vivo* applications, PEG increases the circulation half-life by avoiding phagocytosis by the MPS system, thus imparting the particle with "stealth" which can be exploited for drug-delivery applications. The circulation half-life increases with increase in molecular weight.

Thus, here we use a 1000 g/mol (M.W.) of heterobifunctional PEG:

$\text{NH}_2\text{—(O-CH}_2\text{-CH}_2)_n\text{—CH}_2\text{-CH}_2\text{-COOH}$ for functionalizing nickel surface.

Further, to reduce chaining of nanowires, the ends of the ferromagnetic nanowires are capped with diamagnetic Au layers. The Au layers have low permeability and thus, reduce the flux density at the nanowire ends.

5.2.4 Surface of Ni nanowires: XPS

Developing a surface chemistry for nickel segments requires characterization of the nickel surface to determine the oxidation state(s). From XPS analysis of nickel nanowire surfaces, deconvolution of Ni 2p3 spectra yields three peaks as shown in figure 5.11(a). Peak 1 (~853 eV) corresponds to Ni^0 oxidation state or Ni metal. Peaks 2 (~857 eV) and peak 3(~862 eV) arise from overlay of nickel oxides Ni^{2+} as well as hydroxides. To test for intercalated or adsorbed OH^- ions on the surface of the nanowire, the O 1s spectra is also obtained in figure 5.11(b).

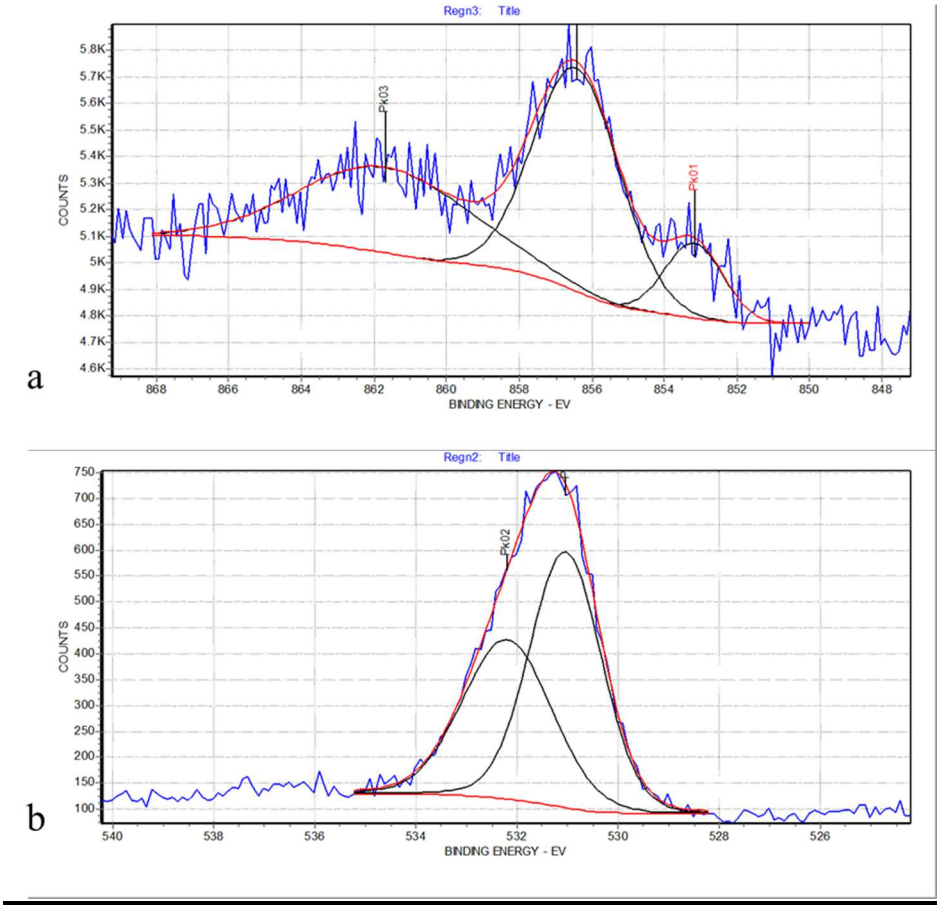

Figure 5.11. XPS spectra obtained from uncoated Ni nanowires. (a) Ni 2p3 spectra (b) O 1S spectra.

Deconvolution of O 1s spectra reveals peak 1 (~ 530.5 eV) from O^{2-} and peak 2 (532.5 eV) from OH^-. Thus, this analysis shows that, in addition to a main oxide component, there are OH^- ions on the surface of the nanowire which arises due to hydration in aqueous solutions. In this case, release and processing/cleaning of the nanowire samples from the AAO matrix involves multiple rinsing steps with water. This would have led to the adsorption of OH^- ions on the surface.

To further test this hypothesis, free Ni nanowires were immersed in sterile water and stored in it for 7 days. An XPS spectroscopy on nanowires collected after 7 days storage from this sample reveals one main oxidation state of Ni (~857 eV). Deconvolution of O 1s spectra reveals one major peak at ~ 532 eV which arises from OH^- ions. Thus, extended storage in water causes formation of nickel hydroxide $Ni(OH)_2$.

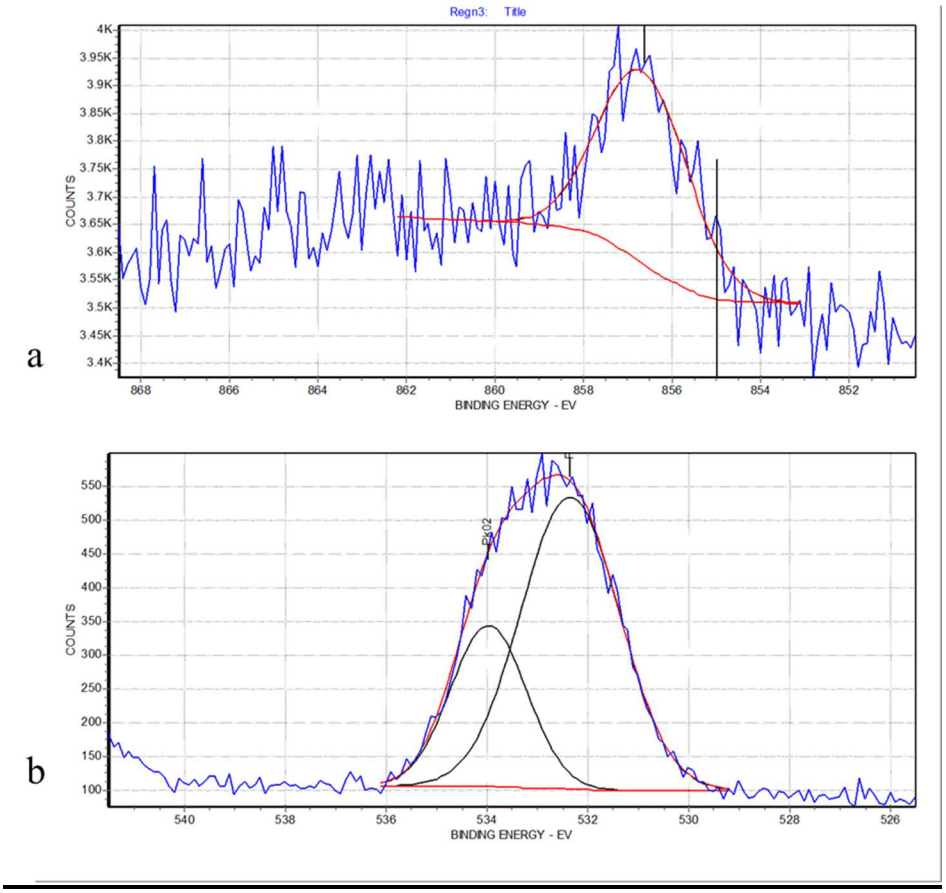

Figure 5.12. XPS spectra obtained from Ni nanowires after storage in sterile water for 7 days. (a) Ni 2p3 spectra (b) O 1S spectra.

5.2.5 Pegylation of Ni segments in barcoded nanowire: recipe and kinetics.

Nickel nanowires fabricated through electrodeposition have a thin oxide layer on the surface as indicated by XPS and literature[50,81]. This layer is formed largely due to the AAO etch step with 1M NaOH. Nickel oxide has a point of zero charge (PZC) close to 11.3 (maximum value reported)[82]. At a pH greater than 11.3, the Nickel Oxide surface develops a negative charge. A pH of 12-12.5 was therefore chosen for the pegylation recipe. At this pH, the zwitterion $^{+}H_3N$-PEG-COO^{-} , formed from the

bifunctional PEG, has a positive charge on the amine group and a negative charge on the carboxyl group (see calculations below for rate constants and species formation). The positively charged amine group binds to the negatively charged oxide layer through an ionic bond[83]. This is better demonstrated in figure 5.13(a). The advantage of functionalizing the surfaces using this method is that terminal carboxyl groups are available on the nanowires. These can be used to bind antibodies or peptides utilizing carbodimide chemistry as discussed in the experimental section. Using charged functional groups on the PEG, as used here, also allows electroplating of PEG to the particle surface. This gives good control over thicknesses, ligand density and the morphology/geometry of tethered ligands. While TiO implants have been functionalized in a similar way[83] , this is the first time nickel nanoparticles have been functionalized this way.

The ligand density and morphology are interrelated, and can be controlled by the synthesis method: electroplating vs immersion (figures 5.13(b&c)). A brush-like morphology of PEG chains result from electroplating PEG on the Ni nanowire surface (figure 5.13(b)). Here, the distance d between the chains is smaller than the chain length R_f (also called the Flory radius), thus resulting in a high ligand density[84,85]. This close spacing between the chains forces the chains to apply lateral repulsive forces, thus causing them to stretch out from the surface in parallel brush-like structures. On the other hand, coating Ni nanowire surfaces with PEG by immersion of nanowires in the PEG solution results in a mushroom configuration. In this case, $d > R_f$, resulting in a lower

density of ligands[84]. These morphologies can be characterized from the N 1s spectra from amine group attached to the Ni segment of the nanowire using XPS (section 5.2.7).

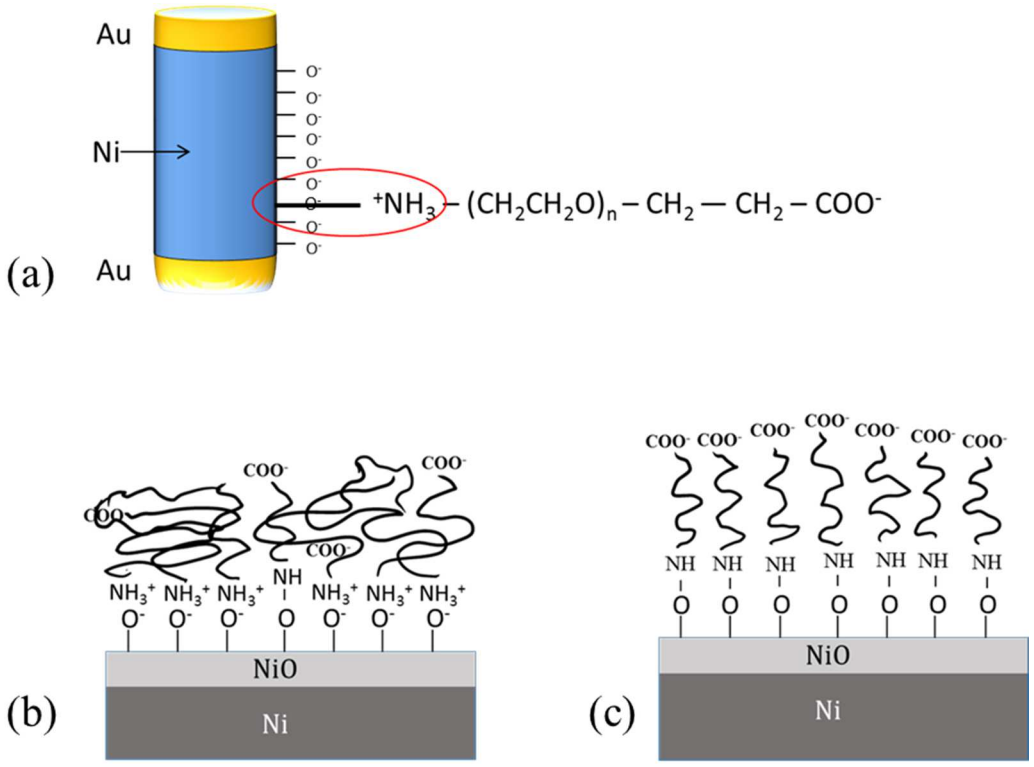

Figure 5.13 Surface functionalization of Ni with heterobifunctional PEG. (a) Schematic showing binding of bifunctional PEG (1000 M.W.) to nickel nanowire surface. The Au caps of the nanowires are not functionalized in this scheme. Depending on whether the PEG is electroplated to the Ni surface or immersion deposited, the orientation of the PEG molecules can vary from (b) mushroom-like orientation for immersion deposition to (c) brush-like for electroplated PEG.

Kinetics:

At pH 12-12.5, NH_2-PEG-COOH forms two species[86]

H_2N-PEG-COO^- and ^+H_3N-PEG-COO^- zwitterion. By calculations shown below, H_2N-PEG-COO^- would be the dominant species.

$pH = pK_{a2} + \log[A^-/HA]$

pK_{a2} for H_2N-PEG-COO^- is 11.7

Therefore, by Henderson-Hasselbach equation

$A^-/HA = 10^{0.8} = 6.3 \rightarrow$ H_2N-PEG-COO^-/ ^+H_3N-PEG-COO^- = 6.3

Hence confirming that the dominant species is H_2N-PEG-COO^-, in theory.

However, at pH 12.5, H_2N-PEG-COO^- gets further hydrolyzed to ^+H_3N-PEG-COO^- as per the following reaction[27]:

H_2N-PEG-COO^- + $H_2O \rightarrow$ ^+H_3N-PEG-COO^- + OH^- (1)

A-	HA +	OH^-
F-x	x	x

For initial concentration of 0.002M (0.1g/1000g/mol PEG in 50ml NaCl solution), and therefore F for the dominant species H_2N-PEG-COO^- = 6.3/7.3*0.002M = .00172M, let x mM of the zwitterion be formed.

Therefore,

$x^2/F\text{-}x = k_w/k_{a2} = 10^{-2.3} = 0.005$

$x^2+0.005x-0.0086=0$

Solving for x yields,

0.00135 M zwitterion.

Thus, hydrolysis of H_2N-PEG-COO^- yields the zwitterion. At pH 12-12.5, the zwitterion becomes the dominant species in solution (78.48% of H_2N-PEG-COO^- and thus, 67.5% of the original 0.002M PEG added).

5.2.6 Imaging PEG coatings: Fluorescence and SEM

Fluorescence

The amine binding of the PEG to the Nickel nanowire and availability of the terminal carboxyl groups for further binding was confirmed by conjugation of a primary antibody (mouse-anti-EPCAM) to the PEG-nanowires using standard coupling with EDC-NHS (1-ethyl-3-[3-dimethylaminopropyl]carbodiimide hydrochloride-N-hydroxysuccinimide) (section 5.1.9). A secondary antibody fluorophore conjugate (FITC-goat-anti-mouse IgG) was then used to target the primary antibody. Again, fluorescence was seen from each nanowire also observed by DIC (figure 5.14(a&b)), indicating successful conjugation of the primary antibody to the terminal carboxyl groups on the PEG-nanowires. As shown in figure 5.14 (c), fluorphores, like FITC, can be attached to the gold end using a thiol linker molecule for identification of nanowires in flow cytometry (FACS) or fluorescence microscopy. Thus, the nickel segment of the nanowire is free for functionalization with RGD or other ligands at various densities. An example of such use of Au ends is shown in figure 5.21. Attaching a fluorophore to RGD instead can compromise the functionality of the peptide by masking it from the integrins (receptors) on the cell-membrane.

SEM

SEM images of Au/Ni/Au nanowires show clustered bare nanowires (figure 5.14(d)) vs pegylated (PEG-coated) (figure 5,14(e)) nanowires. As observed in figure 5.14(d), when a permanent magnet is held at the top right corner, nanowire clusters are observed to stack and chain. These clusters exist because of (1) non-uniform etching of nanowire growth contact in which case the nanowire are held together physically, (2) magnetic stacking and chaining of nanowire clusters due to magnetostatic interactions. When the growth contact is uniformly etched through efficient dry/wet etching methods and a PEG coating is applied on the nanowire surface, the nanowires appear as shown in figure 5.14(e), when a permanent magnet is held on the top right corner. A waxy PEG coating is observed on the nanowire surface and clustering is mitigated. However, these nanowires still form some chains on the application of an external field. The wires used for here were 100nm in diameter with 3 +/- 0.3μm lengths of Ni with 100 +/- 10nm Au end segments. These dimensions were analyzed using SEM in both secondary electron imaging (SEI) and back-scattered electron (BSE) modes.

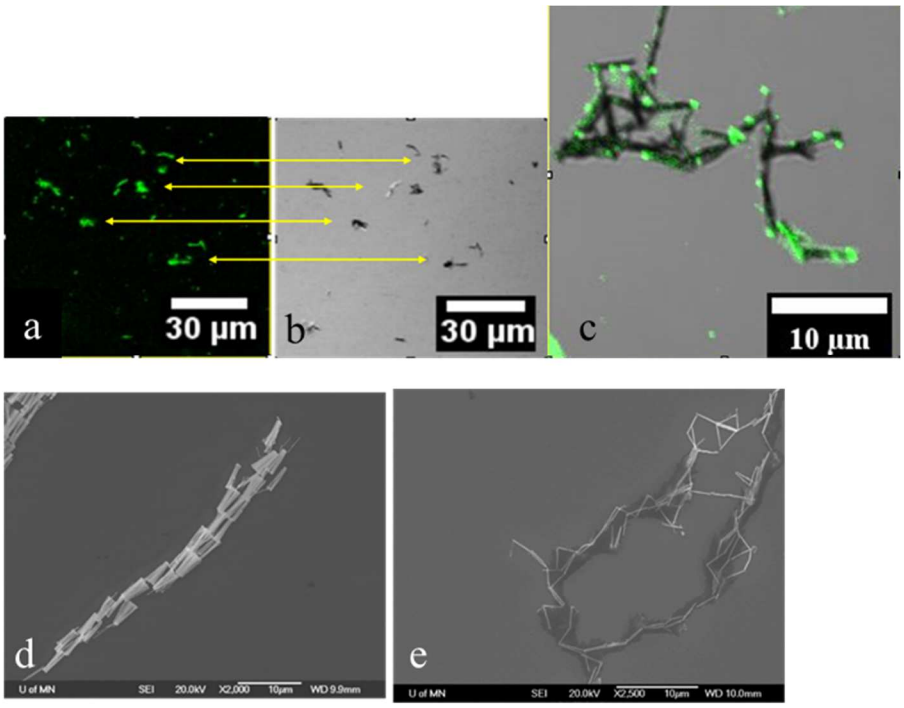

Figure 5.14 Fluorescence microscopy and SEM of PEG-coated nanowires. (a) shows fluorescence from nanowires functionalized with NH_2-PEG-COOH, which was conjugated to a primary antibody (mouse anti-EpCAM) through EDC-NHS cross linking and then to a secondary antibody-fluorophore (FITC goat anti-mouse IgG), which confirmed the availability of the terminal carboxyl group for further conjugation(*). (b) shows corresponding DIC image. (c) Overlaid fluoresence and DIC microscopy images from Au segments of the 3µm Au/Ni/Au nanowires where the Au segments were functionalized with FITC using a thiol linker. (d) SEM image of clustered nanowires chaining along the applied field gradient. (e) SEM image of PEG-coated nanowires.

5.2.7 Characterizing chemical binding of NH_2-PEG-COOH to nanowire surfaces using FTIR and XPS

5.2.7.1 Fourier transform Infrared spectroscopy (FTIR):

FTIR of functionalized nanowires in a KBr pellet was performed to detect the functional groups (carboxyl and amine) and the carbon backbone of PEG from the coated nanowires. A positive control measurement of the bifunctional PEG (powder) used for nanowire surface coating is shown in figure 5.15a. C=O ,C-O-C, O-H stretch peaks and O-H bend peaks from the carboxyl functional groups are detected. N-H wag, C-N stretch, N-H bend and N-H stretch peaks from amine functional group are also detected and marked in the figure.

The samples bc12_pegylated and bc12_bare are taken from Au/Ni/Au nanowire barcode 12 (bc12). In sample bc12_pegylated, Ni segments are pegylated by immersion of Ni nanowires in PEG solution. In sample bc12_bare, Ni segments are uncoated. S105_peg represents a sample of nickel nanowires where PEG was electroplated on the Ni surface. The uncoated sample shows no peaks except for water (O-H stretch and bend) which was due to residual adsorbed water on the nanowire surface retrieved from uniformly ultrasonicated nanowires in DI water. Sample bc12_pegylated shows the CH_2 bend groups from the carbon backbone in the PEG polymer groups which overlap with CH_2 bend groups from the positive control. The electroplated sample s105 shows two more peaks, C-N bend associated with the amine group and O-H bend group at 989cm^{-1}. The reduction in number of peaks detected in the nanowire samples in comparison to the positive control is largely because of suppression of a number of vibrational modes on attachment to nickel surface. Also, strong peaks are observed from the PEG-terminal

functional groups in the electroplated sample. This is due to difference in morphologies or orientation of the PEG molecules in the two samples (figure 5.13(b&c)). In electroplated samples, the PEG molecules (chains) deposit on the nickel oxide surface in brush-like configuration (figure 5.13(c)). This makes a high density of terminal functional groups "available" for detection. In immersion samples, PEG chains are oriented in a mushroom-configuration (figure 5.13(b)). While terminal functional groups are available for imaging and conjugation, these are available at a relatively lower density compared to the brush-like configuration. Thus, the FTIR output in the immersion case is dominated by the carbon backbone while the FTIR signatures from the functional groups are lost in the noise.

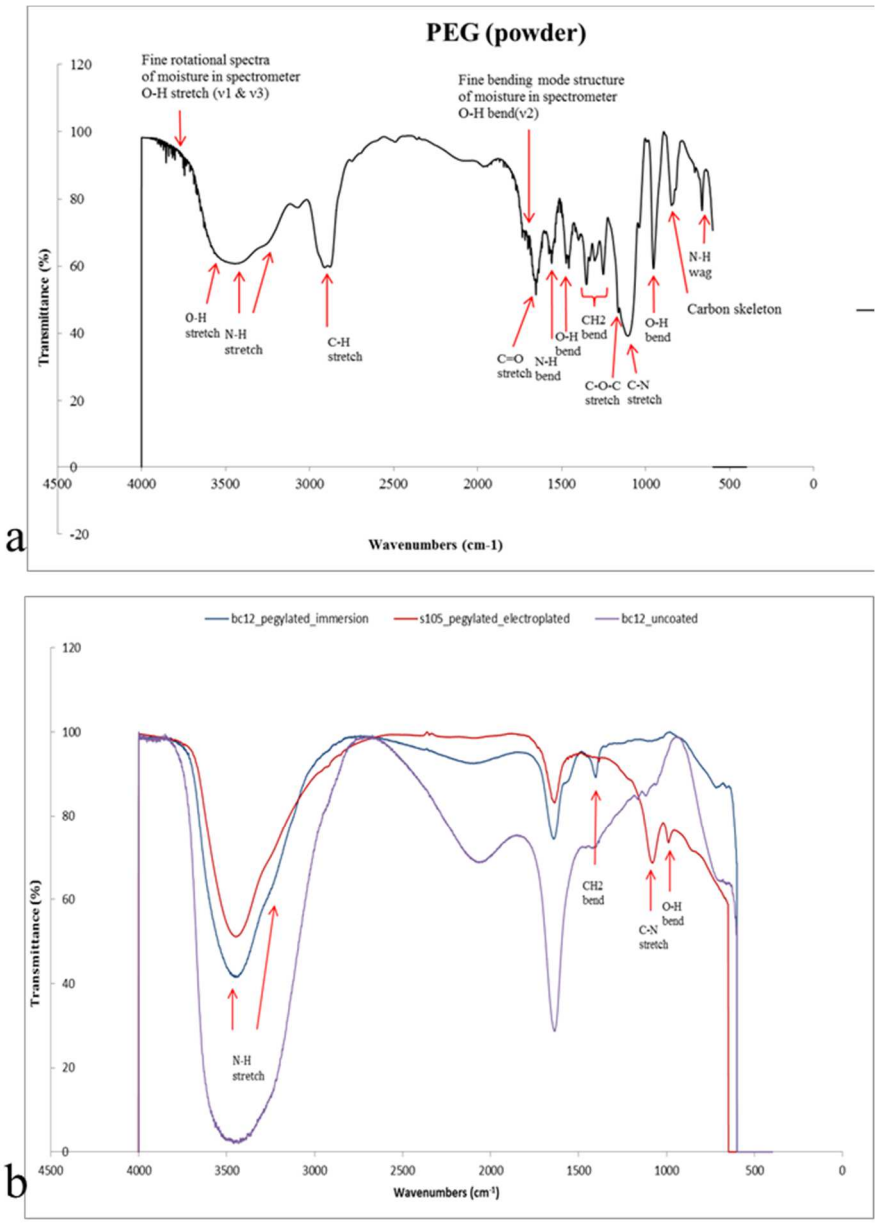

Figure 5.15: FTIR characterization of PEG-coating on nanowires (a) FTIR plot of the bifunctional PEG (powder) mixed with KBr pellet (b) FTIR plot of nanowire samples in KBr pellet. S105_peg is electrodeposited PEG on nanowire surface. Sample bc12_pegylated nanowires are functionalized with PEG using immersion. Sample bc12_

bare are bare nanowires with no surface coating. The total length of the nanowires in all cases is 3µm and diameter is 100nm.

5.2.7.2 X-ray Photoelectron Spectroscopy (XPS):

To characterize the immobilization of the bifunctional PEG on the Ni nanowire surface and confirm the bonding of the amine group of PEG to Ni, XPS was performed. Nitrogen (N 1s from amine) was obtained to verify bonding of amine group to nickel surface in both cases of electroplated-PEG and immersion-PEG (figure 5.16).

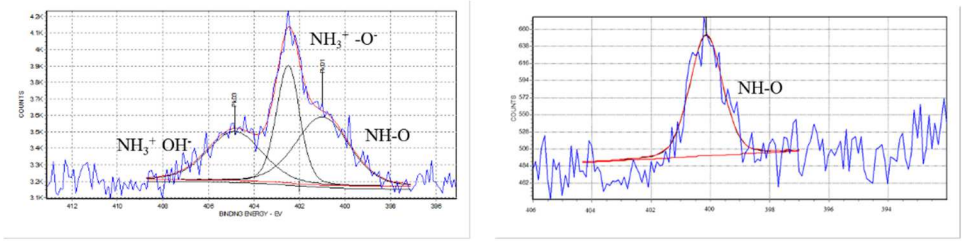

(a) Immersion PEG N 1S spectra (b) Electromigrated PEG N 1S spectra

Figure 5.16. XPS characterization of PEG coating on Ni nanowire. (a) N 1S XPS spectra obtained from PEG-coated Ni nanowires where PEG was coated on Ni surface through immersion of nanowires in PEG solution. (b) N 1S XPS spectra obtained from PEG-coated Ni nanowires where PEG was electroplated on Ni nanowires.

In the case of immersion-PEG, deconvolution of N 1s results in three peaks. The peak at ~ 400.5 eV is due to covalent bonding of the amine to the nickel oxide (NH-O bond) [87]. The peak at ~402.5 eV is due to electrostatic attraction between NH_3^+ from the bifucnctional PEG and O^- from nickel oxide [87]. Finally, the peak at ~ 405 eV is from electrostatic attraction between NH_3^+ from bifunctional PEG and OH^- from

hydroxylated sites on the nickel oxide surface[87]. Thus, for PEG coated on the Ni segments through immersion, amine binding to the nanowire surface exhibits partial ionic and covalent bonding.

In case of electroplated PEG, deconvolution of N 1s spectra results in only one peak at ~ 400.5 eV which corresponds to the covalent NH-O bond[88].

5.2.8 Characterizing performance/stability of nanowire suspensions using VSM and UV-vis-NIR spectrophotometry

5.2.8.1 Measuring stability of nanowire suspensions using VSM

The efficacy of the PEG coating in minimizing nanowire clusters was analyzed using hysteresis loops as measured by vibrating sample magnetometry (VSM). The saturation moment of electrodeposited Ni is 415emu/cc (figure 5.17(a), inset and from literature [23]). An aqueous stock solution of PEG-nanowires (3μm long with 100nm diameter and 100nm Au ends) was prepared, and the saturation moments of 100μl samples were measured to calculate a stock concentration of 0.49±0.02pM (picomoles of PEG-nanowires per liter de-ionized water). This measurement was highly reproducible with approximately ± 4% variation in saturation magnetization between samples. In contrast, solutions of bare nanowires were inhomogeneous, and their saturation moments varied up to 260% from one measurement to the next, depending on the number of magnetic clusters contained in the sample being measured. A typical hysteresis loop for a 100 μl sample of the PEG-nanowire stock solution is shown in figure 5.17(a) with dilution samples containing stock to water ratios of 1:1 and 1:2. The linear changes in

saturation moments with volume demonstrate the even dispersal of these PEG-nanowires in solution and high stability (figure 5.17(b)).

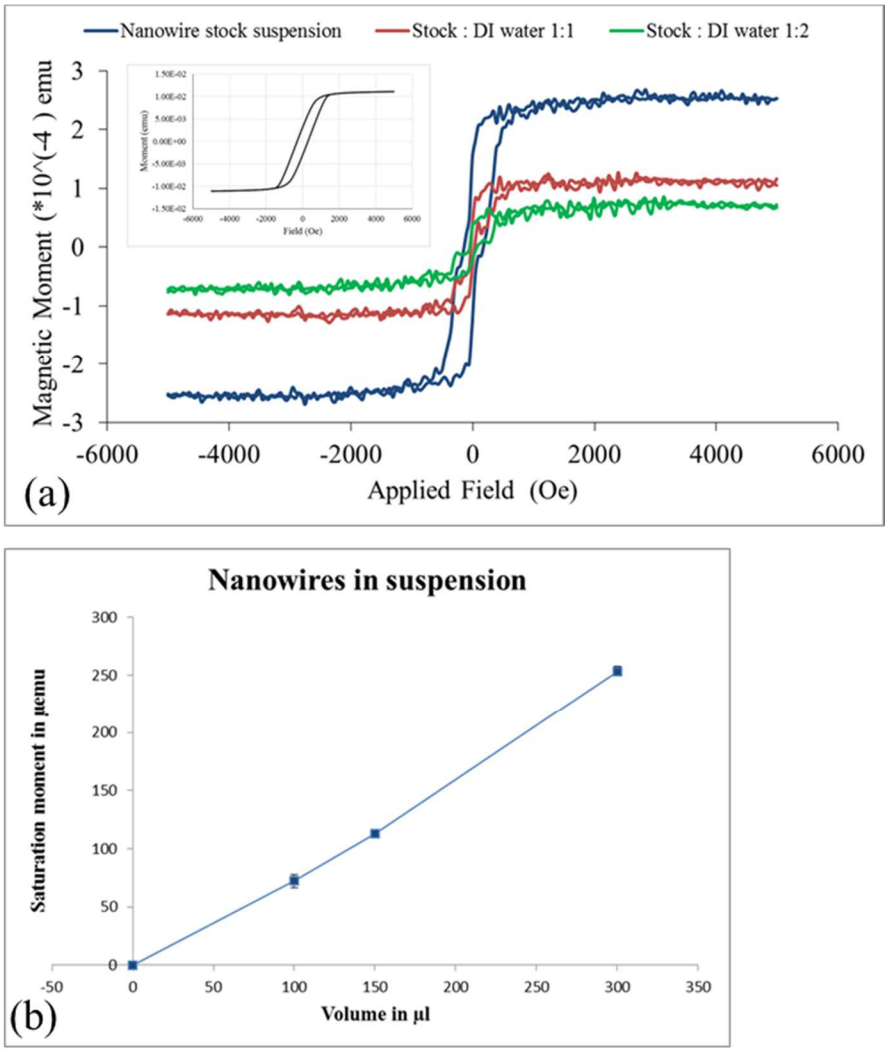

Figure 5.17. Measuring stability of nanowire suspensions using VSM(*). (a) Hysteresis loops obtained for 100µl of a stock solution of nanowires in DI water and scaled concentrations of 1:1 and 1:2 (stock: DI water). Inset shows saturation moment obtained from nanowire array with nanowire density of $2x10^9$ cm^{-2} and plating area of 7.25mm x 8mm. Nanowire dimensions are 3µm length and 100nm diameter. (b) Moment vs volume

relationship for uniformly ultrasonicated nanowires in cell culture medium. Dilutions in the curve were created from a 0.49pM solution (nanowire population) of 3μm long and 100nm diameter nanowires.

5.2.8.2 Measuring stability of nanowire suspensions using UV-vis-NIR spectrophotometer

UV-vis-NIR spectra was obtained from suspensions of 6 μm long uncoated (bare) and PEG-coated Au(50nm)/Ni(5.9μm)/Au(50nm) nanowires in DI-water enclosed transparent cuvettes.

The stability of the nanowire suspensions in aquesous solutions (DI water) were measured for three cases:

(i) uncoated nanowires,

(ii) PEG-coated only on long Ni segment of nanowires and

(iii) mecaptoundecanoic acid coated only on short gold ends of the nanowires.

A transmittance time-lapse was conducted sequentially through cuvettes containing these uniformly sonicated samples in order to evaluate the tendency of the nanowires to sediment in each case. The increase in transmittance over time corresponds to sedimentation of nanowires. The nanowire sample with PEG-coated nickel segments showed the greatest stability with time with a faierly constant transmittance collected over 15 minutes (figure 5.18) . The uncoated nanowires quickly aggregated while in suspension forming huge clusters, which blocked the transmittance further as seen over

the first 500 seconds. However, with increase in aggregation and cluster size, increased sedimentation is observed due to larger weight of the clusters and the transmittance increases continuously with time. In the third case, where only the Au ends are coated with mercaptoundecanoic acid, the stability is low and the nanowires quickly sediment. Thus, the PEG coating on the longer Ni-segments provides the most stable nanowire suspension.

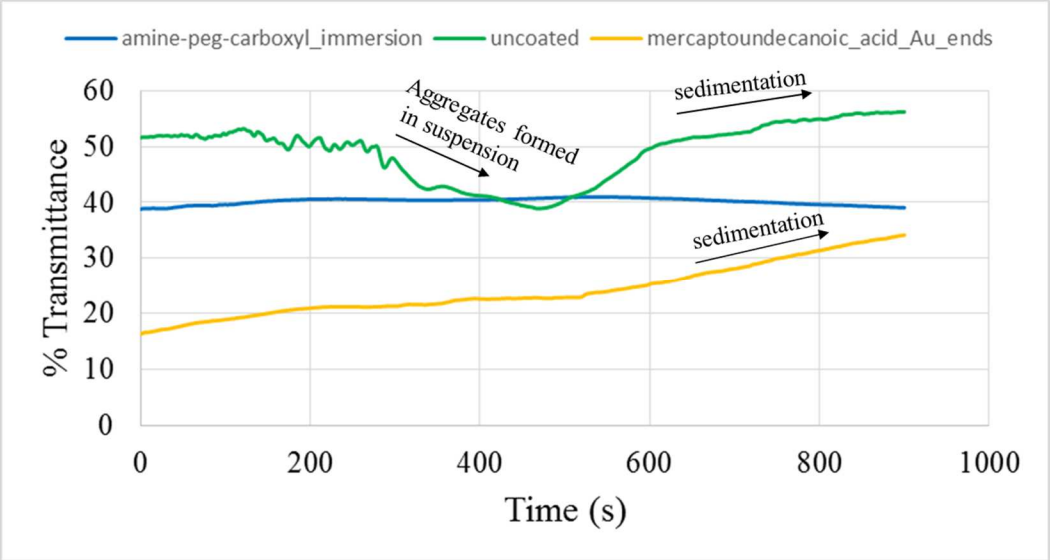

Figure 5.18. Measuring stability of nanowire suspensions using UV-vis-NIR spectrophotometry.

5.2.9 Cytotoxicity assays

Three types of nanowire surfaces were used in this study: bare Ni (bare), PEG as a control coating (PEG-nanowires), and RGD which was adhered using PEG (RGD-PEG-nanowires which I will refer to as RGD-nanowires). Arg-Gly-Asp (RGD), a tri-peptide sequence that is a biological trigger for integrins, which regulate cellular functions such as cell adhesion, proliferation, and motility (chapter 6).

The dose-dependent toxicity of various nanowire coatings was evaluated using a cell type that is highly sensitive to particulate-mediated cell death (primary macrophages from C57/B16 mice). These macrophages are especially sensitive to particulate-mediated toxicity and present a widely accepted model for comparison of cytotoxicity and inflammation data across existing nanomaterial platforms in literature [73,89]. For this study, we incubated a high concentrations (effective concentration of 100 nanowires/cell or 10.5µg/ml, as determined from studying macrophages) of bare and functionalized nanowires with osteosarcoma cells. Metabolic activity was recorded at different time points, for different-length nanowires and for different surface coatings to determine the dependence of cell-viability on these variables. The toxicity of nanowires with each of the coatings was determined by incubation with cells highly sensitive to particulate-mediated cell death (primary macrophages from C57/B16 mice). The cells were activated with lipopolysaccharide (LPS) for 3 hours and then incubated with nanowires at 37ºC and 5% CO_2 for 6 hours. Two measures were used to assess toxicity. The first was a measure of cell death by release of lactate dehydrogenase (LDH), an intracellular enzyme, and the second was a measure of cell metabolism by MTS ((3-(4,5-dimethylthiazol-2-yl)-5-(3-carboxymethoxyphenyl)-2-(4-sulfophenyl)-2H-tetrazolium)). At concentrations of 100 and 200 nanowires per cell, RGD-nanowires resulted in negligible (0% and 1.7%, resp.) cell death, despite the cells being highly sensitized by LPS, compared to the same concentration of bare nanowires (3.25% and 8% cell death, resp.) and PEG-nanowires (2.5% and 6.1% cell death, resp.) (figure 5.19(a)). Crystalline silica (US Silica, MIN-U-SIL), used as a positive control for particulate-mediated cell death, resulted in higher levels of cell death (27.3% for 7.5ng/well and $5x10^5$ cells/well or 75ng/ml silica) even with an order of magnitude lower mass than the nanowires (2.1µg Ni per well or 21 µg/ml for 200 nanowires/cell). For the silica crystals, a poly-dispersed preparation of up to 15µm in length was used in all experiments. Uptake of silica particles can cause apoptosis[90,91]. The cell death mechanisms are different for opsonized vas non-opsonized

particles as discussed in detail in [92]. Although the toxicity is dependent on both the material and its surface conditions, it is worth noting that silica is the material used in microbeads such as AccuBeads (Bioneer). This indicates that RGD-functionalized nanowire meet our criteria of low toxicity even for this highly sensitive cell type. Moreover, the nanowires did not elicit an inflammatory response as measured by interleukin-1β (IL-1β) or tumor necrosis factor-α (TNF-α) secretion, even at concentrations of more than 100 nanowires per cell with and without functionalization (figure 5.20).

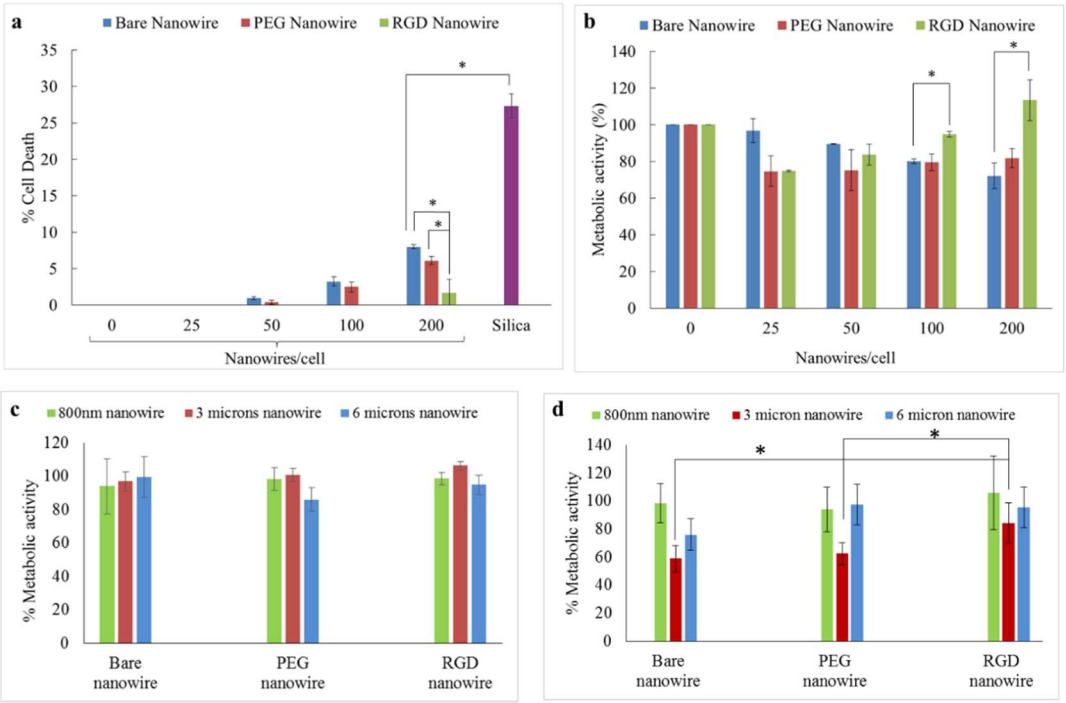

Figure 5.19**.** Results of cytotoxicity studies for nanowires with various functionalization(*). (a) Cell death of primary peritoneal macrophages pooled from C57/Bl6 mice (N=3) as determined by LDH assay. The concentration-dependent effects of nanowires on cell death are shown for 3µm long bare nanowires, PEG-nanowires and RGD-nanowires. Silica was used as a positive control for particulate-mediated cell death. (b) Metabolic activity of primary peritoneal macrophages pooled from C57/Bl6 mice

(N=3) as determined by MTS assay, when titrated with 3μm long bare nanowires, PEG-nanowires and RGD-nanowires and incubated for 6 hours at 37^0C and 5% CO_2. Refer to figure 5.22 for toxicity studies without LPS activation. (c) Nanowire length-dependent and surface-functionalization dependent metabolic activity of osteosarcoma cells (OSCA-8) as determined by MTS viability assay. All sample data are normalized with reference to metabolic activity of osteosarcoma cells without nanowires. Nanowire concentration used in all cases is 100 nanowires to one cell and incubation time is 6 hours at 37^0C and 5% CO_2. (d) Nanowire length-dependent and surface-functionalization dependent metabolic activity of osteosarcoma cells (OSCA-8). All sample data are normalized with reference to metabolic activity of osteosarcoma cells without nanowires. Nanowire concentrations used in all cases is 100 nanowires to one cell and incubation time is 18 hours at 37^0C and 5% CO_2. (*) indicates $p < 0.05$.

Cell viability, as quantified using MTS assays (figure 5.19(b)), showed a surprising increase in metabolic activity up to 115% with increasing doses of RGD-nanowires, up to 200 nanowires/cell. Here, our data shows the bare nanowires have a trend toward reducing viability, which is the inverse of the RGD-nanowire modality. These results are consistent with literature in dose-dependence of bare Ni nanowires [81,93], where 100 nanowires per cell resulted in 80% cell survival with incubation times from 6 hours [81] to 48 hours [93] with little dependence on nanowire length [93]. Finally, the PEG-nanowires resulted in approximately 81% cell survival that was relatively dose-independent (74.6-81.6% for 25-200 nanowires/cell). Interestingly, these

data indicated that RGD-nanowires encourage proliferation in cells while bare nanowires show increasing toxicity with dose. In summary, the 3μm RGD-nanowire modality appears to be non-inflammatory, as well as nontoxic, and the cells appeared to respond to the modality by increasing proliferation.

From the above dose-dependent studies with macrophages, an effective dose of 100 nanowires to 1 cell was used to study the dependence of cellular responses of osteosarcoma cells on nanowire lengths and surface functionalization. Three different lengths of nanowires were used for these experiments: 800nm, 3μm and 6μm, all having the same diameters of 100nm. For each nanowire length, three different surface conditions were used: bare, PEG-coating, RGD-coating. Cellular metabolic activity, recorded via MTS assays, after 6 hours of incubation with different nanowire samples (37^0C, 5% CO_2), revealed high metabolic activity (90-100% with reference to cells incubated without nanowires) in all cases and no specific dependence on length or surface coating was concluded (figure 5.19(c)). The cell viability assay was conducted again, after 18 hours of incubation of cells with various nanowire samples at 37^0C and 5% CO_2. Here, osteosarcoma cells show a significant increase in metabolic activity for 3μm RGD-nanowires compared to 3 μm PEG-nanowires or 3μm bare nanowires (figure 5.19(d)). Short nanowires (800nm length) appear to have low toxicity in all cases of functionalization as indicated by the near 100% metabolic activity of the cells after 18 hours of incubation**.**

Longer (6μm) nanowires have results suggesting that cell-based assays are not completely reliable for showing interactions between long nanowires and cells. This is

most likely because of non-identical interactions of cells with nanowires because of differences in local cellular microenvironment, the local geometry presented by the nanowire at the point of contact with the cell membrane and particle-particle interactions. Heterogeneity in interaction, accentuated by increasing length-dependent shape anisotropy of the nanowire, results in varied nanoparticle loading or internalization [94,95]**.** Therefore, a spectrum of resulting cellular behaviors is not effectively captured by cell-based assays that average such information. Time-lapse and confocal imaging techniques are, therefore, employed in the following section to corroborate the results obtained in the 3µm nanowire case and capture the heterogeneity in the longer nanowire (6µm) case.

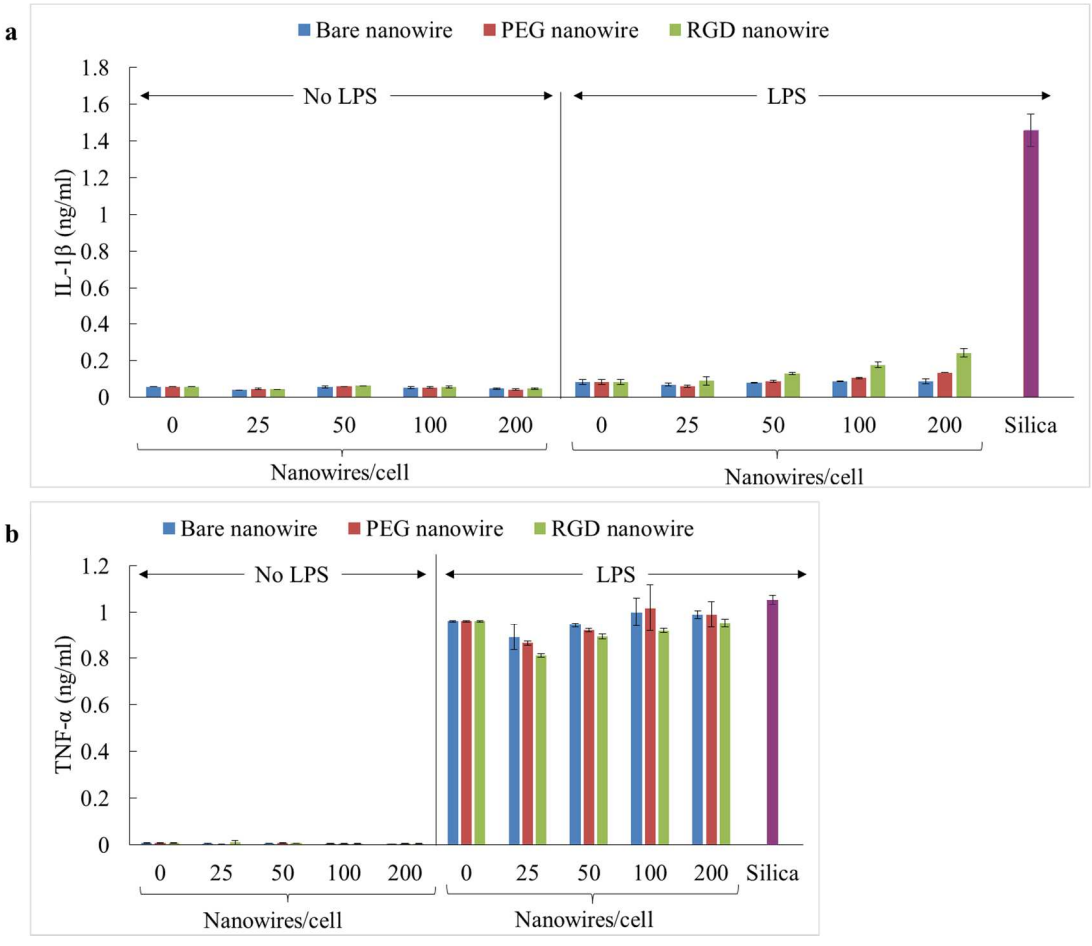

Figure 5.20. Cytotoxicity of nanowires as evaluated by IL-1β and TNF-α assays(*). (a) IL-1β (ng/ml/) of primary peritoneal macrophages pooled from C57/Bl6 mice (N=3) as determined by ELISA. The concentration-dependent effects of nanowires on cell death are shown for bare nanowires, PEG-nanowires and RGD nanowires with and without prior LPS activation. Silica represents positive control for NLRP3 inflammasome dependent particulate cell death. (b) TNF-α (ng/ml) of primary peritoneal macrophages pooled from C57/Bl6 mice (N=3) as determined by ELISA. The concentration-dependent effects of nanowires on cell death are shown for bare nanowires, PEG-nanowires and RGD nanowires with and without prior LPS activation. Silica represents positive control for NLRP3 inflammasome dependent particulate cell death.

Higher precision is obtained using flow cytometry (figure 5.21). Here, in all nanowire length cases (800 nm, 3 μm and 6 μm), the RGD nanowires cause the least cell death (apoptosis and necrosis). Comparing cell death across different lengths of bare nanowires, it is observed that the 800 nm nanowires cause the most cell death and 6 μm nanowires cause the least cell death. As smaller nanowires are phagocytosed relatively easier, higher Ni^{2+} content from intracellular degradation of phagocytosed nanowires is very likely to cause increased necrosis and apoptosis (cell death) [see section 6.1.5 for cell death mechanisms]. Reduction in phagocytosis efficiency with increasing length [72] reduces the intracellular Ni^{2+} content and thus is less likely to cause cell death. For PEG nanowires, the cell death appears to be relatively independent of nanowire length. This is

also expected because the PEG coating, in general, inhibits interaction and phagocytosis of nanowires.

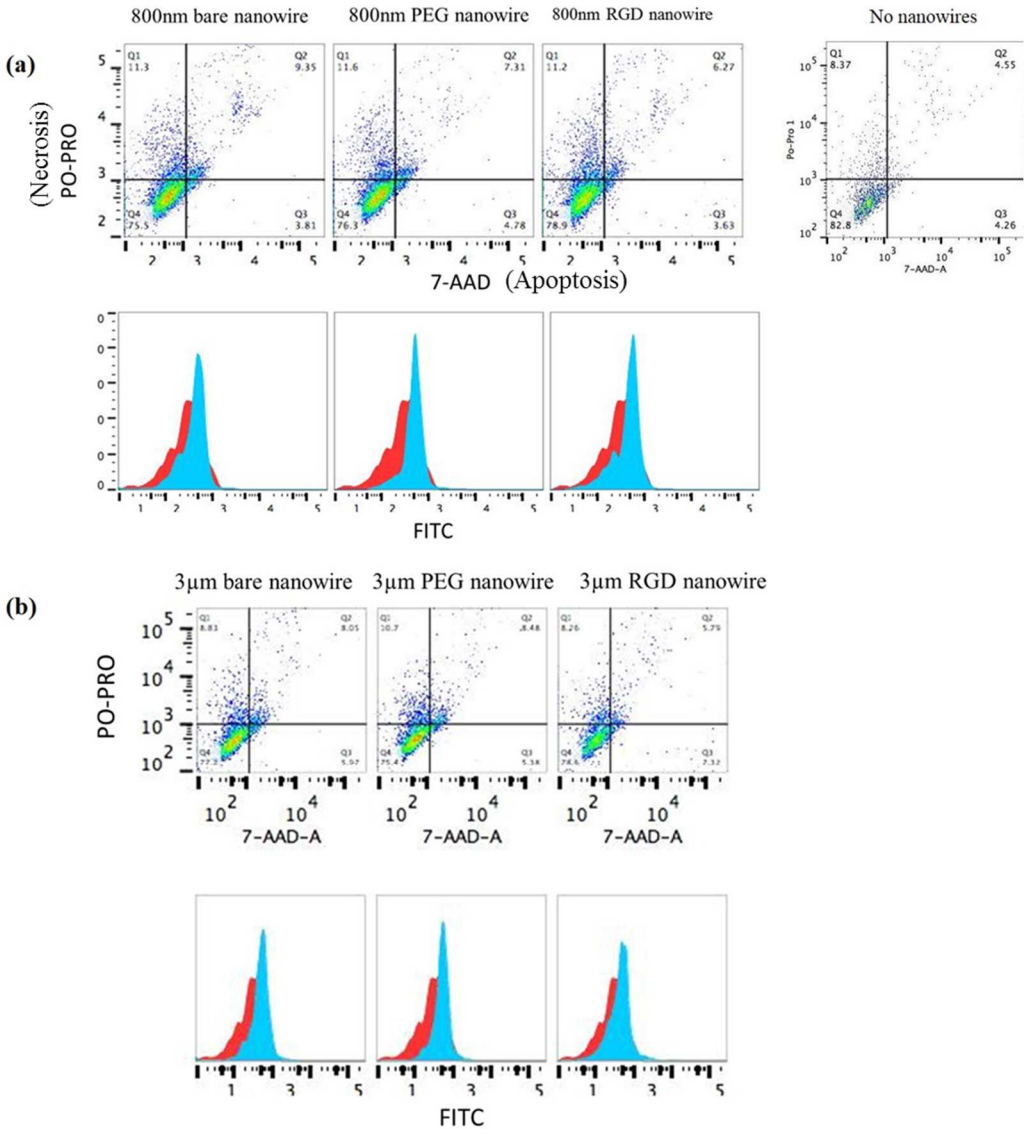

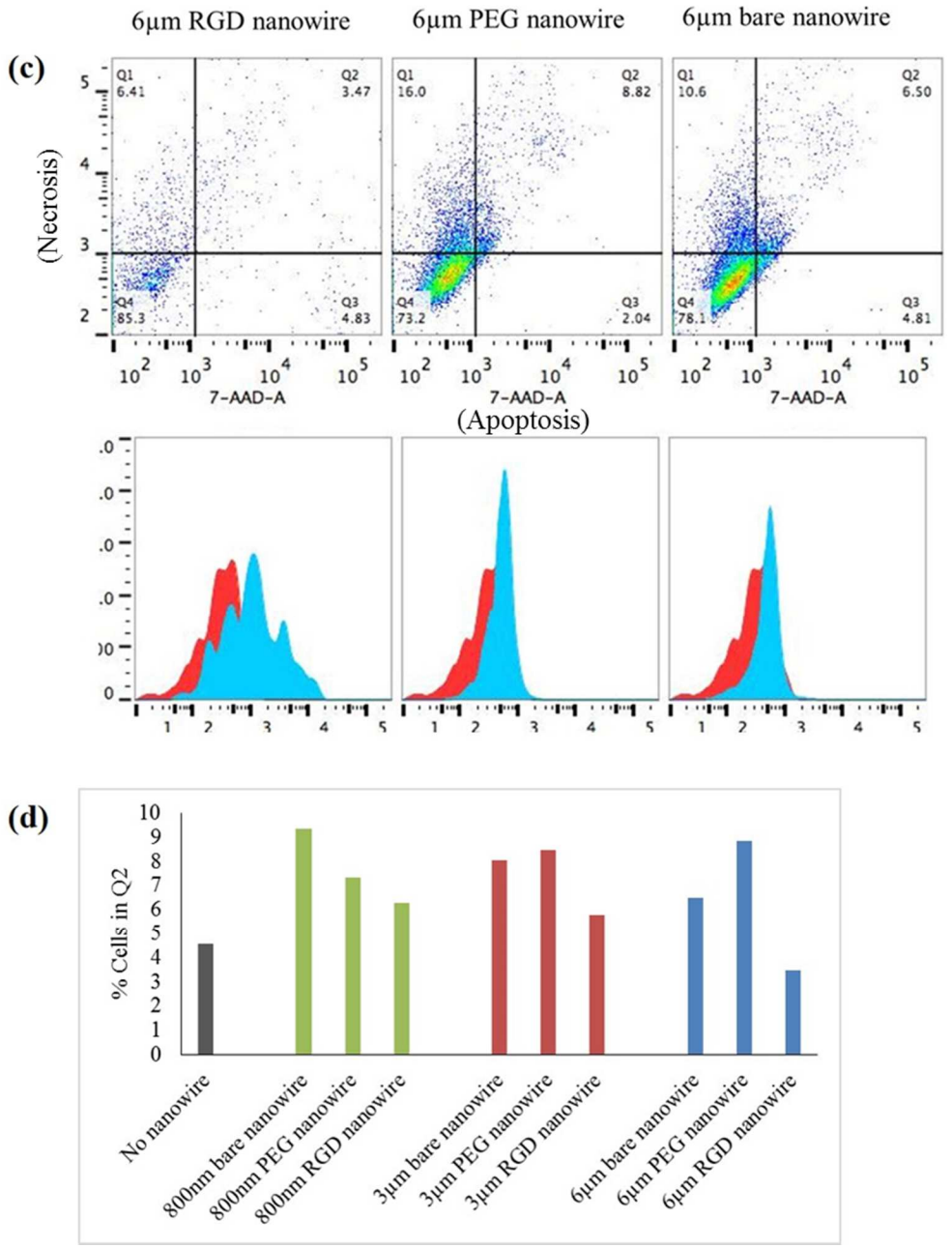

Figure 5.21: Preliminary FACS data obtained from osteosarcoma cells incubated with fixed concentrations (100 nanowires to 1 cell) of different nanowire lengths/surface functionalization for 2 hours at 37^0C and 5% CO_2(*). Here the gold ends of the Au/Ni/Au nanowires were functionalized with FITC using a thiol linker molecule. The cells were stained using membrane permeability/dead cell apoptosis kit (PO-PRO1 and 7-AAD) and

were analyzed for apoptotic and necrotic cells. Quadrant 2 (Q2) corresponds to percentage of cells that stained positive for both PO-PRO and 7-AAD (apoptotic and necrotic). (a), (b) and (c) show data for 800nm, 3μm and 6μm nanowires, respectively. The fluorescence from the FITC-conjugated nanowires was also detected in each case (blue plot), except the control sample, where no nanowires were added (red plot). The percentage of dead cells is plotted in (d) for each case. Overall, RGD nanowires for each length show lower cell death compared to other surface coatings on nanowires of the same length. PEG nanowires appear to induce similar fractions of cell death for all three cases.

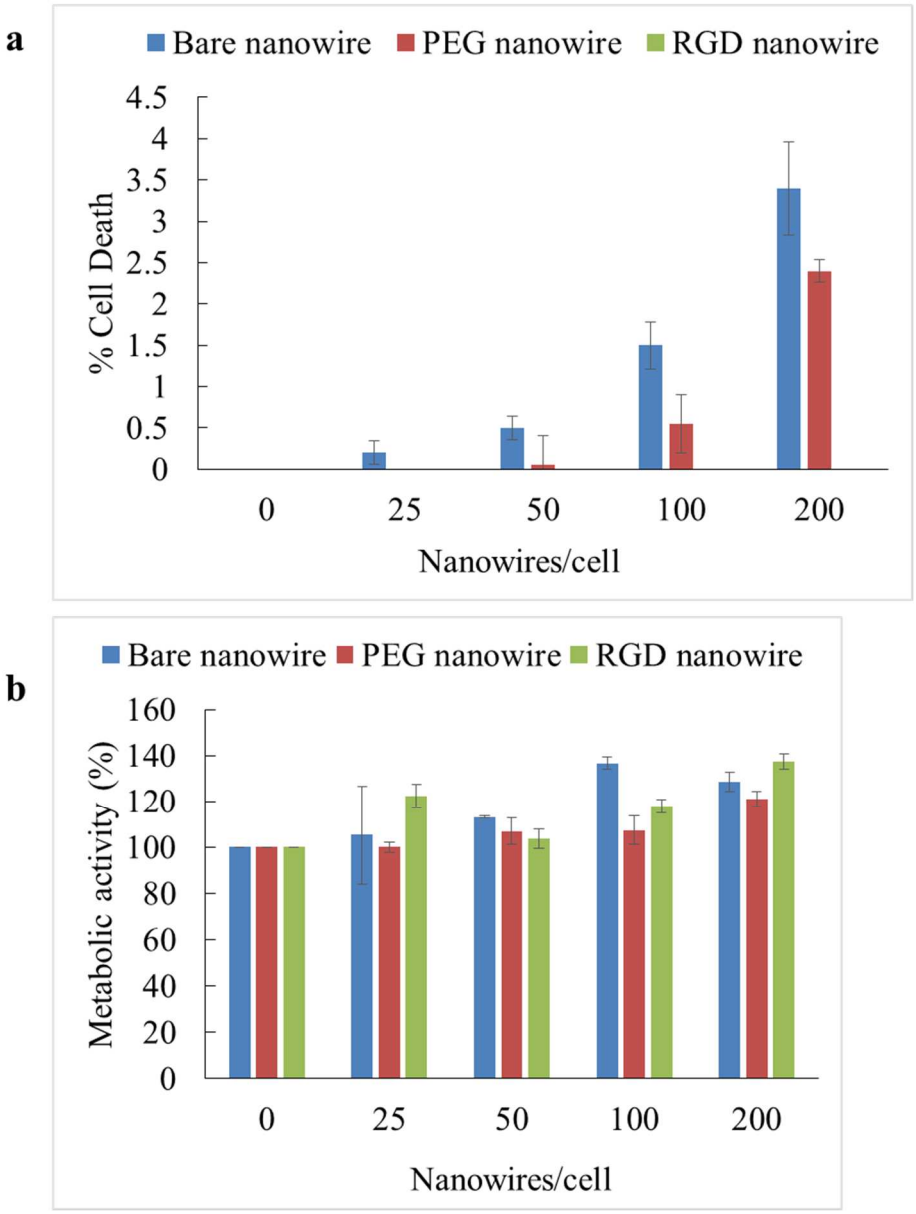

Figure 5.22**.** Results of cytotoxicity studies for nanowires with various coatings without LPS activation**.** (a) Cell death of primary peritoneal macrophages pooled from C57/Bl6 mice (N=3) as determined by LDH assay. The concentration-dependent effects of nanowires on cell death are shown for bare nanowires, PEG-nanowires and RGD-nanowires. (b) Cell survival of primary peritoneal macrophages pooled from C57/Bl6 mice

(N=3) as determined by MTS assay, when titrated with bare nanowires, PEG-nanowires and RGD-nanowires.

Therefore, from all the variables tested (surface chemistry, length, number of nanowires and cell types), the surface coating appears to decide the biologically effective dose below the 6 μm length threshold. The RGD-coated nanowires induce the least cytotoxicity and are biocompatible.

5.3 Methods

5.3.1 Biofunctionalization of nanowires.

0.1g of NH_2-PEG-COOH (0.2 mass %) was dissolved in 50ml of 0.5M NaCl solution and the pH was adjusted to 12-12.5 using 0.1M NaOH. Ni nanowires, immersed in ethanol in a glass vial, were collected at the walls of the vial using a magnetic stand. The ethanol was aspirated and the nanowires rinsed 3x with deionized (DI) water. Next the nanowires were immersed in the PEG solution described above. The nanowires were ultrasonicated (sweep-frequency) 10 minutes for uniform distribution of nanowires in solution and to ensure the availability of PEG molecules to the nanowire surfaces. The sample was allowed to incubate 24 hours at 4°C and ultrasonicated for 5 minutes occasionally in between. Ni nanowires, immersed in PEG solution in a glass vial, were collected at the walls of the vial using a magnetic stand. Next, after aspirating the PEG solution, the nanowires were rinsed 3x with DI water. Pegylated nanowires were then immersed in media of choice based on the cell culture chosen for experiments or

immersed in PBS at 4°C for future use. Degradation of moment is quicker in PBS. So, for long term storage, ethanol is the solvent of choice [50] .To further functionalize the nanowires with a cell targeting peptide such as RGD, the pegylated nanowires were immersed in 0.001% wt. RGD aqueous solution (pH 12) for another 24 hours at 4ºC with occasional ultrasonication followed by a rinse step with PBS (3x) .

5.3.2 Quantification of nanowire concentrations using VSM

After the nanowires are pegylated and freely suspended in DI water in a microcentrifuge tube (0.6ml), they are ultrasonicated for 10 minutes using a sweep frequency ultrasonicator. 100µl of the sample is pipetted out into 100µl polymer capsules for measurement of concentration. At least three samples were taken from each suspension of nanowires. The number of nanowires in the suspension was calculated from the saturation moment obtained from the hysteresis loops, saturation moment of a single nanowire (415 emu/cc at room temperature, figure 5.17(a) inset) and the dimensions of nanowires obtained from SEM. Using magnetic stand, the nanowires in the 1.5 ml tube were collected at the walls of the tube and the DI water was aspirated. Next, calculated volume of DI water is added to the nanowires to make desired concentrations of nanowires. 100µl samples are once again taken from these concentrations of nanowires into polymer capsules and VSM measurements are taken on these samples to confirm that the concentrations desired match the measured values.

5.3.3 96-well plate MTS and toxicity assays

Primary macrophage cells were collected and pooled from C57/Bl6 mice by peritoneal lavage following 72 hours of thioglycollate elicitation. They were plated in 96 well plates at $5x10^5$ cells per well the night before in 10% FBS media and incubated at 37°C and 5% CO_2 overnight. This media is replaced with 80µl of RPMI containing 200ng/ml LPS for hours prior to adding the nanowire, which stimulates the cells to produce the inactive pro-form of IL-1β (pro-IL-1β) and the inflammasome component, NLRP3, thus priming them for IL-1β driven inflammatory cytokine secretion. The nanowires are titrated from the highest range that would be used in practice (for example, 1pM and below). This titration will account for a 1:5 dilution in RPMI when the samples are added to cells. Therefore, prior to adding to cells, solutions of 5, 1 and 0.2 pM, for example, will become 1, 0.2 and 0.04pM, respectively, when 20 µL of these solutions are added to cells already in 80µL of media in a 96-well plate. Nanowires were added at concentrations such that the ratio of nanowires to cells is 0:1, 1:1, 25:1, 50:1, 100:1 and 200:1. If the nanowires detected by cells as toxic particulates, and activate NLRP3 inflammasome, then they will cleave pro-IL-1β into active IL-1β and secrete it out of the cells into the supernatant. This supernatant is collected after 6 hours of incubation at 37°C with 5% CO_2. Cell death was assessed on the supernatants after 6 hours using MTS reagent using working wavelength of 490nm and background measurement at 650nm. MTS absorbance measurements were taken in nanoparticle-free supernatants. The supernatants are also analyzed by enzyme-linked immunosorbent assay (ELISA) quantitatively for the presence of IL-1β and TNF-α using a plate reader.

Osteosarcoma cells were plated in 96-well plates at a density of 15000 cells per well. The cells were incubated for 5 hours in serum-free media at 37^0C and 5% CO_2. Nanowires of different lengths (800nm, 3µm and 6µm) and different surface coatings (bare, PEG and RGD) were incubated with cells in triplicates at fixed concentrations of 100 nanowires to 1 cell for 6 hours and 18 hours in 200µl media and at 37^0C and 5% CO_2. After the incubation period, cells were washed 2x with PBS and were replaced in 100µl media. Cellular-metabolic activity was recorded by analyzing the supernatants using Promega cell-titer proliferation assay and fluorescence-based life technologies PrestoBlue cell viability reagent and associated protocols.

5.3.4 Immunofluorescence of nanowires

NH_2-PEG-FITC (0.1g) was dissolved in 50ml of 0.5M NaCl (pH 12) and dimethyl sulfoxide (DMSO). Ni nanowires, immersed in ethanol in a glass vial, were collected at the walls of the vial using the magnetic stand that applied a face field of 0.1T and field gradient of 20T/m. The ethanol was aspirated and the nanowires rinsed 3x with DI water. Next the nanowires were replaced in the PEG solution described above. The nanowires were ultrasonicated (sweep-frequency) 10 minutes for uniform distribution of nanowires in solution and to ensure the availability of PEG molecules to all nanowire surfaces. The sample was allowed to incubate for 24 hours at 4°C and ultrasonicated occasionally in between. Next, after aspirating the PEG solution, the nanowires were rinsed 3x with DMSO, 3x with PBS and immersed in PBS. 100µl of the ultrasonicated sample was pipetted onto a glass coverslip and was sandwiched using another glass coverslip on top. The sample was covered in foil to protect from light.

For detection of primary antibody and successful conjugation to the carboxyl group from the PEG, a secondary antibody-fluorophore conjugate was used. After pegylation of the nanowires, the nanowires were immunofunctionalized with a primary antibody such as mouse anti-EpCAM using EDC NHS coupling. A secondary antibody labelled with FITC fluorophore (such as FITC goat anti-mouse IgG) was used to target the primary antibody again using EDC-NHS coupling. After rinsing 3x with PBS, the functionalized nanowires were re-suspended in PBS. 100ul of sonicated sample was pipetted out onto a 1.5 glass coverslip and sandwiched on top by another glass coverslip. The sample was covered in foil to protect from light. Using FITC filter and a 63x oil immersion lens of Zeiss Axioplan 2 upright microscope, the nanowire samples were imaged for fluorescence. The fluorescence images were matched one to one with DIC images taken from the same microscope to confirm the presence of nanowires and a functional coating. For functionalizing just the Au segments of the nanowires, HS-PEG-FITC (NANOCS) was dissolved in DMSO: PBS (50:50 v/v) at a concentration of 1mM. The nanowires were immersed in this solution for 2 hours and were ultrasonicated once every 15 minutes for 2 minutes. The nanowires were separated using a magnetic stand and washed with DMSO, water and ethanol and then immersed in ethanol until imaged.

5.3.5 Fourier transform Infrared Microscopy (FTIR) of surface coating on nanowires

Pegylated nanowires (10 to 100 million range) were ultrasonicated in DI water and separated in a microcentrifuge tube using a magnetic stand. The nanowires were mixed uniformly with KBr salt using mortar and pestle. After thoroughly mixing the two

together, a 1cm diameter pellet of the mixture was formed using a screw and bolt. This pellet was studied in transmission mode in Nicolet Series II Magna-IR System 750 FTIR. Gain of 1.0, aperture 50 and moderate attenuation were selected for the beam parameters.

5.3.6 XPS of surface functionalized nanowires

Pegylated nanowires (10 to 100 million range) were ultrasonicated in 0.6ml DI water and 100µl of the suspension was titrated on a Si wafer and the sample was allowed to dry. The XPS measurements were performed on an SSX-100 system (Surface Science Laboratories, Inc.) equipped with a monochromated Al K_α X-ray source, a hemispherical sector analyzer (HSA) and a resistive anode detector. The base pressure of the XPS system was 6.0×10^{-10} Torr. During the data collection, the pressure was ca. 1.0×10^{-8} Torr. Because the sample was not sufficiently conductive, a low-energy electron beam (10 eV) was applied for charge neutralization. The X-ray spot size was 1 x 1 mm^2, which corresponded to an X-ray power of 200 W. The survey spectrum was collected at 150 eV pass energy and 1 eV/step. The high resolution spectra were collected using 50 eV pass energy and 0.1 eV/step. It should be noted that the high resolution of Ni 2p3/2 used 200 scans.

The atomic percentages were calculated from the survey spectra using the ESCA HAWK software provided with the XPS system. For high resolution data, the lowest binding-energy C 1s peak (presumably, C-C/C-H peak) was set at 285.0 eV and used as the reference for all of the other elements. The curve fitting used a combination of Gaussian/Lorenzian function with the Gaussian percentages being at 80% or higher.

5.4 Conclusions

In this chapter, it was shown that both aggregation and cytotoxicity related issues can be effectively resolved by employing a heterobifunctional PEG as surface coating on Au/Ni/Au nanowires using the novel chemistry presented.

The hydrophilic PEG layer evenly disperses the nanowires in suspension imparting them with a collective stability, as verified by VSM and spectrophotometry. This property allows repeatable titrations of nanowires in controlled biochemical experiments aimed at studying specific cellular responses. Further, conjugating the surface coating with natural proteins/peptides such as RGD enhances the biocompatibility of the nanowires. Finally, from all the variables tested including nanowire concentrations, lengths and surface coatings, it was concluded that the surface coating decides the biologically effective dose for nanowires with lengths ≤ 6 μm.

Chapter 6: RGD-functionalized nanowires exhibit enhanced cellular targeting and elicit specific cellular responses: therapeutic applications.

Besides issues related with cytotoxicity and aggregation, the major challenges in drug-delivery include specificity in targeting the tumor. The availability of the nanowires for drug delivery is determined by their ability to become membrane adherent and/or internalized by the cells [96,97].

Given the successful reduction of nanowire cytotoxicity with RGD functionalization (chapter 5), possible multivalent effects owing to the fibrous shape of the nanowire and the unique cell-targeting properties of RGD[98], the hypothesis in this chapter is to show that

(i) RGD-nanowires exhibit enhanced targeting of cells that express integrins.

(ii) RGD-nanowires elicit integrin-specific cellular responses.

(iii) The elicited cellular responses lead to uniform nanowire dispersion through increased cellular binding, internalization and proliferation.

(iv) Internalization and trafficking of nanowires followed by application of rotational magnetic fields to disrupt endosomes is an effective method to reduce tumor drug resistance. This idea can further be extended to disrupt acidic organelles called lysosomes in order to induce cell death, which is a desirable outcome in cancer cell targeting.

These are all important desirable pharmacokinetic properties in drug-carriers[5,7,97,99]. The biological interactions will help understand and eventually modulate cellular behavior for various therapeutic applications such as targeted drug-delivery and diagnostic imaging.

6.1 Theory

6.1.1 Targeting methods for drug delivery

Specificity in tumor targeting is achieved via active or passive targeting. In passive targeting, the size of the nanoparticle plays a vital role. Nanoparticles smaller than the fenestrations of endothelial cells can enter the interstitium of the tumor. Leaky vasculature and poor lymphatic drainage in the tumor result in the enhanced permeability and retention effect (EPR). The same EPR effect that nanoparticle engineers take advantage of also opposes the availability of nanoparticles within the tumor[5,7]. Thus, a more specific method for targeting the tumor is required. This is achieved via molecular recognition of receptors in the tumor using ligands attached to nanoparticle carriers. This method of targeting tumors is called active targeting.

6.1.2 Integrins and RGD:

Integrins belong to a class of transmembrane integral membrane proteins. These proteins span the thickness of the cell membrane and therefore, have domains on either end which interact with the cytosol intracellularly and the extracellular space on the other end[18]. These proteins can be either single spanning (figure 4.1 (c)) or multi-spanning (span the thickness of the membrane multiple times). The membrane-spanning domains of this protein are hydrophobic helices whereas the domains on either end of this protein

are hydrophilic globular structures[100]. One of these domains is facing the cytosol whereas the other is facing the extracellular space.

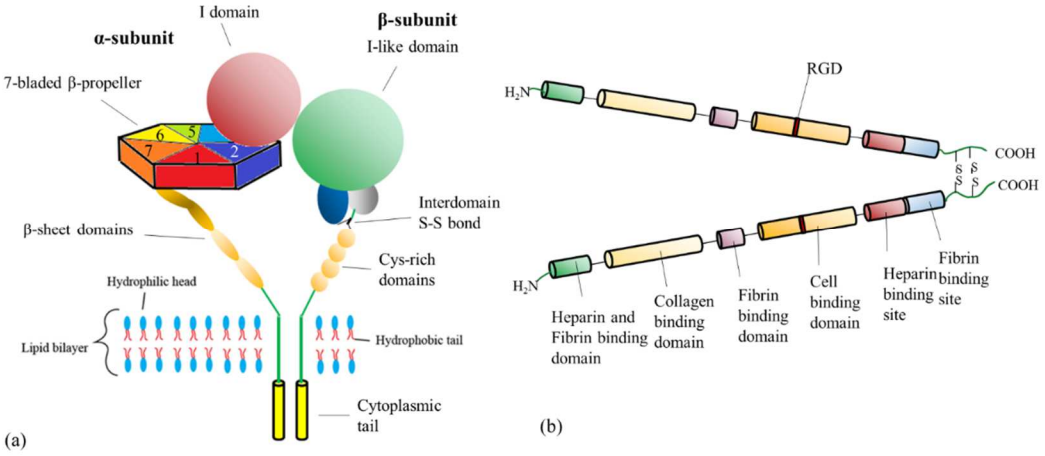

Figure 6.1. Integrins and RGD. (a) Schematic showing integrin structure, a heterodimeric transmembrane protein with two distinct sub-units: α and β-sub units. For complete description of structure, refer to [100]. (b) Schematic showing naturally occurring form of RGD on a fibronectin molecule. Fibronectin consists of two similar polypeptide chains joined together by a pair of disulphide bonds near the C-terminals. Each polypeptide chain is further made of distinct functional peptide units (depicted as colored cylinders) that bind to specific molecules in the extracellular matrix or to cells [100]. The RGD tri-peptide is indicated as a red unit that binds specifically to integrins.

Integrins are composed of two membrane spanning polypeptide chains called the α-chain and the β-chain, respectively. These chains are non-covalently linked to each other through hydrophilic/hydrophobic interactions. The structure of these units is depicted in figure 6.1a.The α and β chains both have short cytoplasmic domains and helix-shaped transmembrane domains. Using amino-acid analysis of the N-terminal of

the extracellular portion of the α-subunit, it is observed that this portion is composed of seven modules, where each module is further composed of 60 amino acids. These seven modules together form a sub-unit in the form of a flattened circular disk called the seven-bladed β-propeller. In half of the naturally existing integrins, the β-propeller is the binding site for extracellular molecules. The rest of the integrins have an extra module, called I domain, composed of approximately 200 amino acids and globular in shape. The I domain, which sits atop the β-propeller, serves as the binding site on the α-chain for the other half of naturally existing integrins. The β-chains are very similar in structure to the α-chains except that they lack the β-propeller unit. Also, in all cases of β-chains, an I-domain or I-like domain exists which serves as the binding site [100].

Integrins play a central role in mediating transmission of signals from the extracellular space to the interior of the cell. Such “outside-in” signaling is initiated by binding of ligands (like fibronectin or laminin in the extracellular matrix) to the extracellular domains of the integrins [100]. This binding induces a change in the conformation of the integrins which is propagated through the transmembrane domain to the intracellular cytoplasmic domain of the integrin. A conformational change in the cytoplasmic end of the integrin can alter the interactions of the integrin with the nearby intracellular proteins. This includes activating nearby cytosolic proteins and signaling cascades which can initiate a host of intracellular processes that can lead all the way to the nucleus. These signals can result in various cellular responses such as growth, division, motility, differentiation and cell death [101]which are observable at the cellular level using microscopy or cell-based assays.

Integrins also play a central role in mediating adhesion of cells to a substrate like the extracellular matrix. Several cytoplasmic proteins that bind to the cytoplasmic domain of the integrins act as adaptors linking the integrins to the actin filaments of the cytoskeleton[102]. Most extracellular materials that bind to the integrins (extracellular matrix materials like fibronectin, collagen and laminin) contain cell binding sites that contain the amino acid sequence arginine-glycine-aspartic acid, also called the RGD sequence[100] (figure 6.1(b)). This RGD segment binds to the I-like domain of the β-subunit of the integrin. The RGD-integrin bond is a highly specific bond. For this reason, it is also called a cell targeting peptide. This property of specificity can be exploited for drug-delivery applications.

6.1.3 Active targeting sites in the tumor

The growth of tumor and metastasis are mediated by angiogenesis, the development of new blood vessels. Angiogenic endothelial cells lining the tumor are a strong target for cancer therapy because they are accessible [8] and they highly express the $\alpha_v\beta_3$ integrins which can be selectively targeted using ligands like RGD. Resting endothelial cells in normal organs do not express these integrins as highly[98].

Thus, a nanoparticle platform, such as the multi-segmented nanowire, can be conjugated on one segment (e.g., Ni) with RGD for specific targeting. An anti-tumor drug, such as Paclitaxel [7][103], can be conjugated to the gold segment via a disulphide linkage that breaks in the reducing environment of the cell and releases the drug.

Radio-ligands have been attached to nanoparticles for *in vivo* nanoparticle tracking [104]. By using a magnetic material such as Ni or Fe as the nanoparticle platform, we have eliminated the need for attaching an extra radio isotope. Instead, the

magnetic properties of the nanowire can be exploited for diagnostic imaging by coupling it with existing technologies in the clinic such as MRI.

6.1.4. Endocytosis mechanisms and intracellular trafficking

Following active targeting of molecular markers on targeted cells, tumors or organs, effective drug delivery often requires intracellular delivery of the drug and release into the cytosol and/or translocation to the nucleus. This is because the targeted molecule is not always localized on the cell membrane. Thus, the efficacy or bioavailability of the drug, in many cases, is influenced by the efficiency of endocytosis and controlled trafficking to specific organelles within the cell.

For nanoparticle-drug conjugates, the efficiency of endocytosis is dependent on the physicochemical attribute of the nanoparticle carrier including size, shape, surface charge, ligands attached to the surface as well as cellular phenotype and the microenvironment. Endocytosis is defined as the general mechanism of internalization of macromolecules and particles into transport vesicles within the cells, which are derived from the plasma membrane[105]. It can proceed via the following pathways[106] (figure 6.2):

1) Phagocytosis: Internalization of solid particles including bacteria by specialized cells such as macrophages, monocytes and neutrophils (analogous to cell “eating”).

2) Pinocytosis: Fluid-phase uptake of extracellular molecules and solutes (analogous to cell “drinking”). Pinocytosis can further be classified into the following sub-types:

(i) Macropinocytosis: Trapping of large pockets of fluid (> 1 μm) by formation and enclosure of membrane protrusions.

(ii) Clathrin-mediated endocytosis: Concentration of transmembrane receptors and bound ligands in coated pits (~ 120 nm) on the plasma membrane formed by assembly of cytosolic proteins such as clathrin.

(iii) Caveolae-mediated endocytosis: Flask-shaped invaginations (~ 50–60 nm) in the cell membrane that mediate uptake of extracellular molecules into the cell by specific receptor binding.

(iv) Clathrin and Caveolae independent endocytosis: This includes raft-mediated endocytosis. Rafts are small structures (40-50 nm) on the cell membrane which sort membrane proteins and glycolipids on the membrane surface.

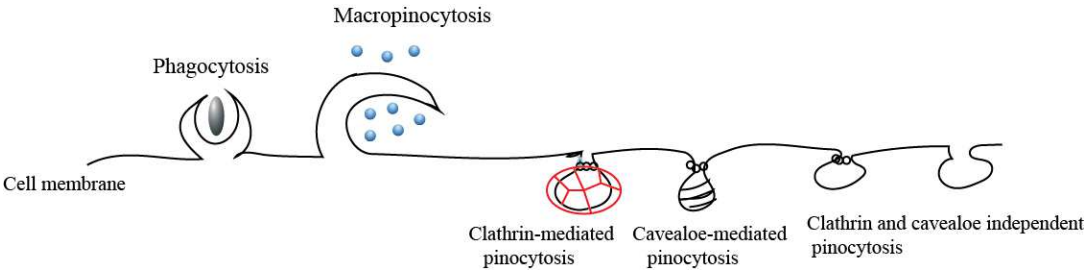

Figure 6.2: Schematic summarizing the main endocytosis mechanisms in a cell[106].

The endocytotic cycle starts with receptor-mediated internalization or non-specific phagocytosis of ligand by the cell at the membrane followed by entrapment of receptor-ligand complexes in endosomes (intracellular membrane-enclosed compartments)[107] (figure 6.3). The receptors and ligands can be sorted within endosomes and subsequently recycled to the cell membrane or trafficked to lysosomes (intracellular acidic compartments) for degradation (this can be done via trafficking or

fusion of endosomes with lysosomes). These late endosomes are often localized in the perinuclear region (region surrounding the nucleus).

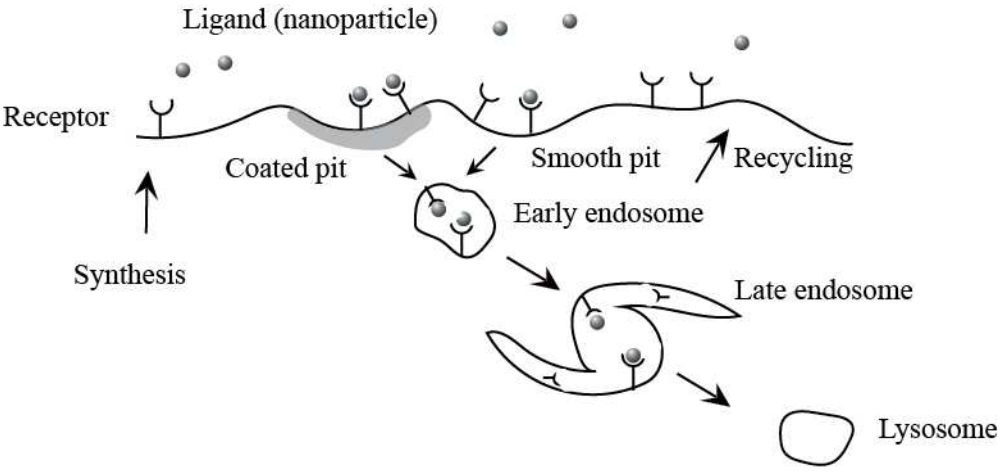

Figure 6.3: Schematic depicting intracellular trafficking of nanoparticles (or receptor-ligand complexes) following endocytosis[107].

6.1.5 Cells death mechanisms

Eucaryotic cells can often identify the physical or biochemical damage (e.g. damage to DNA by alteration of the structure) caused to its organelles. If this damage is large or irreversible, the cells can undergo programmed cell death. Essentially, this means that if the cells cannot repair the damage, they commit suicide by activation of specific intracellular biomolecular pathways[108].

One such mechanism of programmed cell death is called apoptosis. Apoptosis is important in cellular processes as it eliminates damaged and unwanted cells which are competing with healthy cells for nutrients. Some of the characteristic features of apoptotic cells include cell shrinkage or condensation, disintegration of nuclear envelope, collapse of cytoskeleton, blebbing of cell surface, condensation of nuclear chromatin and

breaking up of the cell into smaller membrane enclosed compartments called apoptotic bodies [18]. This process of cell death is controlled and results in neatly packaged and contained bodies that can be ingested by immune cells and cleared from the system thus avoiding an inflammation. As apoptotic cells undergo biochemical changes, they can be detected using fluorescence microscopy or FACS by staining the cells with fluorescent markers [18]. Detection of apoptotic osteosarcoma cells using FACS was shown in figure 5.21.

An alternate, more violent pathway of cell death is called necrosis. This generally results from a more traumatic factor such as acute physical damage or sudden cutoff of nutrients, oxygen or blood supply. This is characterized by swelling and bursting of cells and spillage of cellular contents in the microenvironment. This generally results in an inflammatory response, if it occurs inside an animal [18].

6.1.6 Cells distribute DNA content as well as intracellular organelles among daughter cells

Cells reproduce through a process called mitosis, where each cell divides into two daughter cells distributing its nuclear chromosomal content equally between the daughter cells. This process is also accompanied by distribution of other intracellular cytosolic organelles and contents which cannot be synthesized *de novo* (e.g. mitochondria) within the cells [18].

6.2 Results

The plan adopted to prove the hypothesis in this chapter is to

(i) Incubate a fixed concentrations (effective concentration of 100 nanowires/cell or 10.5µg/ml, as determined from studying macrophages in chapter 5) of bare nanowire, PEG-functionalized nanowires and RGD nanowires separately with osteosarcoma cells. (ii) Using time-lapse confocal fluorescent + DIC microscopy, observe real-time cellular targeting, cellular responses and spatio-temporal distribution of RGD-nanowires.

6.2.1 RGD-nanowires show enhanced cell targeting and induce specific cellular responses

Canine osteosarcoma (OSCA-8) cells, which present a high density of integrins [109,110], were incubated with 3µm long RGD-nanowires at concentrations of 100 nanowires/cell, and time-lapse (18 hour) phase contrast/fluorescence microscopy was used to evaluate the nanowire-cell interactions.

As seen in figure 6.4(a), for an initial concentration of 100 RGD-nanowires per cell, approximately 68% of the cells had membrane-adherent and internalized nanowires at the end of the 18 hour time lapse. As a control environment, PEG-nanowires with the same initial concentration of 100 nanowires per cell, were membrane-attached and internalized by only approximately 32% of cells. The membrane-attached PEG nanowires were also loosely adhered to the cells as can be seen through the time-lapse. Most of the remaining titrated nanowires were observed in the extracellular space in the cell culture dish. These data were taken from time-lapse movies. The enhanced targeting of RGD nanowires compared to PEG nanowires implies that for the same titrated concentrations, the therapeutic efficacy of the RGD nanowire is more than double compared to PEG nanowires. In other words, the IC_{50} (half maximal inhibitory concentration)[96] of the drug is reduced because of enhanced targeting.

Within 1-2 hours of incubation, osteosarcoma cells began internalizing RGD-nanowires, indicated schematically and by red arrows in figure 6.4(b). The internalized RGD-nanowires were enclosed in vesicles, as is typical with endocytotic membrane transport (figure 6.3). Consistent with current models, following receptor-mediated endocytosis and endo-lysosomal fusion, many nanowires accumulated in the perinuclear region within 8 hours of incubation. This perinuclear accumulation is in agreement with published studies [111,112]. Z-sections obtained from confocal and DIC microscopy (figure 6.4(b)), showing nanowires enclosed in a plasma membrane (red) and surrounded by lysosomal compartments (green), further confirm internalization and intracellular trafficking of nanowires. Internalization in the PEG-nanowire case, however, was mediated by weaker non-specific interactions, and vesicles were barely observed after PEG-nanowire incubation.

Uniformity in nanowire dispersal was further facilitated through enhanced cellular proliferation upon incubation with RGD nanowires (figure 6.4(c)). The cells proliferated such that nearly 100% confluence was reached midway through the time-lapse. Specifically, 10.8% of the cells were observed to divide while only 2.28% of the cells died within the 18-hour time-lapse (in serum-free media). The enhanced cellular proliferation led to an increased cell density (35.5±6%), as seen in (figure 6.4(d)). In contrast, when incubated with PEG-nanowires, only 4.7% of the cells were observed to divide while 9.6% died (in serum-free media), and the cells were largely immobile over the 18-hour time-lapse. The cell density only increased by 15.6±8.3% (compared to

20.6±9.6% for media-only cultures). Further, the PEG-nanowires in extracellular spaces prevented any cell motility across those void areas.

Without active dispersal of RGD-nanowires, a 35.5% increase in cell density from start to end of the time-lapse would have reduced the percentage of cells with targeted RGD-nanowires to 46.7%. Instead, we observe 68% of the cells with targeted RGD-nanowires after 18 hours. Therefore, the RGD-nanowire-induced dispersal by cell proliferation alone improves the effective distribution by almost 23%. In the PEG-nanowire case, a 15.6% increase in density over the 18-hour time-lapse would have reduced the percentage of cells with available PEG-nanowires to 29.4%. The observed percentage of cells with targeted PEG-nanowires after 18 hours was 29.9%, almost the same as calculated value. This suggests that, in the PEG-nanowire case, there is no continuing dispersal due to cell proliferation. Overall, compared to PEG-nanowires, the dispersal induced by RGD-nanowires was 32.2% (adherence and internalization) plus 22.2% (proliferation), or 54.4% (factor of 1.544) higher.

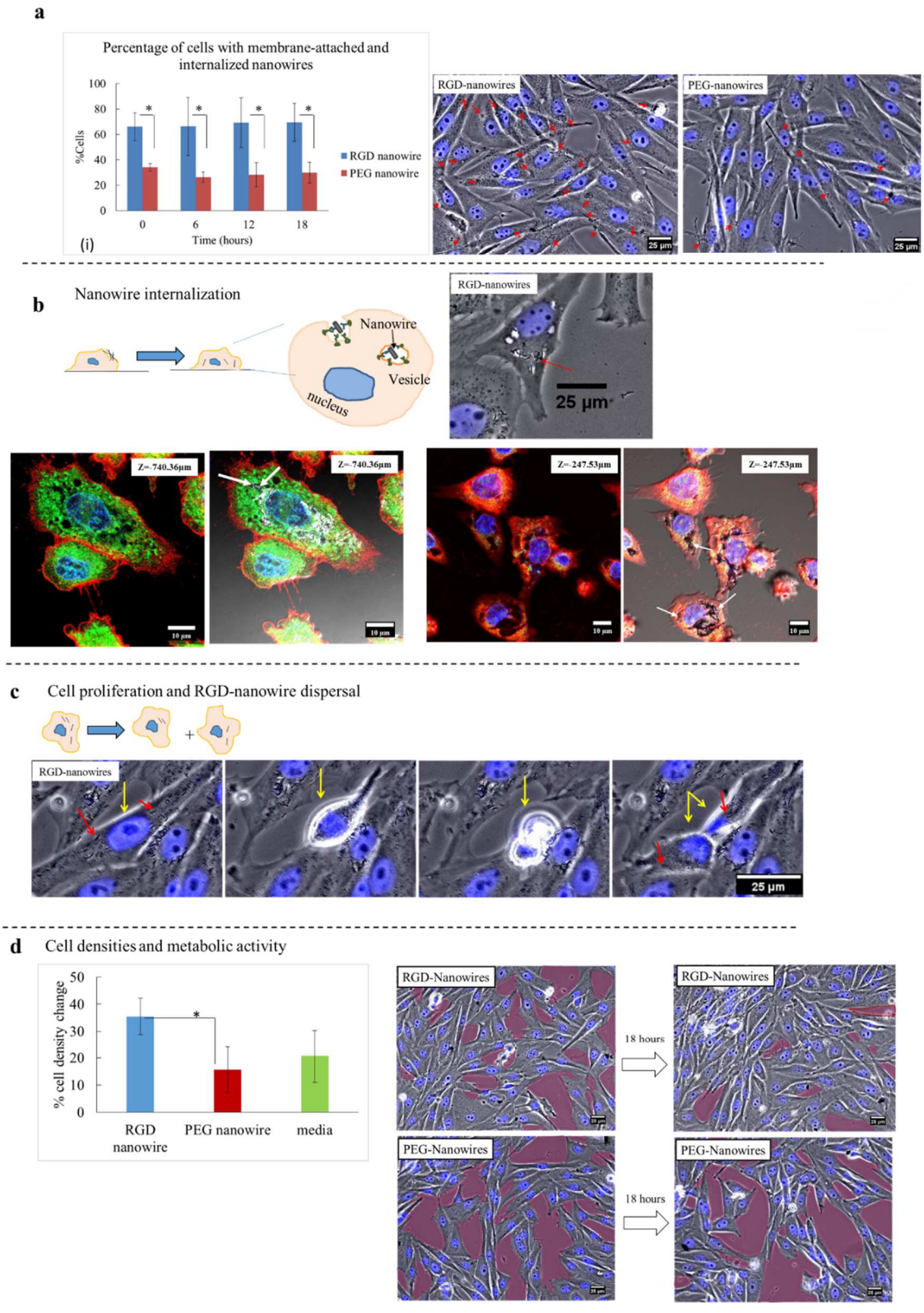
a
Percentage of cells with membrane-attached and internalized nanowires
%Cells
Time (hours)
RGD nanowire
PEG nanowire
(i)
RGD-nanowires
PEG-nanowires
b
Nanowire internalization
Nanowire
Vesicle
nucleus
RGD-nanowires
25 µm
Z=-740.36µm
Z=-247.53µm
c
Cell proliferation and RGD-nanowire dispersal
RGD-nanowires
25 µm
d
Cell densities and metabolic activity
% cell density change
RGD nanowire
PEG nanowire
media
RGD-Nanowires
PEG-Nanowires
18 hours

Figure 6.4. Specific targeting of osteosarcoma cells with RGD-nanowires and elicitation of specific cellular responses(*). (a) Distribution of nanowires through integrin-specific (RGD-nanowires) and non-specific targeting (PEG-nanowires). The histogram shows a higher percentage of targeted cells with RGD-nanowires through the time lapse compared to PEG-nanowires. Examples of images used to acquire this data are also shown. Red arrows show bound and internalized nanowires. Data was collected from three 18-hour time-lapse videos for each case. (b) Internalized nanowires are primarily encapsulated by vesicles. This can be seen in numerous cells throughout the time-lapse, supplementary video 1. 4-channel confocal and DIC microscopy images are included for the 3μm RGD nanowire case after 10 hours incubation at 37^0C and 5% CO_2. The cell-membrane is stained red (CellMask plasma membrane stain), lysosomes stained green (lysosensor green) and nucleus stained blue (Hoechst 33342). Arrows indicate nanowires enclosed in the cell membrane and surrounded by lysosomes. Z-section analysis and more samples are included in figure 6.7. (c) Nanowire dispersal is further facilitated through cell-proliferation. A cell (yellow arrows) with nanowires detaches from the substrate, divides, and daughter cells adhere back to the substrate, each containing nanowires. Cell division was observed frequently throughout the time-lapse. (d) As observed, the RGD-nanowires contributed the highest increase in cell density with 18 hours elapsed time. (*) indicates $p<0.05$. The greater cell density change in the RGD-nanowire environment is clearly visible by comparing void spaces (marked magenta) in time-lapse images acquired at the start and end of the 18 hour time-lapse experiment.

Figure 6.5 shows the disaggregation and dispersal of long RGD-nanowires (6 μm) in real time. Here, a specific x-y focal plane at a fixed z-height with respect to the culture-dish, was imaged over the time-lapse. For each time-lapse image, using MATLAB, the number of black pixels, corresponding to nanowires or nanowire clusters along the y direction, were calculated keeping x constant. Thus, a nanowire-pixel count was obtained for each x in the x-y plane which was plotted as normalized pixel count (normalized with respect to total nanowire pixels in the image) vs x (figure 6.5(c)). Alternating sharp peaks and valleys are seen in this profile at the beginning of the time lapse. These correspond to nanowire aggregates (from dipole-dipole interactions), as seen, distributed unevenly throughout the captured x-y-plane. Towards the end of the 6-hour time lapse, we observe less pronounced and less frequent peaks and valleys in the profile. The waveform in this plot, in essence, flattens over the recorded time showing nanowires spread more uniformly across the cell culture compared to the initial time-

point recorded.

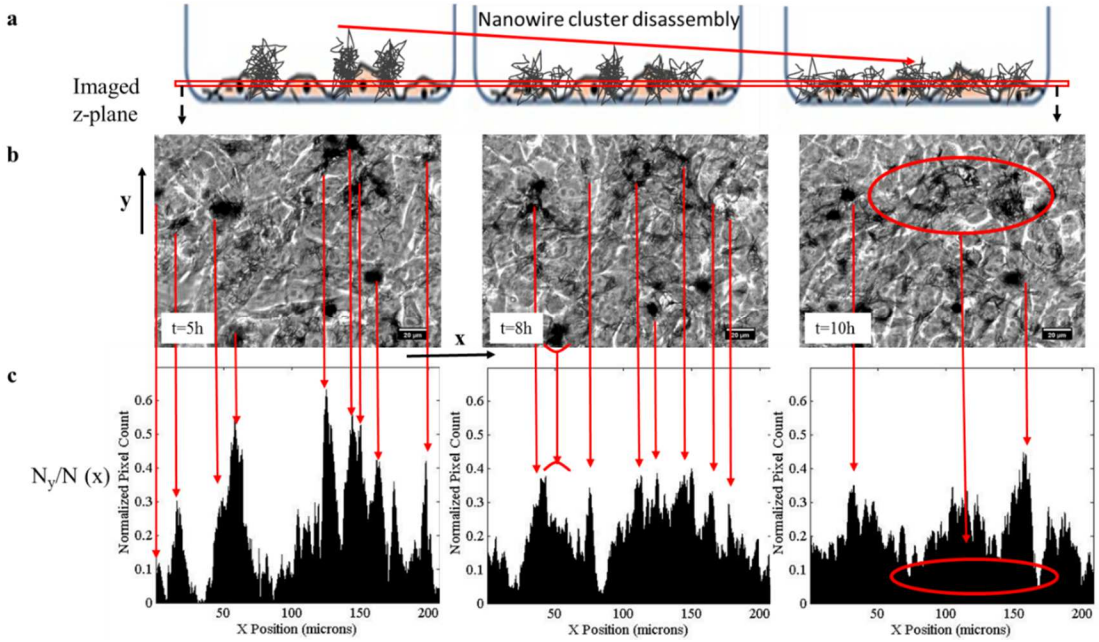

Figure 6.5**:** Disassembly and dispersal of long RGD-nanowires (6μm) and nanowire aggregates in real time(*). (a) Schematic showing dispersal of RGD-nanowires in cell-culture over the elapsed time. The red box indicates the imaged x-y plane at a constant z-height above the cell-culture substrate.

(b) Phase contrast top-down image of the x-y plane under focus (constant-z) in cell culture over the elapsed time. N is the total number of black pixel count in the image corresponding to the nanowires. N_y is the total number of black pixels corresponding to the nanowires along the y-direction for a constant x. (c) Normalized pixel count N_y/N is plotted as a function of x. As the time-elapsed increases from 5 hours to 10 hours, the incidence of high peaks and deep valleys in the plot decreases and the waveform overall flattens indicating dispersal of black pixels corresponding to nanowires across the x-y plane.

In contrast, figure 6.6 shows Osteosarcoma cells incubated with long PEG-nanowires under identical conditions. Nanowire and cellular positions remain relatively unchanged over the time-lapse in this case. This experiment further underscores the importance of time-lapse imaging to capture nanoparticle-cell interactions which would otherwise, get averaged in standardized plate-reading assays.

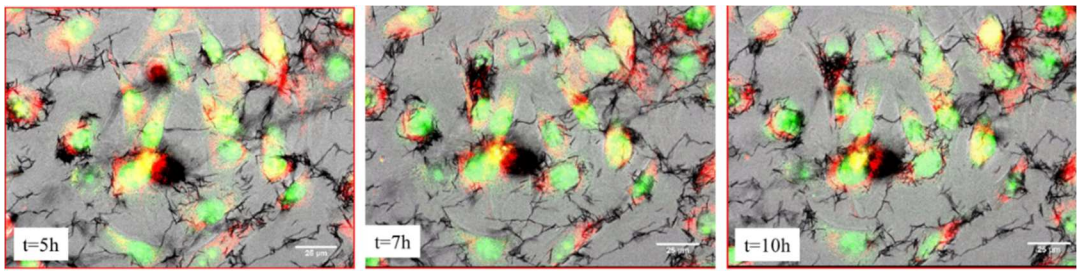

Figure 6.6(*): Time-lapse fluorescent/phase-contrast images showing 6µm PEG-nanowires incubated with osteosarcoma cells. In contrast to figure 6.4, the nanowires and cells mostly retain their positions over the elapsed time. Almost no dispersal or disassembly of nanowires is observed through the time lapse.

Some bare nanowires were shown in chapter 4 to have phagocytosed by OSCA-8 cell line. These nanowires were observed mostly in the cytosolic region and some inside vesicles. The absence of ligands on the nanowire surface suggested that this internalization was non-specific, in agreement with theory [111]. In this study, compared to the RGD nanowires, internalization of PEG nanowires was less frequent as indicated by fewer vesicles, lower incidence of localization in the perinuclear region and a larger fraction of nanowires either on the surface of the cell or in the extracellular space. This agrees with other work on quantum dots [112] that the effect of PEG is to diminish

internalization. The very limited internalization of PEG nanowires is most likely through pinocytosis (non-specific) [112]. Here, data showing a high fraction of cells internalizing RGD nanowires, as indicated by larger number of vesicles, perinuclear accumulation and results from confocal microscopy, is coherent with existing literature on increased internalization rates of RGD functionalized materials [113][98].

Differences in cell proliferation and cell densities can be explained by the differences in adhesiveness presented by the ligands on the nanowire surface. It is well known that DNA synthesis and cell growth are regulated by cell shape for anchorage-dependent cells [114,115]. Further, cell shape is influenced by the adhesiveness of the microenvironment of the cells [114]. PEG-nanowires present a microenvironment which limits cell adhesion [86]. As is seen in the relatively large and unchanging gaps (called wounds in literature [116]**)** in figure 6.4(d), this microenvironment comprised of PEG nanowires constrains the spreading of the cells. This limits DNA synthesis and down-regulates cell growth. As a result, we observe a small relative change in densities compared to the RGD-nanowire case. Our results indicate that interactions between the cell-adhesive RGD ligands on the nanowire surfaces and integrins on the osteosarcoma cells promote spreading of the cells and hence up-regulate cell proliferation and growth. Such enhanced cellular responses with RGD-nanowires can also be due to possible multivalent interactions between the RGD ligands on the nanowire surface and the integrins. Multivalent interactions include simultaneous cell-membrane receptor aggregation and occupancy of receptors by ligands [5,117,118]. There is a higher chance of multiple ligands interacting with integrins simultaneously in the case of a nanowire

compared to a nanosphere, because geometry allows juxtaposition of ligands on the cylindrical nanowire surface. Our future work focuses on quantifying and comparing multivalent cellular interactions in the case of nanowire versus nanosphere.

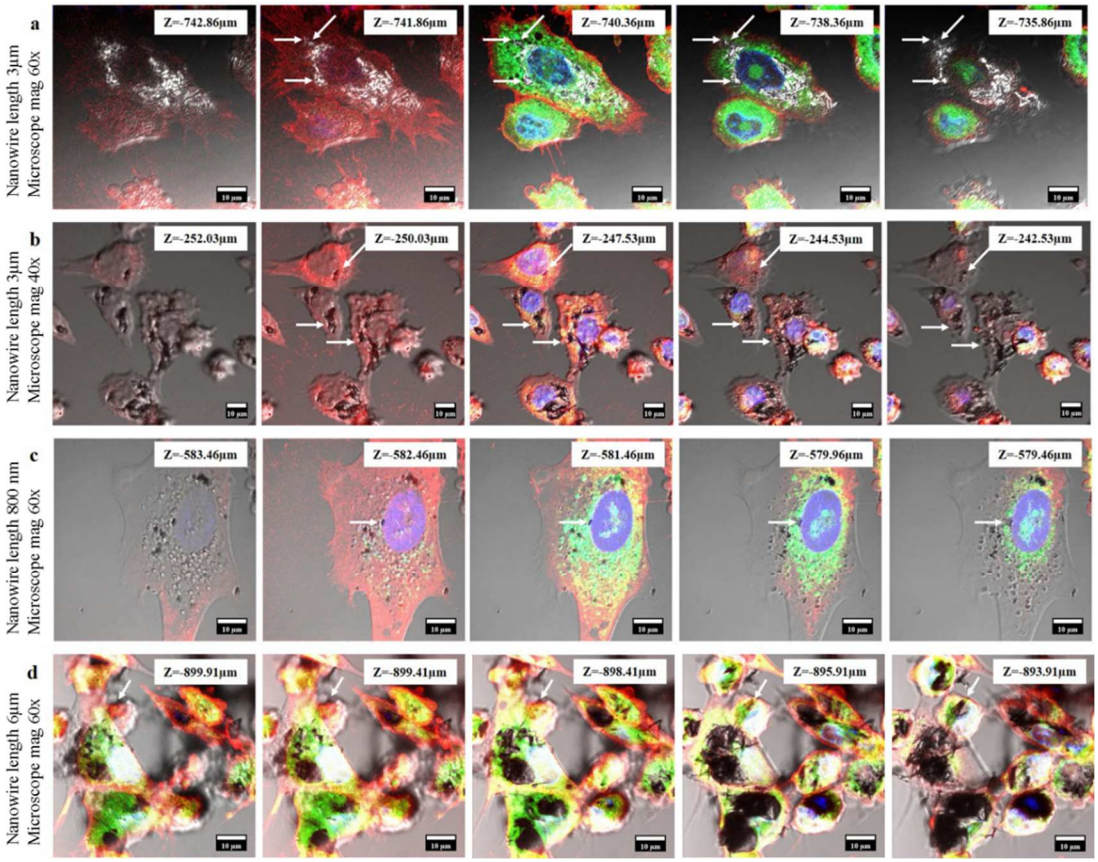

Figure 6.7: Cellular z-sections using 4-channel confocal microscopy. Osteosarcoma cells were incubated with nanowires of different lengths and surface functionalization at a concentration of 100 nanowires to 1 cell for 10 hours at 37^0C and 5% CO_2(*). The cells were stained with cell-mask plasma membrane stain (red), lysosensor green for lysosomes and Hoechst 33342 nucleic acid stain (blue). Arrows indicate internalized nanowires of

interest. As the marked nanowires, imaged using DIC, are brought into focus by increasing z (the nanowires are sharpest for one focal plane), confocal fluorescent microscopy shows that the nanowires are enclosed in the cell membrane (red) and surrounded by lysosomes. Note that there are other nanowires inside the cell and on the cell membrane which become visible as the z value changes. (a) Internalized 3μm RGD-nanowires in osteosarcoma cells at 60x magnification. Z=-740.36μm is the focal plane where the marked nanowires have the sharpest image and are in focus. (b) Internalized 3μm RGD-nanowires in osteosarcoma cells at 40x magnification. Z= -247.53μm is the focal plane where the marked nanowires have the sharpest image and are in focus. (c) Internalized 800nm RGD-nanowires in osteosarcoma cells at 60x magnification. (d) Largely membrane bound and internalized/semi-internalized 6μm long RGD-nanowires in osteosarcoma cells at 60x magnification.

6.2.2 Intracellular trafficking of nanowires

Nanowires are observed within (i) intracellular vesicles (figure 6.4(b)), (ii) within the cytosol (not enclosed by compartments) as confirmed by z-sections from confocal microscopy (figure 6.7) as well as (iii) observed to be localized in the perinuclear region after extended incubation times (24 hours) as evidenced by DIC imaging (figure 6.8). This perinuclear accumulation can be exploited for delivery of drugs to the nucleus [96].

Due to their longer lengths (800 nm to 6 μm), endocytosis of nanowires occur via two main pathways in parallel: phagocytosis and macropinocytosis. Both these mechanisms can be receptor-mediated or non-specific depending on receptor-binding to

the membrane surface or non-specific adsorption of nanowires. Generally, receptor-mediated processes show higher incidence of targeting, internalization and trafficking [ref]. Consistent with theory, differences in spatial distribution (bio-distribution) of nanowires are observed in RGD-nanowires (specific) and PEG-nanowires (non-specific). Specifically, a higher cell targeting efficiency of RGD-nanowires leads to a higher internalization of nanowires in the RGD-nanowire case.

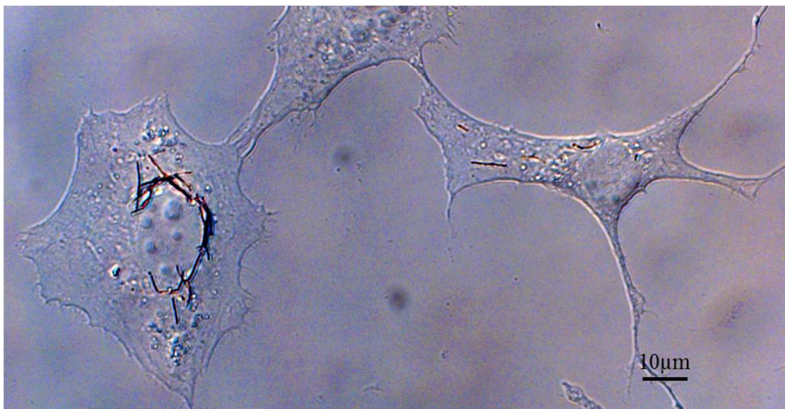

Figure 6.8: DIC image showing intracellular perinuclear accumulation of nanowires following endocytosis.

6.2.3 Disruption of endosomes using spinning nanowires:

Sequestration of chemotherapeutic drugs in endosomes and acidic compartments is responsible for "more than 40% of tissue drug uptake" [119,120]. Once entrapped in acidic endosomes (pH ~ 6), the drugs are acted upon by degradative enzymes and thus, loose their therapeutic properties over time. As observed in figure 6.4, nanoparticle-carriers are often localized within endosomes following endocytosis. To develop more effective drug-carriers and vaccines against infectious diseases and cancer, it is important to facilitate endosomal escape and translocation of the drug to the cytosol [96,121].

One way to achieve endosomal escape is by physical disruption of the endosomal membrane in order to release its contents into the cytosol. Natural toxins such as diphtheria and anthrax operate on this principle [96].

This can be achieved artificially using magnetic nanowire drug-carriers. If a low frequency rotational magnetic field is applied to the ferromagnetic Au/Ni/Au nanowires, they will rotate about the center of the nanowire length as shown in figure 6.9. This motion will agitate the endosomes and eventually physically disrupt the endosomal membrane within minutes.

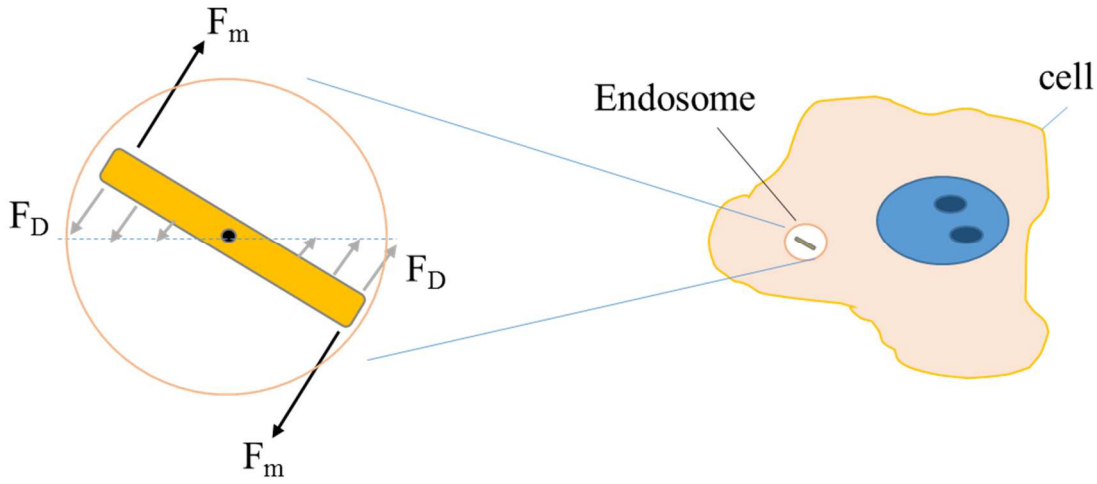

Fig 6.9 shows basic principle of rotation of nanowires entrapped in intracellular endosomes. F_m is the force exerted by the rotational magnetic field on the poles of the nanowires. F_D is the drag force exerted on the nanowire by the aqueous endosomal contents.

The lag angle of the nanowire with respect to the driving field and maximum speed of the nanowire without losing synchronization can be calculated using

$\theta_l = \sin^{-1}[(\eta L^2 C\omega_H)/3M_s r^2 H]$ [122]

$\omega_{w,\,max} = 3M_s r^2 H/\eta^2 LC$ [122]

where, θ_l = lag angle between the field and the nanowire easy axis

η = dynamic viscosity of fluid ~ 0.89mPa/s

L = length of nanowire = 3 μm

C = geometric constant ~ 0.15 [122]

ω_H =driving field speed

M_s = saturation magnetization of Ni = 415 emu/cc

r = radius of nanowire = 50 nm

H= driving field ~ 20 x 10^{-4} T

As long as the driving field speed is below $\omega_{w,\,max}$, the nanowires will rotate synchronously with the field.

Replacing these values in above equation, we find

For 3 μm Ni nanowires,

$\theta_l = \sin^{-1}[(\eta L^2 C\omega_H)/3M_s r^2 H] = 0.2$ radians = 11.45^0

$\omega_{w,\,max} = 3M_s r^2 H/\eta L^2 C = 5181$ rad/s ~ 49480 rpm . Thus, the driving field is well below the synchronous limit of the nanowire. Thus, it is reasonable to assume that the nanowire rotation speed = driving field speed with a lag angle of 11.45^0.

Figure 6.10 shows entrapped nanowires in human lung carcinoma A549 cells, obtained by an overlay of reflectance and fluorescence microscopy using a multiphoton

upright confocal microscope.

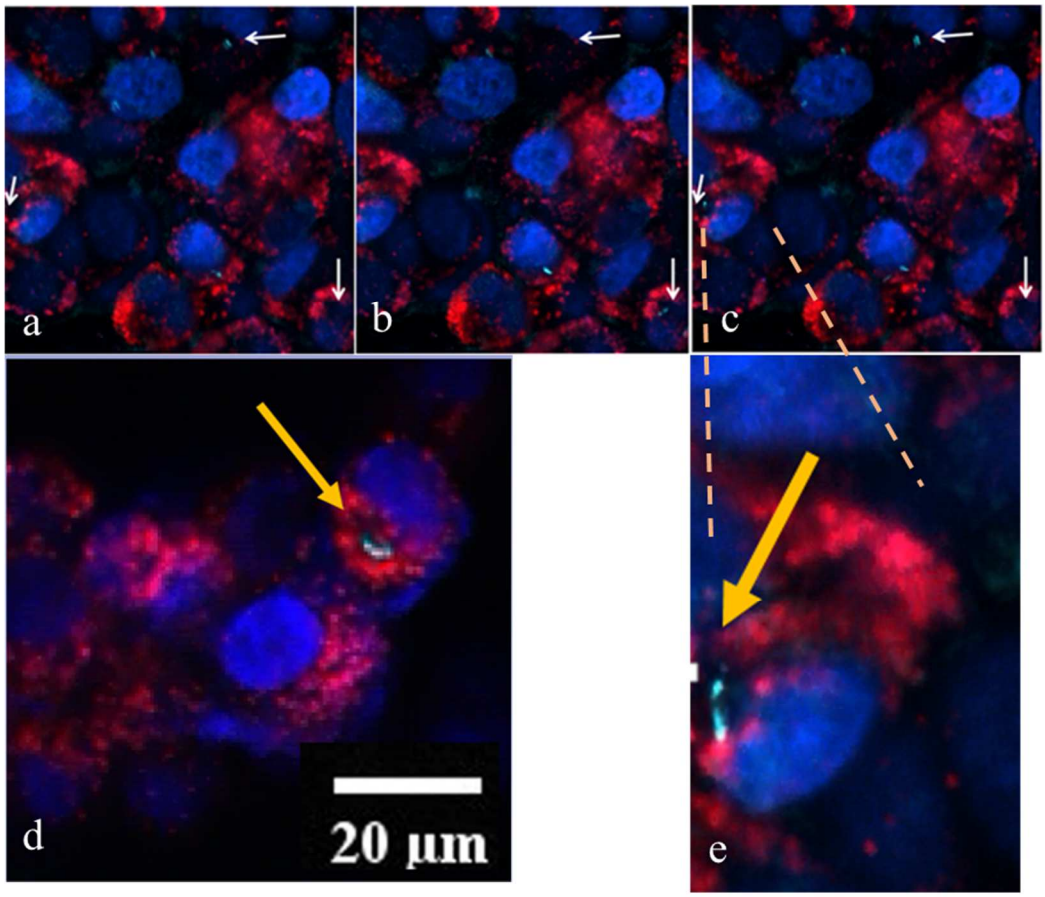

Figure 6.10. Time-lapse confocal microscopy capturing rotation of nanowires entrapped in intracellular endosomes. (a,b & c) Sequence of images acquired through time-lapse confocal + reflectance microscopy showing movement/ rotation of magnetic nanowires (indicated by the arrows) in response to a rotating magnetic field. The nanowires are marked cyan in color (from reflectance signal). The cell nucleus is stained with hoecsht 33342 blue nuclear stain and lysosomes are labelled with red fluorescent marker, lysotracker red. (d) shows nanowire entrapped in endosome surrounded by red lysosomes. This is a late endosome that fuses with lysosomes for degradation of endosomal components. (e) Zoomed in portion of the sample in (c) showing nanowire.

An evaluation of viability using MTS assay before and after spinning endosome-entrapped 3 μm long nanowires at driving field speed of 177.5 rpm for 5 minutes shows a very small change in viability (figure 6.11(a)). To characterize disruption of endosomes, pH-sensitive dyes (acridine orange and lysosensor green) were used to monitor changes in pH associated with endosomal rupture. When Acridine orange binds to DNA, it has an excitation maximum at 502 nm and emission maximum at 525 nm (green). When acridine orange is engulfed in acidic compartments, excitation maximum shifts to 460 nm and emission maximum shifts to 650 nm (red). Thus, this property of acridine orange can be used to simultaneously image lysosomes and the cell using two excitation wavelengths.

As depicted in figure 6.11(b), when cells are stained with acridine orange, acidic compartments fluoresce red whereas other organelles fluoresce green. Following 9 hours of incubation, a high concentration of red fluorescing vesicles are observed in A549 lung carcinoma cells before the nanowires are rotated. After rotation of nanowires for 2 minutes at 236 rpm(at a dose of 10 nanowires to 1 cell), the red fluorescence, characteristic of acidic compartments diminishes (figure 6.11(b)). This was further corroborated using multi-well plate assays and a sensitive pH-indicating dye, lysosensor green. This dye stains acidic compartments in OSCA cells green. After 9 hours of incubation, the nanowires were rotated at 177.5 rpm for 5 minutes. Using a fluorescence plate reader, the fluorescence from acidic compartments was recorded before nanowire rotation and one hour after nanowire rotation. Also, fluorescence was recorded from cells

where nanowires were incubated with cells for 10 hours without rotation (figure 6.11(c)). The data indicates reduction of fluorescence 1 hour after rotation of nanowires. The small reduction in green fluorescence can be attributed to low sensitivity of the dye to endosomal density (pH ~6) as opposed to lysosomal density (pH ~ 5). The sensitivity of the dye falls as the pH diverges from pH 5. Nevertheless, a change in pH is observed which correlates with nanowire rotation suggesting disruption of endosomes.

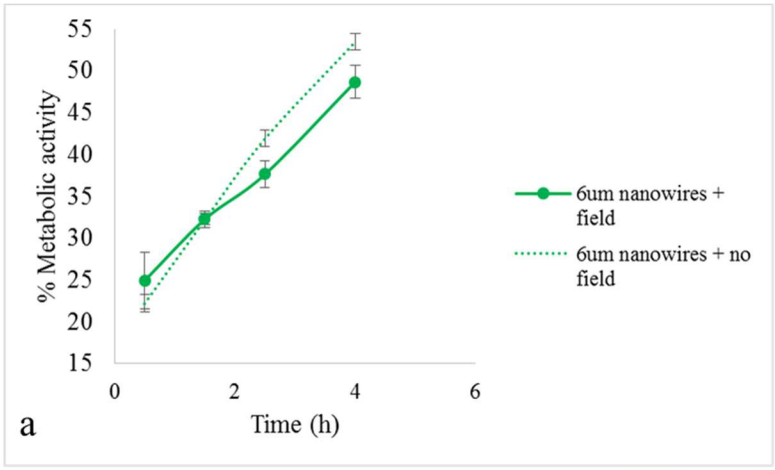
55
50
45
40
35
30
25
20
15
% Metabolic activity
0
2
4
6
Time (h)
6um nanowires + field
6um nanowires + no field
a

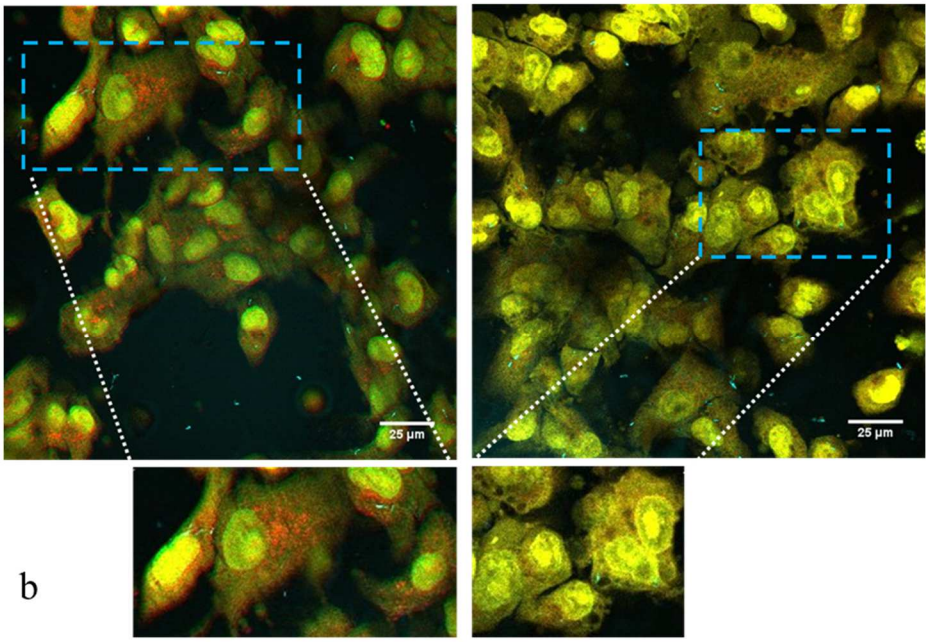
25 µm
25 µm
b

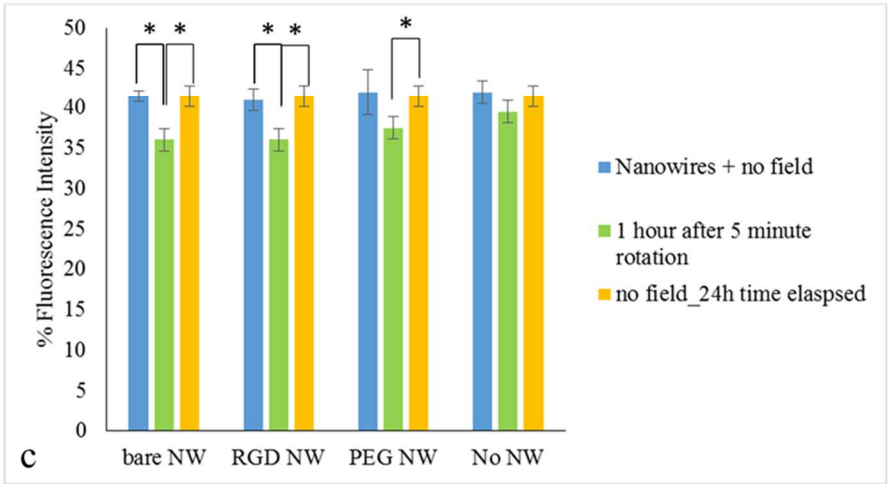
50
45
40
35
30
25
20
15
10
5
0
% Fluorescence Intensity
* *
* *
*
bare NW
RGD NW
PEG NW
No NW
Nanowires + no field
1 hour after 5 minute rotation
no field_24h time elaspsed
c

Figure 6.11 Effects of nanowire rotation on cellular metabolic activity and cellular organelles. (a) Metabolic activity of osteosarcoma cells evaluated using MTS assay for two cases: (i) rotating nanowires at 177.5 rpm for 5 minutes following 6 hour of incubating cells with nanowires (nanowires: cell = 100:1) (ii) control- no magnetic field applied. Note that the optimal measurement for an MTS assay starts at 3 hours after adding the reagent. This explains barely any change in response below 2 hours. (b) Acridine orange stained A549 lung carcinoma cells imaged before and after nanowire rotation. The cells were incubated with nanowires at a ratio of 10:1 nanowires: cell for 9 hours at 37^0C and 5% CO_2. The nanowires were rotated at 233 rpm for 2 minutes and images were recorded using overlay of confocal microscopy and reflectance microscopy. (c) Lysosensor green assay evaluating green fluorescence emission from acidic endosomes and lysosomes in osteosarcoma cells before and after rotation of nanowires. The nanowires were rotated at 177.5 rpm for 5 minutes.

This idea of endosomal disruption can be extended to other cellular organelles such as lysosomes. The permeabilization and rupture of lysosomes results in release of enzymes such as cathepsins into the cytosol[121,123]. This results in cell death through caspase dependent or caspase independent mechanisms[124,125]. Induced cell death through this technique works around the defects in classic apoptotic pathways to which cancer cells may have acquired resistances. Moreover, many chemotherapeutic anti-cancer drugs rely on DNA damage and a p53 (tumor suppressor gene) dependent pathway for apoptosis. However, this gene is mutated in several tumors (“more than 50 %

[125]"), leading to tumor drug resistance. Thus, a p53 independent path is required. Thus, lysosomal targeting and disintegration provides an alternative pathway. Finally, transformed/immortalized cells show higher susceptibility to lysosomal membrane permeabilization based death. Thus, this technique has many advantages.

6.3 Methods:

6.3.1. Time-lapse phase contrast/fluorescence microscopy

For 18-hour time-lapse video recording of osteosarcoma cells with nanowires, Nikon biostation IM phase contrast and fluorescence microscopy was used to image the cells in chambers of the ibidi 4-chamber μ-dish. Stained osteosarcoma cells were plated in all the chambers at a loading density of 0.3 million cells per ml. The cells were then starved overnight in serum-free media. The working volume for each chamber was 180μl. Chamber 1 served as a control and included only osteosarcoma cells in serum-free media. In chamber 2, PEG-nanowires were plated with the cells at a ratio of 100 wires to 1 cell in serum-free media. In chamber 3, RGD-nanowires are plated with cells at a ratio of 100 nanowires to 1 cell in serum-free media. After titration of nanowires to cells, the dish was immediately taken to the microscope and the microscope was setup for image acquisition by specifying the x,y and z coordinates for the 4 chambers. All imaging was done at 37°C and 5% CO_2. Phase contrast and fluorescence (using UV filter) images were acquired once every eight minutes using both 20x and 40x lenses (NA = 0.8) and a high sensitivity monochrome CCD detector.

6.3.2 Spinning nanowires experimental setup

For this experiment, it is essential that all the wells (and cells inside) being tested, experience the same magnetic field from the magnetic stirrer. Thus, the experimental wells are designed such that they are symmetric about the center as shown in figure 6.12.

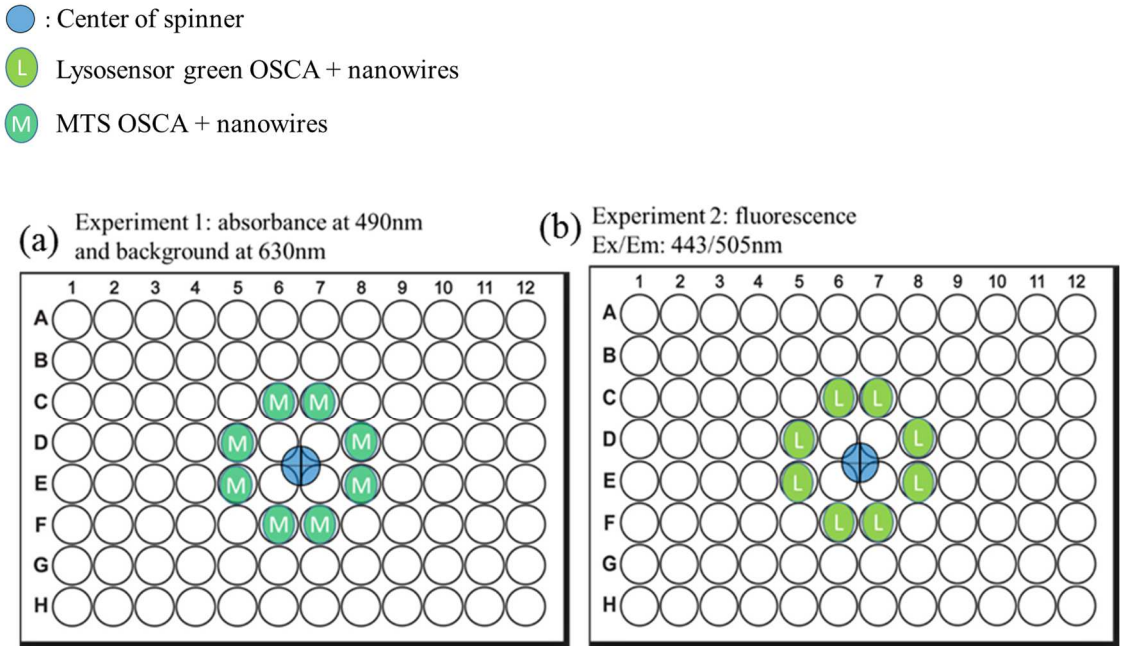

Figure 6.12: Experimental layout for testing (a) MTS metabolic activity (b) endosomal/lysosomal disruption from nanowire rotation.

MTS absorbance test: To test reduction in cell viability after spinning nanowires

1) OSCA-8 cells are loaded into 96 well plates at ~14000 cells per well, according to the shown templates the night (~ 8 hours) before the experiment. They are incubated at 37^0C and 5% CO_2 for approximately 2 hours. Three replicate plates

are prepared for each experiment: 2 plates for each experiment and 1 control plate (no applied magnetic field).

2) After the cells have adhered to the 96 well plates, cells are starved overnight (6 hours) in FBS free media and incubated at 37^0C and 5% CO_2

3) After 8 hours of incubation, the different nanowire samples in media are titrated into the wells at calculated fixed concentrations (2.1µg/well ~100 nanowires per well) and according to shown templates.

4) The plates are incubated for 6 hours at 37^0C and 5% CO_2.

5) After 6 hours of incubation, the wells are rinsed with PBS 3x and replaced with fresh media.

6) Next, the plates are placed on the IKA labdisc magnetic stirrer. Rotational magnetic field at 177.5 rpm is applied for 5 minutes. The control plate is not subjected to any external magnetic field.

7) MTS reagent-media mixture is added to each well right after the field is turned off (MTS protocol in chapter 5).

8) The plates are further allowed to incubate for 3 hours. However, absorbance readings are taken every 30 minutes from the time when MTS reagent is added. Finally after 3 hours, the supernatants are collected from each well and transferred into a fresh 96-well plate for plate reading to avoid errors due to absorbance from nanowires.

Lysosensor green assay: To test disruption of acidic compartments in cells

Lysosensor is a pH-sensitive dye that stains acidic organelles (pH 5-6) in cells green. The fluorescence intensity is proportional to the number of acidic compartments within the cell. Thus, any disruption of acidic organelles followed by release of acidic cathepsins into the cytosol will be characterized with a diminution in green fluorescence intensity. The layout of the 96-well plate is similar to the MTS assay and is shown in figure 6.12 The protocol is as follows:

1) OSCA-8 cells are loaded into 96 well plates at ~14000 cells per well, according to the shown templates the night (~ 8 hours) before the experiment. They are incubated at 37^0C and 5% CO_2 for approximately 2 hours. Three replicate plates are prepared for each experiment: 2 plates for each experiment and 1 control plate (no applied magnetic field).

2) After the cells have adhered to the 96 well plates, cells are starved overnight in FBS free media.

3) After 8 hours of incubation, the different nanowire samples in media are titrated into the wells at calculated fixed concentrations (2.1μg/well ~100 nanowires per well) and according to shown templates.

4) The plates are incubated for 6 hours at 37^0C and 5% CO_2.

5) After 6 hours of incubation, lysosensor green (protocol on life technologies website) is added to the wells and the plates are incubated further for 30 minutes at 37^0C and 5% CO_2..

6) A pre-spin fluorescence emission reading is taken (Ex/Em: 443/505 nm using the plate reader.

7) Next, the plates are placed on the magnetic stirrer. Rotational magnetic field at speed setting 2 (calibrated) is applied for 5 minutes. The control plate is not subjected to any external magnetic field.

8) A post-spin reading fluorescence measurement is taken using the plate reader.

Upright multiphoton confocal microscope with lyso-tracker red and blue nuclear stain (or Acridine orange)

1) Glass bottom cell culture well with an area of 3.5 cm^2 and working volume of 800 µl was used to culture A549 human lung carcinoma cells (triplicated).

2) The cells were incubated for 2 hours at 37^0C and 5% CO_2 to allow them to adhere to the glass surface.

3) The cells were stained with Hoechst blue 33342 nuclear stain and lysotracker red following protocols listed on life technologies website (Lysotracker red stains acidic organelles, especially lysosomes, red). After elapsed staining time, the cells are rinsed with PBS 3x and the media is replaced with fresh media without stain.

4) Next, barcode1 nanowires (Segment lengths 3 µm 0.3 µm Au/ 3.1 µm Ni and diameter 100 nm –barcode 1 (bc1)) were plated into the well at a plating ratio of 33:1 nanowires: cell and allowed to incubate for 6 hours at 37^0C and 5% CO_2.

4) Following incubation, the cell culture dish was placed on the magnetic stirrer (turned OFF) using tape. If Acridine orange is used for staining cells, it is added during this step. No rinsing and replacement of media is necessary and the stain remains in solution. Acridine orange stains the nuclei green however, stains acidic compartments red. Thus, if

acidic compartments are disrupted, the red fluorescence would diminish and green fluorescence would increase.

5) This system was placed for observation and real-time imaging under Nikon A1RMP upright confocal microscope lens (Plan Apo LWD 25x water-immersion, NA 1.1). The 405nm and 561nm laser excitation sources were used for fluorescence excitation (nuclear stain and lysotracker). A reflectance channel was used in parallel to image the nanowires in cell culture.

6) After setting optimal exposure time and gain, the cell culture dishes were imaged for 10 minutes prior to turning on the magnetic field.

7) The magnetic field of the spinner plate is turned on and speed is set to 233 rpm. Simultaneously, image acquisition is started.

6.4 Conclusions

From the presented data, the following conclusions can be made:

(i) RGD nanowires show enhanced targeting of osteosarcoma cells (68% from RGD-nanowires vs 32% from PEG nanowires). This is an important result because enhanced availability at the cell membrane reduces the IC_{50} value of the drug-carrier, thus reducing cytotoxic effects from large concentrations of particles.

(ii) Enhanced cellular proliferation and increased cell densities were observed with RGD nanowires (35.5% from RGD-nanowires vs 15.6% from PEG-nanowires). This further corroborates the biocompatibility of RGD-nanowires observed in chapter 5.

(iii) 3μm RGD-nanowires were uniformly dispersed through integrin-mediated binding, internalization and cell proliferation. This active dispersal of RGD-nanowires

resulted in 23% improvement in nanowire dispersal over PEG-nanowires. These are highly desirable qualities ina a drug-carrier.

(iv) Internalization of magnetic nanowires in endosomes followed by application of a rotational magnetic field to disrupt endosomal trapping is an important technique to reduce tumor drug resistance. Further, this idea can be extended to disrupt lysosomes to promote cell death through apoptosis in cancer cells.

Uniform distribution of nanowires holds great potential in drug delivery, hyperthermia, and separation applications. Also, with additional antibody conjugation, RGD-nanowires hold the potential to promote the regeneration of specifically targeted cell populations. Through this study, we present a candidate nanomaterial, RGD magnetic nanowire, which would be effective for these applications.

Chapter 7. Self-assembled cellular structures and synthetic extracellular matrices using nanowires

In this chapter, the multilayered Au/Ni/Au nanowire will be used as a fundamental building block for the synthesis if artificial extracellular matrices using novel self-assembly methods. Specifically, the following points will be covered

(i) Discussion concerning the need for artificial extracellular matrices.

(ii) A self-assembly experiment using RGD-nanowires and osteosarcoma cells which will form the basis for the rest of the chapter.

(iii) Synthesis of magnetically aligned collagen-nanowire cross-linked networks through self-assembly by application of novel chemistry.

(iv) Characterization of aligned artificial matrices using SEM, DIC imaging and polarized light studies.

(v) Plating of cells on synthetic matrices and mechnoresponses (contact-alignment) of cells to aligned matrices.

7.1 Theory

7.1.1 Synthetic extracellular matrices

Synthetic extracellular matrices have strong applications in mechanobiology and tissue engineering. Cell growth, differentiation and migration are all influenced by mechanical, structural and biomolecular stimuli in the microenvironment and thus, regulation of cell function as it relates to these cues is an extremely important study to undertake as it provides insight into tissue development and disease progression[126]. In naturally occurring extra-cellular matrices, the cellular response is a product of

intertwined physical and biochemical stimuli which are hard to isolate and characterize[127].

Matrix rigidity is sensed by the cells by extension of actin filaments whereas density of soluble and insoluble ligands is sensed using various cell-adhesion molecules and mechanisms such as integrin clustering[128]. In order to isolate various environmental stimuli from genetic factors and from each other, an artificial microenvironment that can recapitulate specific cellular responses by providing controlled mechanical and biomolecular stimuli is very useful. Synthetic matrices provide a platform that help provide controlled mechanical and biomolecular cues and thus, isolate stimuli-response combinations. Synthetic microenvironments have been used to study and thereby, control differentiation of mesenchymal stem cells (MSCs) to neurogenic, myogenic and osteogenic cell lineages with increasing matrix stiffness [129,130].. The specific relationships vary with cell phenotype, though most adherent cells exhibit similar trends.

A high degree of control on cell behavior, through this study, allows assembling 3D tissue-like structures using a bottom-up approach. This field of controlled self-assembly of cells has spawned highly prolific research in tissue engineering where artificial organs and tissues are synthesized to model live animal studies, test therapeutic efficacy *in vitro* in these model systems and organ-transplant *in vivo*[17,131,132]. Further, synthetic matrices have been designed for regenerative medicine. For example, artificial livers showing albumin secretion and urea synthesis have been synthesized using PEG hydrogels [133].

7.1.2 Natural vs diseased extracellular matrices: Mechanobiology of cancer

In order to create artificial microenvironments, it is essential to understand naturally occurring extra cellular matrices from a materials science perspective. Here, specific examples of normal mammary gland and cancerous ones are taken to compare properties of the stroma (extracellular matrices). The mechanical properties compared includes its viscoelastic properties and the forces it induces in cells plated on it i.e., the cytoskeletal tension induced. At the macro scale, the range of stiffness of the stroma varies from 167 Pa in a healthy mammary gland to as high as 4000Pa in a tumor[134]. The reasons for such high stiffness in a tumor include high interstitial pressure and abnormal vasculature. This can pose problems for therapeutic delivery because both factors prevent diffusion and trafficking of drug-carriers within the tumor.

At the cellular level, cancerous cells are stiffer than healthy mammary cells though phenotypic differences exist. External mechanical forces from the matrix regulate integrin expression on the cells. Increased matrix rigidity enhances expression of integrins leading to FAK mediated upregulation of Rho, ERK and ROCK levels that further regulate cytoskeletal tension (talin, viniculin and phallodin) through myosin. [134]. This causes an increase in focal adhesions which eventually encourages cell spreading and growth. Through intricate feedback loops, cytoskeletal tension and cell spreading determine if FAK is phosphorylated, thus controlling Rho activity and eventually controlling growth and cell cycle progression of the cells [134]. Elevated ERK and ROCK levels cause a disintegration of adherens junctions (cell-cell binding)

leading to cell dissemination and metastasis [134]. Further, cellular morphologies change from polar to highly irregular. Consequently, lumen formation is disrupted [134].

These mechanical properties can be recaptured in artificially synthesized matrices such as type 1 collagen. Basement membrane (laminin)/Collagen assemblies with different collagen concentrations (1mg/ml to 5mg/ml, for example) lead to matrices of variable stiffness. Further, biomolecular factors can be added to the matrix in a concentration-dependent fashion. The affinity of integrin-ligand complexes influence formation of focal adhesions and growth [134]. Also, varying stiffness of the matrix also influences the ligand spacing and thus indirectly changes the biomolecular makeup[129]. Thus, mechanical and biomolecular factors are often intertwined and this has to be kept in mind when designing a synthetic matrix.

7.1.3 Design criteria for synthetic microenvironments

Inspired by the properties of naturally occurring ECM, synthetic matrices are expected to meet the following criteria for optimal synthetic microenvironments:

(i) The environmental elements should have nano and micro-scale elements which can interact at the scale of the cells. This is motivated by the dimensions of naturally occurring ECM elements such as type-1 collagen and fibronectin. Further, characterization techniques such as SEM and AFM should be available to characterize the physical properties of the elements.

(ii) The biomolecular composition of the environmental elements should be controllable (soluble and insoluble ligands). The surface composition of the element and ligand

density should be manipulable in order to express proteins (example RGD) and sequences that are observed in naturally occurring extracellular elements.

(iii) Naturally occurring extracellular environments are composed of nanofibers such as collagen and fibronectin that self-assemble into larger networks that present macroscopic properties different from the elements that constitute them. Similarly, the individual elements of the synthetic environment should be capable of interacting with each other controllably to self-assemble into larger networks that have macroscopic properties commensurate with naturally occurring networks. For example, the mechanical properties of a self-assemble collagen network are dictated, among several factors, by the anisotropy of the aligned network of collagen fibers (tendon, ligament) which can be attributed to the fiber shape. A synthetic nanowire is a good candidate element to mimic these properties. A magnetic nanowire allows remote control of assembly or inter-element interactions. Further, characterization techniques should be available to probe the properties of these networks using biochemical assays, histological staining and second harmonic generation imaging mass spectrometry.

(iv)The environment should provide controlled mechanical stimuli to the cells without an invasive energy source[135]. Further, the element should be manipulable over a range of motions- it should have various degrees of freedom in motion.

(v) The environment and its elements should be biocompatible: induce minimal cytotoxicity or variability -measured using metabolic activity and release of pro-inflammatory cytokines.

(vi) The environment and its elements should ensure repeatability: A scientist should be able to re-create the environment in the laboratory to test for repeatability.

(vii) Sensitive detection methods for quantifying the stimuli and cellular responses.

7.1.4 Synthetic microenvironments using nanofibrous scaffolds

Synthetic matrices should ideally resemble naturally occurring matrices, both on the macro and nanoscale. Fibrous scaffolds are preferred because the naturally occurring connective tissue are composed of protein fibers (example, type 1 collagen and elastin) with diameters ranging from tens of nm to 100-200nm and up to 10 microns in length (Type 1 collagen molecules that assemble to form these fibers are 1.5nm in diameter and 300nm in length)[18,127]. Further, adhesive proteins in natural matrices such as laminin and fibronectin are fibrillar in structure, though at a much smaller scale (<10nm). Basement membranes are composed of type IV collagen and laminin fibers in proteoglycan hydrogels[100]. Topographical features on these natural fibrous elements include surface roughness in the range of 20-50nm. These must also be incorporated in a synthetic fibrous scaffold because there are several studies showing dependence of cellular behavior on the fibrous nature and individual fibers of the scaffold [136,137].

A nanowire platform can meet these requirements, provided the nanowire is engineered so that biocompatibility of the particle and repeatability of the experiments are addressed (chapter 5). Special attention has to be given to the dosage, geometry and surface characteristics (ligands and roughness) of the nanowire. Physical dimensions of the nanowires can be controlled by controlling the pore diameters of the AAO pores. Topographical cues can be introduced on the nanowire by designing the AAO pores to have rough walls. Through electrodeposition in the pores, the nanowires take the shape of

the AAO mold (chapter 2). However, metallic nanowires have much larger mechanical strength and low ductility compared to naturally occurring fibers. In this sense, using polymeric nanowires or a mixture of naturally occurring collagen fibers and metallic nanowires would serve as a superior synthetic model.

Other candidate materials include hydrogels, synthetic and natural polymers[133,138,139]. Hydrogels provide variation in stiffness by controlling the extent of polymerization, however in this case, it is difficult to decouple the biomolecular cues from the mechanical cues. Synthetic polymers (polyesters) and natural polymers (alginate) can be functionalized to present biomolecular cues and the stiffness of the fibers can be controlled by varying the cross-link density.

7.2 Results

7.2.1 A self-assembly experiment using only RGD-nanowires and osteosarcoma cells: a prelude to controlled microenvironments.

Following 24 hours of incubation, assays containing RGD-nanowires (100 and 200 nanowires per cell) were rinsed to remove unattached nanowires, and then the osteosarcoma cells were chemically detached from their substrate using 0.25% trypsin-EDTA. Tissue-like spherical aggregates, approximately 3-4 mm in diameter, were formed within two minutes. These aggregates were composed of osteosarcoma cells, membrane adhering nanowires, and cells with internalized nanowires. Reflectance microscopy and DIC images of an aggregate reveal a dense network of cells/nanowires that were strongly intertwined like a matrix, Figure 7.1. The nanowires were more clearly observed in reflectance images, Figures 7.1c and 7.1f, and the cells were more clearly

observed in corresponding DIC images, especially at edges and thin sections of the aggregate, figures 7.1d and 7.1e. These aggregates did not break, even when subjected to vigorous stirring.

When similar 24-hour incubation followed by chemical cell detachment was performed in a PEG-nanowire environment, the cells simply detached and no tissue self-assembly was observed. In fact, this same procedure was followed in environments with bare nanowires and also in environments containing RGD but no nanowires. Tissue self-assembly was only observed in environments containing RGD-nanowires and only at concentrations of 100 or more nanowires per cell (table 3). The fact that self-assembled aggregates do not form with bare nanowires at similar concentrations indicates that the formation of this aggregate is not simply magnetic clustering or resulting from mechanical cues only. It is very likely that the nanowires may stimulate an RGD-integrin cellular response leading to cell-cell interactions. Alternately, the enhanced proliferation of the cells is stimulated by the RGD nanowires and on reaching confluence, cell-cell interactions mediated by cadherins override other factors in the microenvironment [140].

These results suggest that the biomolecular factors on the nanowire surface and nanowire geometry play an active role in this self-assembly. Such self-assembly was not observed with spherical RGD-functionalized nanoparticles upon substrate detachment, even at higher concentrations[141]. Moreover, recent demonstration of aerogel formation through assembly of anisotropic nanoparticles [15] and formation of primary hepatocyte aggregates (spheroids) on nanofibrous galactosylated chitosan scaffold [140] corroborates these results. These 3D agglomerates can be harvested and combined with other 3D

cellular structures to synthesize complex cellular/tissue architectures. 3D self-assembled cellular aggregates are also gaining popularity for cell-sheet harvesting [142]. Controlled aggregation of hepatocytes, for example, has been implicated in selectively inducing or repressing liver specific function[143]. Therefore, our RGD-nanowires represent a truly novel modality that has great potential to influence specific cellular responses, including synthetic tissue formation.

Though RGD-nanowires induce self-assembly of cellular agglomerates/spheroids on cell detachment, it is challenging to create homogenous microenvironments with long nanowires with lengths comparable to collagen fibers (6-10 microns long and 100-200nm in diameters) because of increased heterogeneity in the environment with increasing wire length. Moreover, the mechanical properties of nanowires differ widely from ECM components. Thus, the models discussed henceforth are composed of mixtures of functionalized nanowires and collagen fibers in fixed ratios to modulate the mechanical and biomolecular constitution of the microenvironment to values close to real matrices. The magnetic properties of the nanowire can be exploited to modulate the texture, structural and mechanical properties of the matrix.

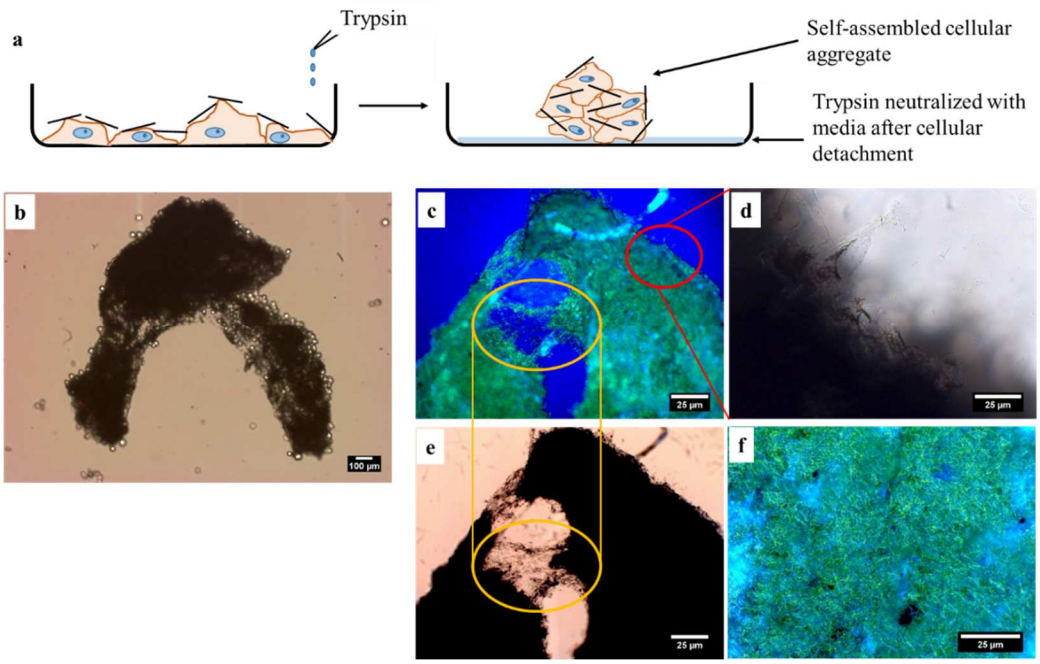

Figure 7.1 Self-assembled tissue-like agglomerate containing osteosarcoma cells and RGD-nanowires. (a) Schematic showing tissue-like aggregate forming within minutes of treatment with 0.25% trypsin. (b) DIC image of a 1.5mm aggregate. Spherical aggregates up to 4mm were observed. (c) Reflectance microscopy image of nanowire-cell aggregate. (d) High magnification DIC image of the edge of the aggregate clearly reveals cells. (e) The circled area in (c) shows a stretched portion of this aggregate, which has a tissue-like continuity that is more easily observed in this DIC image. (f) Another high magnification image using reflectance microscopy clearly shows nanowire-cell aggregates at the top-center of the agglomerate.

Initial Plating of NW:cell	Spheroid formation with bare wires	Spheroid formation with PEGylated wires	Spheroid formation with RGD coated wires
1:1	No	No	No
25:1	No	No	No
50:1	No	No	**Yes**
100:1	No	No	**Yes**

Table 3: Conditions tested for formation of nanowire-cell agglomerate. The agglomerate forms through self-assembly only under very specific conditions: High concentrations of RGD nanowires (>50:1 nanowires: cells) with osteosarcoma cells for incubation periods of at least 24 hours (or until a confluent cell layer is formed) result in agglomerate formation.

7.2.2 Cross linking nanowires and collagen to synthesize artificial matrices with variable mechanical properties:

Type 1 collagen is commonly used for synthesis of artificial matrices, both individually or when mixed with other constituents [127].

Aligned collagen is desirable in order to replicate processes in connective tissues like tendons and ligaments. Also, anisotropy of the microenvironment such as those provided by aligned collagen allows testing of cellular behavior and tissue morphogenesis as a function of various structural and topographical (texture) cues. Further, a composite material made of collagen and nanowires is a controlled environment, where nanowires are spaced apart by collagen fibers, thus heterogeneity

and aggregation are mitigated. The proportions of collagen and nanowires by weight would also tune the mechanical properties. Finally, alternating sheets of aligned collagen mimic collagen found in bone and the cornea[144]. Thus, this technology can be translated to synthesize artificial organs.

Here, we chemically cross-linked collagen molecules to the surface of the nanowire using a novel chemistry. The mechanical/structural properties of collagen were controlled by varying the concentration of collagen (mg/ml) and the nanowires (number per well). The design, crosslinking agent and reaction are shown in the figure 7.2. Next, a uniform magnetic field (~0.1T) was applied in order to align the nanowires. The collagen molecules were allowed to self-assemble under these conditions using established protocols (experimental section) leading to the formation of a gel. The magnetic alignment of nanowires in the collagen-nanowire mixture provides an anisotropic template for the self-assembly of collagen molecules. The advantage of using a multi-segmented nanowires is that the nickel segment can be cross-linked to collagen where as additional growth factors (eg., RGD) can be conjugated to the gold segments via a thiol linker (figure 7.2).

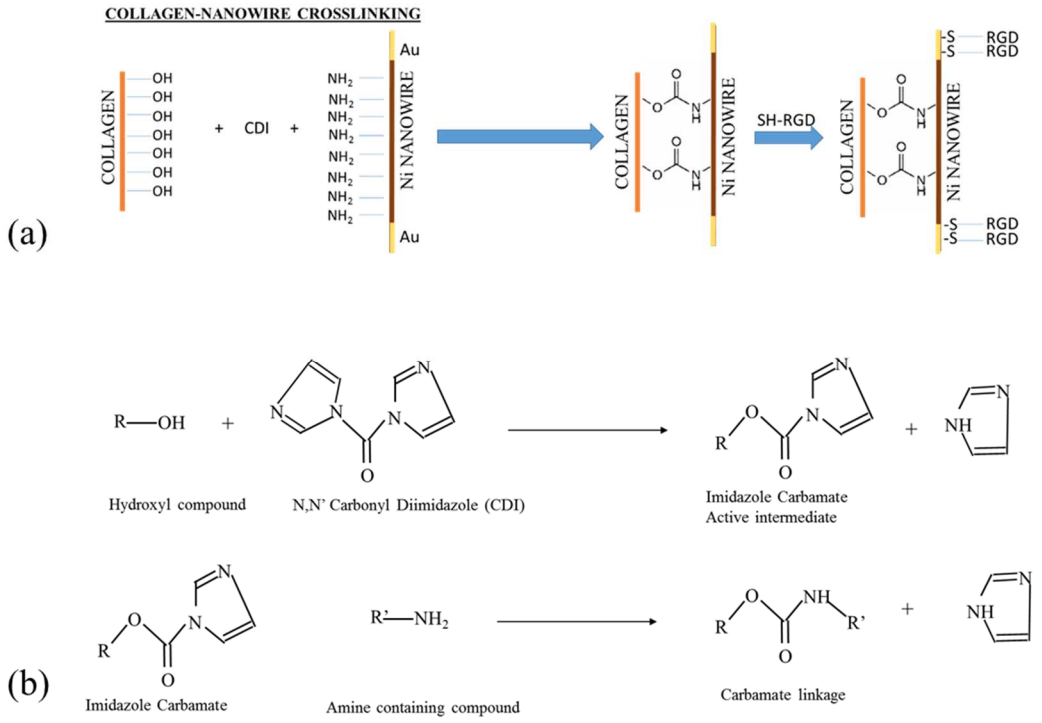

Figure 7.2 Novel chemistry showing cross-linking of nanowires to collagen fibers. (a) Cross-linking scheme. (b) Cross-linking reaction.

7.2.3 Structural characterization of synthetic matrix surface using DIC microscopy and SEM

In order to characterize the topographical features of the surfaces of the synthetically prepared matrices, DIC microscopy was used in conjunction with two cross-polarizers. Fixed concentrations of collagen (2mg/ml) and cross-linking reagent (CDI) were used in these experiments. However, nanowire concentrations were varied relative to collagen concentration; three cases of nanowire concentrations were studied: High, medium and low (see experimental section for exact concentrations and cross-linker

concentration). Figure 7.3(a,b), (c,d)) and (e) show the surface texture of the matrices under high, medium and low nanowire concentrations, respectively.

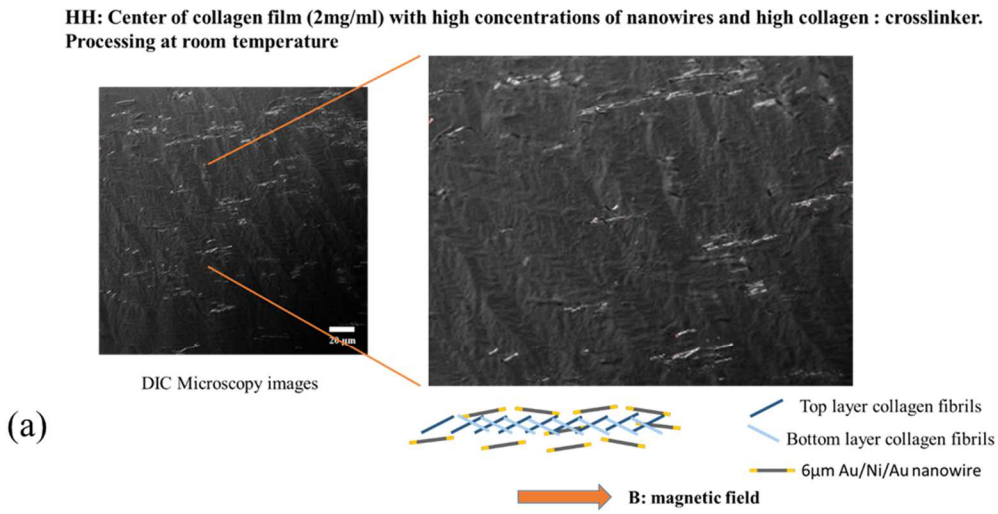

(a)

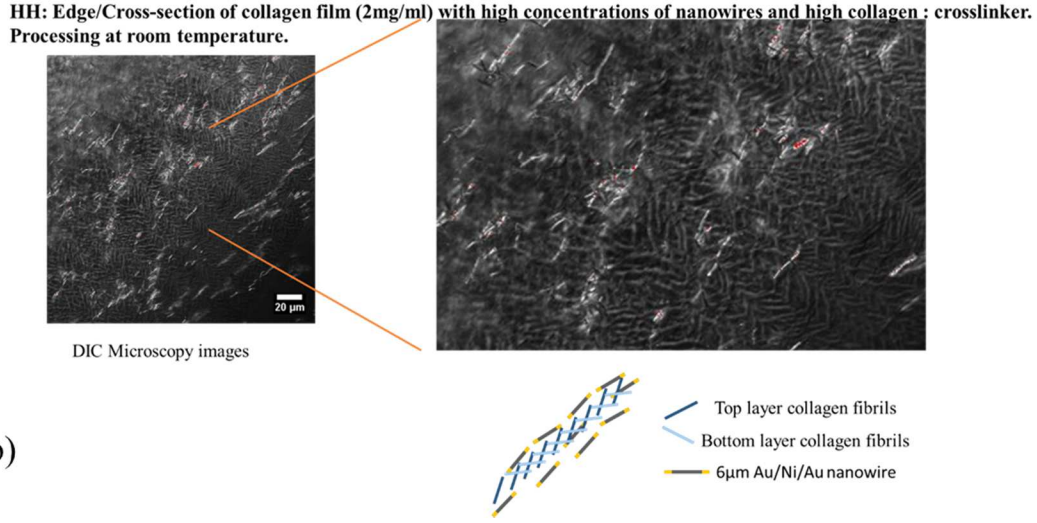

(b)

HM: Center of collagen film (2mg/ml) with medium concentrations of nanowires and high collagen:crosslinker. Processing at room temperature.

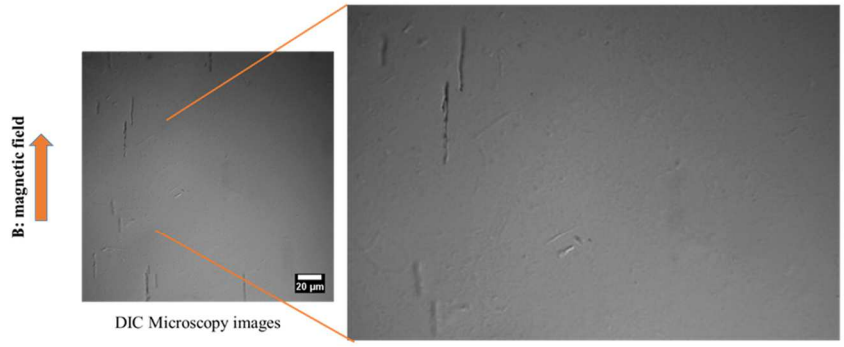

(c)

HM: Edge/cross-section of collagen film (2mg/ml) with medium concentrations of nanowires and high collagen:crosslinker. Processing at room temperature.

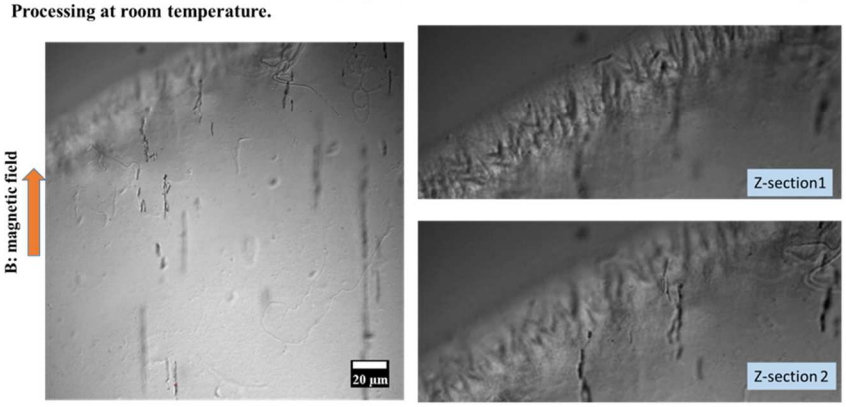

(d)

LH: Center of collagen film (2mg/ml) with high concentrations of nanowires and low conc. of collagen:crosslinker. Processing at room temperature.

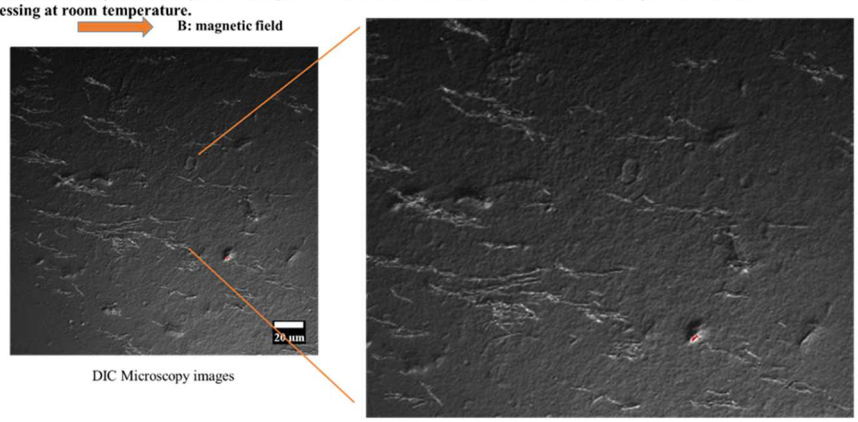

(e)

Figure 7.3: DIC microscopy images of top surfaces and edges of synthetically prepared artificial collagen-nanowire matrices under nanowire concentrations of (a,b) high, (c,d) medium and (e) low. Refer to figure 7.10 and section 7.3.2.

As seen in figure 7.3, a definite topographical zig-zag arrangement of collagen fibers formed only under one specific condition of high nanowire populations coated with the cross-linking reagent (7.3(a,b)). This structure is not found in plain self-assembled collagen films/gels. However, in naturally occurring bones and cornea and under much higher concentrations of collagen (20-30 mg/ml), self-assembly leads to ordered structures[144]. Here, we could controllably align the collagen fibers by providing a template via aligned nanowires at much lower collagen concentrations (2mg/ml). Thus, the mechanical strength and rigidity of the matrices can be controlled by modulating the nanowire and/or collagen concentrations.

In order to resolve the finer features of the aligned matrices, SEM imaging was performed (figure 7.4). Clear alignment of collagen fibers was observed in images taken from different parts of the same aligned gel.

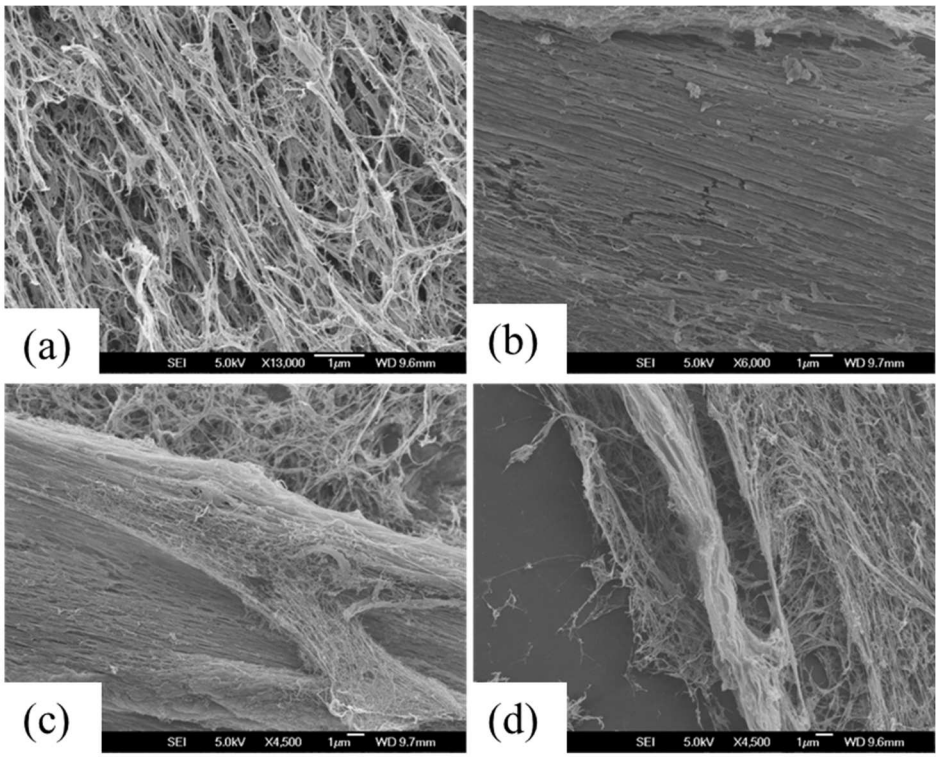

Figure 7.4: SEM micrographs of aligned collagen-nanowire matrices (2mg/ml collagen and high nanowire concentrations). (a) shows an image taken from the top center of the collagen-nanowire gel. (b) shows cross-sectional view and (c&d) show edges of the same gel.

The nanowire-collagen matrices formed using the cross-linking chemistry were compared to matrices formed without the cross-linker. (Figure 7.5). Alignment was only

observed when the cross-linker was used.

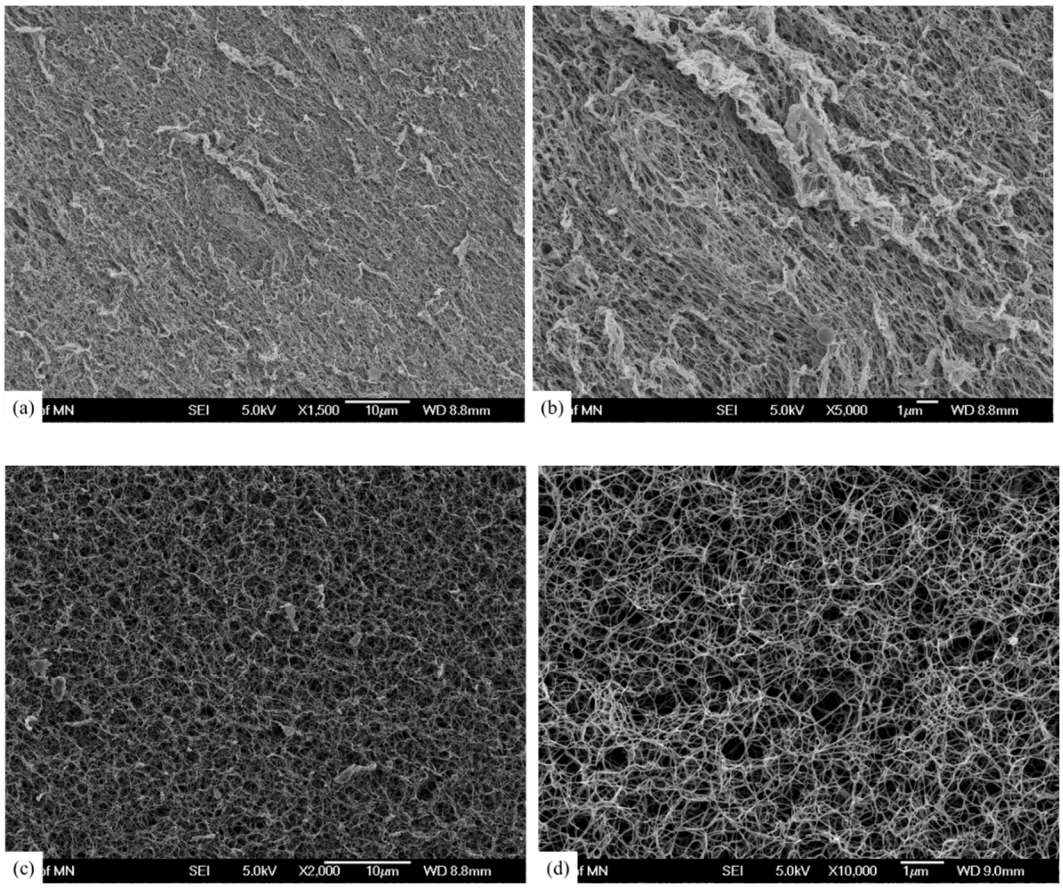

Figure 7.5: Collagen-nanowire matrices self-assembled in a uniform magnetic field, but with and without the chemical cross-linker (CDI). Collagen concentration was constant at 5mg/ml and "high" nanowire concentrations were used in all samples shown above. (a,b) SEM micrographs of collagen-nanowire matrices formed through chemical crosslinking of collagen to nanowires using CDI under uniform magnetic field conditions. (c,d) SEM micrographs of collagen-nanowire matrices formed without the chemical-crosslinker.

As it is difficult to distinguish between nanowires and collagen fibers at the magnifications shown in figures 7.4 and 7.5, higher magnification images

were taken in conjunction with EDX analysis. This was done to ensure that the observed alignment was indeed due to cross-linking between nanowires and collagen fibers (figure 7.6).

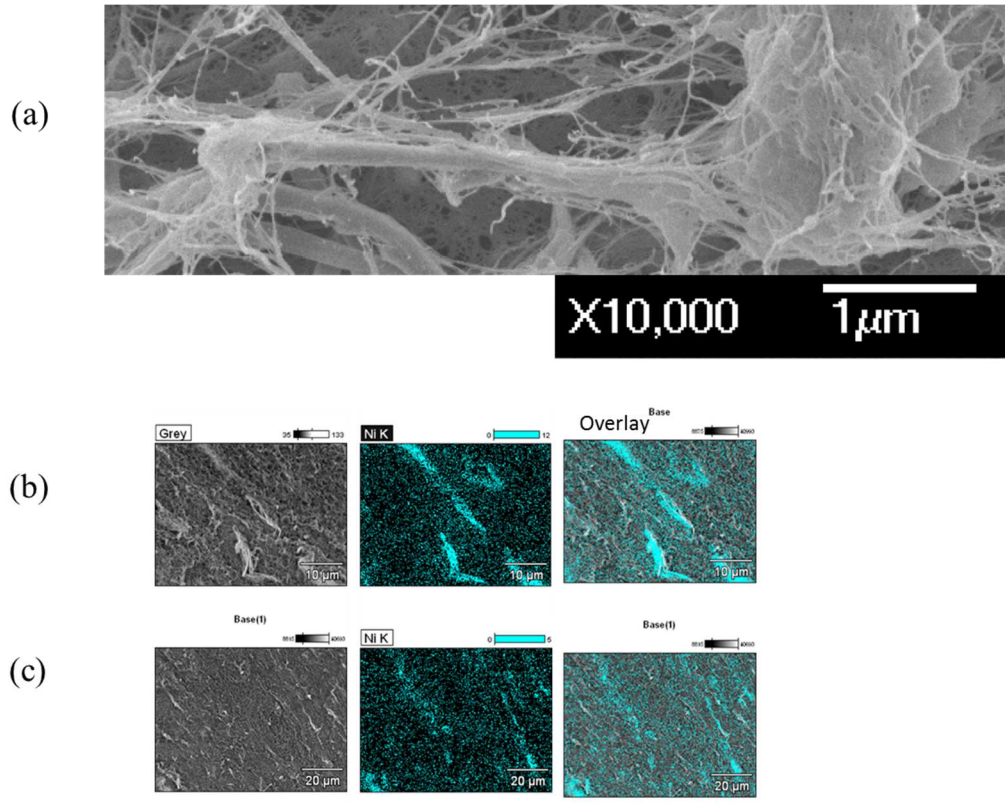

Figure 7.6: High magnification SEM and EDX analysis to show alignment of nickel nanowires (and therefore, applied field direction) and interactions between nanowires and collagen fibers. (a) SEM micrograph showing collagen fibers attached to the Ni surface of Au/Ni/Au nanowire (Au segments of Au/Ni/Au nanowire are 50 nm and thus, the nanowire is mostly Ni). (b, c) EDX analysis of the nanowire-collagen cross-linked matrix formed under uniform magnetic field shows spatial X-ray mapping of Ni (cyan color).

7.2.4 Polarized light transmittance vs matrix orientation

To further characterize the anistropy of the aligned nanowire-collagen matrices, transmittance of polarized light was measured through the matrix as the polarization of light was rotated by 360 degrees. The setup is shown in figure 7.7(a). The magnetically aligned nanowire-collagen matrix had an associated sinusoidal waveform (figure 7.7(d)). On the other hand, neither the blank control (figure 7.7(b)) nor the unaligned matrices (figure 7.7(c)) exhibited this characteristic sinusoidal response.

The transmittance waveform from the magnetically aligned matrices shows four peaks in transmittance as the polarization of light is rotated by 360 degrees. This is consistent with the structure suggested by the DIC images from figure 7.3(a&b). There are two main directions along which the fibers are oriented. Therefore, when the incident light direction is parallel to one of these directions, a maxima in transmittance will be observed. From the proposed zig-zag structure from figure 7.3(a&b), four peaks in transmittance will be predicted. This prediction is verified here through polarized-light transmisttance measurement.

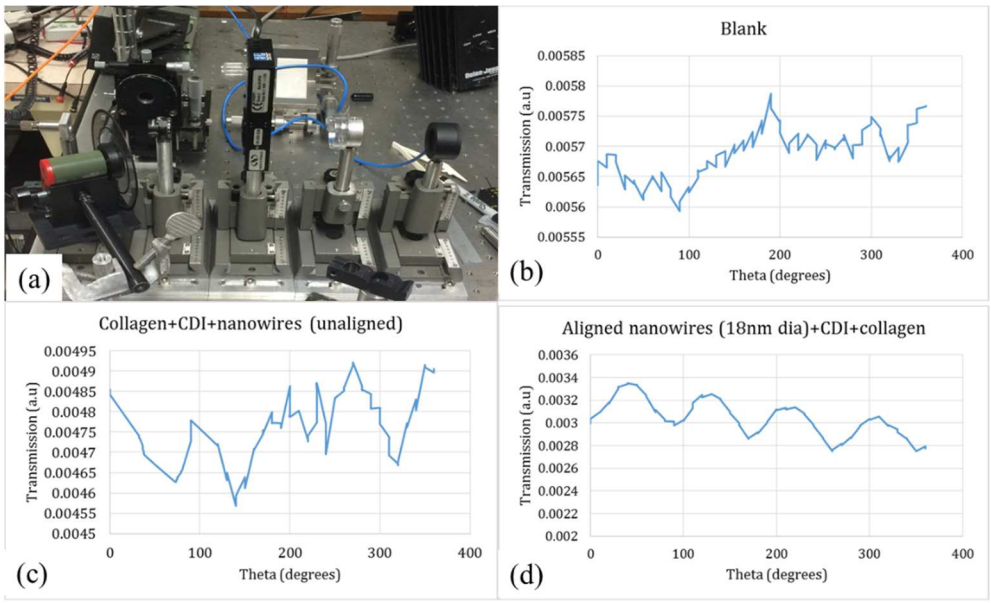

Figure 7.7: Polarized light transmittance vs orientation of the polarization of incident light with respect to the fixed sample (synthetic aligned nanowire-collagen matrix). The light was normally incident on the top surface of the matrix. The polarization was rotated through 360^0. (a) Setup for measuring polarized light transmittance through the matrix. The optical train consists of a 633 nm wavelength HeNe excitation laser, a chopper set at a fixed frequency (380 Hz), linear polarizer, polarization rotator, detector and lock-in amplifier set at chopper frequency. Real-time data was collected using a Labview interface. (b) Transmitance measured through blank control. (c) Transmittance measured through nanowire-collagen matrix, where nanowires were chemically cross-linked to collagen under zero field (no applied magnetic field) conditions. (d) Transmittance measured through nanowire-collagen matrix, where nanowires were chemically cross-linked to collagen under uniform field (0.1T) conditions. The sinusoidal nature of the waveform measured in this case corresponds to anisotropy of the matrix suggesting nanowire-collagen alignment.

7.2.5 Effect of magnetically-aligned synthetic matrices on arachnoid cells: contact alignment

Existing research in cell mechanotransduction and contact alignment suggests that synthetic matrices with specific geometric patterns elicit specific mechnoresponses from cells[145,146]. Having successfully synthesized magnetically aligned matrices, the next step was to test if these matrices are capable of eliciting mechanical responses from cells plated on these substrates.

For this study, arachnoid cells were used as these cells are sensitive to topographical cues from the extracellular matrix[147]. These cells were plated on magnetically-aligned matrices and incubated till confluence (~ 3 days) under controlled environmental conditions (37^0C, 5% CO_2). The cells were stained with a blue nuclear stain (DAPI) and a green actin filament stain following incubation. The hypothesis here was that actin stress fibers (stained green), which control the cytoskeletal shape of the cells, would exhibit an aligned geometry in relation to the aligned matrix. This, in turn, would influence the spreading of cells on this substrate, imparting them with a definite anisotropy.

As shown in figure 7.8 (a-d), an anisotropy is indeed observed in the actin stress fibers (stained green) of the arachnoid cells in relation to the underlying aligned matrix. In contrast, the same cells do not exhibit this behavior when plated on plain collagen gels (without nanowires), figure 7.9(a-d).

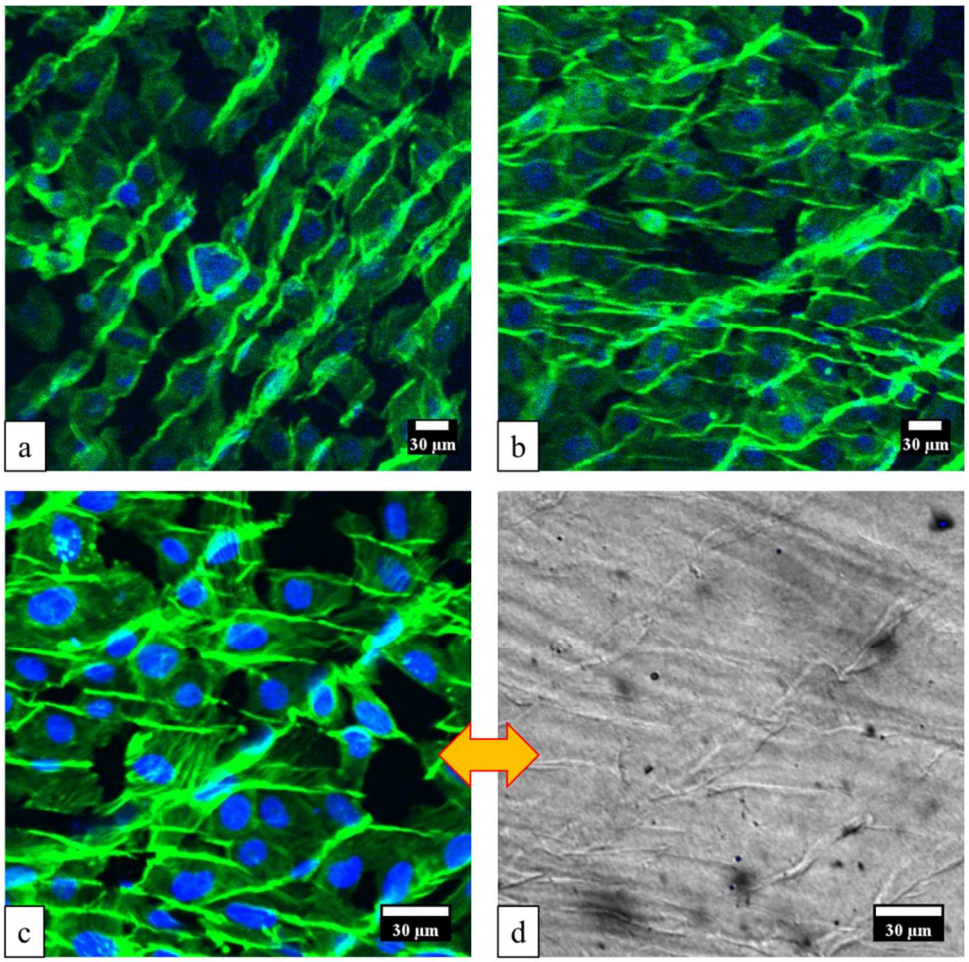

Figure 7.8. Contact alignment of arachnoid cells to magnetically aligned nanowire-collagen synthetic matrices. (a and b) Cellular actin stress filaments (stained green) are observed to accumulate and stretch along specific directions through confocal fluorescence microscopy (10x magnification). Nuclei are stained blue. Throughout the sample, the actin filaments were seen aligned along two directions. This correlates with the zig-zag structure proposed in figure 7.3(a). (c and d). Fluorescence and corresponding DIC image taken at 20x magnification.

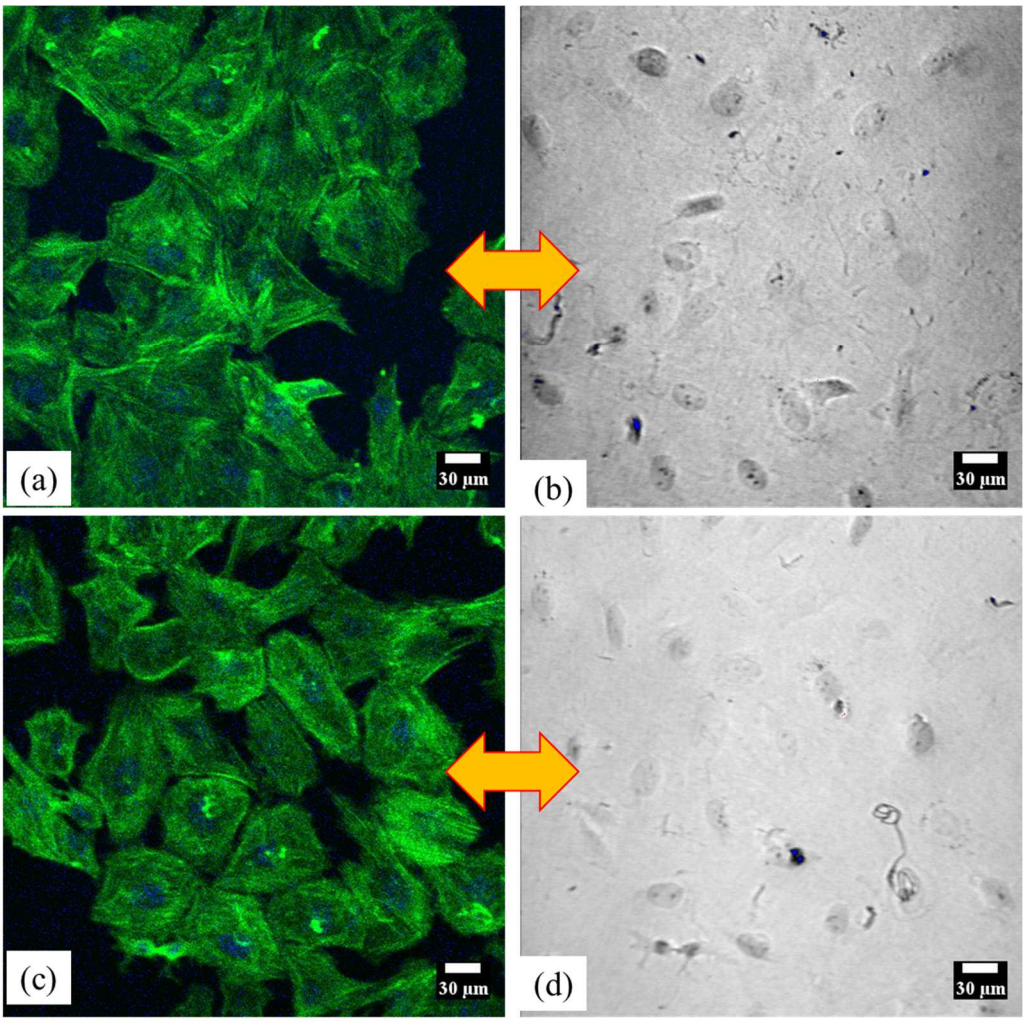

Figure 7.9. Controls for contact alignment experiment. The confocal fluorescence and DIC images are taken form cells plated on unaligned collagen gels. (a and b) 20x Confocal fluorescence and corresponding DIC images of arachnoid cells plated on unaligned collagen matrices. (c&d) show the same results taken from a different part of the same sample.

7.3 Methods:

7.3.1 Cell agglomeration experiment.

For DIC and reflectance imaging of the self-assembled aggregate, 35x10mm cell culture petri-dish was used to culture 1.1 million adherent canine osteosarcoma cells in media (DMEM media, 10% FBS, 1% 4-(2-Hydroxyethyl)piperazine-1-ethanesulfonic acid (HEPES) and 0.2%primocin) at 37°C and 5% CO_2. After reaching 70% confluence, 110 million RGD-functionalized nanowires in media were added to the cells. A working volume of 2.1ml was used. The cells were allowed to incubate for 24 hours with the nanowires. After the elapsed time, the media was aspirated and the cells were rinsed 2x with PBS to remove any unattached nanowires. Next, the cells were treated with 0.25% Trypsin EDTA for 3 minutes. Under laminar flow of trypsin, all cells don't detach from the culture dish. So some agitation is required (either through pipetting or manually tapping the dish) to ensure effective cell detachment during treatment with trypsin. Tissue-like aggregates are observed to form within 1-2 minutes of treating with trypsin. These aggregates do not break even on vigorous titration. Following this, trypsin is neutralized with media and the trypsin-media mixture is aspirated without removing the aggregate from culture. The aggregate is washed 3x with PBS and fixed in 10% formalin for 20 minutes. Following this, the sample was rinsed 3x with PBS. After aspirating the PBS, cells were taken for observation through Zeiss Axioplan 2 microscope using DIC microscopy with a 63x oil-immersion lens (NA = 1.4) and Jenoptik 5MP ProgRes C12 Plus, RGB 12 bit CCD detector.

7.3.2 Synthesis of collagen-nanowire matrices

The nanowire-collagen hybrid hydrogel was formed as follows. The nanowires were synthesized to a given size (35/100 nm diameter, 6 microns long) and soaked in a PEG solution. The sample was sonicated for 10 minutes and stored at 4^0 C overnight. The PEG solution was decanted from the nanowires, and replaced with a 0.2 M CDI solution (0.1 mM HCl, pH 3). The sample was sonicated for 10 minutes and stored at room temperature overnight. The CDI was then decanted and the nanowires were rinsed with 0.1 mM hydrochloric acid. After rinsing, the nanowires were suspended in a soluble type I collagen solution (5 mg/mL, pH 3) at nanowire concentration of 10 million wires/mL (high concentration). Medium and low concentration of nanowires used were 1million/ml and 0.1million/ml. The wires were mixed within the collagen solution with a pipette and kept in the collagen solution overnight. The solution was then mixed and poured into a rubber mold to make a flat rectangular geometry with a 1 mm thickness. The solution was placed under a uniform magnetic field (0.1T) for 2 minutes to allow for nanowire alignment. While keeping the sample under the same magnetic field, then the solution was exposed to ammonia vapor by placing 30 microliters of ammonium hydroxide (30%) next to the sample. Ammonia vapor was trapped by placing a lid over the sample and ammonium hydroxide droplet. This neutralized the collagen solution which caused fibril formation. Control collagen gels were made by using the same procedure with the stock collagen solution. All the experiments (total 36 with applied field and no field.) shown in figure 7.10 were conducted. Alignment was observed only under the conditions marked yellow (HH and HM at room temperature). Cell culture protocol for Arachnoid cells can

be found on ATCC website. Following protocol, the cells were plated on the synthesized matrices and imaged using confocal fluorescence microscopy and DIC microscopy at 10x and 20x magnifications.

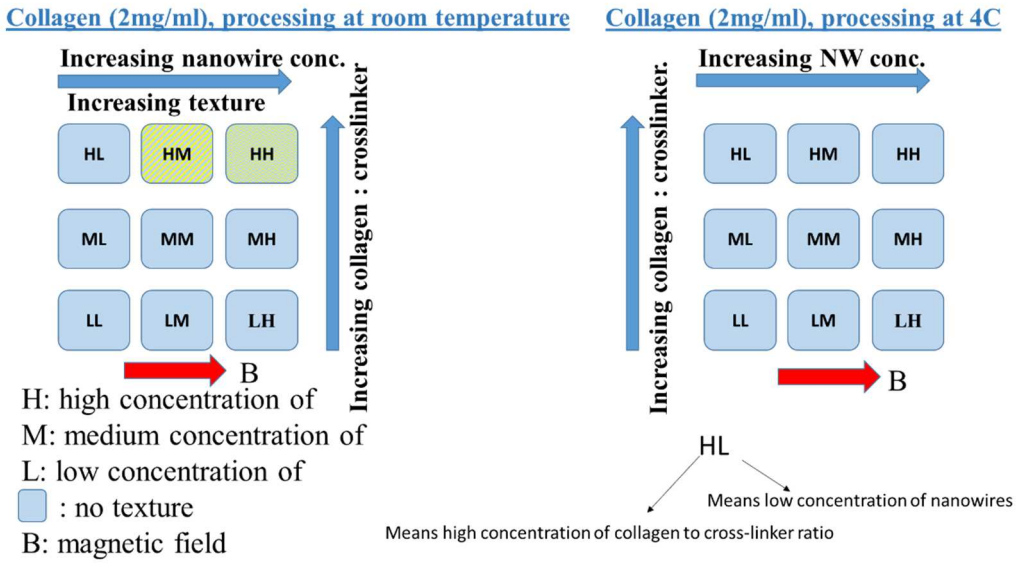

Figure 7.10 Experimental design for synthesis of nanowire-collagen matrices.

7.4 Conclusions

In this chapter, the need for artificial extracellular matrices was discussed in detail. This was followed by a self-assembly experiment using RGD-nanowires and osteosarcoma cells which resulted in the formation of 3D self-assembled cell-nanowire agglomerates. This self-assembly experiment inspired the idea of synthesis of artificial collagen-nanowire matrices where specific structural and topographical properties of the synthesized matrices could be modulated through use of novel developed chemistry and by exploiting the cylindrical shape of the nanowire and its response to magnetic fields. Characterization of aligned artificial matrices was conducted using SEM, DIC imaging and polarized light transmittance studies. Finally, contact alignment of arachnoid cells

plated on aligned synthetic matrices was demonstrated. This work has strong relevance in understanding mechanoresponses of cells and their relation to disease progression. As future work, it is proposed that the observed mechanoresponses should be related to cellular biochemical pathways and eventually cellular responses. This technology can be employed for studying stem cell differentiation into different tissues based on the matrix rigidity and structure, which would contribute heavily to the field of tissue engineering.

Chapter 8: Conclusions and Future work

This work presents a novel multifunctional nanoparticle, the multilayered magnetic nanowire, as a unique, robust and effective diagnostic and therapeutic (theranostic) platform for applications in translational nanomedicine.

This PhD thesis started with the synthesis of multilayered magnetic nanowires through high-throughput electrochemical deposition in porous templates. Here it was shown that pre-patterning AAO before anodization led to the lowest polydispersity in pore-diameters and inter-pore spacing from all the compared methods. Nanowire lengths were precisely controlled in the electrochemical deposition method. Further, nanowire dimensions were characterized using SEM. The multi-layers were resolved by imaging back-scattered electrons from the nanowire samples. This technique was used in conjunction with EDX on bundles of nanowires for elemental-composition analysis. Far-field spectra from Au segments of Au/Ni/Au multilayered nanowires was measured using spectrophotometry. The obtained plasmon resonance wavelength was comparable to calculated Mie scattering results for nanowires. The plasmonic properties of these Au segments can be exploited in biological assays where they can serve as beacons or contrast agents.

Next, it was shown that the magnetic properties of nanowires such as hysteresis, coercivity, and coercivity vs orientation can be controllably designed by controlling the nanowire dimensions. The FORC technique was used to decode a mixture of two magnetically different nanowire samples. This technique could detect one nanowire type from 23 nanowires of second type (1:23) in a mixture with an accuracy of 97.5%. In a

mixture of nanowires with population ratios 1:115, the accuracy reduced to 93.75%. Thus, despite the lowering of accuracy with reduction in concentration of one sample in the mixture, FORC is a strong technique to magnetically decode mixtures of magnetically different nanowires. The sensitivity can be improved by increasing the number of FORCs collected (more data points) and increasing the dwell time per data point in the VSM.

Next, basic interactions of nanowires with biological cells were presented. Following incubation of osteosarcoma cells for fixed periods of time and under controlled environmental conditions, magnetic nanowires were observed to attach to cell membranes and internalized within membrane-enclosed compartments inside the cell. These results were verified through light microscopy (while applying magnetic field gradients to the sample) and SEM/TEM imaging. More importantly, large nanowire clusters were observed in the cell-nanowire samples which resulted in heterogeneity in environmental factors governing cell behavior. This also produced errors in experimental measurements and interpretations. Thus, these experiments emphasized the need for quality control of the nanowire samples in order to employ their full potential in biological applications. Additionally, imaging techniques for nanoparticle-cell experiments were introduced.

Following the conclusions from the previous chapter, it was shown that both aggregation and cytotoxicity related issues can be effectively resolved by employing a heterobifunctional PEG as surface coating on Au/Ni/Au nanowires using the novel chemistry presented. The hydrophilic PEG layer evenly dispersed the nanowires in suspension imparting them with a collective stability, as verified by VSM and

spectrophotometry. This property allowed repeatable titrations of nanowires in controlled biochemical experiments aimed at studying specific cellular responses. Further, conjugating the surface coating with natural proteins/peptides such as RGD enhanced the biocompatibility of the nanowires. Additionally, from all the variables tested including nanowire concentrations, lengths and surface coatings, it was concluded that the surface coating decides the biologically effective dose for nanowires with lengths ≤ 6 μm.

The next chapter focused on the functionality aspect of the coating on the nanowire. It was shown that RGD nanowires exhibited enhanced targeting of osteosarcoma cells (68% from RGD-nanowires vs 32% from PEG nanowires). This is an important result because enhanced availability at the cell membrane reduces the IC_{50} value of the drug-carrier, thus reducing cytotoxic effects from large concentrations of particles. Further, enhanced cellular proliferation and increased cell densities were observed with RGD nanowires (35.5% from RGD-nanowires vs 15.6% from PEG-nanowires) corroborating the biocompatibility results from chapter 5. It was shown that 3μm RGD-nanowires dispersed uniformly through integrin-mediated binding, internalization and cell proliferation. This active dispersal of RGD-nanowires resulted in 23% improvement in nanowire dispersal over PEG-nanowires. These are highly desirable qualities in a drug-carrier. As a means to reduce tumor drug resistance by facilitating endosomal escape of entrapped drugs/drug-carriers, internalization of magnetic nanowires in cellular endosomes was followed by application of rotational magnetic fields to disrupt endosomes. This novel technique was also proposed as a method to disrupt lysosomes to promote cell death through apoptosis in cancer cells. Finally, preliminary novel results in

self-assembly techniques for synthesis of artificial extracellular matrices was presented in the appendix. The use of the nanowire to design artificial extracellular matrices is a novel concept. Through novel surface chemistry, the nanowires were cross-linked to collagen molecules to produce anistropic structures which would serve as a matrix for cell adhesion.

In the final chapter, various self-assembly studies were conducted to produce engineered structures with controllable structural and topographical properties. Specifically, synthesis of artificial collagen-nanowire matrices through use of novel developed chemistry and by exploiting the cylindrical shape of the nanowire and its response to magnetic fields were discussed. Characterization of aligned artificial matrices was conducted using SEM, DIC imaging and polarized light transmittance studies. Finally, contact alignment of arachnoid cells plated on aligned synthetic matrices was demonstrated. This work has strong relevance in understanding mechanoresponses of cells and their relation to cell cycle progression and disease progression.

Thus, this thesis has covered, through the use of magnetic multilayered nanowires, a broad range of applications in nanomedicine which were introduced in chapter 1. The nanowire holds tremendous potential because of its unique cylindrical shape and associated magnetic properties. Some of the proposed future work includes

(i) Testing the nanowire as a theranostic tool *in vivo.*

This includes measuring the efficacy of the nanowires as a drug-carrier in active targeting of tumors in a mouse model. The Au segments of the Au/Ni/Au nanowire can be used as plasmonic imaging beacons. In addition, an anti-cancer drug such as paclitaxel can be

conjugated to the gold segment using thiol-gold chemistry. The Ni segment can be functionalized with PEG-RGD for specific targeting of tumor cells. The PEG coating will act as a stealth layer avoiding detection of the nanowire by the MPS and RES systems. Finally, the magnetic properties of the nanowires can be exploited by application of low and high frequency magnetic fields to internalized nanowires. Low frequency fields will enable mechanical motion of the nanowires in cancer cells. The nanowire dimensions can be designed to disrupt lysosomes internally, thus causing apoptosis of cells. Alternately, high frequency fields will enable generation of heat through hysteresis losses which can be used for a hyperthermia-based treatment. The efficacy of these techniques in destroying tumors should be measured, when employed in combination with each other.

(ii) With additional antibody conjugation, RGD-nanowires hold the potential to promote the regeneration of specifically targeted cell populations. This follows from the observation of increased cell densities with RGD nanowires measured in chapter 6. As a corollary, it would be interesting to test the antibody-conjugated nanowire for vaccination applications.

(iii) The use of nanowires as a constituent element for synthesizing artificial extracellular matrices should be explored further. This novel work is introduced in chapter 7. The ability to design synthetic matrices with controllable mechanical and topographical properties can be exploited in applications where stem cell differentiation can be studied. This will allow us to study disease progression by studying biomolecular pathways in cells activated by mechanical cues from the underlying matrix. This has tremendous potential in regenerative medicine.

References

[1] Srinivas PR, Barker P, Srivastava S. Nanotechnology in Early Detection of Cancer. Lab Investig 2002;82:657–62.

[2] Wagner V, Dullaart A, Bock A-K, Zweck A. The emerging nanomedicine landscape. Nat Biotechnol 2006;24:1211–7.

[3] Whitesides GM. The “right” size in nanobiotechnology. Nat Biotechnol 2003;21:1161–5.

[4] Prud’homme RK, Svenson S. Introduction: Benefits and Challenges for Multifunctional Nanoparticles in Medicine 2012:1–5.

[5] Davis ME. Nanoparticle therapeutics: an emerging treatment modality for cancer 2008.

[6] Li C. A targeted approach to cancer imaging and therapy 2014.

[7] Lammers T, Hennink WE, Storm G. Tumour-targeted nanomedicines: principles and practice 2008.

[8] Swami A, Shi J, Gadde S, Votruba AR, Kolishetti N, Farokhzad OC. Nanoparticles for Targeted and Temporally Controlled Drug Delivery 2012:9–29.

[9] Ito A, Shinkai M, Honda H, Kobayashi T. Medical application of functionalized magnetic nanoparticles. J Biosci Bioeng 2005;100:1–11.

[10] Zadnik PL, Molina CA, Sarabia-Estrada R, Groves ML, Wabler M, Mihalic J, et al. Characterization of intratumor magnetic nanoparticle distribution and heating in a rat model of metastatic spine disease. J Neurosurg Spine 2014.

[11] Murphy CJ, Gole AM, Stone JW, Sisco PN, Alkilany AM, Goldsmith EC, et al. Gold nanoparticles in biology: beyond toxicity to cellular imaging. Acc Chem Res 2008.

[12] Na H, Song I, Hyeon T. Inorganic nanoparticles for {MRI} contrast agents. Adv Mater 2009;21:2133–48.

[13] Gómez-Hens A, Fernández-Romero JM, Aguilar-Caballos MP. Nanostructures as analytical tools in bioassays. {TrAC} Trends Anal Chem 2008.

[14] Taton TA, Mirkin CA, Letsinger RL. Scanometric {DNA} array detection with nanoparticle probes 2000.

[15] Jung SM, Jung HY, Dresselhaus MS, Jung YJ, Kong J. A facile route for {3D} aerogels from nanostructured {1D} and {2D} materials. Sci Rep 2012.

[16] MP L, JA H. Synthetic biomaterials as instructive extracellular microenvironments for morphogenesis in tissue engineering. Nat Biotechnol 2005.

[17] Khademhosseini A, Langer R, Borenstein J, Vacanti JP. Microscale technologies for tissue engineering and biology. Proc Natl Acad Sci U S A 2006.

[18] Alberts B, Johnson A, Lewis J, Raff M, Roberts K, And Walter P. Molecular Biology of the Cell. vol. 54. 2008.

[19] Roller BT, McNeeley KM, Bellamkonda R V. Multifunctional Nanoparticles for Personalized Medicine 2012:277–93.

[20] Gianella A, Read JC, Cormode DP, Fayad ZA, Mulder WJM. Multifunctional Nanoparticles for {Target-Specific} Imaging and Therapy 2012:155–71.

[21] A H, M T, CS C. Cell manipulation using magnetic nanowires 2003.

[22] Hultgren A, Tanase M, Felton EJ, Bhadriraju K, Salem AK, Chen CS, et al. Optimization of Yield in Magnetic Cell Separations Using Nickel Nanowires of Different Lengths. Biotechnol Prog 2008;21:509–15.

[23] Hultgren A, Tanase M, CS C. Cell manipulation using magnetic nanowires. Cell Manip Using Magn Nanowires 2003.

[24] Piraux L, Dubois S, Demoustier-Champagne S, Demoustierchampagne S. Template synthesis of nanoscale materials using the membrane porosity. Nucl Instruments Methods Phys Res Sect B Beam Interact with Mater Atoms 1997;131:357–63.

[25] Rani VS, Yoon SS, Rao BP, Kim C. Template synthesis of NiFe nanowires using diblock copolymers. Mater Chem Phys 2008;112:1133–6.

[26] Routkevitch D, Bigioni T, Moskovits M, Xu JM. Electrochemical Fabrication of CdS Nanowire Arrays in Porous Anodic Aluminum Oxide Templates. J Phys Chem 1996;100:14037–47.

[27] Despić AR. A note on the effect of the electrolyte on the type of growth of anodic oxide on aluminium. J Electroanal Chem Interfacial Electrochem 1985;191:417–23.

[28] Young L. Transient Kinetics of Formation of Anodic Oxide Films on Tantalum in Dilute Sulphuric Acid. Proc R Soc A Math Phys Eng Sci 1961;263:395–406.

[29] Keller F, Hunter MS, Robinson DL. Structural Features of Oxide Coatings on Aluminum. J Electrochem Soc 1953;100:411.

[30] Inada T, Uno N, Kato T, Iwamoto Y. Meso-Porous Alumina Capillary Tube as a Support for High-Temperature Gas Separation Membranes by Novel Pulse Sequential Anodic Oxidation Technique. J Mater Res 2011;20:114–20.

[31] Maqableh M, Huang X, Stadler B. Novel Magnetoresistive Structures Using Self-Assembly and Nanowires on Si. MRS Proc 2011;1160:1160–H03 – 04–FF03 – 04.

[32] Hoar TP, Yahalom J. The Initiation of Pores in Anodic Oxide Films Formed on Aluminum in Acid Solutions. J Electrochem Soc 1963;110:614.

[33] O'Sullivan JP, Wood GC. The Morphology and Mechanism of Formation of Porous Anodic Films on Aluminium. Proc R Soc A Math Phys Eng Sci 1970;317:511–43.

[34] Nanostructured Materials in Electrochemistry. John Wiley & Sons; 2008.

[35] Gorisse T, Buttard D, Zelsmann M. Density multiplication of pores and their propagation in a thin layer of nanoporous alumina on silicon substrates. Appl Surf Sci 2015;343:106–14.

[36] null. Nanostructured Materials in Electrochemistry 2008:1–116.

[37] Gunawardena GA, Hills GJ, Montenegro I. Potentiostatic studies of electrochemical nucleation. Electrochim Acta 1978;23:693–7.

[38] Avrami M. Kinetics of Phase Change. I General Theory. J Chem Phys 1939;7:1103.

[39] Gunawardena GA, Hills GJ, Montenegro I. Potentiostatic studies of electrochemical nucleation 1978.

[40] SR N-P, RG F, BD R, L H, DJ P, ID W, et al. Submicrometer metallic barcodes. Sci {(New} York, {NY)} 2001;294:137–41.

[41] Schultz S. Composite Plasmon Resonant Nanowires n.d.

[42] Chen J, Albella P, Pirzadeh Z, Alonso-González P, Huth F, Bonetti S, et al. Plasmonic Nickel Nanoantennas. Small 2011;7:2341–7.

[43] Lomon EL. Classical Electrodynamics. John David Jackson. Wiley, New York, 1962. xvii + 641 pp. Illus. $13. Science (80-) 1962;136:1046–7.

[44] Bohren CF, Huffman DR. Absorption and Scattering of Light by Small Particles. John Wiley & Sons; 2008.

[45] Jain PK, Lee K, H E-SI, A E-SM. Calculated absorption and scattering properties of gold nanoparticles of different size, shape, and composition: applications in biological imaging and biomedicine. J Phys Chem B 2006;110:7238–48.

[46] Jain PK, Huang X, El-Sayed IH, El-Sayed MA. Noble metals on the nanoscale: optical and photothermal properties and some applications in imaging, sensing, biology, and medicine. TL - 41. Acc Chem Res 2008;41 VN - r:1578–86.

[47] Link S, Link S, El-Sayed MA, El-Sayed M. Spectral Properties and Relaxation Dynamics of Surface Plasmon Electronic Oscillations in Gold and Silver Nanodots and Nanorods. J Phys Chem B 1999;103:8410–26.

[48] Johnson PB, Christy RW. Optical constants of the noble metals. Phys Rev B 1972;6:4370–9.

[49] Martin BR, Dermody DJ, Reiss BD, Fang M, Lyon AL, Natan MJ, et al. Orthogonal Self-Assembly on Colloidal Gold-Platinum Nanorods TL - 11. Adv Mater 1999;11 VN - r.

[50] Raphael MP, Christodoulides JA, Qadri SN, Simpkins BS, Byers JM. Magnetic moment degradation of nanowires in biological media: real-time monitoring with SQUID magnetometry. TL - 21. Nanotechnology 2010;21 VN - r:285101.

[51] Lee H, Sun E, Ham D, Weissleder R. Chip–NMR biosensor for detection and molecular analysis of cells. Nat Med 2008;14:869–74.

[52] Safarík I, Safaríková M. Use of magnetic techniques for the isolation of cells. TL - 722. J Chromatogr B Biomed Sci Appl 1999;722 VN - :33–53.

[53] RDK M. Magnetic Nanoparticle Carrier for Targeted Drug Delivery: Perspective, Outlook, and Design. Nanoplatform Based Mol Imaging 2008:709–24.

[54] Kumar C, Mohammad F. Magnetic nanomaterials for hyperthermia-based therapy and controlled drug delivery 2011.

[55] Cullity BD, Graham CD. Introduction to Magnetic Materials, Second Edition 2008:197–239.

[56] Searson P, Johns Hopkins. Tuning the properties of magnetic nanowires n.d.

[57] Frei EH, Shtrikman S, Treves D. Critical Size and Nucleation Field of Ideal Ferromagnetic Particles. Phys Rev 1957;106:446–55.

[58] Aharoni A. Introduction to the Theory of Ferromagnetism. Oxford University Press; 2000.

[59] Pike C. First-order reversal-curve diagrams and reversible magnetization. Phys Rev B 2003.

[60] Principles of Fluorescence Spectroscopy | Springer n.d.

[61] Chao Y, Zhang T. Optimization of fixation methods for observation of bacterial cell morphology and surface ultrastructures by atomic force microscopy. TL - 92. Appl Microbiol Biotechnol 2011;92 VN - r:381–92.

[62] Lalatonne Y, Richardi J, Pileni MP. Van der Waals versus dipolar forces controlling mesoscopic organizations of magnetic nanocrystals. Nat Mater 2004;3:121–5.

[63] Weinstein JS, Varallyay CG, Dosa E, Gahramanov S, Hamilton B, Rooney WD, et al. Superparamagnetic iron oxide nanoparticles: diagnostic magnetic resonance imaging and potential therapeutic applications in neurooncology and central nervous system inflammatory pathologies, a review. J Cereb Blood Flow Metab 2010.

[64] Cho N-H, Cheong T-C, Min JH, Wu JH, Lee SJ, Kim D, et al. A multifunctional core-shell nanoparticle for dendritic cell-based cancer immunotherapy. Nat Nanotechnol 2011.

[65] Koch SJ, Thayer GE, Corwin AD, De Boer MP. Micromachined piconewton force sensor for biophysics investigations. Appl Phys Lett 2006;89.

[66] Brinker CJ, Scherer GW. Sol-gel Science: The Physics and Chemistry of Sol-gel Processing. Gulf Professional Publishing; 1990.

[67] Beleggia M, Tandon S, Zhu Y, Graef DM. On the magnetostatic interactions between nanoparticles of arbitrary shape. J Magn Magn Mater 2004;278:270–84.

[68] Donaldson K, Poland CA. Nanotoxicity: challenging the myth of nano-specific toxicity. Curr Opin Biotechnol 2013;24:724–34.

[69] Kasprzak KS, FW S, Salnikow K. Nickel carcinogenesis. TL - 533. Mutat Res 2003;533 VN - :67–97.

[70] Costa M, Abbracchio MP, J S-H. Factors influencing the phagocytosis, neoplastic transformation, and cytotoxicity of particulate nickel compounds in tissue culture systems 1981.

[71] Lee YW, Klein CB, Kargacin B, Salnikow K. Carcinogenic nickel silences gene expression by chromatin condensation and {DNA} methylation: a new model for epigenetic carcinogens. 1995.

[72] Murphy FA, Poland CA, Duffin R, T A-JK, Hanene A-B, Nunes A, et al. Length-dependent retention of carbon nanotubes in the pleural space of mice initiates sustained inflammation and progressive fibrosis on the parietal pleura. Am J Pathol 2011;178:2587–600.

[73] Schinwald A, Murphy FA, Adriele P-M, Poland CA, Byrne F, Movia D, et al. The threshold length for fiber-induced acute pleural inflammation: shedding light on the early events in asbestos-induced mesothelioma. Toxicol Sci 2012;128:461–70.

[74] O'Shea JJ, Ma A, Lipsky P. Cytokines and autoimmunity. Nat Rev Immunol 2002;2:37–45.

[75] Kindt TJ, Goldsby RA, Osborne BA, Kuby J. Kuby Immunology. W. H. Freeman; 2007.

[76] Gref R, Domb A, Quellec P, Blunk T, Müller RH, Verbavatz JM, et al. The controlled intravenous delivery of drugs using PEG-coated sterically stabilized nanospheres. Adv Drug Deliv Rev 2012.

[77] Ghibelli L, Mathur S. Biological interactions of oxide nanoparticles: The good and the evil. MRS Bull 2014;39:949–54.

[78] Hermanson GT. Bioconjugate Techniques. Academic Press; 2013.

[79] Methods for etching a less reactive material in the presence of a more reactive material 1994.

[80] Torchilin VP, Trubetskoy VS. Which polymers can make nanoparticulate drug carriers long-circulating? TL - 16. Adv Drug Deliv Rev 1995;16 VN - r.

[81] Byrne F, Prina-Mello A, Whelan A, Mohamed BM, Davies A, Gun'ko YK, et al. High content analysis of the biocompatibility of nickel nanowires. J Magn Magn Mater 2009.

[82] Tewari PH, Campbell AB. Temperature dependence of point of zero charge of cobalt and nickel oxides and hydroxides TL - 55. J Colloid Interface Sci 1976;55 VN - r.

[83] Tanaka Y, Saito H, Tsutsumi Y, Doi H, Nomura N, Imai H, et al. Effect of {pH} on the interaction between zwitterions and titanium oxide. J Colloid Interface Sci 2008.

[84] De Gennes PG. Conformations of Polymers Attached to an Interface. Macromolecules 1980;13:1069–75.

[85] Jeon S., Lee J., Andrade J., De Gennes P. Protein—surface interactions in the presence of polyethylene oxide. J Colloid Interface Sci 1991;142:149–58.

[86] Eliaz N, editor. Applications of Electrochemistry and Nanotechnology in Biology and Medicine I. vol. 52. New York, NY: Springer New York; 2011.

[87] Tanaka Y, Doi H, Kobayashi E, Yoneyama T, Hanawa T. Determination of the Immobilization Manner of Amine-Terminated Poly(Ethylene Glycol) Electrodeposited on a Titanium Surface with XPS and GD-OES. Mater Trans 2007;48:287–92.

[88] Bureau C, Chong DP. Density functional calculations of core-electron binding energies of amines. Application to {(CH} 3) 3 N□ Ni and {(CH} 3) 4 N+□ Ni 1997.

[89] Murphy FA, Schinwald A, Poland CA, Donaldson K. The mechanism of pleural inflammation by long carbon nanotubes: interaction of long fibres with macrophages stimulates them to amplify pro-inflammatory responses in mesothelial cells. Part Fibre Toxicol 2012.

[90] Hornung V, Bauernfeind F, Halle A, Samstad EO, Kono H, Rock KL, et al. Silica crystals and aluminum salts activate the {NALP3} inflammasome through phagosomal destabilization. Nat Immunol 2008.

[91] Costantini LM, Gilberti RM, Knecht DA. The phagocytosis and toxicity of amorphous silica. PLoS One 2011;6.

[92] Gilberti RM, Knecht DA. Macrophages phagocytose nonopsonized silica particles using a unique microtubule-dependent pathway. Mol Biol Cell 2015;26:518–29.

[93] 2013 International Conference on Biological, Medical and Chemical Engineering (BMCE2013). DEStech Publications, Inc; 2014.

[94] Arnida, MM J-A, Ray A, Peterson CM, Ghandehari H. Geometry and surface characteristics of gold nanoparticles influence their biodistribution and uptake by macrophages. Eur J Pharm Biopharm Off J Arbeitsgemeinschaft F{"}{u}r Pharm Verfahrenstechnik {eV} 2011;77:417–23.

[95] Champion JA, Mitragotri S. Role of target geometry in phagocytosis. TL - 103. Proc Natl Acad Sci U S A 2006;103 VN - :4930–4.

[96] Rajendran L, Kn"olker H-J, Simons K. Subcellular targeting strategies for drug design and delivery. Nat Rev Drug Discov 2010.

[97] Goodman TT, Chen J, Matveev K, Pun SH. Spatio-temporal modeling of nanoparticle delivery to multicellular tumor spheroids. Biotechnol Bioeng 2008.

[98] Vivès E, Schmidt J, Pèlegrin A. Cell-penetrating and cell-targeting peptides in drug delivery. TL - 1786. Biochim Biophys Acta 2008;1786 VN -:126–38.

[99] Singh R, Lillard JW. Nanoparticle-based targeted drug delivery. TL - 86. Exp Mol Pathol 2009;86 VN - r:215–23.

[100] Wiley: Cell and Molecular Biology: Concepts and Experiments, 7th Edition - Gerald Karp n.d.

[101] Miyamoto S, Teramoto H, Coso OA, Gutkind SJ, Burbelo PD, Akiyama SK, et al. Integrin function: molecular hierarchies of cytoskeletal and signaling molecules. J Cell Biol 1995;131:791–805.

[102] Yamada KM, Miyamoto S. Integrin transmembrane signaling and cytoskeletal control. Curr Opin Cell Biol 1995;7:681–9.

[103] Danhier F, Vroman B, Lecouturier N, Crokart N. Targeting of tumor endothelium by {RGD-grafted} {PLGA-nanoparticles} loaded with paclitaxel 2009.

[104] Natarajan A, Gruettner C, Ivkov R. {NanoFerrite} particle based radioimmunonanoparticles: binding affinity and in vivo pharmacokinetics 2008.

[105] Conner SD, Schmid SL. Regulated portals of entry into the cell. TL - 422. Nature 2003;422 VN - :37–44.

[106] Verma A, Stellacci F. Effect of Surface Properties on {Nanoparticle–Cell} Interactions. Small 2010;6:12–21.

[107] Illinois UDALAP of of CE and C& SBU of, Michigan AAJLAP of CEU of. Receptors : Models for Binding, Trafficking, and Signaling: Models for Binding, Trafficking, and Signaling. Oxford University Press, USA; 1993.

[108] Wyllie AH. Apoptosis and carcinogenesis. Eur J Cell Biol 1997;73:189–97.

[109] Ruoslahti E, Pierschbacher MD. New perspectives in cell adhesion: {RGD} and integrins. Sci {(New} York, {NY)} 1987;238:491–7.

[110] Mizejewski GJ. Role of Integrins in Cancer: Survey of {Expression Patterns}. Proc Soc Exp Biol Med 1999.

[111] Prina-Mello A, Diao Z, Coey J. Internalization of ferromagnetic nanowires by different living cells. J Nanobiotechnology 2006.

[112] Kelf TA, Sreenivasan VKA, Sun J, Kim EJ, Goldys EM, Zvyagin A V. Non-specific cellular uptake of surface-functionalized quantum dots. Nanotechnology 2010.

[113] Peer D, Karp JM, Hong S, Farokhzad OC. Nanocarriers as an emerging platform for cancer therapy 2007.

[114] Folkman J, Moscona A. Role of cell shape in growth control 1978.

[115] null, Mrksich M, Huang S, Whitesides GM, Ingber DE. Geometric control of cell life and death 1997.

[116] Schinwald A, Chernova T, Donaldson K. Use of silver nanowires to determine thresholds for fibre length-dependent pulmonary inflammation and inhibition of macrophage migration in vitro. Part Fibre Toxicol 2012.

[117] Montet X, Funovics M, Montet-Abou K, Weissleder R, Josephson L. Multivalent Effects of RGD Peptides Obtained by Nanoparticle Display. J Med Chem 2006.

[118] Miyamoto S, Akiyama SK, Yamada KM. Synergistic roles for receptor occupancy and aggregation in integrin transmembrane function. Sci {(New} York, {NY)} 1995;267:883–5.

[119] Daniel WA, Wójcikowski J. Lysosomal trapping as an important mechanism involved in the cellular distribution of perazine and in pharmacokinetic interaction with antidepressants. Eur Neuropsychopharmacol 1999;9:483–91.

[120] Chen VY, Rosania GR. The great multidrug-resistance paradox. {ACS} Chem Biol 2006;1:271–3.

[121] Kornhuber J, Henkel AW, Groemer TW, St"adtler S, Welzel O, Tripal P, et al. Lipophilic cationic drugs increase the permeability of lysosomal membranes in a cell culture system. J Cell Physiol 2010;224:152–64.

[122] Keshoju K, Xing H, Sun L. Magnetic field driven nanowire rotation in suspension. Appl Phys Lett 2007;91.

[123] Leist M, J“a”attel"a M. Triggering of apoptosis by cathepsins. Cell Death Differ 2001;8:324–6.

[124] Boya P, Andreau K, Poncet D, Zamzami N, Perfettini J-L, Metivier D, et al. Lysosomal Membrane Permeabilization Induces Cell Death in a Mitochondrion-dependent Fashion. J Exp Med 2003.

[125] Erdal H, Berndtsson M, Castro J, Brunk U, Shoshan MC, Linder S. Induction of lysosomal membrane permeabilization by compounds that activate p53-independent apoptosis. Proc Natl Acad Sci U S A 2005.

[126] Lutolf MP, Hubbell JA. Synthetic biomaterials as instructive extracellular microenvironments for morphogenesis in tissue engineering. Nat Biotechnol 2005.

[127] Kuo CK, Smith ML. Biomaterial design motivated by characterization of natural extracellular matrices. {MRS} Bull 2014.

[128] Yeung T, Georges PC, Flanagan LA, Marg B, Ortiz M, Funaki M, et al. Effects of substrate stiffness on cell morphology, cytoskeletal structure, and adhesion. Cell Motil Cytoskeleton 2005;60:24–34.

[129] Rowlands AS, George… PA. Directing osteogenic and myogenic differentiation of {MSCs:} interplay of stiffness and adhesive ligand presentation 2008.

[130] Engler AJ, Sen S, Sweeney HL, Discher DE. Matrix elasticity directs stem cell lineage specification 2006.

[131] Atala A. Engineering tissues, organs and cells. J Tissue Eng Regen Med 2007;1:83–96.

[132] Sniadecki NJ, Desai RA, Ruiz SA, Chen CS. Nanotechnology for {Cell–Substrate} Interactions. Ann Biomed Eng 2006.

[133] Underhill GH, Chen AA, Albrecht DR, Bhatia SN. Assessment of hepatocellular function within {PEG} hydrogels. Biomaterials 2007.

[134] Paszek MJ, Zahir N, Johnson KR, Lakins JN, Rozenberg GI, Gefen A, et al. Tensional homeostasis and the malignant phenotype. Cancer Cell 2005;8:241–54.

[135] Kong H, JY W. Materials for biological modulation, sensing, and imaging. Mater Biol Modul Sensing, Imaging 2014.

[136] Woo KM, Chen VJ, Ma PX. Nano-fibrous scaffolding architecture selectively enhances protein adsorption contributing to cell attachment 2003.

[137] Ma Z, Kotaki M, Inai R, Ramakrishna S. Potential of nanofiber matrix as tissue-engineering scaffolds 2005.

[138] Burdick JA, Anseth KS. Photoencapsulation of osteoblasts in injectable {RGD-modified} {PEG} hydrogels for bone tissue engineering 2002.

[139] Hern DL, Hubbell JA. Incorporation of adhesion peptides into nonadhesive hydrogels useful for tissue resurfacing 1998.

[140] Feng ZQ, Chu X, Huang NP, Wang T, Wang Y, Shi X. The effect of nanofibrous galactosylated chitosan scaffolds on the formation of rat primary hepatocyte aggregates and the maintenance of liver function 2009.

[141] Lee JH, Lee K, Moon SH, Lee Y, Park… TG. {All-in-One} {Target-Cell-Specific} Magnetic Nanoparticles for Simultaneous Molecular Imaging and {siRNA} Delivery 2009.

[142] Ito A, Ino K, Kobayashi T, Honda H. The effect of {RGD} peptide-conjugated magnetite cationic liposomes on cell growth and cell sheet harvesting. Biomaterials 2005;26:6185–93.

[143] Ranucci CS, Kumar A, Batra SP, Moghe P V. Control of hepatocyte function on collagen foams: sizing matrix pores toward selective induction of {2-D} and {3-D} cellular morphogenesis 2000.

[144] Giraud-Guille M-M, Besseau L, Martin R. Liquid crystalline assemblies of collagen in bone and in vitro systems. J Biomech 2003;36.

[145] Kim D-HH, Lipke EA, Kim P, Cheong R, Thompson S, Delannoy M, et al. Nanoscale cues regulate the structure and function of macroscopic cardiac tissue constructs. Proc Natl Acad Sci U S A 2010;107:565–70.

[146] Sniadecki NJ, Lamb CM, Liu Y, Chen CS, Reich DH. Magnetic microposts for mechanical stimulation of biological cells: fabrication, characterization, and analysis. TL - 79. Rev Sci Instrum 2008;79 VN - r:44302.

[147] Walsh JF, Manwaring ME, Tresco PA. Directional neurite outgrowth is enhanced by engineered meningeal cell-coated substrates. Tissue Eng 2005;11:1085–94.